Designing and Analyzing Low-Complexity Energy-Efficient Visible Light Communication Systems for IoT and UAV Applications

A THESIS
SUBMITTED IN PARTIAL FULFILLMENT OF THE REQUIREMENTS
FOR THE DEGREE OF

Doctor of Philosophy

By

Dil Nashin Anwar
PhD17105

under the guidance of

Prof. Anand Srivastava
Professor, IIIT-Delhi

INDRAPRASTHA INSTITUTE *of*
INFORMATION TECHNOLOGY **DELHI**

Department of Electronics & Communication Engineering
Indraprastha Institute of Information Technology, Delhi
June, 2023

Designing and Analyzing Low-Complexity Energy-Efficient Visible Light Communication Systems for IoT and UAV Applications

By

Dil Nashin Anwar

PhD-17105

under the guidance of

Dr. Anand Srivastava
Professor, IIIT-Delhi

submitted
in partial fulfillment of the requirements for the degree of Doctor of Philosophy

to
Indraprastha Institute of Information Technology, Delhi
June, 2023

Dedication

To My Loving Family & Teachers

for encouraging me to pursue my dreams

Certificate

This is to certify that the thesis titled "***Designing and Analyzing Low-Complexity Energy-Efficient Visible Light Communication Systems for IoT and UAV Applications***" being submitted by **Dil Nashin Anwar** to the Indraprastha Institute of Information Technology-Delhi, for the award of the degree of **Doctor of Philosophy**, is an original research work carried out by her under my supervision. In my opinion, the thesis has reached the standard, fulfilling the requirements of the regulations relating to the degree. The results contained in this thesis have not been submitted in part or full to any other university or institute for the award of any degree or diploma.

Anand

Prof. Anand Srivastava

Department of Electronics & Communication Engineering
Indraprastha Institute of Information Technology, Delhi

Declaration

This is to be certified that the dissertation entitled "***Designing and Analyzing Low-Complexity Energy-Efficient Visible Light Communication Systems for IoT and UAV Applications***" being submitted by **Dil Nashin Anwar** to the Indraprastha Institute of Information Technology-Delhi, for the award of the degree of **Doctor of Philosophy**, is a bonafide work carried out by me. This research work has been carried out under the supervision of Prof. Anand Srivastava. The study pertaining to this dissertation has not been submitted in part or in full, to any other University or Institution for the award of any other degree or diploma.

Prof. Anand Srivastava

Department of Electronics & Communication Engineering
Indraprastha Institute of Information Technology, Delhi

Acknowledgments

While pursuing PhD and sailing through the inevitable ups and downs of a PhD degree, I learnt many invaluable lessons that will benefit me throughout my life. In addition to research and technical abilities, I have learned how to manage a variety of responsibilities and unforeseen circumstances while juggling through my personal and professional lives. I can certainly say I am much more confident and comfortable to drive any research project independently. I take this opportunity to express my sincere gratitude to everyone who helped make this PhD thesis possible.

To begin with, I would like to say thanks to ***Almighty Allah*** for all the blessings He has bestowed upon me.

I would like to express my special gratitude to **Prof. Anand Srivastava** without whom the completion of this thesis work would not have been possible. I would sincerely like to thank him for his valuable guidance, scholarly input and the consistent encouragement I have received throughout the research work. His infectious delight and love for research inspired me to push through the challenging phases of my PhD pursuit.

This work would not have been possible without support from **Visvesvarya PhD Scheme**, India; thank you for believing in my technical acumen and providing me PhD fellowship. I would also like to thank **Dr. Vivek Ashok Bohara** and **Dr. Abhijit Mitra** (IIT-D) for serving as my committee member and taking out their valuable time for their insightful feedback and useful suggestions on my work.

My word of thanks to my friends Dr. Rizwana Ahmad, Dr. Antra Saxena, Dr. Anand Singh and all my colleagues at COE-LiFi lab (https://coelifi.iiitd.ac.in/people.html) for their constant support and motivation. I am grateful to them for all their help.

I express my most profound appreciation to my husband (Mohammad Arshad Iqubal), my father (A.R. Anwar), my mother (F. Naz), my siblings and my in-laws for their unconditional love, support, and belief in me. I dedicate this thesis to them as a token of gratitude.

Dna

Dil Nashin Anwar
PhD17105

ABSTRACT

Keywords- **Light Communication (LC), Visible Light Communication (VLC), Colour Shift Keying (CSK), Probabilistic Shaping (PS), LiFi, WiFi, IoT, Constellation Optimization, Optical-OFDM, OFDMA, FHT/IFHT, wavelength division multiplexing (WDM), Unmanned Aerial Vehicle (UAV), holographic light shaping diffuser (LSD), RGB LED, User Mobility, Coverage Probability**

IoT interconnect everyday objects via the internet, enabling them to send and receive data by transceivers embedded in it. The number of IoT devices is estimated to reach billions, contributing to half of the global connected devices and connections in the near future. This massive number of connected devices are employed in diverse domains and areas, such as smart cities, smart homes, hospitals, healthcare devices, industries, and transportation systems. Various IoT applications require a vast number of connections per unit area, high aggregate bandwidth, ubiquitous coverage, low power consumption, sustainable energy resources, low latency, low control overhead and a high level of security. With the advent of the emerging IoT paradigm, the already crowded RF spectrum is not expected to serve the projected several billions of IoT devices. A promising communication solution that can address these challenges is light communication.The exponentially increasing demand for wireless data with the onset of wireless devices and internet of things (IoT) everywhere has created scarcity in the radio frequency (RF) spectrum. The existing overcrowded RF spectrum has impelled the hunt for newer technologies. Visible light communication (VLC), having a large amount of unlicensed spectrum, is an emergent alternative technology to supplement the existing short-range wireless systems for faster data transmissions. VLC has numerous unrivalled potentials along with immunity to every day electromagnetic interference, for instance, low energy consumption, data confinement for higher-level security and cheaper installation with existing illumination infrastructure. However, owing to power and hardware limitations of the resource constrained devices (such as IoT and Unmanned Aerial Vehicles (UAVs)), it requires simple, low power, low complex, energy-efficient communication technology. In this dissertation, we have tried to utilize VLC and red, green and blue (RGB) LED in order to support communication with resource constrained devices and their aforementioned requisite.

Firstly, we propose a generalized enhancement scheme for different versions of color shift keying (CSK) modulation schemes, we analyze the performance of CSK modulation schemes with probabilistic shaping (PS) of input data. Specifically, we have considered three variants of CSK with respect to receiver structure namely CSK with one photodetector (PD)

(CSK-1PD), CSK with three PDs (CSK-3PD) and CSK with one avalanche PD (CSK-1APD). The proposed work comprises of developing algorithms to obtain the optimum probability order for maximizing the received signal-to-noise ratio (SNR) gain.

Secondly, in order to support IoT sensor networks with lower cost and higher performance, the low-cost version of standard CSK modulation scheme having single photodetector (PD) at the receiver has been utilized. This work revolves around optimizing the constellation points of CSK-1PD to achieve a more power-efficient modulation scheme.

Thirdly, motivated by the diverse requirements of the heterogeneous users i.e. LiFi users and IoT devices, we propose novel green communication schemes that can be used for the coexistence of LiFi users and light communication (LC) enabled IoT devices under a common LiFi access point. The proposed coexistence schemes utilize the amalgamation of wavelength division multiplexing, OFDMA, Hartley transform based DCO-OFDM, null DC element, interleaved subcarrier mapping, modified data sequence to achieve concurrent interference-free, low complex and reliable communication. Additionally, as the multiple access (MA) techniques affect the choice of modulation techniques and overall performance in the system, an analytical delay and throughput framework to corroborate the decision of an appropriate combination of MA and modulation techniques in the coexistence scheme has been included.

Lastly, we propose energy and user mobility aware three-dimensional (3-D) deployment of VLC enabled UAV so that maximum coverage of users while ensuring fairness is achieved. Moreover, the VLC enabled UAV's coverage area to serve ground users has been enhanced with holographic light-shaping diffusers (LSD). A novel RGB LED solution based on light sensitivity to the human eye is proposed to increase the coverage area for the night scenario.

The proposed frameworks in this dissertation can be utilized in LiFi standards, especially for resource constrained devices such as IoT and UAVs. It will be helpful for LiFi communication engineers to support an energy-aware green communication at the physical layer and deployment level.

Table of contents

List of figures

List of tables

Nomenclature

Acronyms

2-D	Two Dimension
3-D	Three-Dimensional
ACO-OFDM	Asymmetrically Clipped Optical-Orthogonal Frequency-Division Multiplexing
ADC	Analog-to-Digital Converter
AIR	Achievable Information Rate
APD	Avalanche Photodetector
APs	Access Points
AWGN	Additive White Gaussian Noise
BER	Bit Error Rate
BLMS	Block Least Mean Square
BPSK	Binary Phase Shift Keying
BSs	Base Stations
C-Band	Compromise-Band
CBCs	Color Band Combinations
CCDF	Complementary Cumulative Distribution Function
CP	Cyclic Prefix
EMI	Channel State Information
CSK-1APD	CSK with one APD at the Receiver
CSK-1PD	CSK with one PD at the Receiver
CSK-3PD	CSK with three PDs at the Receiver
CSK	Color Shift Keying
DAC	Digital-to-Analog Converter
DC	Direct Current

DCE	DC element
DCO-OFDM$^{\mathrm{F}}$	DFT based DCO-OFDM
DCO-OFDM$^{\mathrm{H}}$	DHT based DCO-OFDM
DCO-OFDM	Direct-Current biased Optical OFDM
DFT	Discrete Fourier Transform
DHT	Discrete Hartley Transform
DM	Distribution Matcher
EH	Energy Harvesting
EMI	Electromagnetic Interference
ESE	Effective Spectral Efficiency
ES	Exhaustive Search Based Strategy
FBLMS	Fast Block Least Mean Square
FD	Frequency-Domain
FDPS	Frequency Domain Pulse Shaping
FEC	Forward Error Correction
FFT	Fast Fourier Transform
FHT	Fast Hartley Transform
FMC	Fair Maximum Coverage
FoV	Field of View
FSM	Finite-State Markov
FU	Farthest User Based Strategy
FWHM	Full Width Half Maximum
GUI	Graphical User Interface
HF	High Frequency
i.i.d.	independent and identically distributed
IDHT	Inverse Discrete Hartley Transform
IFFT	Inverse Fast Fourier Transform
IFHT	Inverse Fast Hartley Transform
IM/DD	Intensity Modulation with Direct Detection
IoT	Internet of Things
IR	infrared

K-Band	Kurtz-Band
Ku-Band	Kurtz (German for short) Under-Band
L-Band	Long-Band
LC	Light Communication
LED	Light Emitting Diodes
LF	Low Frequency
LiFi	Light Fidelity
LIoT	Light communication enabled Internet of Things
LMS	Least Mean Square
LSD	Light Shaping Diffuser
LWIR	Long-wave infrared
MAC	Medium Access Control
MA	Multiple Access
MDS	Modified Data Sequence
MED	Minimum Euclidean Distance
MF	Moderate Frequency
MIMO	Multi-Input Multi-Output
mmWave	millimeter Wave
MSE	Mean Square Error
MWIR	Medium-wave infrared
NDCE	null DC element
NLMS	Normalized Least Mean Square
NLOS	Non-Line-of-Sight
O-OFDMA	Optical Orthogonal Frequency Division Multiple Access
O-OFDM	Optical Orthogonal Frequency-Division Multiplexing
OCP(u,m,e,p)	Optimized constellation points for Uniform, Maxwell, Exponential and Pareto input distribution, respectively
OCPp	Optimized constellation points with Pareto distributed input data
OCPs	Optimized Constellation Points
OCPu	Optimized constellation points for uniform input data
OFDMA	Orthogonal Frequency Division Multiple Access

OFDM	Orthogonal Frequency Division Multiplexing
OOK	On-Off Keying
OPO	Optimum Probability Order
OWC	Optical Wireless Communication
P-Band	Penetration-Band
PAM_{Bp}	PAM with bipolar constellation symbols
PAM_{Up}	PAM with unipolar constellation symbols
PAM	Pulse-Amplitude Modulation
PAPR	Peak-to-Average-Power Ratio
PDF	Probability Density Function
PD	Photo-Detector
PHY	Physical Layer
PIP	Point-in-Polygons
PPM	Pulse Position Modulation
PS-CSK	CSK with probabilistically shaped input data
PSD	Power Spectral Density
PS	Probabilistic Shaping
QAM	Quadrature-Amplitude-Modulation
QoS	Quality of Service
R-OCP(u,m,e,p)	Optimized constellation points with relaxed white tone for Uniform, Maxwell, Exponential and Pareto input distribution, respectively
R-OCPs	Optimized constellation points with relaxed white tone
RF	Radio Frequency
RGB	Red, Green, and Blue
	RMS
RMSE	Root Mean Square Error
RUs	Resource Units
RWP	Random Waypoint
S-Band	Short-Band
S-OCPs	Optimized constellation points obtained with strict white tone
SER	Symbol Error Rate

SE	Spectral Efficiency
SHF	Super High Frequency
SNR	Signal-to-Noise Ratio
SRM	Space Reduction Method
SU	Shifting UAV Based Strategy
SWIR	Short-wave infrared
TDMA	Time Division Multiple Access
TDPS	Time Domain Pulse Shaping
TD	Time-Domain
TIA	Trans-impedance amplifier
TLED	Trichromatic LED
UAVs	Unmanned Aerial Vehicles
$\mathrm{UB_r}$	RF-based UAV-BS
$\mathrm{UB_v}$	VLC-enabled UAV-BS
UHF	Ultra High Frequency
UI	User Interface
UL	Uplink
UV	Ultra Violet
VHF	Very High Frequency
VLC	Visible Light Communication
VLF	Very Low Frequency
WDM	Wavelength Division Multiplexing
X-Band	X for “crosshair” (used in WW2 for fire control radar)-Band
ZA-LMS	Zero Attracting Least Mean Square

Symbols

$(\bar{x},\bar{y})$	Average chromaticity coordinates of the transmitted symbols
$(\bar{x}_d,\bar{y}_d)$	Chromaticity coordinates of desired average white tone
(x_e,y_e)	Chromaticity coordinates of extra RGB LED
α	Optimization weight parameter
$\bar{U}_e$	Average number of effective users covered
β	Optimization tuning parameter
$\boldsymbol{\rho}$	PD responsivity vector consisting of red, green and blue LEDs responsivity, respectively
ΔT	Delay between the LOS and onset of the diffused signals
η	Power conversion efficiency of the indoor solar cell
Γ	Reflectivity of the walls
γ	Instantaneous received SNR
Γ_i	Detection threshold between transmitted symbols s_i and $s_j = s_{i+1}$
γ_b	SNR per bit
Γ_{ij}	Detection threshold between symbols s_i and s_j
λ	Distribution parameter of source distributions
$\mathbb{C}$	Set of photocurrent of all the transmitted M constellation points of M-CSK
$\mathbb{D}_I$	A set of energy-autonomous LC enabled IoT devices
$\mathbb{P}_p$	set of points approximating the white region of 1931 CIE chromaticity diagram
$\mathbb{P}_{SNR}$	Potential population set having SER of feasible solutions at design SNR
$\mathbb{U}_L$	A set of LiFi users
$\mathbf{X0}$	Initial estimate of the constellation point
$\mathbf{X}$	Constellation points in the form of matrix
$\mathbf{X}_o$	Optimized constellation points in matrix notation
$\mathscr{F}(\mathbf{X})$	Objective Function
$\mathscr{S}$	Average service time
$\mathfrak{d}$	Set consisting of all pairwise Euclidean distances
${}^{\boldsymbol{n}}\boldsymbol{P}_{\boldsymbol{r}}$	Permutation

$\overline{\gamma}$	Average received SNR
ϕ	Angle of irradiation
$\Phi_{1/2}$	LED half intensity angle
ψ	Angle of incidence at the PD
Ψ_c	Field of View the PD
ρ	Responsivity of the PD
σ	Random walk parameter
σ_{sh}^2	shot noise variance
σ_{th}^2	thermal noise variance
B	Noise bandwidth
$\wp$	refractive index of the concentrator
ξ	Inverse function of CCDF for a given probability
ζ	PAPR threshold value
A_{room}	Area of the room
A_{PD}	Area of the PD
AP_L	Common LiFi AP
d	Distance between the transmitter (LED) and receiver (PD)
D_I	A single IoT device
d_i	Euclidean distance between transmitted symbols s_i and $s_j = s_{i+1}$
E	Illuminance at the ground users
E_{th}	Illuminance threshold
f_c	Cut-off frequency of the diffuse optical channel
G_{c}	Gain of the optical concentrator
G_{f}	Gain of the optical filter
$H(f)_{\text{LOS}}$	Frequency response of the line-of-sight optical channel
$H(f)_{\text{LOS}}$	Frequency response of the non-line-of-sight optical channel
$H(f)_{\text{VLC}}$	Frequency response of the optical channel
$h(t)$	Impulse response of the optical channel
$h_{\text{LOS}}(t)$	Impulse response of the line-of-sight optical channel
$h_{\text{NLOS}}(t)$	Impulse response of the non-line-of-sight optical channel

I	Sub-carrier mapping factor
I_2	Noise bandwidth factor
I_{rec}	Electrical current generated at the PD to an incident optical power
I_B	Background current
I_c	Electrical current generated at the PD to an incident optical power
k_B	Boltzmann's constant
K_m	Maximum number of IoT devices
L_o	Optimum altitude achieved by VLC enabled UAV
M	Constellation size/order
m	Lambertian order
$n(t)$	Additive white Gaussian noise
$O(.)$	Big O notation describes complexity
$p(s_i)$	Probability of occurrence of symbol s_i
P_{opt}	Received optical power
P_e	Average BER
P_T	Total optical power
P_b	Transmitted optical power of blue LED
P_g	Transmitted optical power of green LED
P_r	Transmitted optical power of red LED
q	electron charge
$R(\phi)$	Lambertian radiation intensity
R	Maximum coverage radius achieved by VLC enabled UAV
R_l	Receiver equivalent load resistance
SE_e	Normalized effective spectral efficiency
SNR_{th}	Minimum average received SNR required at the LOS user end for reliable communication from UB_v
T	UB_v operational time
T_k	Absolute temperature in Kelvin
$t_{up}(k)$	k^{th} update interval
U_L	A single LiFi user
v_n	Number of polygon vertices

V_λ	Luminous efficacy of the human eye
$x'(n')$	TD discrete data sequence before precoding at transmitter
$x(0)$	DC element of OFDM
$X(k)$	FD OFDM discrete data sequence at transmitter
$x(n)'$	TD OFDM discrete MDS at transmitter
$x(n)$	TD OFDM discrete data sequence at transmitter
$x(t)$	TD continuous data sequence at transmitter
$Y(k)$	FD OFDM discrete data sequence at receiver
$y(n)$	TD OFDM discrete data sequence at receiver
$y(t)$	TD continuous data sequence at receiver
Y_1	Average tone luminance
z	Altitude of the VLC transmitter

Chapter 1

Introduction

The chapter starts with a discussion on the motivation of this thesis work. Section 1.2 presents a brief background of the visible light communication (VLC) and enumerates a few auxiliary VLC applications. Section 1.3 provides a quick summary of a typical VLC system. Section 1.4 gives a brief overview of the recent research progress and related works in VLC. Section 1.5 discusses the possible research gap based on the literature survey. Section 1.6 states the major contributions of this dissertation and relevant publications. The overall thesis organization is provided in Section 1.7.

1.1 Motivation

The excessive proliferation of wireless devices in day-to-day life has exponentially increased the demand for wireless data transmission. The advent of intensive data rate applications fuels the quest for designing ultra-high data rate wireless systems. Industries have forecasted an enormous surge in the number of gadgets, connections, and internet users worldwide. Over 70% of the global population will have mobile connectivity by 2023, machine to machine (M2M) connections and internet of things (IoT) will contribute to half of the global connected devices and connections by 2023 [1]. ARM expects a trillion new IoT devices to be produced by 2035 [2]. Overall, the devices and connections are growing faster (10%) than both the population (1.0%) and the internet users (6%). Therefore, resulting in more number of devices and connections per household and per capita [1]. These rapidly growing number of devices and connections, along with internet data traffic, have created a massive spectrum crunch in the radio frequency (RF) band. Further, research studies forecast that the entire RF spectrum-based technologies cannot meet the tremendous growth of data rate requirement and connections [3]. There is an emergent need to move beyond the existing overcrowded RF spectrum and explore other parts of the electromagnetic spectrum (shown in Fig.1.1). In order to meet the expectations of fifth-generation (5G) and beyond-5G (B-5G) communication, there is shift towards higher and higher frequencies (e.g., millimeter (mm)-wave, terahertz (THz)). However, the wavelength becomes of the order of 1 mm or less when frequencies above 300 GHz are used, making communications more susceptible to absorption in matter and air. Additionally, as the communication frequency is increased, it becomes closer to that of visible light and starts showing characteristics similar to that of visible light [4]. Thus, the availability of a large amount of unlicensed visible light and near infrared spectrum, i.e. 430-750 THz and 250-430 THz, respectively, led researchers to devise and investigate a new communication technology: light communication (LC) [7, 8] . Moreover, the sixth-generation (6G) communication technology is envisioned to satisfy the demands of the 2030 intelligent information society by supporting green communication, massive heterogeneous device connectivity (e.g., IoTs, M2Ms), seamless coverage, latency reduction, security improvement, higher user quality-of-experience (QoE) level, autonomous, intelligent and sustainable systems. The 6G is envisaged to provide peak data rate of Tbps order, connection density of 10^7 connections/km^2 (approximately 10x of 5G), and area traffic capacity of 1 Gbps/m^2 [5]. LC can become a promising candidate for serving the demands of B-5G and 6G communication systems owing to the numerous advantages discussed below. LC can potentially utilize 600 THz of unlicensed spectrum while providing immunity to RF interference. LC does not interfere with devices operating at 2.4 GHz, thus it can be used in RF sensitive environments such as aeroplanes and hospitals. LC is inherently secure since its signals can not penetrate walls and provide higher spatial reuse due to its confinement to a smaller area. LC consists of light emitting diodes (LEDs) as transmitters utilizing the visible, infrared (IR) and near-infrared spectrum. LC can achieve high speed data rate due to the larger available bandwidth, high switching rate of LEDs and the high data rate achievable modulation schemes. The LED luminaires used for illumination fall under the visible spectrum, thus when visible light becomes a medium for communication, it is known as visible light communication (VLC) [9–11] . However, LC encompasses all light as a medium of communication, so both VLC and IR light-based communication fall under LC [7]. The visible light as a communication medium is less preferred for uplink, as light would be continuously emitting in an upward direction, which is aesthetically not pleasing from a user's perspective. Therefore, either a WiFi or an IR LED can be used for uplink transmission. The signals from both the WiFi and IR LED transmitters are invisible to human eyes and thus do not distract users. Further, for a bidirectional LC, the use of the infrared spectrum is deemed most appropriate in the literature as it completely obliterates the use of RF waves [12, 13]. From this point forward, the abbreviation LC is utilized for bidirectional communication, whereas VLC has generally been preferred throughout the thesis for downlink communication. Additionally, VLC supports green technology since it makes use of the already-existing, energy-efficient lighting infrastructure—specifically, LED luminaires—for communication, which can become

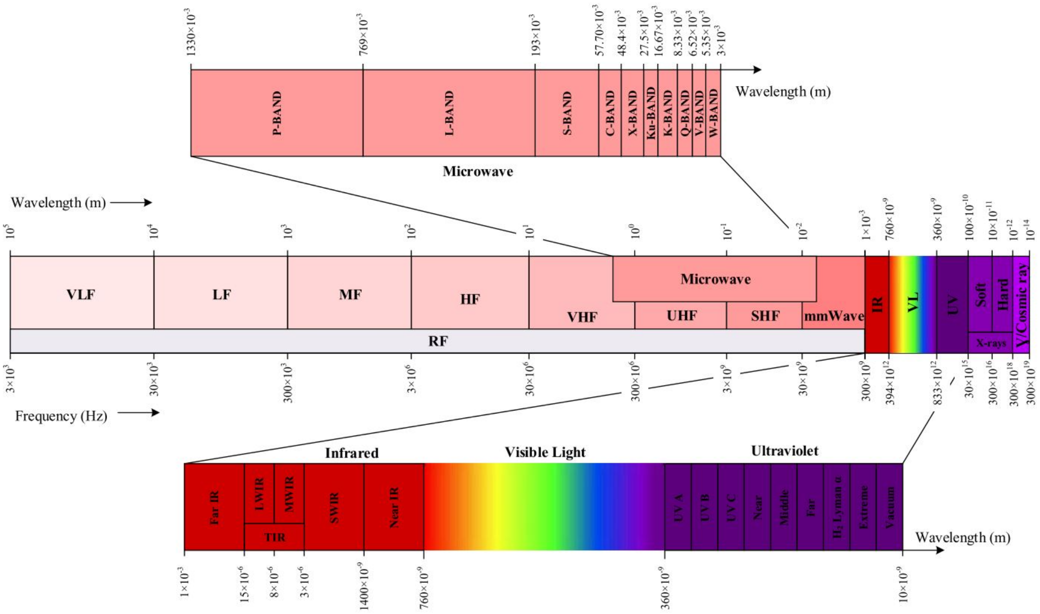

Figure 1.1: Electromagnetic Spectrum [8]

a source for energy harvesting as well. Further, research towards increasing the power conversion efficiency of indoor solar cells would provide compact and low-cost solutions for energy-autonomous VLC receivers. Leveraging the light spectrum for IoT is beneficial as the lighting infrastructure composed of LED luminaires is being adopted extensively to illuminate indoor spaces where IoT communication is most needed [11, 14]. These densely deployed luminaires will act as access points (APs) for the IoT devices to provide a large number of connections per unit area, addressing the challenge of high-density IoT nodes. In literature, indoor high to moderate-speed VLC has been termed as Light Fidelity (LiFi) analogous to WiFi [15]. However, for IoT devices, moderate to low-speed VLC is required.

To pave the way for the development in IoT and beyond, research on 6G wireless networks and their accompanying technological trends has recently received much attention from both academia and industry [16]. As discussed above VLC has the potential to be one of the 6G enabler technologies. VLC will accelerate the applications and deployments of 6G-based IoT networks across the realms of IoT data sensing, device connectivity, wireless communication, and 6G network management [16]. Further, UAVs enhanced with communication capability are considered to play important roles in the 6G networks due to their low cost and flexible deployment [17]. is supposed to be an all-coverage network to provide ubiquitous connections for space, air, ground and underwater [18]. As a consequence, the work in this dissertation attempts to strengthen VLC technology for 6G communication user's experiences and services in devices with limited resources, like IoTs and UAVs.

1.2 VLC Background

The history of optical wireless communication (OWC) can be traced back to ancient Greeks and Romans who used polished shields to send signals by reflecting sunlight during battles [19]. The use of Greek hydraulic semaphores (i.e., use of an apparatus to create a visual signal such as fire, light, sunlight transmitted over distance) dates back to 3rd and 4th century. Also, long distance optical semaphores were used in Europe in 17th and 18 centuries [20]. In 1880, Alexander Graham Bell a well-known scientist invented the photophone, which transmitted speech over several hundred metres using modulated sunlight [22]. In 1960's, IBM studied indoor IR wireless communications [21]. It is worth noting that OWC includes free space optics (FSO) for long-range fixed communications and VLC for short-range communications [23]. This thesis has worked on the VLC aspect of OWC. More recent work in VLC began in 2003 at Nakagawa Laboratory, in Keio University, Japan, using LEDs to transmit data by visible light. The authors Komine and Nakagawa in [24] were motivated by the advancements in solid-state lighting which significantly improved the reliability, lifespan, cost, and energy efficiency of LEDs to develop a digital communication system using white-LEDs for illumination and high-speed communication simultaneously. Since then there have been numerous research activities focused on VLC and subsequently on LC. Consequently, VLC standardization process is conducted within the IEEE 802.15.7 working group. LED lights have already made a name for themselves in illuminating the majority of public and private spaces and are forecasted to cover 84% of illumination infrastructure by the year 2030 [25], thereby assisting VLC to become a ubiquitous technology. The first generation of VLC devices are already available from several enterprises such as PureLiFi, OledComm, Philips, VLNComm and Velmenni. As per neoteric business report, VLC market size is anticipated to reach 80 Billion USD by 2030 [26]. Thus, both IEEE and ITU have initiated efforts for VLC standardization in the form of IEEE 802.15.13 Task Group [27], IEEE 802.11.bb [28] and ITU-T G.vlc [29]. Owing to the several unmatched potentials of VLC such as vast unlicensed bandwidth, existing and increasing LED infrastructure, low power consumption of LEDs, no electromagnetic interference and zero radio exposure to human tissue make LC especially VLC an attractive option for myriad applications, such as:

- Wireless communication: Light can be used to provide wireless connectivity to machine to machine, IoT and LiFi users. VLC can attain low, moderate and very-high-speed wireless connectivity with inherent security. VLC can provide connectivity to indoor [11], outdoor [30, 31], and underwater scenarios [32], either substituting or supplementing RF technology. Currently, VLC can provide a data rate of over 15 Gbps [33] using off-the-shelf LEDs.

  - Indoor: Universities, schools, offices, gaming hubs require seamless high-speed internet access due to higher and constant demand. These indoor scenarios can save money on energy while simultaneously providing high-speed internet access by installing LED lighting.
  - Outdoor: The VLC enabled unmanned aerial vehicles (UAVs) can provide simultaneous communication and illumination for inspection, environmental protection monitoring, first response, urban safety especially at night and emergency communication for disaster recovery [30, 31]. Further, wireless backhaul solution can be improved with VLC [34].
  - Underwater: Acoustic navigation and positioning technology is constrained by bandwidth, whereas RF transmission necessitates a large antenna, high transmitter power, and causes high attenuation (due to the high conductivity of sea water, RF waves cannot properly propagate there). VLC, on the other hand, can provide better data speeds for short-range communication than classic acoustic systems with substantially reduced power consumption [32].

- Smart Cities: IoT plays a huge role in supporting the concept of smart cities. When VLC is integrated in IoT, smart cities can genuinely be transformed [14]. VLC will not only enable large-scale connectivity, but it will also automate many smart city activities such as smart displaying signboards in shopping malls, roads, airports, and bus stops. These signboards formed by an array of LEDs, can be used for broadcasting information by utilizing VLC. VLC can help with efficient navigation and tailored shopping experiences at shopping malls. The potential of true smart cities are infinite with the addition of VLC to this framework.

- Healthcare Industry: The healthcare industry, being one of the most electromagnetic wave-sensitive areas, must adhere to stringent standards. Conventional RF-based communication, for example WiFi is restricted inside hospitals because it can interfere with medical devices such as MRIs and even patient treatment in operation theatres [35]. Li-Fi, on the other hand, provides a viable option for data transfer in electromagnetic Interference (EMI)-sensitive situations [36]. It can also help in robotic surgery and laparoscopy. VLC enabled IoTs and UAVs can further reinforce the Healthcare system.

- V2X communication: Vehicles, street and traffic lights equipped with LEDs can be used to implement VLC on the road. Li-Fi can provide practical solutions and detect scenarios such as pre-crash detection, collisions, lane changes, and traffic signal violations by implementing high-speed communication between vehicle-to-vehicle and vehicle-to-

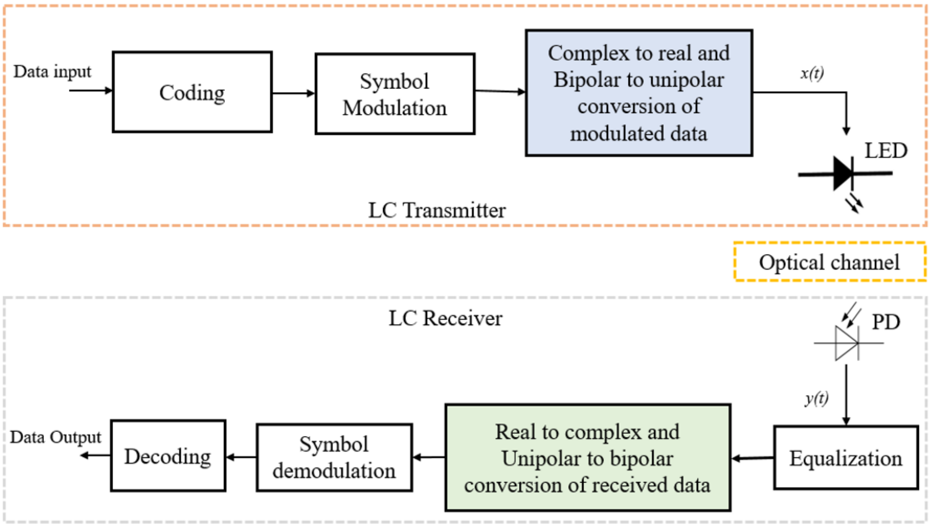

Figure 1.2: A typical VLC system

infrastructure. The current achievements and research challenges associated with the use of VLC for V2X communication are summarized in [37].

- Aviation Industry: RF communication can interfere with the navigational system of the aircraft, therefore internet access on board planes is currently limited. VLC could be a viable choice for data transfer to passengers by utilizing the existing LED lighting system inside an aircraft. Air France Airbus A321 in 2019 demonstrated the first in-flight use of VLC [38].
- Industrial and Other Sensitive Areas: Industrial plants require quick digital connectivity to monitor its manufacturing and processes. WiFi connectivity will not be suitable to many sensitive places such as mining areas due to sensitive radiations, chemicals and locations. VLC in these areas can give a safer and speedier solution. Further, VLC based localization systems can be easily implemented with little additional equipment [39] which can be used to locate employees and assets efficiently in factories.

1.3 Conventional VLC system

Fig. 1.2 shows the basic block diagram of a typical VLC system. In any communication system, a transmitter and a receiver are the integral components. In VLC, a transmitter-receiver prototype is implemented using LED (a semiconductor that produces light) at the transmitter and photo-detector (PD) at the receiver. VLC employs IM/DD as data is modulated only into light intensity, rather than amplitude and phase, due to the incoherent nature of the LED. As shown in Fig. 1.2, the input data is modulated after being coded using source, channel, or precoding methods. The modulated data is converted into a real and unipolar signal to make it compatible with the LED front-end, however if the default modulated data is real and unipolar then there is no need for conversion. It should be noted that the modulation scheme used in VLC has a significant impact on the VLC system's performance. The signal $x(t)$ modulates the optical intensity of LED. The optical signal output from LED traverses across the optical channel to fall on the optical receiver. The PD generates electrical current equivalent to the incoming optical signal, which is amplified by a trans-impedance amplifier (TIA) to produce signal $y(t)$ for data demodulation. Additionally, optical filter and optical concentrator are placed just above the PD to limit the spectrum of light, reduce the impact of ambient light sources, filter out blue light, and then the optical concentrator concentrates the filtered light on the PD.

1.4 Recent Progress in VLC

The multiple benefits of VLC and a recent boom in the usage of LED luminaires have encouraged a significant research on VLC. In addition to standardization efforts for VLC, many research teams are constructing high data rate LC links. Pang et al. [40] published the first attempt to modify visible light via rapid LED switching in 1999. Later, in 2001, the Reasonable Optical Joint Access (RONJA) group [41] employed visible light beams to transport data at 10 Mb/s over a 1.4 km distance. Tanaka et al. from Keio University invented the use of white LEDs for lighting and communication simultaneously [42]. The hOME Gigabit Connectivity (OMEGA) group funded by the European Union, showed a data rate of 125 Mb/s using visible light in 2009 [43], 513 Mb/s in 2010 [44], 803 Mb/s in 2011 [45], and [46] 806 Mb/s in 2012. Around the same time, several other research organizations began active research in this area. While significant progress has been made in LC research [47] towards high speed connectivity and the coexistence of LiFi-WiFi technologies [48], these efforts are less directed at resource-constrained devices such as IoT and UAVs, the coexistence of LiFi-IoT and, modulation schemes and technologies supporting heterogeneous users and devices. Further, red, green and blue (RGB) LED concept has not been utilized in many aspects in research literature to support green communication in VLC systems.

1.4.1 RGB LED based Modulation Schemes

One of the key aspects of a communication system is its modulation scheme. The IEEE 802.15.7 VLC standard [49] outlines various modulation schemes for VLC in indoor applications such as on-off keying (OOK) , M-ary pulse-amplitude modulation (M-PAM) , and M-ary pulse position modulation (M-PPM) and color shift keying (CSK) . Due to the the non-coherent nature of LED transmitters, the conventional RF modulation schemes can not be directly used in VLC. Thus, VLC utilizes intensity modulation with direct detection (IM/DD) technique for communication, which requires real and positive input signal to the LED [8, 50]. RGB LEDs are usually preferred over phosphor-coated LEDs for communication purposes because they support wavelength modulations and have faster responses. The multi-colored LED can be exploited to implement multi-input multi-output (MIMO) systems capable of providing multiplexing and diversity gain [30, 31]. Unfortunately, the conventional blue-phosphor LEDs can only support the 3-dB bandwidth of approximately 3-5 MHz, due to the slow phosphor response [8, 51]. Further, the constant total output power from RGB LED in CSK modulation scheme reduces the imminent human health complications [52]. The complexity of CSK is more than OOK, however it provides $\log_2 M$ higher data rate than OOK [53]. CSK utilizes RGB LED, which can be converted to OOK modulation as well.

One of the research challenges in RGB LED-based modulation schemes (i.e., CSK) of VLC is to make it more suitable for moderate data rate communication in both resource constrained devices and LiFi users. Further, it is difficult to enhance the performance of different versions of CSK modulation schemes with a generalized technique. Another challenge is to design the constellation points for CSK while maintaining white color balance.

1.4.1.1 CSK

Researchers have endeavoured to improve the performance of CSK by using more than three LEDs. For an additive white Gaussian noise (AWGN) channel Ravinder et al. in [54] has enhanced CSK with four LEDs, where they have reported a significant 4 dB electrical signal-to-noise ratio (SNR) gain at a bit error rate (BER) of 10^{-6} over the three-LED scheme. CSK has been combined with PPM scheme for indoor VLC in [55], where 8 dB gain is attained in comparison with the standard 4-CSK (4 is the number of symbols) at a symbol error rate (SER) of 10^{-4}. This improved gain, nevertheless, comes at the expense of a wider bandwidth requirement. To overcome the non-linearity effect of LEDs, Murata et al. in [56] presents a digital version of CSK modulation, which maps the symbol using digitally controlled multiple Trichromatic LEDs (TLEDs). The BER evaluation of the digital CSK (DCSK) system achieves a similar BER as that of standard CSK with a linear variable current driver. Target color control for DCSK with several multi-color LEDs is presented by Igata et al. in [57] for improving the illumination performance of the modulated signals.

1.4.1.2 Constellation Design

Moreover, the growing interests on designing and optimizing the constellation points primarily in terms of lowered received bit/symbol error rates for standard CSK, have led to the emergence of diverse techniques in the literature. The majority of constellation design problems aim to improve color balancing restrictions or data rate transmissions. For the design of CSK constellation points, the authors in [61] proposed a genetic algorithm for multiple LED transmitters at different wavelengths in the VLC system. Drost and Sadler are the first ones to investigate billiards algorithms in [62]. Later, in paper [63], they compensated the channel distortions by designing a framework for optimizing the constellation points for VLC systems employing multiple emitters at different wavelengths. Monteiro et al. designed constellation points for CSK utilising interior-point methods in [64], then in [53] they extended it to higher-order CSK constellations. The authors in [65] presented a power-efficient high dimensional constellation design scheme for the standardized TLEDs.

1.4.2 LiFi-IoT Coexistence

In an indoor environment we cannot expect single-carrier modulation techniques to simultaneously support high-speed LiFi users [8, 9] along with LC enabled IoT (LIoT) devices [14]. The desideratum to coexist both high-speed (e.g., consumer multimedia) and low-speed (e.g., IoT) devices without compromising efficiency is an interesting research challenge in VLC.

Energy-efficient IoT communication is supported by a number of low-power RF wireless technologies, including ZigBee, Bluetooth low energy, low-power wireless personal area networks, and z-wave. However, these existing technologies are limited to few IoT devices in a time slot due to the lack of spatial multiplexing and are not suitable for massive IoT devices connections [66]. Currently, the coexistence technique used in narrowband IoT (NB-IoT) [67] overlays a low-speed signal on a high-speed signal in LTE. The low-speed signal limits the bandwidth requirement to 200 kHz to reduce the power consumption for IoT devices. However, in already overloaded cellular networks, NB-IoT services will not be free. Once there are many IoT devices, end customers would have to pay a monthly subscription to use NB-IoT services, which will be expensive. IoT devices that support LC can receive better node density and larger bandwidth for free. While NB-IoT for RF can be adopted in LC, the implementation of the NB-IoT concept requires substantial change at the transmitter in terms of hardware and software. In order to coexist WiFi with IoT devices, Hossein et al. in [68] have developed energy-efficient IoT communication based on a single subcarrier of OFDM. For concurrent data transfer between the AP and both WiFi and IoT devices, they have proposed beamforming filters.

Owing to energy and computing power limitations of IoT nodes, energy-efficient modulation and medium access (MA) techniques are required for IoT communication. High spectral efficiency (SE) modulation techniques such as OFDM and discrete multi-tone modulations are undesirable for IoT nodes due to their higher computational requirements and high PAPR [14, 69]. Instead, pulse-based modulation techniques such as OOK, PAM and CSK are more appropriate for IoT communication. Chapter 3 and 4 of this thesis have shown the suitability of CSK-1PD for indoor IoT networks [70], and have designed and optimized the constellation points for CSK-1PD [71], respectively. The energy-efficient random number modulation (RNM) technique proposed in [72], transmits b' bits (such that, $2^{b'} > M$ modulation order), if its information data block matches with the random sequence that it has generated in the current time slot, otherwise it remains silent enabling higher energy efficiency. In contrast, a conventional continuous transmission system transmits $\log_2 M$ during every symbol duration. However, RNM does not transmit continuous data, so the communication link needs to be delay-tolerant. This method is therefore appealing for IoT motes that only need to relay data occasionally. The authors in [73] have designed a wavelength-sensitive, low-cost wireless receiver architecture which enables distributed space-frequency diversity in an IoT network. The aforementioned studies in Chapters 3, 4 and papers [72, 73] have made attempts to address the power limits of IoT devices without taking into account coexistence with LiFi users.

1.4.3 VLC enabled UAV

The demand for UAVs have been snowballing over the last few years. The real-time aerial video transmission is one of the myriad applications of wireless communication through UAVs, which is conventionally utilized for remote sensing, surveillance, aerial inspection, and monitoring [74]. UAVs can also be deployed as aerial base stations (BSs) or relays in communication networks [74, 75]. These aerial base stations are referred to as UAV-BS. UAV-BSs can augment the performance of desired communication network owing to their high mobility, maneuverability in the three-dimensional (3-D) space, fast deployment and ease of accessibility in remote areas. Whereas, VLC relies on LEDs for signal transmission which makes them particularly suitable for scenarios like search and rescue in which both illumination and communications are required. LEDs outperform the other light sources with their high electrical-to-optical conversion efficiency, long life span, small size, light weight, low cost and modulation performance [76]. Therefore, the energy-efficient LEDs further reinforce the emerging VLC technology. The concept of incorporating LEDs in UAVs for illumination in applications like disaster recovery and urban safety has been put out by the authors of [77]. Draganfly Innovations [78] is designing and producing UAVs with LEDs for use during nighttime operations. The recent use of LED mounted on a UAV inspires the researchers to combine VLC and UAVs to provide simultaneous communication and illumination for inspection, environmental protection monitoring, first response, urban safety especially at night and emergency communication for disaster recovery [30, 31, 77]. The research into VLC-enabled UAVs, which can meet the dual requirement of illumination and communication of ground users by visible light, has been furthered by the current interest in VLC-enabled vehicular networks. Further, above mentioned utilization of LEDs in UAVs for communication and illumination eliminate the extra cost and energy required in UAVs for RF-based communication [79, 80]. Owing to the numerous advantages of VLC, VLC-enabled UAV-BS ($\mathrm{UB_v}$) communications can become a promising technology.

However, low cost and energy-efficient three-dimensional (3-D) placement of $\mathrm{UB_v}$ networks is challenging, as it depends on many factors such as deployment environment e.g., geographical area, locations of ground users, air-to-ground channel characteristics, etc. Another challenge in $\mathrm{UB_v}$ is to maintain quality of service (QoS) such as illumination and reliable communication.

1.4.3.1 UAV Deployment

The literature is replete with RF-based UAV-BS ($\mathrm{UB_r}$) networks and its deployment. The optimized deployment of static and mobile $\mathrm{UB_r}$ has been discussed in [81]. In case of static $\mathrm{UB_r}$ deployment, the position of $\mathrm{UB_r}$ remains same for the entire duration of operational time whereas for mobile $\mathrm{UB_r}$, the deployment position changes many times during allotted operational time [82]. In [83], the joint optimization of the $\mathrm{UB_r}$ 2-D positioning and the update interval has been done with the standard exhaustive search based strategy (ES) algorithm integrated with the greedy approximate approach [84]. Further, the optimization of $\mathrm{UB_r}$ deployment becomes even more challenging when mobility of ground users is taken into consideration as it requires multiple updates based on the user mobility [85]. The $\mathrm{UB_r}$ deployment was updated using a reinforcement-learning (RL) based approach for dynamic heterogeneous networks in [86]. The $\mathrm{UB_r}$ trajectory is obtained in [87] using a multi-agent Q-learning based method and is based on the prediction of users' positions. RL technique has been adopted in fair maximum coverage deployment of UAVs in [88], where the convergence of the proposed algorithm takes training episodes of the order of 10^4. The time complexity of RL depends on its training convergence. Concept of fixed update interval has been introduced in [85] and [87] to quantify the repeated updates for mobile $\mathrm{UB_r}$. The multi-UAV-based heterogeneous flying ad hoc networks (FANET) in [89] has been surveyed with more focus on the concept of gateways in the network to connect small and mini UAVs via a communication network.

1.4.3.2 Related works in VLC enabled UAV

The existing work in $\mathrm{UB_v}$ system primarily focuses on its power efficient deployment. In a multi-$\mathrm{UB_v}$, multi-user scenario, to jointly satisfy the users' data rate and illumination, location of $\mathrm{UB_v}$s and the cell associations (different sub-regions corresponding to the deployed $\mathrm{UB_v}$s) are optimized under illumination and communication constraints in [30]. However, the impact of interactions between several $\mathrm{UB_v}$s has not been taken into account. In order to meet the various data rate and illumination needs of ground users, an optimization problem is constructed to optimize performance by minimizing the transmit power consumption of interacting UAVs in [31]. The work in [90] provides a deep learning (DL) based strategy for the deployment of $\mathrm{UB_v}$s that is power-efficient. Specifically, they simulate the long-term historical illumination distribution and forecast the illumination distribution of the ground users using a machine learning framework comprising gated recurrent units (GRUs) and convolutional neural networks (CNNs). In order to achieve the huge connection requirements for 5G and beyond, the work in [91] examines the integration of non-orthogonal multiple access (NOMA) with $\mathrm{UB_v}$s. This technique also helps to serve more users compared to the VLC system without NOMA. A joint problem of power allocation and $\mathrm{UB_v}$'s placement is solved to maximize the sum rate of all users, subject to constraints on power allocation, QoS of users as well as $\mathrm{UB_v}$'s position. Nevertheless, the benefit of multiple access provision in $\mathrm{UB_v}$s comes at the cost of higher complexity. $\mathrm{UB_v}$s meant for communication should avoid lag and latency, therefore most of the decision should be taken by $\mathrm{UB_v}$s only.

1.5 Research Gaps

Despite the significant advancements in LC and VLC research [47], focusing on high-speed connectivity and the compatibility of LiFi and WiFi technologies [48], there is a lack of attention directed towards resource-constrained devices such as IoT and UAVs, as well as the coexistence of LiFi and IoT and the modulation schemes and technologies that support diverse users and devices. Additionally, the potential of utilizing the RGB LED concept to support green communication in VLC systems has not been fully explored in current research. This section specifically aims to identify the potential research gaps in CSK modulation scheme, LiFi-IoT coexistence and VLC enabled UAVs through above mentioned literature survey while focusing on the research goals of this thesis, i.e., to explore solutions utilizing VLC in order to provide low-cost and energy-efficient communication for resource-constrained devices and pave the way for 6G communication.

1.5.1 CSK

A crucial area of investigation for the RGB LED based modulation scheme known as CSK is determining how to optimize it for energy efficiency and cost-effectiveness. Additionally, it is important to examine the possibility of modifying the CSK scheme to make it suitable for resource-constrained IoT devices.

Previous works related to enhancement of CSK scheme relies on change in the modulation-demodulation methods, color control, CSK constellation design and number of LEDs or PDs (hardware) of CSK schemes to enhance the CSK system. Further, it is noted that not all enhancement techniques are suitable for different CSK schemes. In [92], the PPM technique applied in CSK-1PD shows poor performance for the constellation point $M = 4$. The four LED scheme [54] does not work for CSK-1PD as the constellation point range remains the same for three and four LEDs. To the best of the authors' knowledge, the existing literature lacks generalized enhancement scheme for different versions of CSK modulation schemes.

The work in this thesis for the very first time proposes a common enhancement method using probabilistic shaping (PS) for various schemes of CSK, especially, CSK-1PD and CSK-1APD. The technology to shape the occurrence of the symbols (or constellations) on the basis of a given probability is known as probabilistic shaping. The literature is replete with various promising PS technologies in optical fiber communication systems. However, the concept of applying PS technology to CSK VLC systems has not been explored before. The research goal of this thesis is to explore PS as a generalized technique to enhance CSK schemes, which does not require extra hardware (LEDs or PDs) and modification in the constellation symbols, modulation and demodulation techniques of different CSK schemes.

1.5.1.1 Probabilistic Shaping Related Work and Research Gap

Recent research works [58–60] in fiber-optic communication have applied PS and have shown shaping gains. Pilori et al. in [58] has compared PS-64-quadrature amplitude modulation with lower cardinality uniform constellations at the same net data rate in long-haul optical communications systems. Experimental evidence has shown that the maximum reach gains vary from 15.5 to 34 percent. However, it was also shown that in a fibre with non-zero dispersion shift, PS performance degrades more drastically than anticipated. The short auto-correlation of nonlinear phase noise, which cannot be compensated by conventional carrier phase estimation (CPE) techniques, is the cause of the poorer performance. Additionally, it has been demonstrated that selecting the right CPE scheme at the receiver is essential for maximizing the performance of PS technology. In [59], Eriksson et al. has applied PS using exponential distribution in direct detection PAM system and has shown an increase in the achievable information rate of 0.16 bit/symbol which corresponds close to 10 percent increase in the net data rate. Ivan B. Djordjevic et al. in [60] has evaluated non-uniform 8-PAM signalling scheme for data centre communications and demonstrated that for the same feasible information rate, the low-density parity-check (LDPC) coded 8-PAM with exponential distribution performs better than the LDPC coded 8-PAM with uniform distribution by 1.8 dB.

Most of the aforementioned studies have not considered the optimum probability order (OPO) while applying PS technique to the input symbols. PS technique may act as a generalized enhancement technique in CSK. Thus, research on source distribution and the probability order that provides the best possible performance gain in CSK is intriguing. In earlier works, the CSK modulation scheme was improved by using an extra LED, changing the color combination or by modifying the internal hardware system. A low complex version of CSK modulation scheme is required to provide moderate data rate with low complexity to support LiFi users as well as resource constrained devices such as IoT devices. The proposed work in this thesis presents a rigorous investigation by designing and analyzing the performance improvement of PS-CSK modulated VLC system from communication perspective. To the best of authors' knowledge, this work for the very first time, incorporates probabilistic shaping of input symbols in different variants of CSK modulated VLC systems. Moreover, the proposed PS scheme in this work [70] can be employed to the existing improved CSK-3PD schemes available in the literature [54] [55], to obtain additional SNR gain.

1.5.2 CSK-1PD

The low-cost version of standard CSK modulation scheme having single PD at the receiver can become an alternative to on-off keying (OOK) in IoT sensor networks as an M-ary CSK modulation scheme provides $log_2 M$ times more data rate than that of OOK. CSK with one PD at the receiver (CSK-1PD) is a low-cost color space-based modulation scheme, which can be exploited in implementing IoT sensor networks in a smart home or hall scenario for communication as well as illumination, where resources are constrained and thus, low-cost and power-efficient systems are preferred. The constellation design of CSK-1PD has been performed solely in [92] till date, which has stated numerical optimization solution for designing CSK-1PD constellations points for uniform input data only. Additionally, the maintenance of white tonality in illumination is one of the fundamental requirements for any VLC modulation scheme especially RGB LED based. The CIE 1931 chromaticity diagram's white zone (as shown in Fig. 4.2) may not always include the average colour obtained from the CSK constellation symbols, leading to colour imbalances that can be seen by the human eye [61, 92]. IEEE 802.15.7 standard has already proposed the adoption of a pseudo-random sequence, known as scrambler to overcome the color unbalance problem. In order to keep the output light in CSK-1PD at an average white tone for consistent input data, the scrambler has been utilized at the transmitter in [92]. The actual input data can be obtained at the receiver by a descrambler. Nevertheless, using a scrambler and descrambler can increase the hardware cost further. Therefore, a research gap exists in the optimization of the constellation points of the CSK-1PD modulation scheme.

In this thesis, the research objective is to design PS-CSK-1PD constellations for various input data and maximize energy efficiency by minimizing the required SNR at the FEC limit SER within optimization constraints, while preserving white tone [71].

1.5.3 LiFi-LIoT Coexistence

The research literature is replete with cognitive radio concepts to coexist WiFi-IoT, but it lacks LiFi-IoT coexistence works [93–95]. Nevertheless, these technologies are limited to spectrum sharing only as they sense unused frequency bands of the primary user to communicate to the secondary user, e.g., an IoT device. The complex beamforming filters can be replaced by wavelength division multiplexing (WDM) in VLC, which can be directly implemented with RGB LEDs. Moreover, the multi-carrier modulation schemes of VLC [50, 96] can at least support high data-rate requirements of LiFi users but can not support the resource constrained IoT devices simultaneously.

Therefore, the coexistence of LiFi users and LC-enabled IoT communication necessitates a thorough investigation of how much it can benefit from using light as a communication medium for green communication. In existing literature, there is a lack of comparison between different subcarrier modulation techniques in O-OFDM considered for LiFi-IoT coexistence. Techniques such as Pulse Amplitude Modulation (PAM), Quadrature Amplitude Modulation (QAM), and CSK have not been compared in a comprehensive manner to determine the most suitable scheme for the coexistence. These research gaps have driven the objective of this thesis to explore an alternative energy-efficient LC compatible indoor communication solution that can concurrently support both LiFi users and IoT devices. Specifically, the objective of this research is to develop a standard solution that supports both high-speed and low-speed devices in a manner that is energy-efficient and cost-effective while promoting green communication for IoT devices and existing indoor LiFi users [97].

1.5.4 VLC enabled UAV

This thesis focuses on myriad applications of VLC for resource constrained devices. Since UAVs are also power limited and size constrained devices, the utilization of visible light for communication and illumination in UAVs can help in reducing energy and air-frame cost. The placement of $\mathrm{UB_V}$ networks in a 3-D space that is both low-cost and energy-efficient is a challenging task. This is due to the various factors that must be considered, such as the deployment environment, the location of ground users, and the characteristics of the air-to-ground communication channel. Another significant challenge in UB_v networks is ensuring a high level of quality of service, including adequate illumination and reliable communication. The research gaps in relation to the existing literature are covered in more detail in the following paragraph.

For vertical deployment in UB_v, one cannot consider the same height as UB_r since in UB_v the aim is to simultaneously provide communication and illumination. In case of UB_r, the altitude is mostly fixed based on certain communication parameters such as achievable data rate, error rate or SNR. Therefore, a plethora of works in RF-equipped UAVs are for two-dimension (2-D) deployment. However, in UB_v, the vertical deployment depends on two factors; communication and illumination especially for night scenario or say low light scenarios. Further, VLC channel gain is different from the RF channel gain. Therefore, UB_v can not be deployed at the same altitude as of UB_r. Secondly, for the user mobility aware 2-D deployment one may expect that similar deployment technology can be used for both UB_r and UB_v. However, the maximum coverage radius changes for UB_v from UB_r because the altitude and quality-of-service (QoS) metrics are different in both cases. Due to UAV power and size restrictions, very complex algorithms are also less preferred for UB_v networks. In these works [30, 31, 90] the power efficient deployment of UAVs has been done in 2-D with fixed altitude of UB_v. There is lack of research works which have focused on minimizing the flight time of UB_v and maximizing the coverage probability of ground users with energy-aware and low complex methods. Additionally, two of the challenges and open issues presented in [89] which is mobility modelling of UB_v with user mobility awareness and energy-efficient scheme have been investigated in this thesis for UB_v. Further, no existing work in UB_v has considered the variation of day and night scenario in coverage.

The research goal of this thesis is to investigate UB_v coverage radius with respect to its altitude to provide reliable communication for day scenario, and both reliable communication and illuminance for night scenario. The 3-D deployment of UB_v has been done to maximize the number of covered users and minimize the UB_v flight time with energy and user mobility awareness [98].

1.6 Major Contributions

By reviewing previous and related research works of VLC, the study in this thesis intends to partially cover the aforementioned research gaps related to CSK modulation scheme, LiFi-IoT coexistence and VLC enabled UAV. The major contributions of this dissertation and relevant publications are summarized below.

- In order to propose a generalized enhancement scheme for different versions of CSK modulation schemes, we analyze the performance of CSK modulation schemes with PS of input data. Specifically, we have considered three variants of CSK with respect to receiver structure namely CSK with one PD (CSK-1PD), CSK with three PDs (CSK-3PD) and CSK with one avalanche PD (CSK-1APD). For shaping the CSK input symbols, four different source distributions are considered viz. uniform, exponential, Maxwell-Boltzmann and Pareto. The proposed work comprises of developing algorithms to obtain the optimum probability order for maximizing the received SNR gain. The performance metric considered in this work is SNR gain at forward error correction (FEC) limit, thereby, indicating the energy-efficiency in the proposed work. The proposed systems have been analyzed for computational complexity. Further, the closed-form expressions for SER have been derived for the proposed PS-CSK schemes. It has been observed that proposed PS-CSK schemes provide different SNR gain for different source distributions at a given SER. The results show that PS based on Pareto distribution gives the best performance gain at unity achievable information rate among all considered source distributions.

    – **Dil Nashin Anwar** and Anand Srivastava, "**Design and Analysis of Probabilistic Shaping in Color Shift Keying Modulation Schemes**," ***IEEE System Journal***, vol. 15, no. 1, pp. 1433-1444, March 2021, doi: 10.1109/JSYST.2020.3007391.

- This work revolves around optimizing the constellation points of CSK-1PD to achieve a more energy-efficient modulation scheme. The optimization has been done with and without average white tone constraint for uniform and non-uniform (exponential, Maxwell-Boltzmann, Pareto) source distributions. The constellation design strategy is based on maximizing the minimum distance among the differently distributed symbols. In the case of non-uniform distributions, the constellations points have been optimized by geometrically shaping the points based on their PS. The optimized constellation points (OCPs) of CSK-1PD without white tone constraint provide higher SNR gain at FEC limit SER as compared with strict white tone constraint. Further, the strict white tone constraint has been relaxed by considering the whole white light region in the CIE 1931 chromaticity diagram as white tone. The OCPs for uniform data with relaxed white tone constraint achieves SNR gain similar to without white tone constraint. However, for probabilistically shaped symbols, the SNR gain achieved from OCPs improves from strict white tone constraint but remains less than the without white tone constraint. A novel method to utilize an additional RGB LED at the transmitter side has been proposed and designed to maintain any white tone light in the white light region without degrading the maximum achieved SNR gain.

  - **Dil Nashin Anwar** and Anand Srivastava, "**Constellation Design for Single Photodetector based CSK with Probabilistic Shaping and White Color Balance**," ***IEEE Access***, vol. 8, pp. 159609-159621, August 2020, doi: 10.1109/ACCESS.2020.3020403.

- Owing to power limitations and hardware constraints of the IoT device, it requires simple, low power, low complex, energy-efficient communication technology. In contrast, LiFi users require high data rates and reliable connectivity. Motivated by the diverse requirements of these heterogeneous users, this thesis proposes novel green communication schemes that can be used for the coexistence of LiFi users and LC enabled IoT devices under a common LiFi access point. The proposed coexistence schemes utilize the amalgamation of wavelength division multiplexing, OFDMA, Hartley transform based DCO-OFDM (DCO-OFDM$^{\mathrm{H}}$), null DC element, interleaved subcarrier mapping, modified data sequence to achieve concurrent interference-free, low complex and reliable communication. The utilization of the optical-orthogonal frequency division multiplexing (O-OFDM) [99] scheme assists in supporting simultaneous data transmission to LiFi users and IoT devices by assigning a single O-OFDM subcarrier to an IoT device. Additionally, as the MA techniques affect the choice of modulation techniques and overall performance in the system. This work includes an analytical delay and throughput framework to corroborate the decision of an appropriate combination of MA and modulation techniques in the coexistence scheme. We present a comprehensive analysis of the proposed coexistence schemes against conventional DCO-OFDM$^{\mathrm{H}}$ coexistence schemes in-terms of system complexity, peak-to-average-power ratio, effective-SE, the maximum number of IoT devices, power saving with respect to QAM based DCO-OFDM$^{\mathrm{H}}$, energy harvesting, and SNR. The results suggest that the proposed downlink (DL) and uplink (UL) coexistence schemes reduce the complexity and increase the energy efficiency at the user's and device's terminals.

  - **Dil Nashin Anwar**, Rizwana Ahmad and Anand Srivastava, "**Energy-Efficient Coexistence of LiFi Users and Light Enabled IoT Devices**," ***IEEE Transactions on Green Communications and Networking***, vol. 6, no. 2, pp. 930-950, June 2022, doi: 10.1109/TGCN.2021.3116267.

- To cover maximum of mobile ground users while ensuring fairness, we propose energy and user mobility aware 3-D deployment of UB$_{\mathrm{v}}$. The UB$_{\mathrm{v}}$ coverage area to serve ground users has been enhanced with holographic light-shaping diffusers (LSD) [100, 101]. The optimum angle of the LSD has been obtained based on LED optical transmitted power and desired UB_v maximum coverage. A novel RGB LED solution based on light sensitivity to the human eye is proposed to increase the coverage area for the night scenario. Moreover, we derive the analytical expressions to determine the maximum coverage radius and UB_v optimum altitude for the defined QoS metrics. Since, UAVs in general are resource constrained devices, therefore the aim of this work is to reduce the complexity of computing the optimal UB_v placement to cover maximum possible users with energy awareness. The farthest user and shifting UAV based solution have been proposed for the joint optimization of UB_v placement and the update interval. The complexity of the proposed algorithms is lower than the exhaustive-search based solution, thus, making the UB_v network energy-efficient. Finally, the proposed UB_v network is evaluated in terms of average update interval, average number of effective users, average number of update instants, average service time and complexity.

- **Dil Nashin Anwar**, Mansi Peer, Kanak Lata, Anand Srivastava and Vivek Ashok Bohara,“ **3-D Deployment of VLC Enabled UAV Networks with Energy and User Mobility Awareness**”, ***IEEE Transaction on Green Communications and Networking***, vol. 6, no. 4, pp. 1972-1989, Dec. 2022, doi: 10.1109/TGCN.2022.3171920.

1.7 Thesis Layout

In this thesis, we design and analyze low-complexity energy-efficient VLC systems for resource constrained devices and applications such as IoT devices and UAVs. Chapter 2 presents a detailed explanation of optical channel. Afterwards, various VLC modulation schemes including CSK and O-OFDM are discussed. Finally from Chapter 3 onward, the major works of this thesis are presented. This chapter shows the integration of PS in CSK and its performance achieved. Chapter 4 specifically design and optimize the constellation points of non-uniform source distributions in PS-CSK-1PD to achieve higher energy-efficiency compared to its uniform source distribution counterpart. Chapter 5 provides a comprehensive performance evaluation of different variants of proposed and conventional $\text{DCO-OFDM}^{\text{H}}$ coexistence schemes in-terms of various performance metrics. The 3-D placement of UB_v and update interval while maintaining illuminance and SNR threshold have been discussed in Chapter 6. Chapter 7 concludes the dissertation and suggests the possible future research directions. The last chapter, Chapter 9, discusses additional research works published during the tenure of PhD.

Chapter 2

VLC Channel and Modulation Schemes

In this chapter, Section 2.1 cover more specifics about the VLC physical layer such as the channel model. The effects of various impairments in a VLC system, such as thermal noise and shot noise, are discussed in Section 2.2. Followed by Section 2.3 which discusses various VLC modulation techniques.

2.1 Optical Channel

The VLC optical channel can be modelled as:

$$y(t) = \rho \; x(t) * h(t) + n(t), \tag{2.1}$$

where, "*" stands for a convolution operator, ρ indicates the responsivity of the PD. The property of PD to generate specific electrical current to an incident optical power of a given wavelength is known as the responsivity of the PD for that wavelength. The optical channel impulse response is denoted by $h(t)$ and $n(t)$ represents the overall noise present in the VLC system which follows the property of additive white Gaussian noise (AWGN), as explained in Section 2.2. The optical channel impulse response $h(t)$ can be expressed as:

$$h(t) = h_{\mathrm{LOS}}(t) + h_{\mathrm{NLOS}}(t), \tag{2.2}$$

where $h_{\mathrm{LOS}}(t)$ is the impulse response of the line-of-sight optical channel, i.e., the direct link between the transmitter LED and receiver PD and $h_{\mathrm{NLOS}}(t)$ is the impulse response of the non-line-of-sight (NLOS) optical channel, i.e., the indirect link between the LED and PD which consists of reflections from the walls and the diffused components from near by objects. Fig. 2.1 shows the LOS and NLOS links between the transmitter LED and receiver PD.

The frequency domain representation of optical channel is as follows:

$$H(f)_{\text{VLC}} = H(f)_{\text{LOS}} + H(f)_{\text{NLOS}}. \tag{2.3}$$

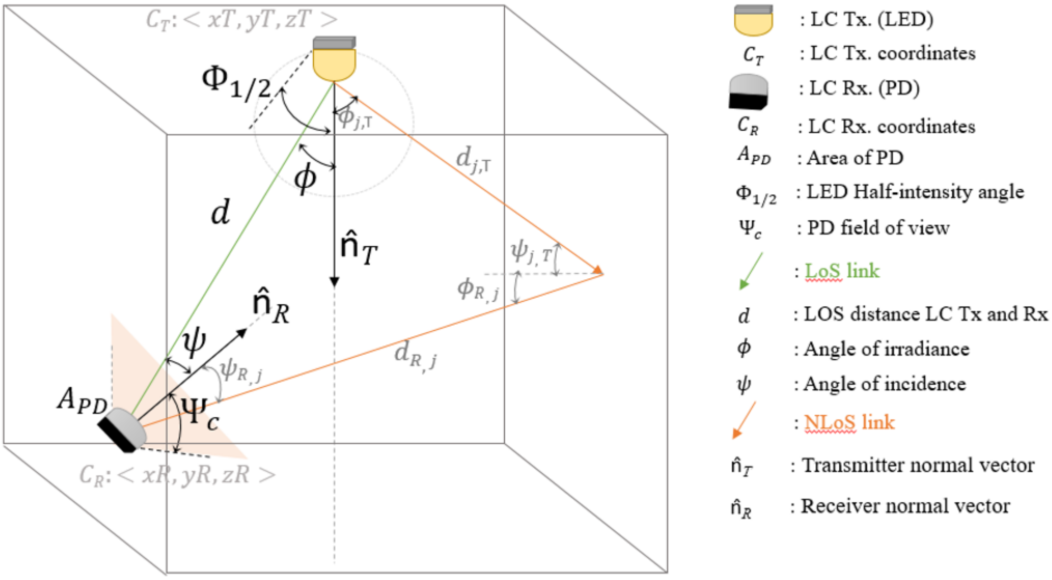

Figure 2.1: Optical channel model representing LOS (green) and NLOS (orange) link

2.1.1 LOS Link

The light emitted by LED can be modelled as Lambertian radiation pattern $R(\phi)$. The Lambertian radiation intensity depends on the angle of irradiance and can be modelled as [24, 102]:

$$R(\phi) = \frac{(m+1)\cos^m(\phi)P_t}{2\pi}, \tag{2.4}$$

where ϕ represents the angle of irradiation, m denotes the Lambertian order which specifies the directionality of the source, and P_t is the transmitted optical power. The value of m can be calculated from the LED half-intensity angle, $\Phi_{1/2}$, which is defined as:

$$m = \frac{-\ln(2)}{\ln(\cos(\phi_{1/2}))}. \tag{2.5}$$

The angle of irradiance ϕ, is the angle between the transmitted ray falling on the receiver and the normal direction ray of the LED, which can be expressed as:

$$\cos(\phi) = \hat{n}_T \frac{(C_R - C_T)}{||d||}, \tag{2.6}$$

where, $\widehat{n}_T$ is the orientation of the transmitter LED. The positions of source and receiver, are C_T and C_R, respectively.

The impulse response of LOS link between LED and PD can be modeled as [103]:

$$h_{LOS}(t) = \begin{cases} \frac{R(\phi)A_{PD}\cos(\psi)}{d^2}\delta(t-\frac{d}{c}), & : \ \psi < \Psi_c \\ 0, & : \ \psi > \Psi_c \end{cases} \tag{2.7}$$

where, d is the distance between the transmitter LED and receiver PD, $\delta(.)$ is the Dirac delta function, c is the speed of light. The angle of light incidence at the receiver ψ, is the angle of view of the transmitter position (relative to normal direction of the PD) when looking from the receiver, It can be given as:

$$\cos(\psi) = \widehat{n}_R \frac{(C_T - C_R)}{||d||}, \tag{2.8}$$

where $\widehat{n}_R$ is the orientation of the receiver. The angle of incidence ψ, at the PD should not exceed the field-of-view (FOV) angle (Ψ_c) of the PD for proper data reception. The physical area A_{PD} and the Ψ_c of the PD impacts the received optical power and thus electrical output current. Therefore, above mentioned parameters associated with PD are present in the impulse response of the optical channel.

The DC channel gain for LOS is defined as [104–106]:

$$H(0)_{\text{LOS}} = \frac{(m+1)A_{\text{PD}}}{2\pi d^2}\cos^m(\phi)G_{\text{f}}G_{\text{c}}(\psi)\cos(\psi), \tag{2.9}$$

where, G_{f} defines the gain of the optical filter; and G_{c} denotes the gain of optical concentrator, and is given as:

$$G_{\text{c}}(\psi) = \begin{cases} \frac{\wp^2}{\sin^2(\psi)}, & 0 \leq \psi \leq \Psi_c \\ 0, & \psi > \Psi_c \end{cases} \tag{2.10}$$

where $\wp$ is the refractive index of the concentrator.

2.1.2 NLOS Link

The light rays reaching the PD indirectly after being reflected from different walls of a room are considered in the NLOS link. The NLOS component's channel gain is specified as [107]:

$$H(f)_{\text{NLOS}} = \frac{\Gamma A_{\text{PD}} e^{j2\pi f \Delta T}}{A_{\text{room}}(1-\Gamma)(1+j\frac{f}{f_c})}, \tag{2.11}$$

where Γ is the reflectivity of the walls, ΔT is the delay between the LOS and onset of the diffused signals, A_{room} is the area of the room, and f_c is the cut-off frequency of the diffuse optical channel [108].

2.2 Noise in VLC

VLC system majorly have three sources of noise.

1. Shot noise: The intrinsic randomness in the photon's particle results in fluctuating current which cause shot noise at the optical receiver. The generated shot noise depends on the incident optical signal [109–111]. For a large number of photons, shot noise can be modelled as an additive white Gaussian noise (AWGN). The variance of shot noise is given as:

$$\sigma_{sh}^2 = 2qI_{\text{rec}}\text{B} + 2qI_B I_2 \text{B}, \tag{2.12}$$

   where q is the electron charge, I_{rec} is the electrical current generated at the PD to an incident optical power which is a linear combination PD responsivity and average power of incident optical signal at the receiver (P_{rec}), equated as $I_{\text{rec}} = \rho P_{\text{rec}}$. I_B is the background noise current, and I_2 is the noise-bandwidth factor, and B is the effective bandwidth of the optical receiver which is determined by the minimum of signal modulation bandwidth or the receiver bandwidth.

   In case of indoor scenario, the distance between transmitter and receiver is less and the dominant signal is LOS [106], thus the incident optical power at PD is large. Additionally, practical indoor VLC systems require high incident optical power to maintain typical illumination and communication [112]. As a result, shot noise is more pronounced and cannot be neglected in indoor environments where the incident optical signal at the PD is relatively high due to illumination criteria.

2. Thermal noise: The random thermal motion of electron carriers in the receiver circuit result in fluctuating voltage known as thermal noise. Thermal noise can be described as [113]:

$$\sigma_{th}^2 = \frac{4k_B T_k B}{R_l}, \tag{2.13}$$

   where, k_B is the Boltzmann's constant, T_k is the absolute temperature in Kelvin and R_l represents receiver equivalent load resistance. The resistance of the transimpedance amplifier (TIA) is a major source of thermal noise. This noise can also be modelled as an AWGN. In case of strong ambient light, the impact of thermal noise is more pronounced and the shot noise becomes low. Thus, the noises at the VLC system are assumed to be independent of the received signal [114–116].

The additive white Gaussian process jointly approximates the thermal and shot noise components of a PD [53, 106], thus the overall noise in VLC is considered to be AWGN.

3. Ambient light noise: In indoor VLC, indirect sunlight and other light sources such as fluorescent light may affect the communication whereas in outdoor direct sunlight during day time and street and infrastructure luminaires during night time may affect the performance of VLC. However, ambient light noise in an environment remains constant for a larger period of time than the communicating light. Therefore, the impact of ambient light noise can be significantly removed with a high pass filter [10, 30].

2.3 VLC Modulation Schemes

In case of VLC, since the same LED will be responsible for both illumination and communication, modulation techniques must meet both illumination and communication requirements. However, in case of LC with IR LED no such illumination constraint is required as infrared rays are invisible to human eyes. It is important to note that in an indoor scenario where LED luminaires are present then VLC is adopted to support green technology instead of IR LED. Therefore, VLC modulation schemes should prevent flickering by changing light intensity faster than a human eye can detect (i.e., faster than 200 Hz) and provide a certain illuminance. Consequently, various modulation techniques for the VLC physical layer proposed by IEEE 802.15.7 and IEEE 802.15.13 have been discussed below.

2.3.1 On-off Keying (OOK)

OOK is the primary modulation scheme meant for low to medium baud rate optical wireless communication systems in which when the LED is on then digital "1" is transmitted and if the LED is dimmed which is assumed to be off then digital "0" is transmitted. The off state does not indicate that the LED has been turned off, but rather that the light intensity has been significantly reduced. OOK is simple to set up, but has some drawbacks, including inter-symbol interference (ISI) at higher transmission speeds because the OOK pulse bandwidth exceeds the LED 3-dB bandwidth [117] and limits the data rate. The optical power is not constant as long runs of ones and zeros in OOK may cause nausea and epilepsy in human beings due to light flashes [52, 53]. Further, with off-the-shelf components OOK can only handle a limited amount of data [49, 50, 118].

2.3.2 Variable Pulse Position Modulation (VPPM)

In VPPM, the pulse width is varied according to the dimming requirement and the position of the pulse is modulated according to the data for communication. Fig 2.2 displays VPPM with different dimming percentages. It can be observed that VPPM is a combination of pulse width modulation (PWM) and pulse position modulation (PPM) that support concurrently illumination with dimming control and communication [119]. The key characteristics of VPPM is that pulses are positioned in a fixed time period and the position of the pulses within the time period is varied to represent the amplitude of the analog signal. This provides an advantage to VPPM, as error rate becomes robust to noise which may impact the signal amplitude. The advantage of VPPM is that the amount of dimming does not impact the data transmission [120, 121]. However, one of the main drawbacks of VPPM is that it is sensitive to timing jitter and clock drift, which can result in errors in the recovered signal. Additionally, the receiver must have knowledge of the variable pulse widths used by the transmitter in order to correctly decode the information.

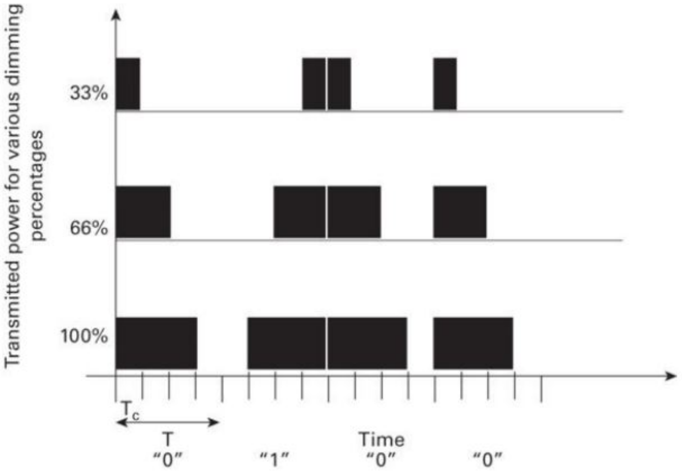

Figure 2.2: VPPM with different dimming percentages, showing the modulation of “0 1 0 0" data stream [121].

2.3.3 Color Shift Keying (CSK)

The less computationally complex modulation schemes for VLC include OOK, PPM, and colour intensity modulation (CIM). However, as per IEEE 802.15.7 standard [49] for VLC, these modulation schemes can cause large inrush currents when used with large arrays of LEDs and require constant flicker management [53]. The power-controlled version of CIM, known as colour shift keying (CSK) can be an alternative. The optical power of the visible light emitted by multi-colour LEDs such as red, green and blue (RGB) LEDs in the trichromatic LED

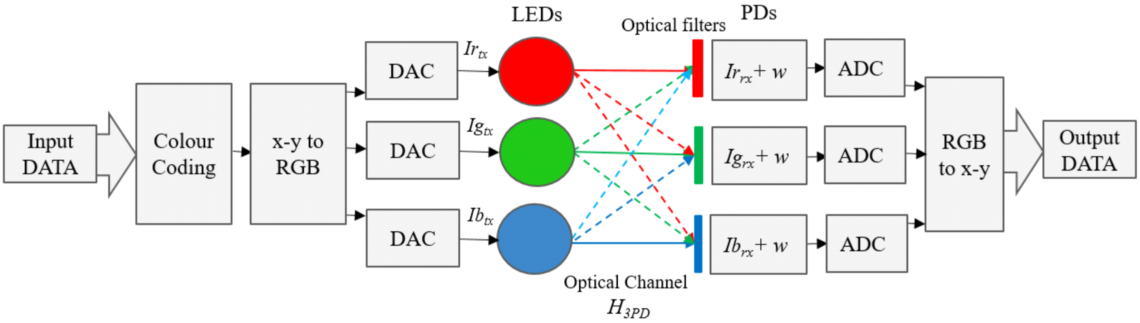

Figure 2.3: Block diagram of a typical CSK modulation scheme in VLC.

(TLED) lighting source is modulated for data transmission keeping constant signal envelope power. The RGB LEDs in CSK modulates data to provide communication along with white light illumination suitable for indoor environments in buildings. CSK maintains a constant instantaneous luminance across each constellation, preventing intensity flicker and sudden flux of currents in LED devices. CSK reduces the fluctuations in light intensity that may induce nausea and epilepsy in human beings [52, 53]. The M-CSK system where $M = 2^q$, provides q times data rate than that of OOK by mapping q bits into a symbol [53].

Fig. 2.3 shows the block diagram of the standard CSK VLC system as proposed in the physical layer-III of the IEEE 802.15.7 standard [49, 53]. The CSK modulation scheme includes a color coding block that maps the input symbols into an x-y color coordinates. The CIE 1931 [49] color space chromaticity diagram represents all the colors visible to the human eye with their color coordinates x and y as seen in Fig. 2.4. Each constellation point is represented by a unique binary input symbol which gets a particular combination of RGB intensity according to the color coding scheme. The IEEE 802.15.7 standard provides eight color coding schemes, also known as color band combinations (CBCs)) to modulate symbols in CSK [122]. In Fig. 2.3, after color coding, the mapping from x-y color coordinates to RGB intensity vector ensures LEDs illumination for the specific RGB intensity. The intensity transformation from x-y to RGB with a set of equations has been discussed in detail in [53, 54]. The digital voltage values (to drive LEDs) are converted to analog values using digital-to-analog converter (DAC) and then fed to the LEDs to illuminate with the corresponding intensity of light. The mathematical equations for transmitted and received symbols in CSK modulation schemes have been established in terms of electrical current for consistency with the notation of electrical current generated at the PD receiver. The instantaneous current driving each RGB LED represents the CSK transmitted symbols. The current driving each RGB LED is obtained from RGB intensities [53]. The set A has all M-CSK symbols i.e., the instantaneous RGB LED driver current vector denoted by $\mathbf{s}_k$ for the k^{th} symbol. The proposed work considers $M = 4$

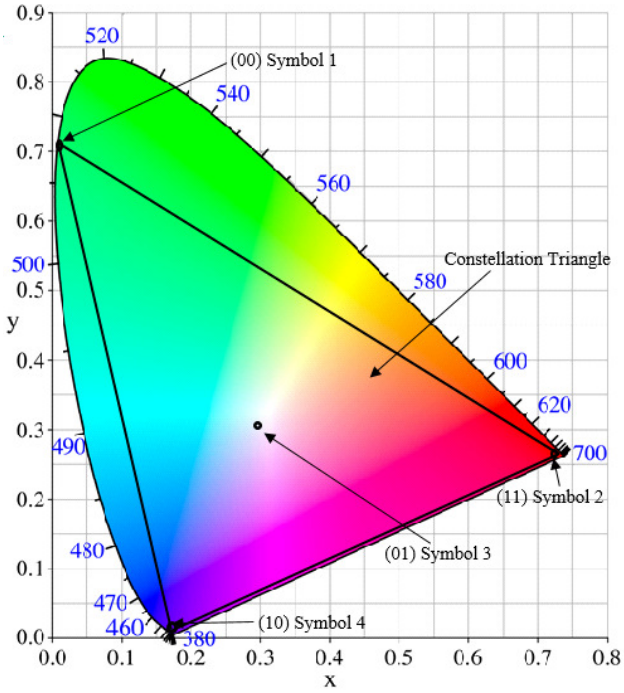

Figure 2.4: Color space chromaticity diagram showing RGB constellation triangle and four symbols of CSK-3PD [122].

constellation size for the analyses.

$$A = \{\mathbf{s}_1, \mathbf{s}_2, \mathbf{s}_3, ..., \mathbf{s}_M\}, \tag{2.14}$$

$$\mathbf{s}_k = [Ir_{tx}, Ig_{tx}, Ib_{tx}]_k, \tag{2.15}$$

where, Ir_{tx}, Ig_{tx}, and Ib_{tx}, represent the instantaneous driver current for the red LED, green LED, and blue LED, respectively. The three symbols of 4-CSK form a triangle-shaped diagram (formed by black lines) in Fig. 2.4. A 4-CSK constellation symbol consists of two bits and is defined by a combination of three visible light wavelengths (RGB). The mixture of red, green and blue light generated from RGB LED source gets corrupted by AWGN noise (represented by $\mathbf{w}$) at the receiver PD. Three PDs receive the mixed optical signal, each having red, green, and blue light filters, respectively in front of them as shown in Fig. 2.3. The mixed optical signal is thus received separately as the filter in front of each PD filters the specific light. The PDs convert the specific light to output electrical currents. The electrical currents Ir_{rx}, Ig_{rx} and Ib_{rx} represent the received symbol as shown in Fig. 2.3. These received analog currents are converted to digital values using analog-to-digital converter (ADC).

It should be noted that in CSK modulation, the chromaticity of an LED is modulated, rather than the overall intensity or the wavelength. Chromaticity is defined as the combination of hue and saturation and is represented by a point on a standardized color space such as CIE 1931 XYZ. For example, in RGB color space, the chromaticity is defined by the ratio of the red, green, and blue components. When using CSK modulation, the goal is to achieve a high modulation depth, which is defined as the ratio of the change in chromaticity to the original chromaticity. The modulation depth depends on various factors, including the LED's spectral power distribution, the receiver's sensitivity, and the distance between the transmitter and receiver. In CSK analysis, most of the researchers have assumed the peak wavelength of the colored LEDs to be the dominant one. Therefore in most of the CSK related research work the single wavelength (i.e., dominant one) have been considered [53–57, 61–64, 92]. Further this assumption simplifies the analysis of the CSK system. Although LEDs do have a wide spectrum, the spectral power distribution is not continuous, and the LED's peak wavelength dominates the output spectrum. The spectral width of an LED is typically on the order of a few nanometers, which is narrow enough to assume that the LED emits light at a single wavelength for analysis purposes.

In research papers, it is assumed that the received optical power of the respective color light is obtained by filtering the received signal using an appropriate filter that isolates the color of interest. At the receiver end, we have a photodetector that receives the transmitted signal. To obtain the received optical power of lets say red light, we would use a red filter that transmits only the light in the red part of the spectrum and blocks all other colors. When the transmitted signal is received by the photodetector, it generates a current proportional to the optical power of the received signal. The output of the photodetector is typically converted into a voltage using a transimpedance amplifier. The voltage can then be measured and used to calculate the received optical power of the filtered light. For simplicity in the CSK analysis, the filter gain is assumed to be ideal, i.e., 1 and the focus is kept more on the photodetector's responsivity to the filtered light[53–57, 61–64, 92]. Thus, in this thesis work, the above two assumptions have been considered in CSK-related work.

2.3.4 Optical Orthogonal Frequency Division Multiplexing (O-OFDM)

Orthogonal frequency division multiplexing (OFDM) has been proposed for low bandwidth (LB) and high bandwidth (HB) PHY modes of IEEE 802.15.13. OFDM has several advantages over single carrier schemes: it achieves high data-rate by using multiple orthogonal subcarriers to concurrently transmit parallel data streams, eliminates the need for complex equalizers, embodies an inherent resilience to combat ISI; and can be directly extended to medium access schemes. However, the conventional OFDM used in WiFi communication have bipolar and complex symbols. In order to make the complex bipolar OFDM signal compatible with IM/DD, the conversion of complex bipolar signal to real and unipolar signal is done in Optical-OFDM

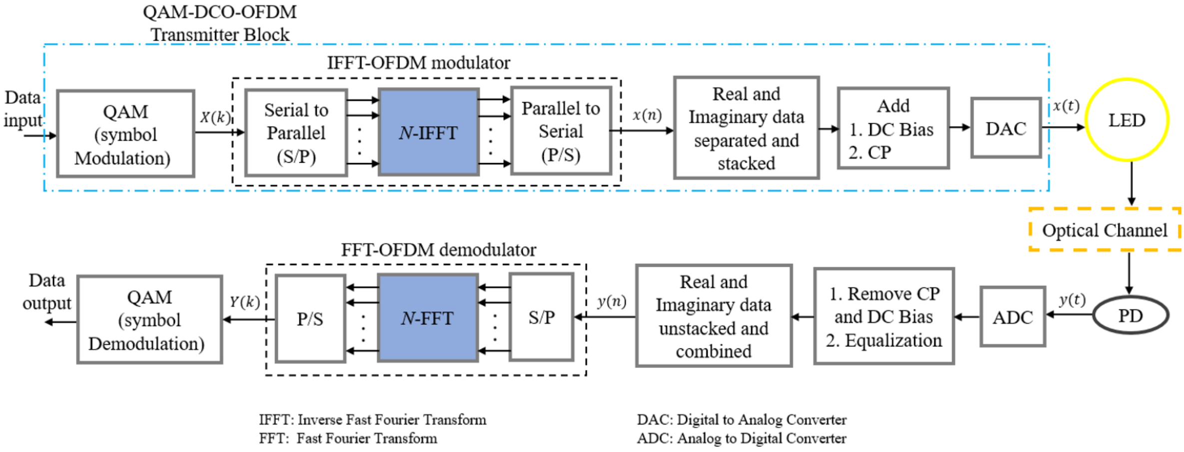

Figure 2.5: Block diagram of QAM based DCO-OFDM for data transmission

(O-OFDM) [99]. More precisely, discrete Fourier transform (DFT) based OFDM outputs a complex bipolar signal which can not be directly transmitted over LEDs. In order to make the complex bipolar OFDM signal compatible with IM/DD, the conversion of complex bipolar data to real data can be done by utilizing Hermitian symmetry or segregating the real and imaginary components of data followed by DC bias addition or negative signal clipping for real and unipolar data. For VLC, the modified OFDM is known as optical-OFDM. O-OFDM has drawn much attention due to its high data rate, decent spectral efficiency, simple equalization and robustness to the inter-symbol interference (ISI). O-OFDM being a multi-carrier modulation scheme helps in overcoming the large ISI caused due to the non-linear frequency response of LEDs [99]. Fig. 2.5 shows the block diagram of direct current biased O-OFDM (DCO-OFDM). The input data bits are subcarrier modulated and then converted from serial to parallel to perform inverse fast Fourier transform (IFFT) operation. In order to obtain real valued bipolar signal after IFFT, Hermitian symmetry is usually applied. However, Hermitian symmetry is computationally complex and $N/2-1$ unique symbols [99, 123] will be transmitted to the receiver whereas in case of segregating method [96] (as shown in Fig. 2.5) $N/2$ unique symbols can be transmitted with lower complexity. It is observed that O-OFDM utilizes N subcarriers to send data, but in true sense the lesser number of unique data are transmitted because the conversion of complex to real data reduces number of information carrying subcarriers. Moreover, it should be noted that different variants of O-OFDM uses different processing block to convert the complex and bipolar signal into real and unipolar signal, such as:

1. DC biased optical OFDM (DCO-OFDM): In DCO-OFDM, appropriate DC bias is applied to the real valued bipolar signal (as shown in Fig. 2.5) to obtain unipolar signal. The addition of DC bias results into higher PAPR and high PAPR causes clipping distortion. Therefore, the performance of DCO-OFDM degrades due to clipping distortion and

becomes less power efficient due to high PAPR [69, 124, 125]. Assuming N to be total number of subcarriers, the actual information carrying subcarriers become $(N/2)$ in DCO-OFDM due to segregating method [96].

2. Asymmetrically clipped optical OFDM (ACO-OFDM): In ACO-OFDM, the bipolar signal is clipped at zero level to achieve unipolar signal before transmission to the LED. The actual information carrying subcarriers become $N/4$ in ACO-OFDM due to consideration of odd subcarriers only for data [99, 123].

3. Flip-OFDM: The polarity separator in flip-OFDM divides the positive and negative components of a bipolar signal into two frames. These frames are multiplexed so that the first subframe has the positive component and the second subframe contains the flipped negative component, resulting in a frame with real unipolar signal [126]. Flip-OFDM and ACO-OFDM have similar performance and spectrum efficiency as both are non-DC approaches. Therefore, Flip-OFDM and ACO-OFDM can be regarded comparable with the exception of receiver complexity. DCO-OFDM, on the other hand, is more spectral efficient but less power efficient than ACO-OFDM and Flip-OFDM [126].

Chapter 3

Design and Analysis of Probabilistic Shaping in CSK

This chapter incorporates probabilistic shaping (PS) of input data in color shift keying modulation techniques to enhance the performance of the VLC physical layer. In order to improve various CSK schemes, PS has been investigated as a generalized technique that does not call for additional hardware (LEDs or PDs) or changes to the constellation symbols, modulation, or demodulation techniques of different CSK schemes. These, together with the absence of a generalized enhancing scheme in past research studies (refer Section 1.4.1 for additional information), served as motivation. This work [70] explores four different source distributions, uniform and three non-uniform (namely exponential, Maxwell-Boltzmann and Pareto) to shape the CSK input symbols according to their probability distribution. The three CSK modulation schemes considered have distinct receiver structure in terms of number and type of photodetector. The standard CSK modulation scheme is the uncoded IEEE 802.15.7 CSK, which uses an RGB LED at the transmitter and three PDs at the receiver (as discussed in detail in Chapter 2.3.3). Another method to implement CSK is by using a single PD at the receiver (as discussed in detail in Chapter 9.1.1). The former is referred to as CSK-3PD while the latter, CSK-1PD, in this report. The third variant of the CSK modulation scheme utilizes one avalanche PD (APD) and has been referred to as CSK-1APD.

Section 3.1 outlines the contributions of this work and presents a brief background of CSK scheme variants. Section 3.2, describes the proposed work based on PS. Section 3.3 explains in detail the noise effect in probabilistic shaping and the derivation of analytical BER expression. The analytical and simulation results are presented in Section 3.4. Finally, Section 3.5 concludes the chapter.

3.1 Contribution

The key contribution of the proposed work can be summarized as follows:

1. This work for the very first time integrates probabilistic shaping of input symbols in the CSK modulation schemes of a VLC system for power-efficiency.
2. The generalized expression of achievable information rate (AIR) has been derived. For a fair comparison among all the scenarios, the unity AIR has been procured for various source distributions according to the distribution parameter (λ).
3. It has been observed that the M symbols in CSK could be shaped by assigning any probability order out of ${}^{n=M}P_{r=M}$ (P stands for permutation) probability orders. However, all the probability orders do not necessarily give the same performance. Algorithms have been developed to obtain the optimum probability order (OPO), i.e., the probability order at which the maximum SNR gain is achieved.
4. The computational complexity and closed-form SER expressions for all CSK schemes have been derived.

3.1.1 CSK variants

Different variants of CSK can be achieved by modifying the number of LED transmitters such as four or five [54]. However in this work the different CSK variants have distinct receiver structure in terms of number and type of photodetector. We have considered three variants of CSK with respect to receiver structure namely CSK with one photodetector (PD) (CSK-1PD), CSK with three PDs (CSK-3PD) and CSK with one avalanche PD (CSK-1APD).

3.1.1.1 CSK-3PD:

The proposed work assumes the generalized property of the VLC channel to be flat (with no inter-symbol interference) and noise to be AWGN. In [53], optical channel estimation for IEEE standard CSK as discussed in detail in Section 2.3.3 of chapter 2 has been carried out by applying a known driving current, i.e., 100 mA or 200 mA, to each RGB channel independently and then recording the photo-response of each detector to each LED. The non-linear relationship between the driver current and the emitted light power of LEDs limits the choice of driving current [113]. This estimation method includes the physical phenomena of distance-based LOS optical channel as shown in (2.9) and considers AWGN for each of the wavelengths (RGB). The channel gain values change as the channel considers NLOS light path, blocking, shadowing, and user-movement [53, 54]. However, this work considers LOS and AWGN, so the channel gain matrix termed as $\mathbf{H}_{3PD}$ is a combination of three IM/DD channels. Each element of $\mathbf{H}_{3PD}$ depicts the gain between the i^{th} LED and j^{th} PD. The estimated independent channel gain matrices in [53] have been utilized to simulate the CSK-3PD VLC system. The average of the simulated results has been considered as the final result. Therefore, the received symbol can be represented by the following optical channel model

$$\mathbf{r}_k = \mathbf{s}_k\mathbf{H}_{3PD} + \mathbf{w}_k, \tag{3.1}$$

where $\mathbf{r}_k$ is the k_{th} received symbol, and $\mathbf{w}_k$ is its respective noise vector. The received symbol is equalized and mapped to x-y chromaticity coordinates and then to data bits. For CSK-3PD, out of eight color band combinations [49], CBC-2 has been selected as it performs better than the other seven CBCs in terms of SNR gain in an AWGN channel [127]. The received symbol expression in (3.1) is in terms of electrical current symbols, the expression changes if it is in terms of intensity and chromaticity [54].

3.1.1.2 CSK-1PD:

In this work, we have considered popular and commercially available PIN structure PDs consisting of a p-type semiconductor, an intrinsic semiconductor, and an n-type semiconductor. PIN diodes have large depletion region which improves the performance by increasing the volume of light conversion. Moreover, the implementation cost of PIN diode is low, therefore in most of the VLC related literature [51, 53, 54] PIN based PDs have been used for research. For more details regarding CSK-1PD [92] refer Section 9.1.1 of Chapter 9. The power received at the PD is the transmitted power multiplied by LOS channel gain (H_{LOS}) [105, 128]. The optical channel gain for CSK-1PD in this work is denoted by H_{1PD}, which is equivalent to H_{LOS}. The k^{th} electrical current (I_k) received at the output of the PD is represented by I_{rec} in (3.2).

$$I_{rec} = I_k H_{1PD} + w_k. \tag{3.2}$$

The CSK-1PD modulation behaves similar to basic PAM [92]. However, it is important to note that CSK-1PD modulation is less susceptible to noise and interference compared to basic PAM, as it uses three LEDs at the transmitter and does not rely solely on the intensity modulation of a single LED as in basic PAM. This feature makes CSK-1PD modulation more efficient in transmitting more bits per symbol with a lower error rate, thereby improving spectral efficiency in VLC. However, basic PAM design is simpler and easier to implement than CSK-1PD modulation. It is also worth mentioning that this study specifically focuses on investigating RGB LED modulation schemes, which are variants of CSK, in line with the study's goals. Hence, CSK-1PD modulation has been considered. In CSK-1PD, the four symbols lie on the same axis (i.e., the x-axis as shown in Fig. 3.3) in a constellation diagram. The M-ary amplitude detection is performed by computing the minimum Euclidean distances (d_{min}) between the received signal and four unique $I_{k=1,2,3,4}$ levels as

$$d_{min} = \min_{I_k \in \mathbb{C}} |I_{rec'} - I_k|. \tag{3.3}$$

Where the set $\mathbb{C}$ has the single-PD photocurrent of all the transmitted M constellation points as computed in Section 9.1 of chapter 9. The symbol that is closest to the equalised received signal ($I_{rec'}$) is mapped to its standard bit representation at the receiver. The RGB LED and PD responsivity vector have been kept same for CSK-3PD and CSK-1PD simulations.

3.1.1.3 CSK-1APD:

CSK-1APD has avalanche PD as the receiver. APD is quite similar to a PIN detector but is highly sensitive. It requires a considerable large reverse bias so that the initial charge carrier is accelerated rapidly, and the resulting collisions have sufficient energy to create new charge carriers, which gives an internal current gain due to avalanche-like effect [113]. CSK-1APD adapts the working principle of CSK-1PD with APD responsivity vector ($\boldsymbol{\rho}_{APD}$). Hence, CSK-1APD can be called a version of CSK-1PD where the responsivity range has increased. The manufacturing cost of APD is much higher than the PD. In this work, the APD considered is from Thorlabs [129], where, $\boldsymbol{\rho}_{APD} = [0.52, 0.37, 0.09]$ for the central wavelengths of red, green, and blue light, respectively.

3.2 Proposed Work

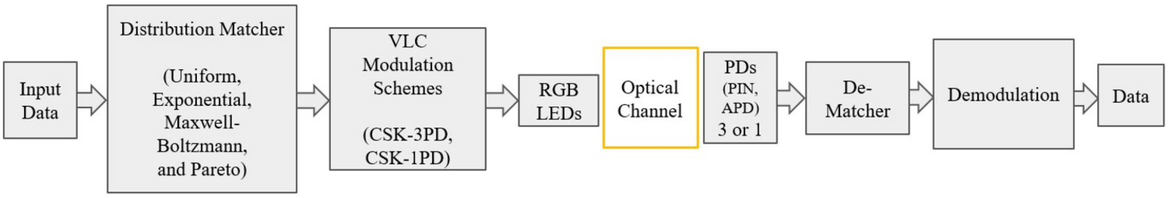

Figure 3.1: Block diagram of the proposed work integrating probabilistic shaping in CSK modulation schemes.

The proposed work consists of four subsections. The first subsection includes shaping of input symbols with various source distributions and the generalized AIR equation. The second subsection explains the algorithm for OPO. The computational complexity of the algorithms and the proposed system have been analyzed in the third subsection. The fourth subsection annotates the derivation of the closed-form SER expressions. Fig. 3.1 illustrates the proposed work with a basic block diagram. The input symbols are probabilistically shaped according to unity AIR and OPO for a chosen CSK scheme in a DM block. The VLC modulation block modulates the PS symbols for the chosen CSK scheme. Based on the modulation scheme, the modulated symbols (LED driving currents) are fed to the RGB LEDs. The mixed optical signal travels through the optical channel to be received at the PD. The received symbols are demodulated according to the VLC modulation scheme. The inverse DM shapes the collected data to the original input data.

3.2.1 Probabilistic Shaping

Wireless communication channels usually consider input data to be random and uniformly distributed. Nowadays, non-uniform input distributions (in which occurrence of all the symbols are not equal) help achieve higher capacity wireless communication systems. The capacity (C) of a communication channel has been defined by Shanon as the maximum of the mutual information between the input (X) and output (Y) symbol of a communication channel [131]. The mutual information ($I(X;Y)$) depends on the input symbol entropy ($H(X)$) and conditional entropy of input and output symbol ($H(X/Y)$) as shown in (3.4). The entropy and conditional entropy depends on the input distribution and conditional distribution ($p(x)$ and $p(x/y)$), respectively [131]. A non-uniform input distribution will impact $H(X)$ and $H(X/Y)$ in (3.4) which will ultimately impact the mutual information and the capacity of the communication channel [132]. The technology to shape the occurrence of the symbols (or constellations) on the basis of a given probability (non-uniform probability distribution) is known as probabilistic shaping [132]. The critical component in the implementation of PS technology is the distribution matcher (DM), which transforms independent Bernoulli distributed data into desired distribution. The DM serves as a shaping encoder and maps data bits to specific distributed (shaped) sequences, which are then modulated accordingly. A dematcher (or inverse matcher) is needed at the receiver side to perform the inverse operation and recover the input bits from the output symbols.

$$\begin{aligned} C &= \max I(X;Y), \\ I(X;Y) &= H(X) - H(X/Y), \\ H(X) &= -\sum_{x} p(x)\log_2 p(x)), \\ H(X/Y) &= -\sum_{x,y} p(x/y)p(x)\log_2 p(x/y). \end{aligned} \tag{3.4}$$

A DM can be considered as a source coder where n input bits are transformed into $k = \mathbb{E}[l(Y)]$ output bits. The average length of output bits from DM is represented by $\mathbb{E}[l(Y)]$. The proposed work adopts arithmetic DM (ADM) to shape input symbols. ADM can transform randomly long input sequences online, i.e., no codebook needs to be stored as opposed to the existing algorithms which require complete codebook to be calculated and stored beforehand for distribution matching [130].

The performance of different source distributions is compared at the same AIR for a fair comparison. Therefore, to frame the expression of AIR, the normalized informational divergence ($\mathbb{D}$) is required to calculate the difference between the actual DM output distribution and the expected distribution [132]. $\mathbb{D}$ is bounded by (3.5) and approaches zero for a large length of input bits [130, 132].

$$\frac{\mathbb{D}(P_Y|P_Z)}{\mathbb{E}[l(Y)]} \leq \frac{\log_2 \frac{1}{p_{code}(1-p_{code})}}{\mathbb{E}[l(Y)]}, \tag{3.5}$$

where P_Y and P_Z are the probability of actual DM output, and the expected DM output, respectively. The aim of DM is to emulate input data with a pre-decided target distribution where $p_{code} = P_Z(0)$ and $P_Z(0)$ is the probability of the symbol "00" in the probability distribution. Since the mapping is one-to-one, so $\mathbb{E}[l(Y)] \geq \mathbb{H}(P_Y) = n\mathbb{H}(P_S)$ where P_S is the probability of input data which is same for all data [130, 132]. Therefore, the average output length depends on informational divergence and source entropy ($\mathbb{H}(P_S)$) as

$$\mathbb{E}[l(Y)] \leq n\mathbb{H}(P_S) + \mathbb{D}(P_Y|P_Z). \tag{3.6}$$

The code rate $R_c = \frac{n}{\mathbb{E}[l(Y)]}$, of a PS data contributes in deciding the AIR. The generalized maximum AIR equation for uniformly and non-uniformly distributed data, has been realized in the following equation.

$$AIR = \mathbb{H} - (1 - R_c)q/n, \tag{3.7}$$

where q is the number of bits per symbol and $\mathbb{H}$ is the entropy. In uniformly distributed input data, 4-CSK scheme, $R_c = 0.5$, $q = 2$, $n = 1$, and $\mathbb{H} = 2$. Consequently, the maximum AIR comes to be 1. The AIR of uniform distribution has been taken as a reference. Thus, the AIR of all other non-uniform distributions has been matched to unity to retain a consistent AIR. Entropy depends on the probability of symbols $p(s_i)$, which in turn depends on the distribution parameter (λ) of the particular distribution and constellation points s_i of the modulation scheme. The suitable choice of λ value yields $AIR = 1$ for non-uniform distributed input data. The subsections below describe the various distributions in terms of λ and their corresponding λ for unity AIR in CSK schemes.

3.2.1.1 Uniform Distribution

In a communication system, long sequences of random data are usually distributed close to uniform distribution. The occurrence of all the symbols is equal in a uniform distribution. The

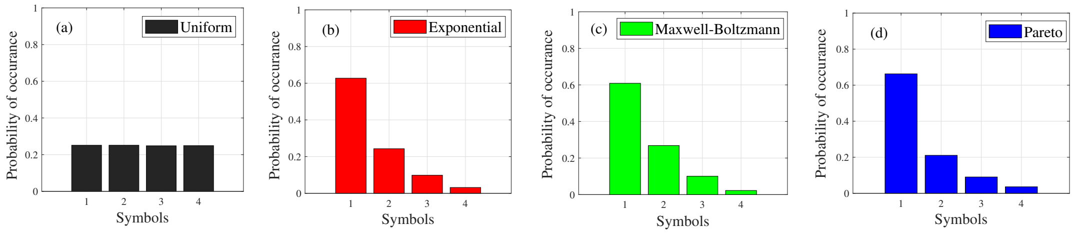

Figure 3.2: PDF of (a) uniform, (b) exponential, (c) Maxwell-Boltzmann and (d) Pareto source distributions for PS-CSK-1PD scheme.

performance of CSK variants with uniformly distributed data is set as a reference to compare the performance of non-uniform PS-CSK systems. Therefore, the Uniform distribution is the one among the four distributions considered in this work. The probability density function (PDF) plot of the uniformly distributed random signal having four symbols has been shown in Fig. 3.2 (a).

3.2.1.2 Exponential Distribution

The aim of utilizing PS is to have non-uniform distribution of the input data. The PS distribution is chosen based on its ability to provide significant difference in the probability of symbols, where the highest probabilities of the non-uniform source distributions could be assigned to the symbols having the largest minimum Euclidean distance so as to get lower error rate at the receiver. Further, exponential distribution is a well-known non-uniform distribution, which has been considered in literature in PS of input data [58–60]. The probability $p(s_i)$ at which different constellation points (i.e., s_i) are transmitted in an exponential distribution is given by (3.8). Fig. 3.2 (b), shows a considerable difference between the highest value probability and the rest probabilities provided by the exponential distribution.

$$\begin{aligned} p(s_i) &= \frac{exp(\text{-}\lambda\,\|s_i\|)}{Z(\lambda)} \qquad \lambda \geq 0, \\ \text{where,} \quad Z(\lambda) &= \sum_{i=1}^{M} exp(\text{-}\lambda\,\|s_i\|). \end{aligned} \tag{3.8}$$

3.2.1.3 Maxwell-Boltzmann Distribution

Employing the same reasoning behind selecting the non-uniform PS distribution, the Maxwell-Boltzmann distribution has been taken into consideration. The probability distribution of transmitted constellation points are calculated from (3.9) and unity AIR λ.

$$\begin{aligned} p(s_i) &= \frac{exp(\text{-}\lambda \|s_i\|^2)}{Z(\lambda)} \qquad \lambda \geq 0, \\ \text{where,} \quad Z(\lambda) &= \sum_{i=1}^{M} exp(\text{-}\lambda \|s_i\|^2). \end{aligned} \tag{3.9}$$

$$\begin{aligned} p(s_i) &= \frac{\lambda s_{i_{min}}{}^{\frac{\lambda}{(s_i)^{\lambda+1}}}}{Z(\lambda)} \qquad \lambda \geq 0, \\ \text{where,} \quad Z(\lambda) &= \sum_{i=1}^{M} \lambda s_{i_{min}}{}^{\frac{\lambda}{(s_i)^{\lambda+1}}}. \end{aligned} \tag{3.10}$$

3.2.1.4 Pareto Distribution

The Pareto distribution has been selected based on the same justification as that of exponential and Maxwell-Boltzmann distributions. Additionally, another key consideration when choosing the PS distribution is that the lowest probable symbol should not have zero probability. The probability of occurrence of symbol s_i is given by (3.10) where $s_{i_{min}}$ is the minimum valued symbol among all symbols.

The λ obtained to achieve unity AIR for different distributions has been shown in Table 3.1. Equations (3.8), (3.9) and (3.10) calculate the probability distribution of all CSK schemes for corresponding non-uniform distributions. For example, the 4-CSK-1PD PDF plot after employing exponential, Maxwell-Boltzmann and Pareto DM at unity AIR has been presented in Figs. 3.2 (b), 3.2 (c), and 3.2 (d), respectively.

Table 3.1: Calculated distribution parameter (λ)

Distributions	**λ for CSK -**		
	1PD	**3PD**	**1APD**
Exponential	15	5	7
Maxwell-Boltzmann	26	6	15
Pareto	3.5	0.9	0.5

The PS gain, which is evaluated through mutual information (MI), varies for different ranges of SNR intervals as the distribution parameter λ is varied [58, 60]. Therefore, each λ value can provide its maximum PS gain to a specific SNR region. This variability in PS gain can be beneficial for time-varying channel conditions, especially when incorporating channel-aware PS input data [58, 60].

Additionally, it has been observed that different modulation schemes have their specific SNR regions with the highest MI [133]. This information is demonstrated in the SNR versus

SER plots shown in Figs. 3.6-3.8, which shows varying SNRs at the FEC limit SER for different modulation schemes.

The proposed system in the paper considers a static VLC channel and aims to achieve a low-cost and less computationally complex system. To ensure a fair comparison, the authors have chosen a unity AIR λ as the fixed criterion to measure the PS gain for various CSK schemes around the FEC limit SER. Therefore, the authors have not considered the criterion of varying PS gain.

In summary, the PS gain is influenced by the distribution parameter λ, which can provide different maximum PS gains for different SNR intervals. This is particularly advantageous for time-varying channel conditions with channel-aware PS input data. Additionally, different modulation schemes have their specific SNR regions with the highest MI, which are demonstrated in the SNR versus SER plots. The authors have focused on measuring the PS gain for various CSK schemes around the FEC limit SER for a unity AIR λ to ensure a fair comparison.

3.3 Optimum Probability Order (OPO)

Noise has a profound effect on the detection of different probable symbols. The four symbols of 4-CSK system can be transmitted with any of the given probabilities, p_1, p_2, p_3 and p_4 where, $p_1 > p_2 > p_3 > p_4$. There are $^{\boldsymbol{n}}\boldsymbol{P_r}$ possible probability orders to assign r different probabilities to n different symbols, where $r = n = M = 4$. The possible ways to assign probability orders follow the example of 24 possible permutations of 4 different objects. The performance of the system does not change for uniform distribution at any probability order while, for the non-uniform probability distribution, probability order influences the performance. The requisite for probability order allocation in non-uniform probability distribution has been explained in below subsections. It is exhaustive to simulate all 4! probability order combinations to obtain the best performing probability order. The received constellation points are averaged out for a large number of iterations and then used in the two algorithms (1, and 2), for CSK-1PD or CSK-1APD (CSK-1PD/1APD), and CSK-3PD, respectively to estimate the best performing probability order in terms of SNR gain. Additionally, exhaustive simulations have been performed to confirm the accuracy of the algorithms.

3.3.1 CSK-1PD

The transmitted symbols s_1, s_2, s_3, and s_4 have been obtained in the form of normalized electric currents 0.22, 0.28, 0.34, and 0.42, respectively as shown in Table. 9.1 of chapter 9. The simulated transmitted and received symbols have been plotted in the constellation diagram (as shown in Fig. 3.3) to show the effect of noise. The transmitted as well as received symbols,

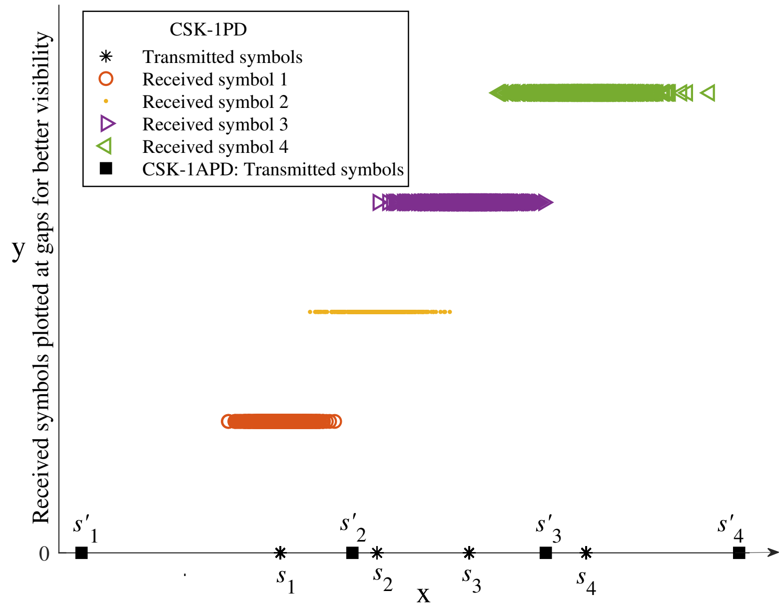

Figure 3.3: Constellation diagram of CSK-1PD and CSK-1APD transmitted symbols $s'_{i=1,2,3,4}$ and CSK-1PD received♩ symbols.

♩: All the received symbols actually lie on x-axis only. However, the received symbols are plotted in gaps in the y-axis for better visibility of the noise spread.

all appear in the x-axis only, implying the behaviour of CSK-1PD as PAM [92]. For better visibility of the spread of the received symbols in Fig. 3.3, the symbols are placed in gaps in the y-axis.

The possibility of error in detection is higher when two close valued symbols interfere more into each other. The source distribution impacts the error in detection if two interfering received symbols occur frequently. It has been observed that the spread of the larger valued transmitted symbols is more at the receiver due to PD shot noise, which is directly proportional to the power of the transmitted symbols [113]. Algorithm 1 provides the OPO for CSK-1PD by scrutinizing the mentioned conditions. The Euclidean distance ($\tilde{d_i}$) between all received symbols (r_i) are calculated with the limits as shown in the first step of the Algorithm 1. The Euclidean distances obtained can be sorted in ascending or descending order. The Algorithm 1 adopts ascending order for further calculations. The highest probability p_1 is assigned to the symbol which only belongs to the maximum Euclidean distance ($\tilde{d_1}$). The second-highest probability p_2 is assigned to the symbol which belongs to both the maximum and the second maximum ($\tilde{d_2}$) Euclidean distance. Similarly, the rest of the probabilities are assigned based on the above concept. CSK-1APD follows the same ruling of CSK-1PD for OPO, but with its own constellation points (as shown in Fig. 3.3). The OPO for CSK-1PD/1APD through exhaustive simulations as well as Algorithm 1 comes out to be same as $p(s_1) > p(s_2) > p(s_3) > p(s_4)$.

Algorithm 1 Algorithm for best probability allocation order in 4-CSK-1PD

```
1. Find all possible Euclidean distances between received symbols.
$\tilde{d_i} = |r_i - r_j|, \quad \begin{cases} s.t. \quad j = i+1, \\ i \in \{1,\ldots,(M-1)\}, \text{ and} \\ j \in \{2,\ldots,M\} \end{cases}$
2. Sort all $\tilde{d_i} = [\tilde{d_1},\ldots,\tilde{d}_{M-1}]$ in ascending order. Assuming initialized ascending order as,
$[\tilde{d}_{M-1}$ <, ... ,< $\tilde{d_1}]$.
for $i \leq M$ do
    if $r_i \in \{\tilde{d_1}\}$ only then
        symbol $s_i \leftarrow p_1$
    else if $r_i \in \{\tilde{d_1},\tilde{d_2}\}$ then
        symbol $s_i \leftarrow p_2$
    else if $r_i \in \{\tilde{d}_{M-1},\tilde{d}_{M-2}\}$ then
        symbol $s_i \leftarrow p_3$
    else if $r_i \in \{\tilde{d}_{M-1}\}$ then
        symbol $s_i \leftarrow p_4$
    end if
end for

return (Symbols with assigned probabilities)
```

3.3.2 CSK-3PD

The symbols s_1, s_2, s_3 and s_4 in Fig. 3.4 (black dots) represents the transmitted symbols of CSK-3PD in color space chromaticity diagram. Similarly, the received symbols (r_i) are converted to x-y values to detect the transmitted symbols. Transmitted symbols having maximum Euclidean distances cause less error while detection at the receiver. The constellation points of CSK-3PD in Fig. 3.4 is in two dimension (2-D). Therefore, Euclidean distance between s_1 and s_2 is calculated in x-y chromaticity plane. The noise effect and spreading in CSK-3PD is in 2-D, unlike one dimension in case of CSK-1PD.

The logic to obtain the OPO for the four symbols of CSK-3PD has been explained in Algorithm 2. The probabilities are assigned based on the Euclidean distances of a particular symbol with all other symbols, which is very similar to the basic concept of Dijkstra's algorithm [134]. The first step of Algorithm 2 calculates the Euclidean distances between all received symbols $r_i = [\text{x, y}]_{r_i}$ and then sorts them in ascending order. One can use any of the two sorting methods ascending or descending. Ascending order has been opted in Algorithm 2 for further calculations. Descending order can be used by appropriately reversing the algorithm

Algorithm 2 Algorithm for best probability allocation order in 4-CSK-3PD

```
1. Find all possible Euclidean distances between received symbols (i.e., constellation points).
$\tilde{d}_{ij} = \left\| [\mathrm{x},\, \mathrm{y}]_{r_i} - [\mathrm{x},\, \mathrm{y}]_{r_j} \right\|, \begin{cases} s.t. \quad i \neq j \ \&\ ij \neq ji, \\ i \in \{1, \dots, M\}, \ \text{ and} \\ j \in \{1, \dots, M\} \end{cases}$
2. Sort all $\tilde{d}_{ij} = [\tilde{d}_{12}, ..., \tilde{d}_{(M-1)M}]$ in ascending order. Assuming initialized ascending order as,
$[\tilde{d}_{12} < \tilde{d}_{13} <, ... ,< \tilde{d}_{(M-2)M} < \tilde{d}_{(M-1)M}]$.
3. Find average Euclidean distance for all symbols with constraints in step 1.
        $\overline{d}_{r_{i=1}} = \frac{\sum_j^M \tilde{d}_{1j}}{(M-1)}$
4. Sort all $\overline{d}_{r_i}$ in ascending order. Assuming initialized average Euclidean distance as,
$[\overline{d}_1 <, ... ,< \overline{d}_M]$.
for $i \leq M$ do
    if $r_i \in \{\overline{d}_{r_i}\} \ s.t. \ \overline{d}_{r_i} == \overline{d}_M$ then
        $symbol \quad s_i \leftarrow p_1$
    else if $r_i \in \{\tilde{d}_{(M-1)M}\} \ \& \ \overline{d}_{r_i} \neq \overline{d}_M$ then
        $symbol \quad s_i \leftarrow p_2$
    else if $r_i \in \{\tilde{d}_{(M-2)M}\} \ \& \ \overline{d}_{r_i} \neq \overline{d}_M$ then
        $symbol \quad s_i \leftarrow p_3$
    else if $r_i \in \{\overline{d}_{r_i}\} \ s.t. \ \overline{d}_{r_i} == \overline{d}_1$ then
        $symbol \quad s_i \leftarrow p_4$
    end if
end for

return (Symbols with assigned probabilities)
```

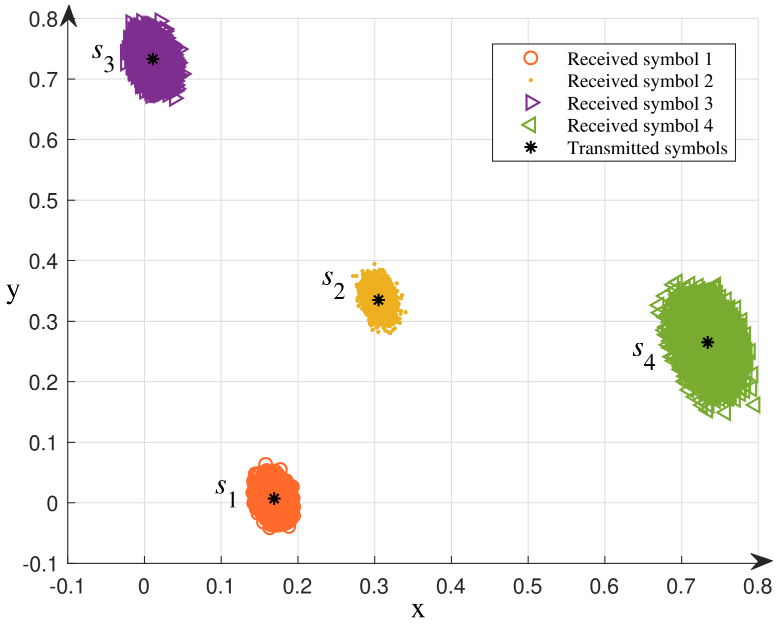

Figure 3.4: Constellation diagram of transmitted and received symbols in CSK-3PD.

for ascending order inside the **for** loop. The highest probability p_1 is assigned to the symbol which belongs to the maximum average Euclidean distance $\overline{d}_M$ with all other symbols. All the constellation points lie within the constellation triangle (as shown in Fig. 2.4). Hence, the algorithm uses the property of a triangle in which the sum of the distance from vertices to a point inside that triangle is less than the triangle perimeter. Therefore, using triangle inequality, it comes out that all the symbols lying at the vertex have higher average Euclidean distance than the symbol lying inside the constellation triangle. The second highest probability p_2 is assigned to the symbol which belongs to the maximum $\tilde{d}_{(M-1)M}$ Euclidean distance (as shown in Algorithm 2) but does not have the largest average Euclidean distance with all other symbols. Likewise, the rest of the symbols are assigned their probabilities. If two symbols have the same average Euclidean distance or maximum Euclidean distance, then randomly any of them can be chosen in the Algorithms 1 and 2. The sorting logic in the algorithm places two same values randomly one after the other. Algorithm 2 returns the OPO for CSK-3PD to be $p(s_3) > p(s_4) > p(s_1) > p(s_2)$. Besides, exhaustive simulations confirm the same probability order.

A conceptual proof for the algorithms can be done by referring constellation optimization process at the transmitter where one wants to increase the minimum Euclidean distance between the symbols to get lower SER at the receiver [53, 92]. In the case of constellation optimization one has to determine the symbols from a continuous space, so, the optimization solution may get trapped in local optima [53, 92]. Whereas, in case of assigning probability order, the constellation symbols are known. Algorithm 1 and 2 get a finite and discrete set to work upon and thus provide a global optimum solution.

3.3.3 Complexity Analysis

In case of Algorithm 1, the complexity of finding Euclidean distance is $O(1)$ as the subtractions, squares, additions, and square root are linear in M (M is the number of different input symbols). Hence, for all possibilities $(M-1)*O(1)$=$O(M-1)$. The sorting is done through the Matlab function “sort”, which is based on one of the fastest algorithms for sorting, the standard quicksort algorithm. It is an $O((M-1)*\log(M-1))$ operation in Algorithm 1. The for loop statement and if-else statements are of $O(1)$ complexity because of basic arithmetic operations. In the case of, if-then-else statements, any one of the sequences will get execute. Therefore, the worst-case time for the complete if-then-else statement would be $O(1)$ only as all the statements have the same $O(1)$ complexity. The for loop variable (i) is incremented by a constant amount till M, so the complexity of for loop will be $M*O(1)$=$O(M)$ [135]. Therefore, the total complexity to obtain OPO for CSK-1PD/1APD is O_{Alg1}=[$O(M-1)+O((M-1)\log(M-1))+O(M)$]. The step 3 of Algorithm 2, includes finding average which involves summing up the $M-1$ numbers and then dividing by $M-1$; hence it has $O(M-1)$ linear complexity. Therefore, the total computational complexity for obtaining OPO for CSK-3PD is O_{Alg2}=[$O((M-1)M)+O((M-1)M*\log(M-1)M)+M*O(M-1)+O((M)*\log(M))+O(M)$] on following the same complexity analysis rules as in Algorithm 1. The two extra big O notations are due to the two extra steps in Algorithm 2 from Algorithm 1.

The computational complexity of the proposed system depends on two main blocks, one consisting of CSK modulation schemes, and another is distribution matcher. In CSK-3PD, x-y to RGB converter requires linear equations to solve which demands a complexity per symbol of $O(3^3)$ (where the complexity is measured in terms of the number of multiplication operations) [92]. Whereas, in CSK-1PD/1APD, a lookup table operation maps data bits directly to the emitted optical power of each LED which demands a complexity per symbol of $O(1)$ [135]. The DM used in the work is based on arithmetic coding [130]. Assuming infinite precision addition and multiplication take constant time, the computational complexity of the DM becomes $O(M*(Q+Q_o))$ [135, 136], where Q is the length of input bits which are encoded to Q_o output bits. Further, the complexity to obtain probability distribution for a given distribution type is of constant order $O(1)$ as it requires only basic arithmetic operations [137]. Hence, the computational complexity including encoding, decoding, modulation, demodulation, and finding OPO of the four symbols in PS-CSK-3PD, and PS-CSK-1PD/1APD systems become [$O_{Alg2}+2*O(M*(Q+Q_o))+O(1)+2*N*O(3^3)$], and [$O_{Alg1}+2*O(M*(Q+Q_o))+O(1)+2*Q'*O(1)$], respectively. Q' denotes the input size. The computational complexity of the proposed systems can be further reduced by exploring lesser computationally complex DMs [138]. It is observed that the complexity of the proposed systems depend less on the PS part, whereas more on the modulation part. Therefore, the complexity of PS-CSK-3PD system is greater than PS-CSK-1PD/1APD.

3.3.4 Theoretical Error Performance

The closed-form SER expressions of the proposed VLC systems have been derived to validate simulated results. The total probability of symbol error (P_s) in CSK-1PD can be calculated using the fundamental equations to calculate SER for both equiprobable and non-equiprobable symbols, as shown in (3.11). The probability of error for symbol s_i is denoted by $p(e|s_i)$ and the conditional probability by $p(s_j|s_i)$. The set of symbols closest to s_i is denoted by ζ_j. In uniform distribution, probability of occurrence of all the symbols are equal therefore, $p(s_i) = 0.25$ for all $i = 1,2,...,M$. CSK-1PD behaves as PAM, so the analysis of symbol error probability for PAM modulation scheme under AWGN condition [139] can be exploited. The noise follows the Gaussian probability distribution function with $\mu = 0$ and noise variance, $\sigma^2 = \frac{N_0}{2}$. The minimum distance between symbols is denoted by d_{min}. Hence, in terms of d_{min}, one can obtain SER in an M-level optimum detector PAM system. Thus, the P_s for the CSK-1PD system can be estimated by (3.12). When the symbols are non-equiprobable the detection threshold for received signal shifts from the midway point between two symbols [140].

$$\begin{aligned} P_s &= \sum_{i}^{M} p(s_i)p(e|s_i), \\ p(e|s_i) &= \sum_{s_j \in \zeta_j} p(s_j|s_i). \end{aligned} \tag{3.11}$$

$$P_s = \frac{(M-1)}{M}\text{erfc}\left(\sqrt{\frac{d_{min}^2}{4N_0}}\right). \tag{3.12}$$

$$p(r|s_i) = \frac{1}{\sqrt{\pi N_0}} e^{-(r-s_i)^2 \big/ N_0}. \tag{3.13}$$

$$\Gamma_{ij} = N_0 \ln \frac{p_{s_i}}{p_{s_j}}. \tag{3.14}$$

$$\begin{aligned} p(s_i|s_j) &= \frac{1}{2}\text{erfc}\left(\sqrt{\frac{(\left|d_{ij}\right|^2 - \Gamma_{ij})^2}{4\left|d_{ij}\right|^2 N_0}}\right), \\ &\text{when,}\quad \Gamma_{ij} - \left|d_{ij}\right|^2 < 0, \end{aligned} \tag{3.15}$$

$$p(s_j|s_i) = \frac{1}{2}\text{erfc}\left(\sqrt{\frac{(\left|d_{ij}\right|^2+\Gamma_{ij})^2}{4\left|d_{ij}\right|^2 N_0}}\right), \tag{3.16}$$

$$\text{when,} \quad \Gamma_{ij}+\left|d_{ij}\right|^2 > 0.$$

$$P_{PS}^{1PD} = \sum_{i=1}^{M-1}\left[\frac{p(s_i)}{2}\text{erfc}\left(\sqrt{\frac{(|d_i|^2+\Gamma_i)^2}{4|d_i|^2 N_0}}\right)+\frac{p(s_{i+1})}{2}\text{erfc}\left(\sqrt{\frac{(|d_i|^2-\Gamma_i)^2}{4|d_i|^2 N_0}}\right)\right]. \tag{3.17}$$

The conditional PDF has been obtained from equation (3.13) for received signal r when s_i is transmitted [139]. The detector decides from conditional PDF in (3.13) in favour of s_i given that s_j was transmitted when $p(s_i)e^{-(r-s_i)^2/N_0} > p(s_j)e^{-\left(r-s_j\right)^2/N_0}$. Thus, the new detection threshold Γ_{ij} as shown in (3.14) depends on the probability of symbols. The two conditional probabilities between two symbols i.e. $p(s_i|s_j)$, and $p(s_j|s_i)$ are shown in (3.15), and (3.16), respectively. The Euclidean distance between s_i and s_j is represented by d_{ij}. The PS-CSK-1PD probability of symbol error (P_{PS}^{1PD}) has been derived and shown in (3.17) using equations (3.15) and (3.16) in (3.11). The d_i notation in (3.17) denotes the same Euclidean distance described in section 3.3.1, but for transmitted symbols and Γ_i (obtained from (3.14)) takes the same two symbols which are used to calculate d_i.

Further, the theoretical expression in (3.17) to find the SER of PS-CSK-1PD works for PS-CSK-1APD as well. In CSK-1APD, only the set of constellation symbol points and their corresponding noise varies, which in turn changes the Euclidean distance between the symbols with respect to CSK-1PD.

The theoretical BER of CSK-3PD has been derived in the literature [54, 141, 142]. The references [141], and [142] have shown the exact BER analysis of the CSK-3PD by considering symbol decision regions. In this work, the basic idea to obtain theoretical SER of CSK-3PD comes from (3.11) as discussed earlier. The only difference is in the way transition (or conditional) probabilities are calculated. The transition probabilities are computed in 2-D signal space using decision region partitioning method [142]. The transition probability, $p(s_j|s_i)$ from a transmitted symbol (s_i) to the estimated symbol (s_j) is the probability of the presence of the noise corrupted received symbol in the decision region $\mathscr{D}_j$ of s_j, where i and j $\in \{0,\ldots,3\}$. The transition probability is expressed in polar coordinates as

$$p(s_j|s_i) = \int\int_{\mathscr{D}_j} P_w(l,\theta)dld\theta, \tag{3.18}$$

where symbol s_i is considered origin, l and θ represents the length and the angle of the vector from $s_{i=0}$ to the decision points A and B as shown in Fig. 3.5. The PDF of AWGN in the CSK-3PD system is denoted by $P_w(l,\theta)$ in (3.18). The transition probabilities are divided into three different types based on the transition of symbols from center-to-vertex (c2v), vertex-to-center

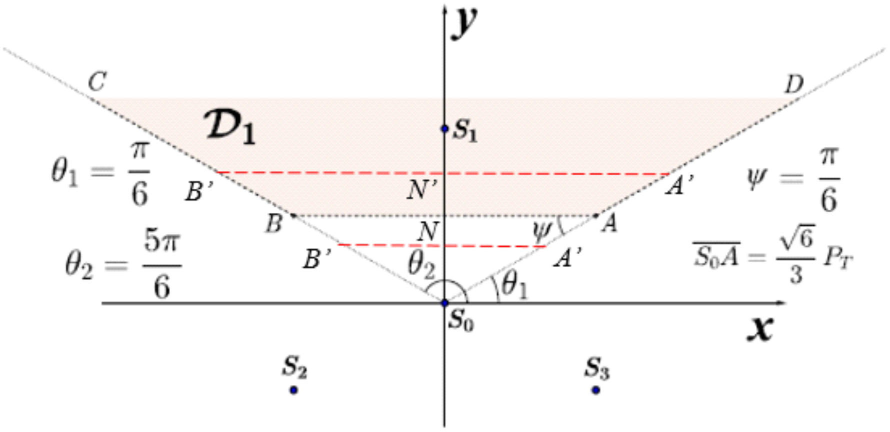

Figure 3.5: The transition of centre symbol s_0 to vertex symbol s_1 in probabilistically shaped 4-CSK-3PD. Figure adapted from Fig. 4 in [142].

(v2c), and vertex-to-vertex (v2v). For computational ease, the decision region $\mathscr{D}_j$ is partitioned at times as a combination (addition or subtraction) of type I basic shape ($\mathscr{D}_{typeI}$) and type II basic shape ($\mathscr{D}_{typeII}$). Fig. 3.5 shows the transition of central symbol s_0 to vertex symbol s_1 in CSK-3PD system displaying AB as the threshold line for equiprobable symbols. The decision region $\mathscr{D}_1$ (DABC) is not segregated further as it is an open region of $\mathscr{D}_{typeI}$. The equation in (3.18) can be simplified to single integration,

$$p((\mathscr{D}_1|s_i) = \frac{1}{2\pi}\int_{\theta_1}^{\theta_2} exp\left[-\frac{\alpha\gamma_s \sin^2\psi}{sin^2(|\theta-\theta_1|+\psi)}\right]d\theta, \tag{3.19}$$

where $\alpha = 1.2z^2$, and z is the ratio between $\overline{S_0A}$ and P_T. The total intensity (P_T) is related to the average symbol energy E_s. The probability of symbol transition can be calculated by substituting $\alpha = 0.8$ into (3.19), obtained from $\overline{S_0A} = \frac{\sqrt{6}}{3}P_T$ [142]. Fig. 3.5 explains the θ_1, θ_2, ψ and $\overline{S_0A}$. The received SNR has been represented by γ_s. The transition probability in (3.19) can be approximated as a function of θ_1, θ_2, ψ and α in $|G(\theta_1, \theta_2, \psi, \alpha)|$.

In case of non-equiprobable symbols, the decision point shifts up and down based on the probability of the symbols. The line AB having noise point "N" shifts to $A'B'$ by adding or subtracting the threshold Γ_{ij} in (3.14), thereby changing the value of noise point to N'. The modified vector from origin to decision point A' is denoted by $\overline{S_0A}'$. The shifted line $A'B'$ thus formed is always parallel to the line AB.

$$\frac{\overline{S_0B}}{\overline{S_0B}'} = \frac{\overline{S_0A}}{\overline{S_0A}'} = \frac{\overline{S_0N}}{\overline{S_0N}'}, \tag{3.20}$$

$$\overline{S_0A}' = \frac{\sqrt{6}}{3}P_T\left(1 \pm \frac{2\Gamma_{01}}{d_{01}}\right), \tag{3.21}$$

$$\alpha_{ij} = 1.2\left[\text{¢}\left(1 \pm \frac{2\Gamma_{ij}}{d_{ij}}\right)\right]^2, \tag{3.22}$$

$$P_{PS}^{3PD} = \sum_{\substack{j=1\\ j\neq c}}^{M}\left[p_c\,|G(\chi_{c2v},\, \alpha_{cj}^{c2v})| + p_j\left(|G(\chi_{v2c},\, \alpha_{cj}^{v2c})| + \sum_{\substack{i=1\\ i\neq c,\, j}}^{M}|G(\chi_{v2v},\, \alpha_{ij}^{v2v})|\right)\right]. \tag{3.23}$$

The basic proportionality theorem for triangles can be extended to multiple parallel lines cut by transversals. The two parallel lines AB and $A'B'$ are cut by two transversals (S_0D and S_0C), which divide the transversals proportionally. The value of $\overline{S_0A}'$ can be calculated directly from the equation $\overline{S_0A}' = \frac{\frac{d_{01}}{2}\pm\Gamma}{sin\psi}$ or from the proportionality equation in (3.20) and $\frac{\overline{S_0N}}{\overline{S_0N'}} = \frac{\frac{d_{01}}{2}}{\frac{d_{01}}{2}\pm\Gamma}$ as shown in (3.21). The Euclidean distance between symbols s_0 and s_1 is denoted by d_{01}. The noise point N divides d_{01} into two equal lengths for equiprobable symbols.

The values of different θ, ψ and $\overline{S_0A}$ for c2v, v2c, and v2v transitions are obtained from the work in [142]. The values do not change with changing noise point and can be directly applied to equation (3.19). The value of α is computed from $\overline{S_0A}'$ which varies for all twelve ($^{(4)}P_2 = 12$) transitions. The generalized equation to calculate α for symbol transition between s_i and s_j is obtained in (3.22), where $\text{¢} = \frac{\sqrt{6}}{3}$ for c2v, v2c and v2v transitions except some decision regions in v2v, where $\text{¢} = \frac{2\sqrt{6}}{3}$. The transition probability for c2v can be written as $|G(\chi_{c2v},\, \alpha^{c2v})|$, where χ_{c2v} is $(\theta_1, \theta_2, \psi)_{c2v}$ in c2v. The total probability of error for PS-CSK-3PD can be obtained using equation (3.11), (3.19), (3.21) and (3.22). The expression of theoretical SER for PS-CSK-3PD (P_{PS}^{3PD}) is computed in (3.23), where p_c, and p_j are the probability of central, and vertex symbols, respectively. The α calculated for transition between central (c) and vertex (j) symbols in c2v is represented by α_{cj}^{c2v}. Hence, the transition probability from centre to vertex symbol is expressed by $|G(\chi_{c2v},\, \alpha_{cj}^{c2v})|$. Similarly, other notations $|G(\chi_{v2c},\, \alpha_{cj}^{v2c})|$ and $|G(\chi_{v2v},\, \alpha_{ij}^{v2v})|$ can be inferred.

3.4 Results and Discussion

The simulation parameters considered for this work are stated in Table 3.2. The performance results of different PS-CSK-1PD VLC system has been shown in Fig. 3.6. It is observed that Pareto distributed input symbols in CSK-1PD performs better than uniform, Maxwell-Boltzmann, and exponential distribution, by 2.7, 1.45, and 0.95 dB of SNR at SER of 10^{-3}, respectively. Fig. 3.7 shows the performance of different PS-CSK-3PD VLC system. It has been observed that the Pareto distribution still gives higher performance gain at SER of 10^{-3} by a margin of 0.65 dB, 1.65 dB, and 2 dB from exponential, Maxwell-Boltzmann, and uniform distribution, respectively. The performance of PS-CSK-1APD VLC system has been

Table 3.2: Simulation parameters.

Parameters	Value
Distance between Transmitter and Receiver	100 cm
Number of LEDs	1 (RGB)
RGB Optical power	1 mW
PD responsivity CSK-3PD/1PD	[0.42, 0.32, 0.22]
PD responsivity CSK-1APD	[0.52, 0.37, 0.09]
m	45
PD area	92 mm^2

shown in Fig. 3.8. It is interesting to observe that all the non-uniform distributions give a good margin of performance gain as compared to uniform distribution, though Pareto still gives the best performance with 5.9 dB. The union bounds and the assumptions considered in analytical SER expressions play an essential role in emulating the simulation results. However, a good agreement between the simulated and theoretical plots can be observed in all the results [139]. Table 3.3 summarises the obtained values of SNR at FEC limit SER for the different distributions with all variants of CSK, i.e., CSK-1PD, CSK-3PD, and CSK-1APD.

It is observed from all the results (Figs. 3.6-3.8) that, non-uniform (exponential, Maxwell-Boltzmann and Pareto) distributions perform better than uniform distribution in any of the CSK schemes. The reason behind the performance gain of non-uniform distributions over uniform distributions can be attributed to the difference in the probability of symbols, where the highest probabilities of the non-uniform source distributions get assigned to the symbols having the largest minimum Euclidean distance so as to get lower SER at the receiver. Hence, as the higher value probability and its difference with other probabilities get further greater in any non-uniform source distribution, then that distribution provides better performance by decreasing the probability of occurrence of large error causing symbols pairs. It has been observed that Pareto distribution outperforms all other distributions (uniform and other two non-uniform distributions considered in the work) in all the results (Figs. 3.6-3.8). It is noticed in Fig. 3.2, at AIR=1, the probability distribution obtained for Pareto distribution has more gap between the highest value probability and the rest probabilities compared to other distributions. Pareto distribution provides the highest and lowest probability values in its probability distribution which increases the probability of occurrence of minimum error causing symbols pairs and therefore offers greater performance gain. Further, it is observed that PS in CSK-3PD (Fig. 3.7) does not provide the same amount of SNR performance gain as

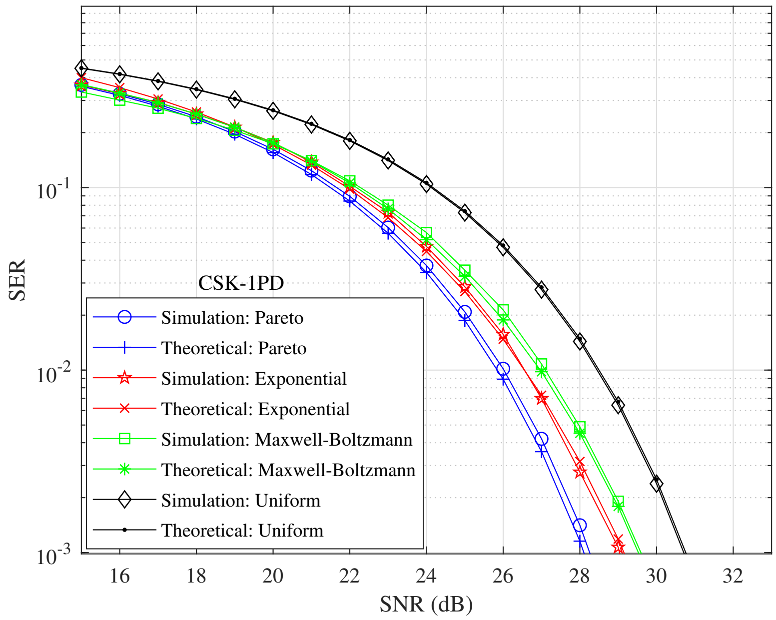

Figure 3.6: SNR versus SER performance of CSK-1PD for various various PS input symbols.

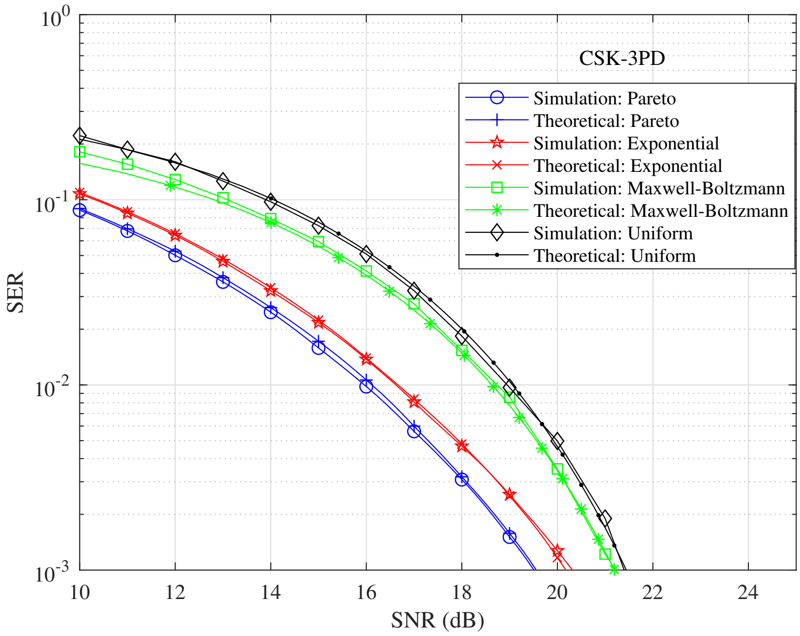

Figure 3.7: SNR versus SER performance of CSK-3PD for various PS input symbols.

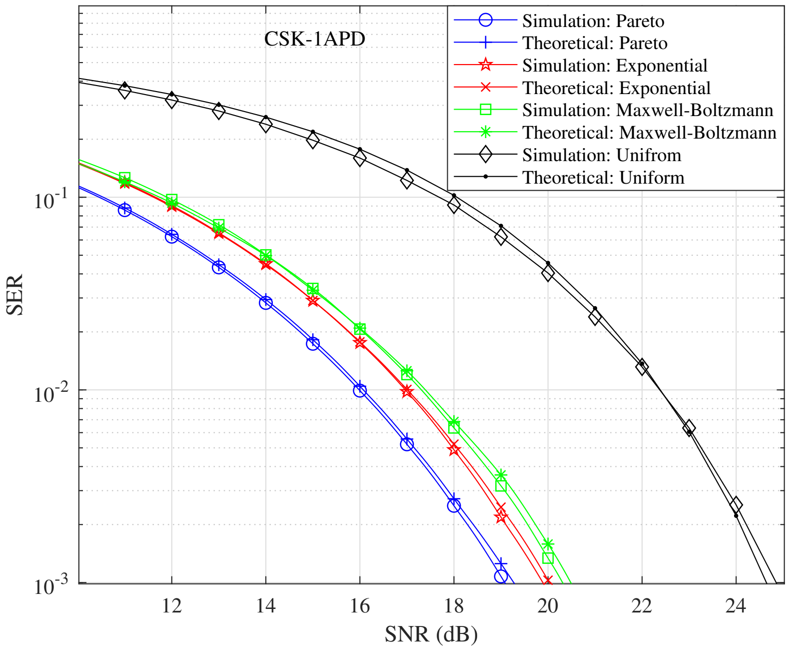

Figure 3.8: SNR versus SER performance of CSK-1APD for various PS input symbols.

Table 3.3: SNR of probabilistically shaped CSK schemes for different input distributions.

Input data distribution type	**SNR (dB) at SER of 10^{-3} for PS-CSK-**		
	1PD	**3PD**	**1APD**
Uniform	30.75	21.45	24.90
Maxwell-Boltzmann	29.50	21.10	20.25
Exponential	29.00	20.10	20.00
Pareto	28.05	19.45	19.00

in CSK-1PD (Fig. 3.6). This behaviour can be associated with the difference in modulation and demodulation techniques of CSK modulation schemes. In case of CSK-1APD (Fig. 3.8), the extra PS gain achieved with respect to CSK-1PD (Fig. 3.6) is because of the APD responsivity vector. The relatively greater gap in the responsivity values of RGB lights in APD than simple PD provides larger Euclidean distances between the received symbols. The gain in CSK-1APD comes with additional hardware cost of APD. It can hence be deduced from the results that the amount of PS gain obtained depends on the modulation schemes.

Previous work relies on change in the modulation-demodulation methods, color control, CSK constellation design and number of LEDs or PDs (hardware) of CSK schemes. Therefore, the results obtained from the PS technique should not be directly compared to the performance enhancement methods of CSK, as reported in the literature. Nevertheless, to show the effectiveness of the proposed scheme, research works which have presented their results in terms of SER versus SNR can be quoted. The four-LED CSK-3PD scheme in [54] achieves 3.5 dB electrical SNR gain at SER of 10^{-3} over the three-LED scheme for an AWGN channel. The conversion of BER to SER and SNR per bit to SNR per symbol has been done by a factor of $\log_2 M$, which closely approximates the conversions and is widely accepted in literature [140]. CSK-3PD has been combined with the PPM scheme for indoor VLC in [55], where 4.7 dB gain is attained in comparison with the standard 4-CSK-3PD at an SER of 10^{-3} at the cost of increased bandwidth. Further, the PPM technique applied in CSK-1PD shows poor performance for the constellation point $L = 4$ among all other constellation points in the paper [92]. To the best of the authors' knowledge, most of the existing literature is about enhancing CSK-3PD. At the same time, this paper for the very first time proposes a common enhancement method for various schemes of CSK, especially, CSK-1PD and CSK-1APD. The proposed work considers $M = L = 4$ CSK-1PD scheme, to keep consistency with all other CSK schemes considered in the paper. The highest PS gain, i.e., 5.9 dB, has been observed in this work in the case of Pareto CSK-1APD. Moreover, the proposed PS scheme in this thesis can be employed to the existing improved CSK-3PD schemes available in the literature [54] [55], to obtain additional SNR gain.

3.5 Summary

This chapter introduces the probabilistic shaping of input symbols in the CSK-modulated VLC system. The suggested research demonstrates the significance of OPO for achieving the highest performance gain in the PS-CSK system. The source distributions have been designed to realize unity AIR for a fair comparison. The performance of the CSK schemes is enhanced by the PS using non-uniform source distributions, particularly Pareto. In case of Pareto PS-CSK-1APD, the maximum SNR gain achieved is 5.9 dB at FEC limit SER of 10^{-3}. The derived analytical SER expressions validate the SNR gain improvements of the simulated results. Thus, the proposed work illustrates the suitability and compatibility of the PS technique in CSK VLC system. The PS-CSK-1PD and PS-CSK-1APD have the potential to enable power-efficient, less computationally complex and low-cost architecture for VLC enabled IoT sensor networks in indoor scenarios.

Chapter 4

Constellation Design of CSK-1PD with White Color Balance

This chapter revolves around designing and optimizing the constellation points of single PD based CSK (CSK-1PD) to achieve a more energy-efficient modulation scheme, which is highly motivated by the research gaps (refer Section 1.5) observed from literature review in Section 1.4.1.2. The optimization has been done with and without average white tone constraint for uniform and non-uniform (exponential, Maxwell-Boltzmann, Pareto) source distributions (as discussed in 3.2.1). Finally, a novel method to maintain any desired white tone light as CSK-1PD modulated output light has been proposed. CSK-1PD has been described in detail in Section 9.1.1 of chapter 9.

Section 4.1 outlines the contributions of this work [71]. Section 4.2, formulates the constellation design problem and proposes algorithms to solve it. Section 4.3 explains the different constraints considered in detail. In Section 4.4, novel solutions for average white light have been discussed. The different optimized constellation points obtained have been presented and analyzed in Section 4.5. Section 4.6 summarizes the chapter. Finally, Section 4.7 briefs the code book designing work being extended to VLC-based sparse code multiple access (SCMA).

4.1 Contribution

The key contribution of the proposed work can be enumerated as follows:

1. This paper proposes a rigorous framework to design and optimize the constellation points for uniform and non-uniform source distribution in CSK-1PD to reduce the received SER.

2. The constellation points of non-uniformly distributed input symbols in CSK-1PD are optimized by geometrically shaping (GS) the symbols based on their preceding probabilistic shaping (PS). The consecutive PS-GS technique to optimize the constellation points has been scantly investigated hitherto.

3. A relaxed white tone constraint has been formulated by considering the whole white light region in CIE 1931 chromaticity diagram to maintain a white color balance with reduced SER.

4. A novel technique to maintain any desired average white tonality light without degrading the SNR gain by inserting an extra RGB LED at the transmitter.

4.2 Constellation Design and Optimization

4.2.1 Problem Formulation

Fig. 9.1 shows the block diagram of CSK-1PD modulation scheme in VLC. The constellation symbols of M-CSK-1PD at the transmitter side can be represented by RGB optical powers whereas at the receiver side it is physically realized with electrical currents and denoted by symbols (s_i, $i \in 1,2,...M$). M is the number of different symbols. The receiver performs symbol detection in M-CSK-1PD by computing the minimum Euclidean distances between the received and the transmitted symbols in the form of electric currents. Therefore, the constellation design strategy is based on maximizing the minimum Euclidean distance among the differently distributed symbols.

In this chapter, the constellation optimization problem is formulated by adopting the widely accepted constellation design problem. It defines a constrained optimization strategy that maximizes the minimum Euclidean distance among the constellation symbols ($s_{i,j}$) while maintaining some of the aspects such as constant output power, average white color balance with and without PS. The constellation points are designed for the minimization of SER at the receiver. The optimization problem, as shown in (4.1), becomes a max-min problem, and therefore the objective function becomes a non-convex problem [143]. The pairwise Euclidean distance of symbols s_i and s_j is denoted by $|s_i - s_j|$. The objective function is both non-convex and non-differentiable, making it difficult to solve analytically [64, 92]. Further, the minimum function of the objective function is discontinuous, which makes it incompatible with efficient, gradient-based techniques [61–64]. The $M = 4$ constellation symbols ($s_{i,j}$) have been investigated in the paper for CSK-1PD which are in the form of electrical currents.

$$\begin{aligned} &\text{maximize} \quad \min_{\substack{i,\, j\, \in\, \{1,\ldots,M\} \\ i \neq j}} |s_i - s_j|, \\ &\text{subject to} \quad constraints \text{ (described in section 4.3)}. \end{aligned} \tag{4.1}$$

4.2.2 Objective function

To solve this non-convex problem, researchers have suggested many approaches; one of them is the differential approximation which removes the non-differentiable nature by using well known "log sum-exponentials" continuous approximation [143]. The approximated objective function in (4.2) still remains non-convex; however, optimization techniques based on the derivation of the Hessian of the objective function can find the locally optimal symbol sets. For non-convex problems, commercially available optimization algorithms exclusively discover local minima [64]. However, the likelihood of realizing a global optimum is improved by optimizing the objective function multiple times over a small set of random starting points and tuning the β parameter where β determines the accuracy of the approximation between (4.1) and (4.2) as discussed in [61].

The PS of input data already provides SNR gain in optical fiber [60, 133] and VLC systems as shown in chapter 3. The optimized constellation points obtained from (4.2) for uniform input data can be further optimized for non-uniform input data by adapting the concept of hybrid probabilistic shaping and geometric shaping [133, 144]. In this work, we found that applying PS to the CSK-1PD scheme allows for the possibility of shifting the constellations based on the PS, which is not possible in the conventional CSK-1PD scheme. This creates an opportunity for geometric shifting of PS constellation symbols according to their known PS to minimize SER. The PS CSK-1PD constellation points are designed in the confined region of constellation symbols according to the probability of occurrence of symbols, which combines probabilistic shaping and geometric shaping. Thus, in this work, the PS constellation symbols are shifted geometrically according to the known PS of the symbols to get minimum SER. Therefore, the objective function in (4.2) needs to be modified to include the probability of symbols.

$$\begin{aligned} &\text{maximize} \quad -\frac{1}{\beta} \ln \left(\sum_{\substack{i,\, j\, \in\, \{1,\ldots,M\} \\ i \neq j}}^{M} e^{-\beta |s_i - s_j|} \right), \\ &\text{subject to} \quad constraints \text{ (described in section 4.3)}. \end{aligned} \tag{4.2}$$

$$\begin{aligned} &\text{maximize} \; -\frac{1}{\beta}\ln\left(\sum_{\substack{i,\, j \,\in\, \{1,\ldots,M\} \\ i \neq j \\ p(s_i) > p(s_j)}}^{M} e^{-\beta|s_i - s_j|\ln\frac{p(s_j)}{p(s_i)}}\right), \\ &\text{subject to} \quad \mathit{constraints} \text{ in section 4.3.} \end{aligned} \tag{4.3}$$

The PS in constellation symbols follows optimum probability order obtained in Section 3.3 of chapter 3, employing the highest probabilities to the minimum error causing pair of symbols. The probability of occurrence of symbol s_i is represented by $p(s_i)$ for non-uniform source distributions which has been calculated at unity AIR to match it with the uniform source distribution AIR, to retain a consistent AIR in results for a fair comparison as discussed in chapter 3. The plot of PDF of 4-CSK-1PD for uniform, exponential, Maxwell-Boltzmann, and Pareto source distributions at unity AIR has been presented in Figs. 3.2 (a), 3.2 (b), 3.2 (c), and 3.2 (d), respectively. The optimum probability order for CSK-1PD in an AWGN channel follows $p(s_1) > p(s_2) > p(s_3) > p(s_4)$ where $s_1 < s_2 < s_3 < s_4$.

When the symbols are non-equiprobable the detection threshold for received signal in an AWGN channel shift from the midway point between two symbols based on the logarithmic ratio of the probability of occurrence of symbols [140]. Henceforth, the pairwise Euclidean distances of non-equiprobable symbols get affected by the logarithmic ratio of the likelihood of occurrence of symbols as shown in (4.3). The logarithmic ratio alters the pairwise Euclidean distances so that the minimum of log sum-exponentials procures the pairwise Euclidean distance of minimum error causing pair of symbols.

4.2.3 Optimization Algorithm

As stated in section 4.2.1, finding the analytical solution of the non-convex optimization problem becomes a difficult task, so usually, this type of optimization problem is solved with numerical optimization algorithms [145]. The continuous approximated objective functions can be solved using commercially available algorithms such as MATLAB's *fmincon*, which finds the minimum of a constrained nonlinear multivariate function. The maximum of a function can also be found by *fmincon*, by taking negative of the functions in (4.2) and (4.3). This work [71] utilizes MATLAB's *fmincon* based on an interior-point algorithm to obtain the optimized constellation points (OCPs) of CSK-1PD with the constraints (explained in the upcoming section 4.3). The numerical optimization algorithm process is summarized in Algorithm 3. The objective function $\mathscr{F}(\mathbf{X})$, has been formulated for constellation points in the form of matrix $\mathbf{X}$. The set of pairwise Euclidean distances is denoted by (4.4), which can be obtained from matrix

X and a sparse matrix formed out of $\boldsymbol{\rho}$.

$$\eth = \{|s_i - s_j|\} \quad \forall \quad \begin{cases} j = i+1, \\ i \in \{1,\ldots,(M-1)\}, \\ j \in \{2,\ldots,M\}. \end{cases} \tag{4.4}$$

Algorithm 3 Numerical Optimization Algorithm

```
Initialize: Random initial constellation points, X0,
which satisfies power, geometric and range constraints.
X ← X0
$\beta \leftarrow 1$
for $\beta \leq$ 1000 do
    $\mathscr{F}(\mathbf{X}) \leftarrow \max \quad -\frac{1}{\beta}\ln\left(\sum_{k=1}^{\binom{M}{2}} e^{-\beta d_k}\right)$
    subject to Constraints.
    if X obtained satisfies the constraints to become a feasible solution then
        X0 ← X
        $\{\mathbb{P}_{SNR}\} \leftarrow$ SNR(X)
        MED Constraint(X0) ← MED Constraint(X)
        $\beta \leftarrow \beta + 2$
    else
        non-feasible solution obtained
        X0 ← X, where X provides min $\{\mathbb{P}_{SNR}\}$
    end if
end for

return $(\mathbf{X}_o)$
```

The tuning parameter β in Algorithm 3 produces poor result for smaller values (of the order of 10-100), whereas, for arbitrarily large values (of the order of 500-1000), the large gradients cause the algorithm to converge slowly. Therefore, the objective function applies the interior point method for multiple iterations, starting with a smaller β and increasing β in each iteration [64]. This approach provides a reliable approximation without slow convergence and with each successive β the optimal solution of the previous β acts as the starting point for the next. However, the solution obtained at each successive β may not always be feasible with respect to the linear inequality constraints. Therefore, in Algorithm 3, the basic concept of the genetic algorithm to produce good solutions by avoiding the trajectory towards bad solutions has been used [146]. It helps in avoiding the non-feasible solutions. The minimum Euclidean distance (MED) constraint updates itself for every feasible solution and thus along with genetic algorithm reduces the number of iterations for the optimization process with β. The SER of feasible solutions at design SNR is calculated until the occurrence of the first non-feasible solution to form a potential population set $\mathbb{P}_{SNR}$. The choice of design SNR is medium to high SNRs as the SER expression with union upper bound is fairly tight in those SNRs [147]. Further, the SER is greater than 0.5 in SNRs below 15 dB, optimizing points for lower SNRs may not completely optimize the points for higher SNRs. In this study [71], the SNR performance gain has been inspected at the FEC limit SER. Hence, the design SNR is 15 dB, the average of SNRs at worst, and FEC limit SER. For faster computation the theoretical CSK-1PD SER expression (3.17), obtained in chapter 3 has been considered in the algorithm, as reiterated in (4.5).

$$P_{PS}^{1PD} = \sum_{i=1}^{M-1} \left[\frac{p(s_i)}{2} \operatorname{erfc}\left(\sqrt{\frac{(|d_i|^2+\Gamma_i)^2}{4|d_i|^2 N_0}} \right) + \frac{p(s_{i+1})}{2} \operatorname{erfc}\left(\sqrt{\frac{(|d_i|^2-\Gamma_i)^2}{4|d_i|^2 N_0}} \right) \right], \tag{4.5}$$

where,

$$\begin{aligned} d_i = |s_i - s_j| \quad & \begin{cases} where, \quad j = i+1, \\ i \in \{1, \ldots, (M-1)\}, \\ j \in \{2, \ldots, M\}, \end{cases} \\ \Gamma_i = N_0 \ln \frac{p(s_i)}{p(s_j)}, \quad & s.t. \quad p(s_i) \geq p(s_j). \end{aligned} \tag{4.6}$$

At the occurrence of non-feasible solution the best fitting solution, i.e., the constellation points providing minimum SNR from the potential population set is chosen as the starting point. The solutions obtained by the numeric algorithm depend on the initial estimate of the constellation points (**X0**) used to start the optimization process [144]. The random starting points must be a strictly feasible constellation points (as shown in Table. 4.1), fulfilling the optical power and geometric constraint with strict inequality range constraint (as explained in section 4.3). Algorithm 3 can be used for optimizing constellations of any size with convex constraints.

Table 4.1: Random 4-CSK-1PD Constellation Points. The light-grey shaded part forms the matrix **X0**.

RGB optical power vector	P_r	P_g	P_b	**Symbols in normalized current**
$\mathbf{p}_1$	0	0	1	$s_1 \rightarrow 0.220$
$\mathbf{p}_2$	0.2503	0.2884	0.4612	$s_2 \rightarrow 0.299$
$\mathbf{p}_3$	0.4732	0.2799	0.2469	$s_3 \rightarrow 0.340$
$\mathbf{p}_4$	1	0	0	$s_4 \rightarrow 0.420$

4.3 Constraints Formulation

The constellation design in CSK-1PD scheme for uniform input data without white color balance requires optical power based constraint, geometric and range constraint. Additionally, it requires MED constraint, which updates with updated starting constellation points **X0** in the optimization process in Algorithm 3. For non-uniform input data; optical power, geometric and range constraints remain the same, whereas the PS of symbols modifies the MED constraint as shown in section 4.3.3. Later, to maintain white-tone output light in both uniform and non-uniform source distributions, color constraints have been discussed.

4.3.1 Optical Power Constraint

The signal envelope in CSK scheme has a non-varying power as it modulates data for constant output power. Constellation points have been designed to keep the desired total optical power, P_T, as a positive non-zero constant. The optical powers P_r, P_g, and P_b may take any non-negative value less than its peak values (4.7). P_{pr}, P_{pg}, and P_{pb} denote the peak optical powers of red, green, and blue LEDs, respectively. The peak powers and P_T are considered 1 to work on normalized values. The constant optical power constraint is analogous to the constant energy condition of many optimization processes. The optical power constraint, as shown in (4.8) is a mandatory constraint for designing constellation points in CSK-1PD.

$$\begin{aligned} 0 &\leq P_r \leq P_{pr}, \\ 0 &\leq P_g \leq P_{pg}, \\ 0 &\leq P_b \leq P_{pb}. \end{aligned} \tag{4.7}$$

$$P_r + P_g + P_b = P_T. \tag{4.8}$$

4.3.2 Geometric and Range Constraint

The geometric condition for CSK-1PD symbols as shown in (4.9) is that each RGB optical power vector formed by the difference of any two symbols should not be orthogonal to the responsivity vector $\boldsymbol{\rho}$ (as discussed in chapter 9.1.1). To have a unique set of symbols, it is necessary to prevent the receiver from receiving the same symbols (i.e., in the form of electric current) from any of the constellation points.

$$\langle\ (\mathbf{p}_i - \mathbf{p}_j) \cdot \boldsymbol{\rho}\ \rangle \neq 0, \tag{4.9}$$

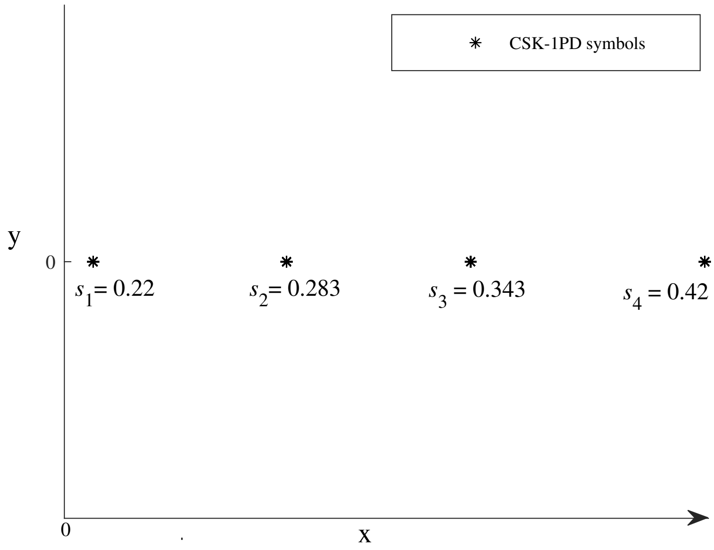

Figure 4.1: Constellation diagram of CSK-1PD obtained using responsivity $\boldsymbol{\rho}$ and OCPs in [92].

The region of CSK-1PD constellation points in terms of normalized electrical current is limited to one dimension (1-D) only as seen in Fig. 4.1. The 1-D region range depends on the responsivity of respective red, green and blue lights on the photodetector, as shown in (4.10). The maximum and minimum range of a constellation point (in terms of normalized electrical current) remains the same in an RGB LED as the highest, and lowest responsivity corresponds to red, and blue color LEDs, respectively. Therefore, the values of all possible constellation points lie between the normalized electrical currents defined by the highest and lowest responsivities. The electrical symbols corresponding to the two extremes of responsivity values provides the maximum Euclidean distance between any two symbols in the constellation set. Hence, the additional range constraint, as shown in (4.11) has been included in the optimization process for complete range constraint. Constraint in (4.11) can be further reduced to (4.12), when the matrix **X0** and **X** have rows always arranged in increasing current fashion from top to bottom as seen in Table 4.1. The matrix arrangement has been kept the same in all the simulations and results. The constraints have been expressed as a set of linear equalities and inequalities as per *fmincon* solver.

$$\langle\ [0\ 0\ 1]\cdot\boldsymbol{\rho}\ \rangle \leq \langle\ \mathbf{p}_i\cdot\boldsymbol{\rho}\ \rangle \leq \langle\ [1\ 0\ 0]\cdot\boldsymbol{\rho}\ \rangle. \tag{4.10}$$

$$\max\{\langle\ (\mathbf{p}_i-\mathbf{p}_j)\cdot\boldsymbol{\rho}\ \rangle\} \leq |\langle\ [1\ 0\ 0]\cdot\boldsymbol{\rho}\ \rangle - \langle\ [0\ 0\ 1]\cdot\boldsymbol{\rho}\ \rangle|, \tag{4.11}$$

$$\langle\ (\mathbf{X0}_{R_4}-\mathbf{X0}_{R_1})\cdot\boldsymbol{\rho}\ \rangle \leq |\langle\ [1\ 0\ 0]\cdot\boldsymbol{\rho}\ \rangle - \langle\ [0\ 0\ 1]\cdot\boldsymbol{\rho}\ \rangle|. \tag{4.12}$$

The vector dot product changes to matrix dot product on considering all the four constellation points in a matrix, i.e., **X0**. $\mathbf{X0}_{R_1}$, and $\mathbf{X0}_{R_4}$ represent the first, and fourth row of the matrix **X0**. The results are simulated in matrix notation to obtain all four symbols in one go in the matrix notation $\mathbf{X}_o$.

4.3.3 Minimum Euclidean Distance Constraint

The optimization process takes random initial constellation points, as shown in Table 4.1. The minimum Euclidean distance between any two symbols among all the symbols in the initial random constellation points, **X0**, is taken as a constraint for next optimization iteration (t). The MED constraint is updated according to the successive optimized constellation points (**X**) in $(t+1)$ iteration of β for much faster convergence. The only difference in this constraint for uniform (in (4.13)) and non-uniform (in (4.14)) input data is the logarithmic factor.

$$\eth(t+1) \;\geq\; min\;\{\eth(t)\}, \tag{4.13}$$

$$\begin{aligned} \eth(t+1) \;\geq\; min\;\{\eth(t) * \ln\frac{p(s_j)}{p(s_i)}\}, \\ s.t.\;\; p(s_i) \geq p(s_j). \end{aligned} \tag{4.14}$$

4.3.4 Strict White Tone Constraint

Practically, CSK should have a white tone operating color. IEEE 802.15.7 standard for VLC accepts the most widely used model of human color perception, CIE 1931, to adhere to all applicable luminary standards. The CIE 1931 chromaticity gamut [148] has been shown in Fig. 4.2. The color of any visible light wavelength can be represented by the chromaticity coordinates (x,y). CIE 1931 color space typically considers eleven mean white tonalities at different color temperatures for white light evaluation. Table 4.2, shows the chromaticity coordinates producing white tones.

The constellation points consist of RGB LED optical power vector for a given symbol. Equation (4.15) provides a relation between x,y chromaticity coordinates and LED output power for a given wavelength of light. Hence, from **X0** one can find the value of (x,y) in the CIE 1931 chromaticity diagram as follows

$$\begin{aligned} x = x_r \cdot P_r + x_g \cdot P_g + x_b \cdot P_b, \\ y = y_r \cdot P_r + y_g \cdot P_g + y_b \cdot P_b, \end{aligned} \tag{4.15}$$

where the coordinates of central wavelength of red LED light is (x_r, y_r), green LED light is (x_g, y_g) and blue LED light is (x_b, y_b) in the CIE chromaticity color space. The central

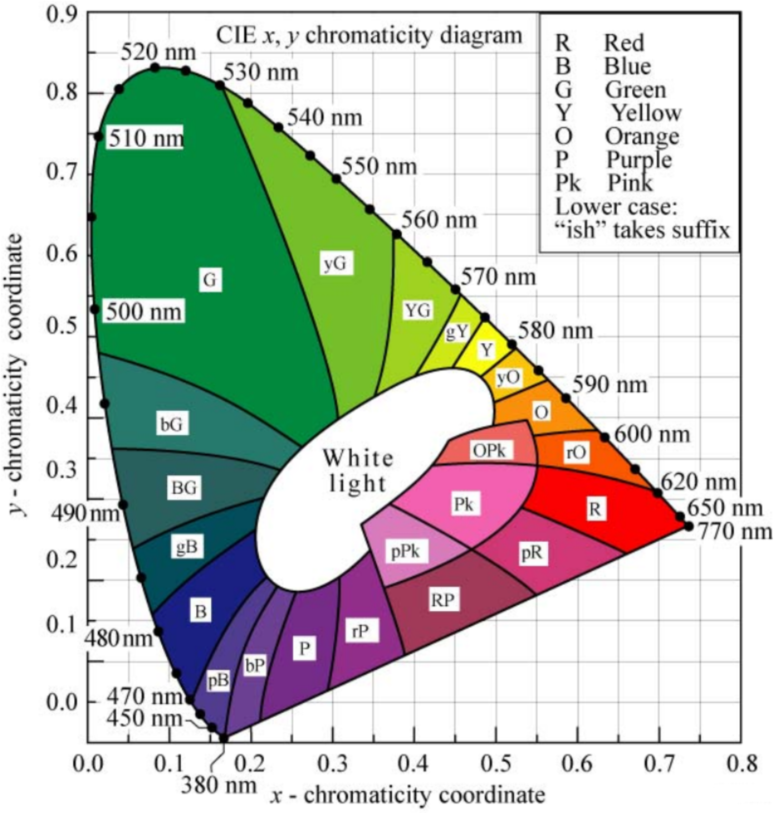

Figure 4.2: 1931 CIE chromaticity diagram with areas attributed to different colors [148].

Table 4.2: Mean white tonalities having different temperatures in CIE 1931 RGB color space.

Serial No.	**Coordinates** x	y	**White color Temperature, T_c(K)**
1	0.418	0.390	3100
2	0.389	0.362	3500
3	0.369	0.350	4000
4	0.354	0.340	4500
5	0.342	0.333	5000
6	0.334	0.328	5500
7	0.324	0.321	6000
8	0.317	0.317	6500
9	0.310	0.313	7000
10	0.305	0.310	7500
11	0.300	0.305	8000

wavelength coordinates are known from the CIE 1931 color space as shown in Table 4.3. The

Table 4.3: The corresponding coordinates of central wavelengths of RGB LEDs in CIE 1931 color space.

LED light color	**Wavelength**	**Coordinates** x	y
Red	640 nm	0.7190	0.2809
Green	530 nm	0.1547	0.8059
Blue	465 nm	0.1355	0.0399

CSK-1PD constellation symbols on an average should emit white color light. The average white tone can be obtained in terms of chromaticity coordinates as

$$(\bar{x},\bar{y}) = \sum_{i}^{M} p(s_i)(x,y)_{s_i}, \tag{4.16}$$

where $(\bar{x},\bar{y})$ are the chromaticity coordinates representing the average perceived color of the transmitted symbols and $(x,y)_{s_i}$ are the chromaticity coordinates of symbol s_i. When $(\bar{x},\bar{y})$ represents a perceived white color from any of the eleven mean white tones (refer Table 4.2), the constellation symbols are said to have a white color balance. In order to fix the perceived color to white tone, an average white tone constraint is required on the constellation symbols as follows

$$(\bar{x},\bar{y}) \in \{(0.418,0.390),...,(0.300,0.305)\}, \tag{4.17}$$

$\{(0.418,0.390),...,(0.300,0.305)\}$ forms the set of eleven mean white tones. The optimization is done by considering one out of eleven mean white tones at a time which makes it a strict constraint. The average white tone constraint is given by the affine equality for a color temperature of 3100 K, $(\bar{x},\bar{y}) = (0.418,0.390)$. Similarly, optimization is done for all other white tones.

The average tone chromaticity coordinates of OCPs obtained without color constraint (OCPs shown in Section 4.5) has been calculated for different source distributions. It is clear from Table 4.4, that none of the OCPs fulfills the white tone balance. Therefore, a white tone constraint is required for maintaining average white tone in the constellation points.

There is limitation to this white tone constraint as the OCPs with strict white tone constraint reduces the SNR gain of the system in comparison to the OCPs without white tone constraint. Further, not all the white tones can be achieved by the constellation points optimized for minimum SNR, however, the desired white tones are achieved with reduced SNR performance. Therefore, in this chapter two alternatives have been suggested to manage white tones in the optimized CSK constellation points.

Table 4.4: The average tone coordinates of different source distributions.

Source Distribution	**Coordinates**	
	$\bar{x}$	$\bar{y}$
Uniform	0.3877	0.2541
Maxwell	0.2152	0.1567
Exponential	0.2216	0.1439
Pareto	0.2146	0.1413

4.4 Solutions for Average White Light

The CIE 1931 chromaticity diagram in Fig. 4.2 shows a wide area for white light. The strict white tone constraint can be extended to the whole white region to achieve SNR gain close to OCPs of without white tone constraint. The white region constraint has been derived in section 4.4.1, which relaxes the strictness of the previous mean white tone constraint. Another way to obtain white tone output light can be the addition of another RGB LED at the transmitter side. The use of an extra RGB LED can help in maintaining white tone with the OCPs obtained without considering the white tone constraint. The extra RGB LED method has been described in section 4.4.2.

4.4.1 Relaxed White Tone Constraint

The strict white tone constraint considers only eleven mean white tones, so it is not possible to get optimized constellation points for all the eleven white tones. The relaxed white tone constraint regards any (x, y) coordinates falling inside the white region (see Fig. 4.2) as desired white. The white light region has been extracted out from the CIE 1931 chromaticity diagram in Fig. 4.3 for deriving the approximate mathematical model of the region. Every (x, y) coordinates in the whole white region does not give pure white light; however, (x, y) coordinates inside the white light region has been considered in designing LEDs in literature [149–152]. There is a trade-off between the purity of white tone and SNR performance; the focus of the proposed work is to obtain optimized constellation points which maintain the bare minimum acceptable white light.

The desired (x, y) coordinates of the OCPs lie inside the white light region, which is an irregular shape. The research literature is replete with algorithms to determine whether a point is within a polygon or not. Therefore, the most common approach is to first approximate an irregular shape into a polygon from the set of points, $\mathbb{R}$, forming the irregular shape. Once the irregular shape is decomposed to a polygon, deciding whether a point lies inside is the point-in-polygon (PIP) test problem. The irregular shape can be decomposed to triangles using polygon triangulation method [153]. The triangulation method chooses a subset of points, $\mathbb{P}_p$, from the set $\mathbb{R}$ to approximate the white region as a mesh of triangles. All the points

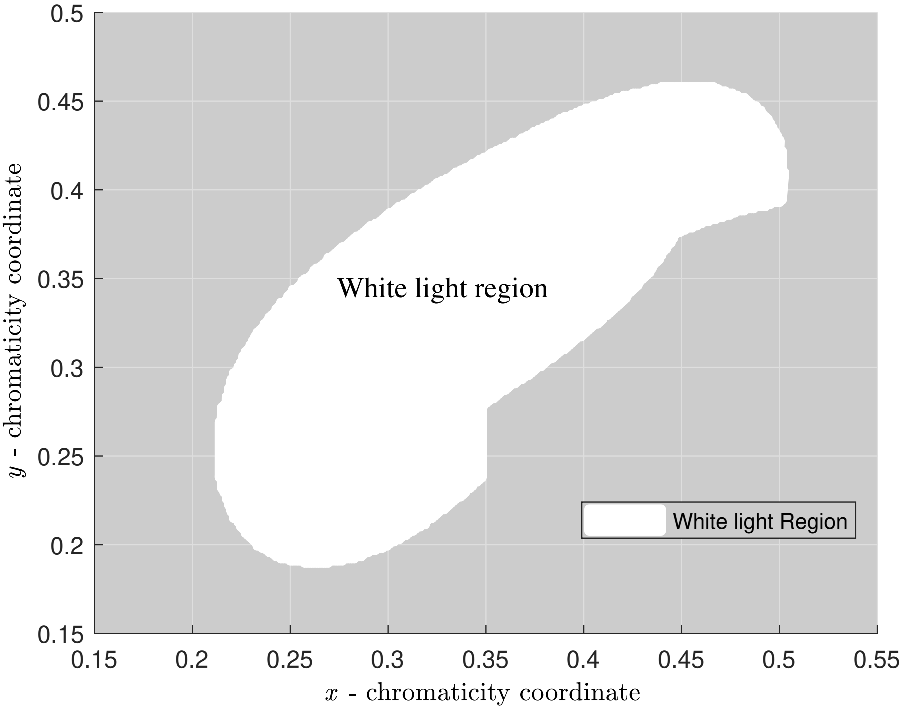

Figure 4.3: White light region extracted from the 1931 CIE chromaticity diagram.

from $\mathbb{P}_p$ form the vertices of the white light region, hence with the triangulation method, the white region can be approximated to an arbitrary polygon with few points. In polygonal representation, the curved shapes are represented using tangential approximations in the form of straight lines, which ultimately depends on the number of vertices considered. Therefore, there is always an approximation error (a_e), which can be realized in terms of percentage of area left uncovered by the polygon approximation. Since the white region is in two dimensions (2-D) only, there are a number of algorithms for the 2-D PIP problem. The authors opted for the efficient standard algorithm in paper [154], which is capable of solving PIP problem for any arbitrary polygon, convex or non-convex. Further, during the optimization process, the algorithm shall be called so often, hence an accelerated algorithm that grows linearly with the number of polygon vertices (v_n) is a viable choice. Therefore, the complexity of the PIP algorithm used in this work is $O(v_n)$. The polygonal representation of white light region depends on PIP algorithm as well and thus becomes an optimization problem as follows:

$$\begin{aligned} v_n = & \ \min \ \{G(v_n, a_e)\}, \\ \text{where,} \ \ G(v_n, a_e) = & \ O(v_n) + a_e, \end{aligned} \tag{4.18}$$

where a_e decreases with more number of v_n while the PIP algorithm complexity increases with more number of v_n. The complexity and error approximation have normalized values between $[0 \;\; 1]$. They have been weighted equally in the minimization problem. The number of vertices which provides minimum complexity and area error has been obtained and shown in Fig. 4.4. The white light region ($\mathscr{W}$) in CIE 1931 chromaticity diagram has been approximated to polygon in Fig. 4.5 with vertices, $v_n = 35$.

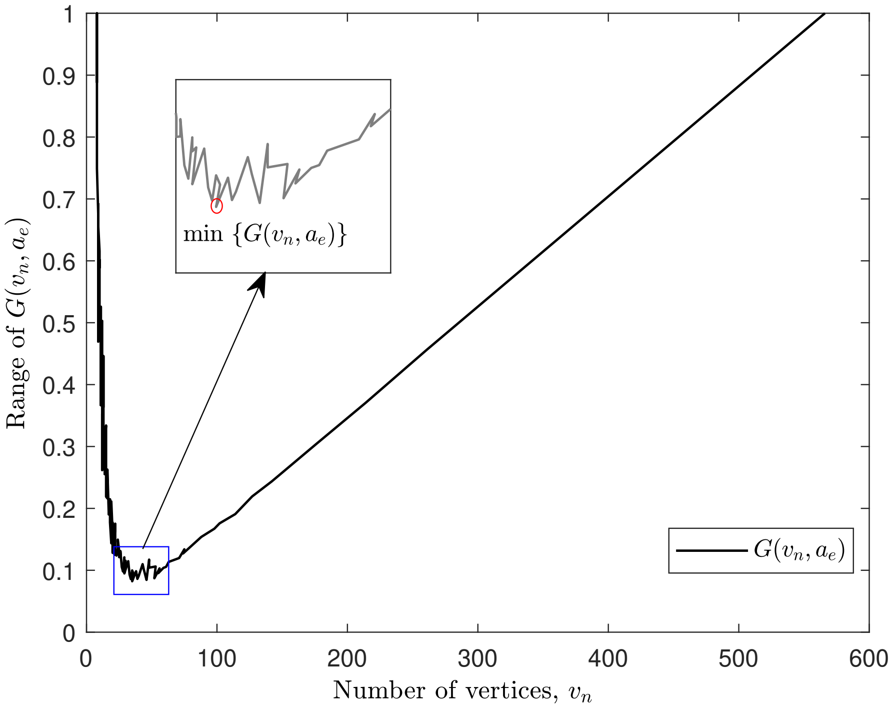

Figure 4.4: The minimum value obtained for $G(v_n, a_e)$.

The relaxed white tone constraint ensures $(\bar{x}, \bar{y}) \in \mathscr{W}$, and has been formulated as follows:

$$PIP_{alg}(\bar{x}, \bar{y}, x_P, y_P) - 1 = 0, \tag{4.19}$$

where, x_P and y_P belongs to the x and y coordinates of polygon points $\mathbb{P}_p$. The PIP algorithm returns logical 1, whenever a point is inside or on the polygon.

4.4.2 Extra RGB LED

Researchers have used scrambler for maintaining white tone in CSK-1PD [92]. Linear feedback shift register (LFSR) based scrambler is not very expensive; however, its complexity increases with increase in the length, l. The color balance in [92] is achieved for uniform input data at $l > 20$. The input data scrambled for length $l > 20$, provides color balance by averaging (P_r, P_g, P_b) to get values around (0.33, 0.33, 0.33), which corresponds to a single chromaticity

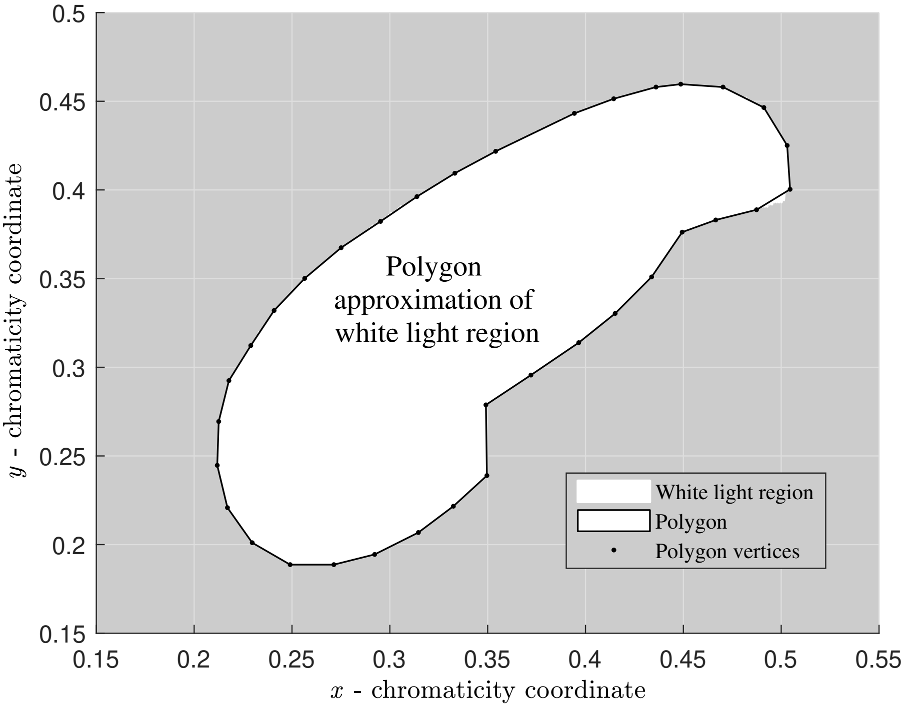

Figure 4.5: Polygon approximation of the white light region

coordinates (0.3330, 3718). The scrambler needs to be designed specifically for different PS input data, and a particularly designed scrambler can produce only one type of white tone. The scramblers used for this purpose are usually additive, so it must be reset by the frame synchronization bits otherwise massive error propagation happens [49]. Further, with the non-uniformity in the input data, the length in scrambler may increase, which in turn increases the complexity drastically.

In order to escape the problems mentioned above, we have proposed the utilization of an extra RGB LED at the transmitter to maintain any white tone in the white light region without hampering the SNR gain obtained from specific OCPs for source distributions [71]. One can design a constant color light with the extra RGB LED to mix with the RGB modulated symbols to produce the desired average white tone $(\bar{x}_d, \bar{y}_d)$. It provides flexibility and removes the constraint on the length or number of the input symbols. Further, RGB LEDs being inexpensive does not incur much cost to the system. The chromaticity coordinates (x_e, y_e) of extra RGB LED can be obtained as

$$\begin{aligned} x_e &= \frac{(\bar{x}_d * (Y_1 + Y_e) - \bar{x})}{Y_e}, \\ y_e &= \frac{(\bar{y}_d * (Y_1 + Y_e) - \bar{y})}{Y_e}, \end{aligned} \tag{4.20}$$

where Y_e and Y_1 are the luminance corresponding to, extra RGB LED chromaticity coordinates, and average tone coordinates obtained from the specific OCPs for source distributions, respectively. The normalized range of luminance is between 0 to 1 [155]. (x_e, y_e) can be expressed in the form of RGB LEDs optical powers by substituting (4.15) in (4.20) with the following constraint

$$\begin{aligned} P_r + P_g + P_b = 1, \\ \text{where,} \quad (P_r, P_g, P_b) \geq 0 \quad \text{and} \quad 1 \geq Y_e > 0. \end{aligned} \tag{4.21}$$

The computational complexity of this method depends on designing the RGB optical powers of extra LED, which forms linear equations in five variables on considering (4.20) and (4.21). There are five unknown variables with their respective upper and lower bounds and three linear equations. Therefore the linear equations are solved for different values of Y_1 to obtain (P_r, P_g, P_b) in terms of Y_e and then Y_e can be obtained from (4.21). The PD receives the combined light of RGB LED modulated signal and extra RGB LED signal. The receiver side knows the excess current generated because of the additional RGB LED. The total current generated shifts the symbols with additional electric current values, hence on subtracting the incremental current yields corresponding current of the modulated signal. It is analogous to removing the constant ambient light noise at VLC receiver. Henceforth, with linear computational complexity at the transmitter and receiver, the concept of using an extra RGB LED can be a better option for color rendering and balancing.

4.5 Results and Discussion

The SNR performance gain with respect to SER for 4-CSK-1PD with and without white tone for uniform and non-uniform input data has been obtained and reasoned in the following sections. The simulation parameters have been kept same for this work [71] as in Section 3.4 of chapter 3 for fair comparison. The possibility of maintaining any desired white tone has been validated by finding non-negative RGB optical powers for the desired white tone in section 4.5.3.

4.5.1 OCPs of the Source Distributions Without Considering White Tone Constraint

Table. 4.5 shows the OCPs of all the source distributions considering all constraints as discussed in section 4.3 except white tone constraint. The SNR in dB for FEC limit SER can be observed in Fig. 4.6 for different source distributions utilizing their specific OCPs.

Table 4.5: Optimized CSK-1PD constellation points for uniform, exponential, Maxwell-Boltzmann, and Pareto input data without white tone constraint.

Source Distributions:	**RGB vectors:**	**Optical powers:** P_r	P_g	P_b
Uniform	$\mathbf{p}_1$	0	0	1
	$\mathbf{p}_2$	0.1880	0.2905	0.5215
	$\mathbf{p}_3$	0.5217	0.2902	0.1881
	$\mathbf{p}_3$	1	0	0
Exponential	$\mathbf{p}_1$	0	0	1
	$\mathbf{p}_3$	0.2261	0.2803	0.4936
	$\mathbf{p}_3$	0.5939	0.2252	0.1809
	$\mathbf{p}_2$	1	0	0
Maxwell-Boltzmannl	$\mathbf{p}_1$	0	0	1
	$\mathbf{p}_2$	0.2084	0.3096	0.482
	$\mathbf{p}_3$	0.5531	0.2793	0.1676
	$\mathbf{p}_3$	1	0	0
Pareto	$\mathbf{p}_1$	0	0	1
	$\mathbf{p}_2$	0.2185	0.3109	0.4706
	$\mathbf{p}_3$	0.5606	0.2768	0.1626
	$\mathbf{p}_3$	1	0	0

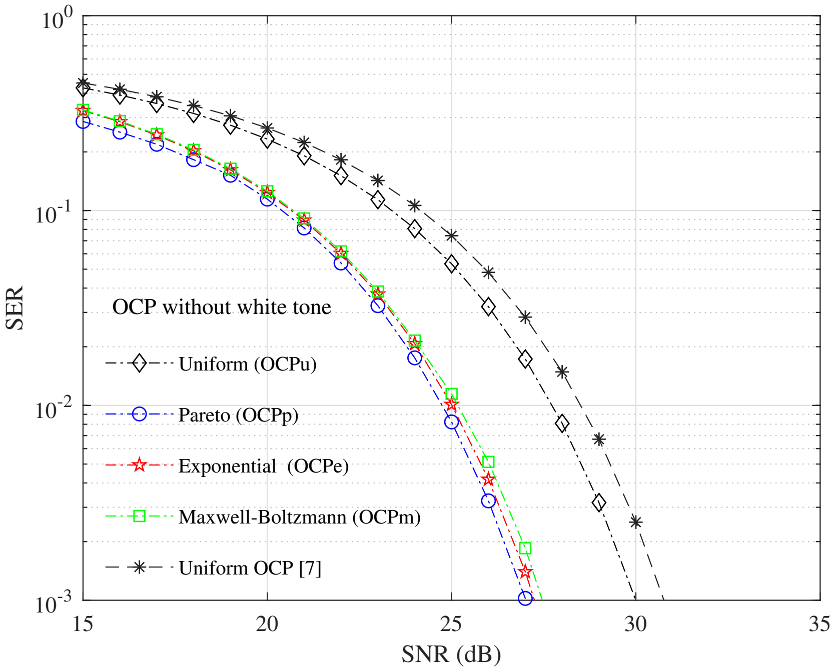

Figure 4.6: SNR versus SER plot of different source distribution at their specific optimized constellation points.

It has been observed that the optimized constellation points for uniform input data (OCPu) perform better than the OCP of uniform from [92] by 0.75 dB. The OCPu results in equidistant normalized electric current symbols, which is equivalent to the analytically known global optimum placement of equiprobable symbols in pulse amplitude modulation (PAM) for minimum SER [140]. The normalized design range for CSK-1PD is just a straight line, so following the equidistant symbol spacing criteria for equiprobable symbols yields the same $d_i = 0.0667$ for all i (check equation (4.6) for d_i). The OCPu achieve a minimum Euclidean distance of 0.0667 for all d_i.

It has been observed that the SNR performance of non-uniform source distributions utilizing specific OCPs obtained in this work provides improved SNR gain as compared to the work

Table 4.6: SNR of CSK-1PD without considering the white tone constraint for different source distributions with specific OCPs and uniform OCPs [92] for all.

Input data distribution type	**SNR (dB) at SER of 10^{-3} considering** OCP without white tone constraint: **uniform OCP [92]**	**Specific OCP(u,m,e,p)**
Uniform	30.75	30
Maxwell-Boltzmann	29.50	27.4
Exponential	29.00	27.25
Pareto	28.05	27

in chapter 3, where OCPs designed in [92] for uniform source distribution is utilized. The respective SNR values have been tabulated for comparison in Table 4.6. In the case of specific OCPs, the constellations points are further optimized by geometrically shaping the symbols based on their probability of occurrence. Therefore, the improved performance of non-uniform distributions in case of specific OCPs is because of the consecutive PS based GS technique. It is interesting to note that with specific OCPs the performance of non-uniform source distributions approach close to each other which is again due to the specific shifting of symbols according to PS.

4.5.2 OCPs of the Source Distributions Considering White Tone Constraint

The constellation points are optimized so as to get average white tone light as the transmitted output.

4.5.2.1 Strict Constraint

The constellation points are obtained considering all constraints in section 4.3 along with strict white tone constraint in (4.17). The OCPs obtained with strict white tone are abbreviated as S-OCPs. The uniform and Pareto (non-uniform) source distribution OCPs are obtained and shown in Table. 4.7.

Table 4.7: Optimized CSK-1PD constellation points with strict white tone constraint for uniform and Pareto input data.

Source Distribution	P_r	P_g	P_b	**Mean white tone coordinates** $(\bar{x},\bar{y})$
Uniform	0	0.056	0.944	(0.334, 0.328) at temperature 5500K
	0.1	0.35	0.55	
	0.255	0.65	0.095	
	0.969	0.031	0	
Pareto	0	0	1	(0.369, 0.350) at temperature 4000K
	0.11	0.343	0.547	
	0.52	0.38	0.1	
	1	0	0	

The corresponding mean white tone chromaticity coordinates can be seen in the last column. The SER versus SNR plots in Fig. 4.7, demonstrates the impediment of considering strict white tone constraint. The SNR for uniform distribution is 31.4 dB and for Pareto is 30.2 dB at 10^{-3} SER. It can be observed that the performance of both uniform and Pareto have decreased from OCPu and OCPp, respectively. The chromaticity coordinates of the four OCPs do not lie in the white region except one, and for maintaining average white tone, the optimum position of symbols in terms of SNR is changed and therefore reduces the SNR gain.

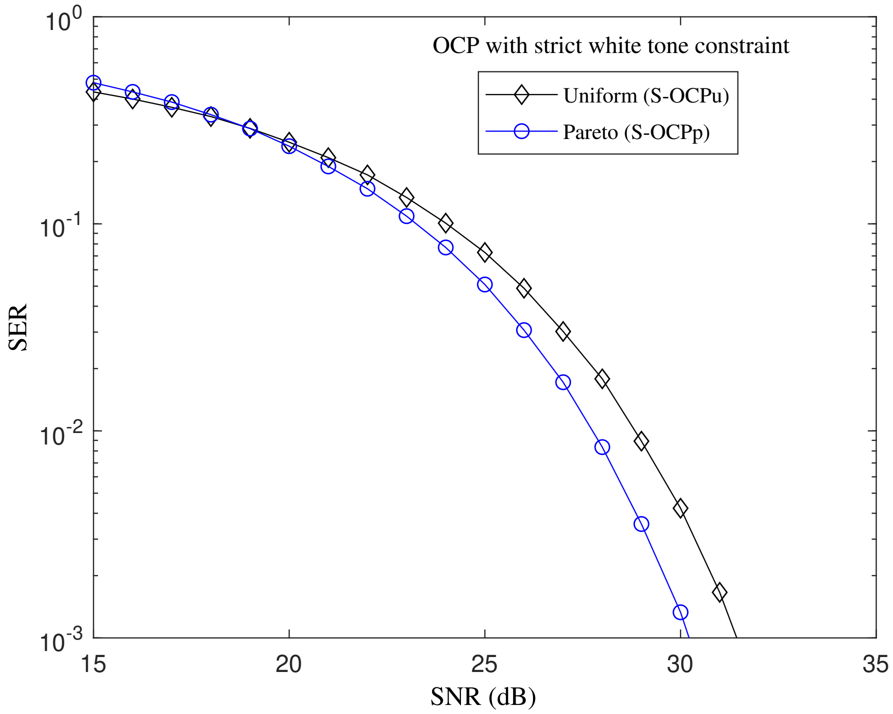

Figure 4.7: SNR versus SER plot of uniform and Pareto source distributions with optimized constellation points maintaining white tones.

4.5.2.2 Relaxed Constraint

In this case, the whole white region has been considered in the white tone constraint of the optimization process. Table. 4.8 shows the OCPs of all the source distributions considering all constraints and the relaxed white tone constraint. The respective white tone coordinates can be seen at the last row. The SNR at FEC limit SER can be observed in Fig. 4.8 for different source distributions considering OCPs for relaxed white tone (R-OCPs). The SNR values for FEC limit SER have been enumerated in Table. 4.9 for comparison. It has been observed that SNR performance gain of uniform has achieved the optimum SNR gain of OCPu. The equiprobability of symbols in uniform distribution assist it to render ideal white color balance with optimum SNR gain. However, for non-uniform distributions, SNR gain has improved from the strict white tone constraint, whereas it is still less than the without white

Table 4.8: Optimized CSK-1PD constellation points with relaxed white tone constraint for uniform, exponential, Maxwell-Boltzmann, and Pareto input data.

Source	**Optical powers:**			**Average white tone**
Distributions:	P_r	P_g	P_b	**coordinates,** $(\bar{x}, \bar{y})$
Uniform	0	0	1	(0.3504, 0.3424)
	0.1507	0.3655	0.4837	
	0.4842	0.3653	0.1505	
	1	0	0	
Exponential	0.0234	0.0782	0.8984	(0.2247, 0.2115)
	0.1795	0.4144	0.4061	
	0.5842	0.2847	0.1312	
	1	0	0	
Maxwell-Boltzmannl	0.0202	0.0625	0.9172	(0.2247, 0.2115)
	0.2069	0.4096	0.3835	
	0.5743	0.3011	0.1245	
	1	0	0	
Pareto	0.0262	0.0954	0.8784	(0.2247, 0.2114)
	0.1916	0.4218	0.3866	
	0.5930	0.2790	0.1277	
	1	0	0	

Table 4.9: SNR of CSK-1PD at specific OCPs for different source distributions with and without white tone constraint.

Input data distribution type	**SNR (dB) at SER of 10^{-3} considering OCP** without and with white tone constraint:	
	OCP(u,m,e,p)	**R-OCP(u,m,e,p)**
Uniform	30	30
Maxwell-Boltzmann	27.4	28.65
Exponential	27.25	28.7
Pareto	27	28.44

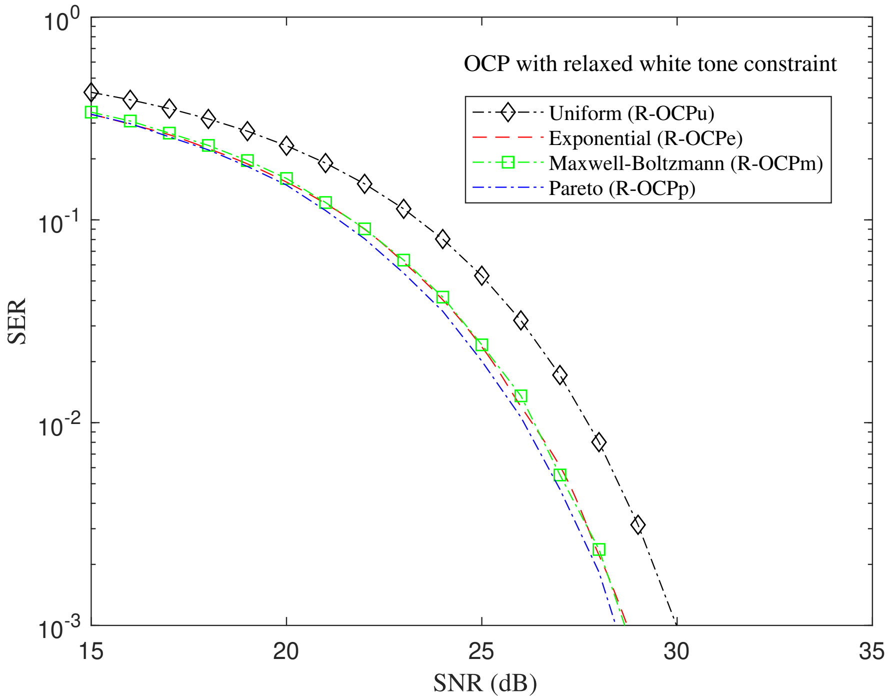

Figure 4.8: SNR versus SER plot of different source distributions using optimized constellation points with relaxed white tone constraint.

tone OCPs performance gain. The range of choice of chromaticity coordinates has increased here tremendously, and hence the performance of the R-OCPs in comparison to S-OCPs. The non-uniformity of symbols with s_1 ($\mathbf{p}_1$ in terms of RGB power) as highest probable symbol sabotage the reach to optimum SNR gain in R-OCPs. Moreover, the average white tone chromaticity coordinates of non-uniform source distributions are precisely the same, but the OCPs are different. The reason behind this comes from Table. 4.4, where the average tone of non-uniform distributions is close to each other. Hence, during optimization with white tone constraint, the different distributions look for a nearby valid white tone coordinates for optimized SNR gain with distinct OCPs.

4.5.3 With Extra RGB LED

The chromaticity coordinates of extra RGB LED for the vertices of the white light region (see Fig. 4.5) in Pareto distribution have been obtained and shown in Fig. 4.9 for different values of luminance Y_1. The extra RGB LED coordinates gets skewed to remain inside the CIE chromaticity diagram. The non-negative RGB optical powers of LED fulfilling all the linear equalities and inequalities have been obtained. The RGB optical powers obtained for the extra LED can be viewed in Table. 4.10.

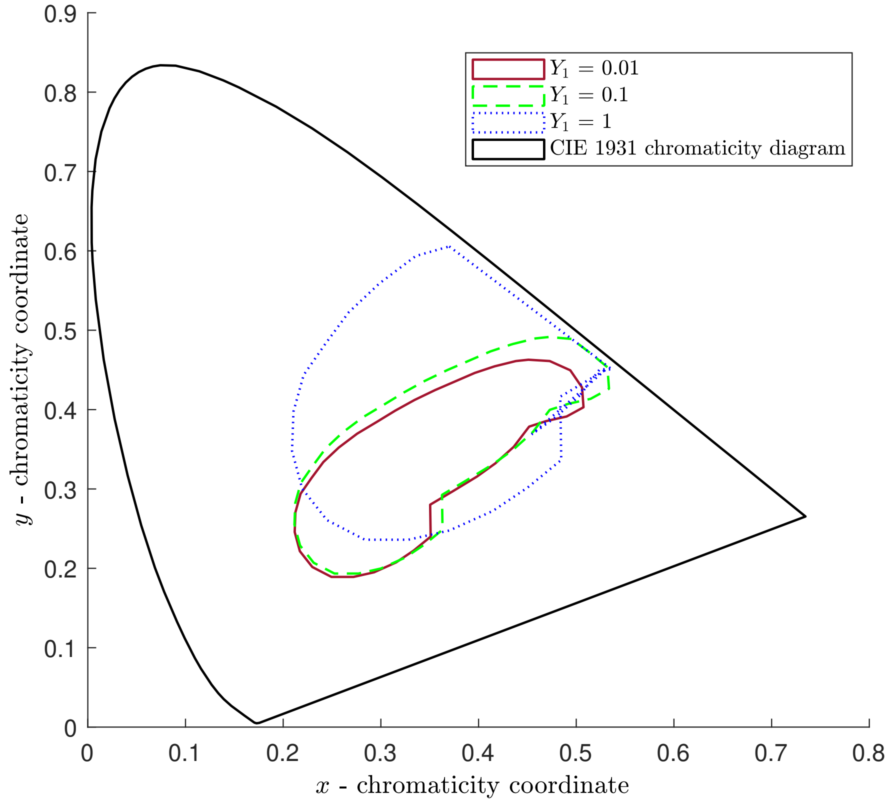

Figure 4.9: Extra RGB LED coordinates for Pareto source distribution forming polygon for the white light region.

Table 4.10: Optical powers of extra RGB LED for the desired white tone of CSK-1PD at specific OCPs of Pareto source distribution.

No.	**Desired whitetone coordinates**		**Average tone luminance**	**Extra RGB LED: Optical power**			**Extra RGB LED: Coordinates and Luminance**		
	x_d	y_d	Y_1	P_r	P_g	P_b	x_e	y_e	Y_e
1.	0.3496	0.2389	0.01	0.3644	0.1465	0.4891	0.3509	0.2399	1
2.	0.2751	0.3674	0.01	0.2285	0.3586	0.4129	0.2757	0.3697	1
3.	0.3496	0.2389	0.1	0.3851	0.1514	0.4635	0.3631	0.2487	1
4.	0.2751	0.3674	0.1	0.2371	0.3825	0.3804	0.2812	0.3900	1
5.	0.3496	0.2389	1	0.5917	0.2011	0.2072	0.4846	0.3365	1
6.	0.2751	0.3674	1	0.3226	0.6212	0.0562	0.3357	0.5935	1

4.6 Summary

For the first time, the work in this chapter attempts to optimise the CSK-1PD constellation points for uniform and non-uniform (exponential, Maxwell-Boltzmann, and Pareto) source distributions, both with and without average white tone. The specific OCPs without white tone constraint gives improved SNR performance gain in all the source distributions with respect to the OCPs of [92]. However, the OCPs with strict white tone constraint maintains the white tone on an average with SNR gain reduced by 1.4 dB and 3.2 dB from without white tone constraint for uniform and pareto distribution, respectively. The entire white region is taken into account in the optimization process for OCPs with relaxed white tone constraints to boost the SNR gain. The R-OCPs for uniform input data achieves the same SNR gain (30 dB) as OCPu. However, the R-OCPs still perform 1.25–1.45 dB worse for non-uniform than the non-uniform OCPs without a white tone restriction. In addition, this research suggests a novel way to employ two RGB LEDs at the transmitter, one for modulation and the other for maintaining white tone. Results show that the RGB optical powers of extra RGB LED can be designed for any desired chromaticity coordinates inside the white light region retaining maximum SNR gain with specific OCPs for uniform and non-uniform source distributions.

4.7 Extended work

The following work extends the code book designing to VLC based sparse code multiple access (SCMA), which has been published in collaboration as follows:

Saumya Chaturvedi, **Dil Nashin Anwar**, Vivek Ashok Bohara, Anand Srivastava and Zilong Liu, "Low-Complexity Codebook Design for SCMA-Based Visible Light Communication", ***IEEE Open Journal of the Communications Society***, vol. 3, pp. 106-118, 2022, doi: 10.1109/OJCOMS.2022.3141800.

SCMA, as a code-domain non-orthogonal multiple access (NOMA) scheme, has received considerable research attention for enabling massive connectivity in future wireless communication systems. In this work, we present a novel codebook (CB) design for SCMA based VLC system, which suffers from shot noise. In particular, we introduce an iterative algorithm for designing and optimizing CB by considering the impact of shot noise at the VLC receiver. Based on the proposed CB, we derive and analyze the theoretical BER expression for the resultant SCMA-VLC system. The simulation results show that our proposed CBs outperform CBs in the existing literature for different loading factors with much less complexity. Further, the derived analytical BER expression well aligns with simulated results, especially in high signal power regions. In this work [156], a novel low-complex CB design technique has been proposed for SCMA-VLC system impaired by shot noise. This work emphasizes that the designing of specific CBs is required for the SCMA-VLC system. The proposed CBs are generated by optimizing the log-sum of exponentials of rotated Euclidean distances between the superimposed codewords. With the inclusion of shot noise in the SCMA system, the overall noise variance is dependent on the strength of the incident signal. The proposed CBs provide improved BER performance as compared to CBs proposed in the existing literature along with reduced complexity. Further, the theoretical analysis of BER is also performed for the shot noise incorporated SCMA-VLC system. The simulated results are validated, and both the theoretical and simulated curves are in good agreement for high signal power regions.

Chapter 5

Energy-Efficient Coexistence of LiFi Users and Light Enabled IoT Devices

Owing to power limitations and hardware constraints of the IoT device, it requires simple, low power, low complexity, energy-efficient communication technology. In contrast, LiFi users require high data rates and reliable connectivity. Motivated by the diverse requirements of these heterogeneous users and research gaps in earlier works (refer Section 1.4.2 and 1.5), the work [97] in this thesis explores the coexistence of the LiFi users and LC enabled IoT devices (LC includes visible and IR light) under a common LiFi access point to fulfill the aspects of green communication with both spectrum and infrastructure sharing. The remainder of the work is organized as follows:

Section 5.1 outlines the contributions of this work in detail. Section 5.2 illustrates the proposed LiFi-IoT coexistence schemes. Section 5.3 describes the various performance metrics. The analytical expressions have been derived and shown in Section 5.4. Section 5.5 analyzes and discusses the simulated and theoretical results. Section 5.6 summarizes the work.

5.1 Contributions

This work proposes novel energy-efficient communication schemes for the coexistence of LiFi users and LC enabled IoT devices. The proposed schemes are compared and analyzed to suggest appropriate green DL and uplink (UL) communication schemes. The coexistence schemes are developed on a baseline optical OFDM (O-OFDM) technique. The different variants of direct current (DC) biased optical-orthogonal frequency division multiplexing (DCO-OFDM) [99] technique with discrete Hartley transform (DHT) [157, 158] have been proposed for the coexistence of heterogeneous users to achieve a greener communication solution. The choice of the baseline modulation technique (i.e. DHT based DCO-OFDM (DCO-OFDM$^{\mathrm{H}}$)) has been made based on the advantages provided by DHT and inverse DHT (IDHT) operated DCO-OFDM in the coexistence environment explained in section 5.2.1.1). The IoT devices require simple, low power, energy-efficient communication technology, whereas the LiFi users need high data rates and reliable connectivity. Thus, a coexistence scheme incorporating modulation techniques combined with multiplexing techniques is required at the common LiFi AP to support the above requirements. Further, indoor solar cells can enable light energy harvesting capability at the receiver's terminal since light is being used for communication. In addition, as some LiFi and IoT applications are delay-sensitive and a multiple access (MA) technique can influence the delay, throughput and overall performance of the coexistence system. Therefore, in this work, the delay-throughput profile for time division multiple access (TDMA) and orthogonal frequency division multiple access (OFDMA) for VLC has been theoretically derived and analyzed. Therefore, this work proposes a suitable combination of modulation techniques (QAM, PAM, CSK), DHT, DCO-OFDM, removal of DC element, interleaved subcarrier mapping, modified data sequence and MA techniques (WDM, OFDMA) to form the coexistence schemes for heterogeneous LiFi and LC enabled IoT users. The proposed coexistence schemes have been evaluated against conventional DCO-OFDM$^{\mathrm{H}}$ with respect to various performance metrics such as system complexity, peak-to-average-power ratio (PAPR), effective spectral efficiency (ESE), the maximum number of IoT devices the scheme can support (K_m), power saving, energy harvesting (EH) and SNR at FEC limit SER. The conventional variants of DHT based DCO-OFDM utilize subcarrier modulation techniques such as QAM, PAM and CSK without any modifications. Overall, in this work, the best-suited coexistence scheme has been suggested for DL and UL communication.

The key contributions of this chapter can be summarized as follows:

1. It proposes green coexistence scheme for the heterogeneous LiFi users and LC enabled IoT devices under a common LiFi AP for UL and DL communication.
2. This work illustrates a comprehensive analysis of the various proposed and existing variants of DCO-OFDM$^{\mathrm{H}}$ in the coexistence schemes in terms of several performance metrics viz. system complexity, PAPR, ESE, K_m, power saving, EH and SNR at FEC limit SER, in order to suggest best-suited coexistence schemes.
3. The theoretical closed-form SER and PAPR expressions for the proposed coexistence schemes have been derived and validated.
4. The analytical framework for delay-throughput performance analysis of dynamic TDMA and OFDMA for mobile users have been derived for VLC.

5.2 LiFi and IoT communication coexistence

The coexistence environment has been illustrated in Fig. 5.1. Table 5.1 summarizes the VLC

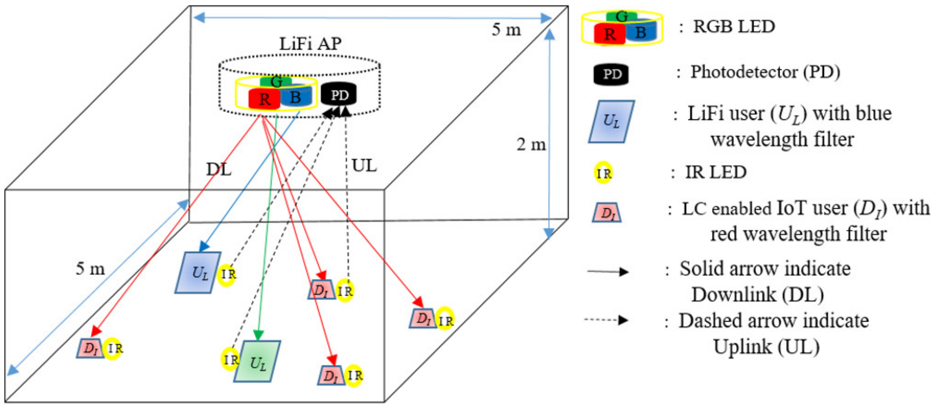

Figure 5.1: A future indoor LiFi system coexisting LiFi users and LC enabled IoT devices.

Table 5.1: Simulation Parameters.

Parameter	**Symbol**	**Value**
PD active area	A_{PD}	1 cm^2
Altitude of AP_L	z	2 m
LED half-power semiangle	$\phi_{1/2}$	60°
LED's angle of irradiance	ϕ	60°
Angle of incidence at PD	ψ	60°
PD critical angle of incidence	Ψ_c	80°
Optical filter gain	G_f	1
Concentrator gain	$G_\text{c}(\psi)$	1
Power conversion efficiency of the indoor solar cell	η	23%
Physical area of the indoor solar cell	A_{cell}	4 cm^2
Duration of energy harvesting	t	1 s
PD Responsivity	ρ	1 A/W
Transmitted optical power	P_t	1 W
Noise variance	N_o	1×10^{-21}
VLC channel bandwidth	B_w	10 MHz

simulation parameters. The proposed work assumes LOS VLC channel and AWGN discussed in Section 2.1.1, and Section 2.2) of chapter 2, respectively. The aim of this work is to propose a green communication solution that can be used to simultaneously serve both LiFi users ($\mathbb{U}_L$) and energy-autonomous LC enabled IoT devices ($\mathbb{D}_I$) from a common LiFi AP (AP_L) on the same spectrum band in either DL or UL. Please note, $\mathbb{U}_L$ represents a set of LiFi users, whereas U_L symbolizes a single LiFi user. Similarly, for set $\mathbb{D}_I$, D_I denotes a single IoT device. The DL and UL transmission techniques are discussed in the following subsections.

5.2.1 Downlink Transmission

For the DL transmission, one may consider TDMA-based protocol to enable the coexistence of $\mathbb{U}_L$ and $\mathbb{D}_I$ to avoid mutual interference and create interference-free environments for their respective time-domain (TD) communications. However, the TDMA-based approach tends to sacrifice the quality of service (QoS) for $\mathbb{U}_L$ since a considerable portion of airtime gets allocated to the IoT users [68]. Further, to coexist a large number of LiFi users and IoT devices, LiFi AP can have more LEDs. However, LEDs operating at the same wavelength would cause interference between $\mathbb{U}_L$ and $\mathbb{D}_I$ DL communication. Therefore, in the proposed work, we have leveraged the RGB LEDs as a transmitter in VLC to implement WDM to avoid interference among $\mathbb{U}_L$ and $\mathbb{D}_I$.

For WDM, red, green or blue wavelength filters at the receiver side assist in receiving data of that particular wavelength and discard the rest two-wavelength signals. The WDM channel gain matrix has close to zero values caused by cross-talks between wavelengths [54]. Therefore it is usually assumed that after the utilization of filters, there is negligible interference [54, 159, 160]. The advantages of WDM are manifold as it can be deployed easily with RGB LED in a VLC system. It helps in sending data independently and simultaneously with negligible interference in the coexistence environment. Unlike RF, it avoids the requirement of precoding filters at the AP to mitigate interference [68]. Since the beamforming filters require decoding of beamformed signals at the receiver, their removal further minimizes the receiver's complexity. WDM circumvents the requirement of precoding and decoding filters for beamforming at the transmitter and receiver, respectively. With WDM, the average white tone of the combined RGB light may get disrupted. Nonetheless, this can be managed by incorporating an extra RGB LED as proposed in chapter 4, which will inherently reinforce both illumination and energy harvesting. It may please be noted that the extra RGB LED does not affect the generality and trend of the results obtained in this work.

Furthermore, for DL communication over a particular wavelength, O-OFDM can be utilized. The utilization of the O-OFDM scheme to send data assists in supporting simultaneous data transmission to K_m IoT devices by assigning a single O-OFDM subcarrier to an IoT device.

The orthogonal subcarriers in O-OFDM further reduce the interference among IoT devices (detail explanation in section 5.2.1.2). In this work, WDM is implemented utilizing RGB LEDs. Thus, three different wavelengths of light establish a multi-LED AP scenario (as shown in Fig. 5.1) to communicate with K_m IoT devices with red wavelength and two LiFi users with green and blue wavelength (operating at the maximum O-OFDM data rate) simultaneously, thereby eliminating interference and improving aggregate SE and scheduling flexibility. It may be noted that one can include one more U_L being served by the red wavelength, though it will decrease the data rate of U_L to half the maximum data rate if half of the O-OFDM subcarriers support $\mathbb{D}_I$. This scheme can support several combinations of U_L and D_I by distributing the subcarriers among U_L and D_I according to the requirement. The trade-off between the number of users being supported and users' data rate governs the number of resources allocated to U_L and D_I. Thus, the feasible number of U_L and D_I being supported by the coexistence scheme.

5.2.1.1 LiFi AP to LiFi Users

The AP_L runs on the legacy [161] architecture where various subcarrier modulation techniques with DC element (DCE) removal and precoding techniques have been explored in DCO-OFDM$^{\mathrm{H}}$ to propose a single best suited DL coexistence system. Discrete Fourier transform (DFT) based OFDM outputs a complex bipolar signal which can not be directly transmitted over LEDs. In order to make the complex bipolar OFDM signal compatible with IM, the conversion of complex bipolar data to real and unipolar data can be done by utilizing Hermitian symmetry or segregating the real and imaginary components of data followed by DC bias addition (a.k.a. DCO-OFDM) or negative signal clipping (a.k.a. ACO-OFDM), which has been explained in detail in Section 2.3.4 of chapter 2. In the case of ACO-OFDM and further variants of optical OFDM such as single-carrier optical (SCO)-OFDM, the spectral efficiency is lower than that of the DCO-OFDM (section 4.4.1, [96]). In ACO-OFDM, only the odd subcarriers carry data symbols, while the even subcarriers form a bias signal to ensure that the transmitted OFDM signal meets the non-negativity requirement. Hence, the use of only half of the subcarriers to carry actual data in ACO-OFDM is inefficient in terms of bandwidth as compared to DCO-OFDM [99]. Therefore, DCO-OFDM has been considered to support higher spectral efficiency, which in turn supports more IoT devices in the coexistence environment. Please note for DCO-OFDM, the DC biasing equivalent to the minimum value of $x(n)$ has been used in all the considered schemes.

Fig. 5.2 illustrates the PHY design of DCO-OFDM for data transmission from AP_L to U_L with QAM as a subcarrier modulation technique and DHT as frequency-domain (FD) transform. The motivation of using DHT in this work is that it provides real output for real input constellation symbols. In DFT based DCO-OFDM (DCO-OFDM$^{\mathrm{F}}$), the system will use N subcarriers to send data, but in true sense $N/2$ (in case of segregating method) [96]

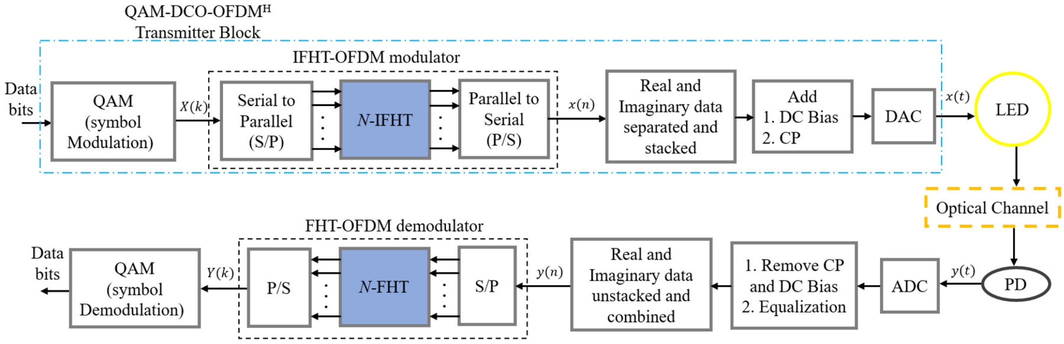

Figure 5.2: Downlink PHY design of QAM based DCO-OFDM$^{\mathrm{H}}$ for data transmission from LiFi AP to LiFi user.

and $(N/2-1)$ (in case of Hermitian symmetry [99]) unique symbols will be transmitted to the receiver. On the other hand, when one utilizes real input constellation symbols and DHT, the output is already real (in case of PAM) and thus does not require complex to real conversion for IM. Hence, N subcarriers can send unique N data symbols. Thereby, the spectral efficiency of PAM based DCO-OFDM$^{\mathrm{F}}$ (effective $\frac{N}{2}$ symbols) becomes half of PAM based DCO-OFDM$^{\mathrm{H}}$ (effective N symbols) [96, 157, 158]. Though, for QAM, the DCO-OFDM$^{\mathrm{H}}$ signal $x(n)$ is complex and requires conversion to real and positive signal for VLC by using real and imaginary components segregation (as shown in Fig. 5.2). Therefore, in QAM based DCO-OFDM$^{\mathrm{H}}$ or DCO-OFDM$^{\mathrm{F}}$ scheme, the spectral efficiency remains the same. However, when compared to PAM based DCO-OFDM$^{\mathrm{H}}$ (refer Fig. 5.3, further discussed in the upcoming paragraph), the QAM based DCO-OFDM$^{\mathrm{H}}$ (Fig. 5.2) has half spectral efficiency. Hence, modulation techniques with real constellation symbols are more suitable to DHT based O-OFDM. Practically, DHT is implemented with a fast algorithm, known as fast Hartley transform (FHT) [157]. Consequently, real output based modulation techniques such as PAM or CSK in DCO-OFDM$^{\mathrm{H}}$ reduce complexity by alleviating the extra computation required for data conversion.

In Figs. 5.2-5.8, N denotes the number of subcarriers that corresponds to N point FHT or inverse FHT (IFHT). The FD and TD data sequence of an OFDM symbol are denoted as $[X(0),X(1),\ldots,X(N-1)]$, and $[x(0),x(1),\ldots,x(N-1)]$, respectively. The TD data sequence can be obtained through IFHT operation from the FD data sequence as follows:

$$x(n) = \frac{1}{\sqrt{N}} \sum_{k=0}^{N-1} X(k).\mathrm{cas}(\frac{2\pi nk}{N}), \tag{5.1}$$

where, $\mathrm{cas}(x) = \cos(x) + \sin(x)$ and $n,k \,\varepsilon\, \{0,1,\ldots,N-1\}$. For VLC no carrier frequency up-conversion is required. Hence, the baseband OFDM signal $x(n)$ directly adds cyclic prefix (CP), which is fed to the digital-to-analog (DAC) conversion block and than DC biasing is done to yield $x(t)$. At the receiver PD, the received TD signal $y(t)$ is converted back to $y(n)$

after analog-to-digital (ADC) conversion and equalization. $Y(k)$ approximates $X(k)$ with DHT operation in (5.2). It is clear from (5.1) and (5.2) that DHT is involuntary and avoids complex arithmetic [162].

$$Y(k) = \frac{1}{\sqrt{N}} \sum_{n=0}^{N-1} y(n).\text{cas}(\frac{2\pi nk}{N}). \tag{5.2}$$

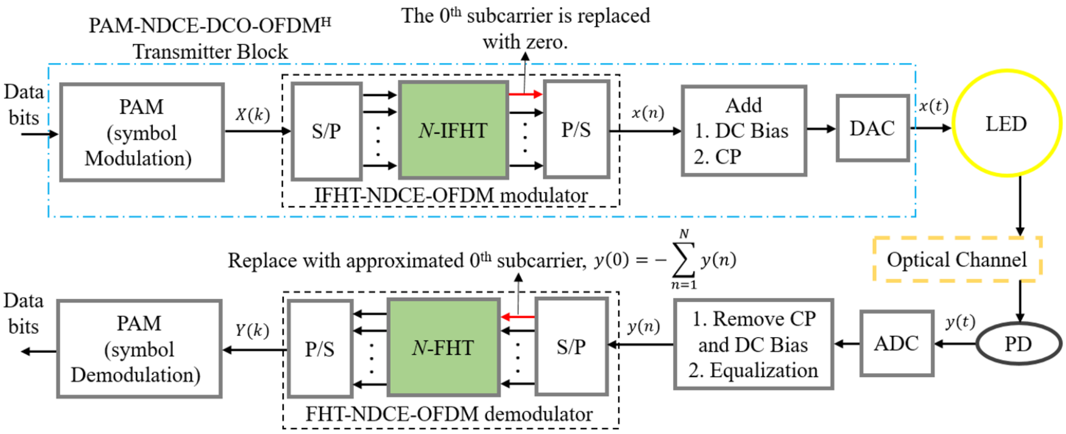

Figure 5.3: Downlink PHY design of PAM-NDCE-DCO-OFDM$^{\text{H}}$ for data transmission from LiFi AP to LiFi user.

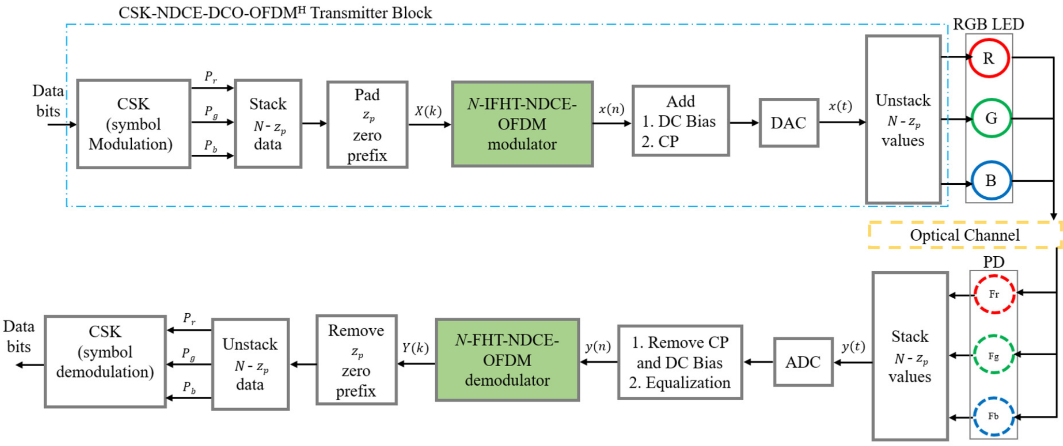

Figure 5.4: Downlink PHY design of CSK-NDCE-DCO-OFDM$^{\text{H}}$ for data transmission from LiFi AP to LiFi user.

Figs. 5.3 and 5.4 show the proposed null DC element (NDCE) DCO-OFDM$^{\text{H}}$ technique with PAM and CSK subcarrier modulation technique, respectively. It is significantly inspired by the criteria to reduce the PAPR of O-OFDM signal for real-positive constellation symbols. The first element of O-OFDM data sequence $x(n)$ is termed as the DC component in literature. It has the highest value with respect to all $x(n)$ terms ($\forall\ n\ \varepsilon\ \{1,\ldots,N-1\}$) and has significant impact on the PAPR. The proposed NDCE method removes the first element and transmits the rest of the elements ($\forall\ n\ \varepsilon\ \{1,\ldots,N-1\}$). However, at the receiver side, the first element, i.e., $x(0)$, is required for the correct estimation of data sequences via N-point FHT. The mathematics behind the approximation of DC element $x(0)$ at the receiver using the rest of the elements $x(n)$ have been derived and shown below. The first element $x(0)$ of TD data sequence of DHT based OFDM (OFDM$^{\mathrm{H}}$) (valid for DHT based O-OFDM (O-OFDM$^{\mathrm{H}}$) as well) can be obtained from (5.1) and is expressed as

$$x(0)=\frac{1}{\sqrt{N}}\sum_{k=0}^{N-1}X(k). \tag{5.3}$$

The first element of FD data sequence $X(k)$ is kept zero for deriving OFDM$^{\mathrm{H}}$ property to get the relation between TD first element and rest elements, so $X(k)$= $[0,X(1),\ldots,X(N-1)]$. Hence, $[x(0),x(1),\ldots,x(N-1)]$ can be expressed using (5.3) and (5.1),

$$\begin{aligned}
x(0)&=\frac{1}{\sqrt{N}}\sum_{k=1}^{N-1}X(k),\\
x(1)&=\frac{1}{\sqrt{N}}\sum_{k=1}^{N-1}X(k).\mathrm{cas}(\frac{2\pi k}{N}),\\
&\vdots\\
x(N-1)&=\frac{1}{\sqrt{N}}\sum_{k=1}^{N-1}X(k).\mathrm{cas}(\frac{2\pi(N-1)k}{N}).
\end{aligned} \tag{5.4}$$

The sum of TD data sequence $\forall\ n\ \varepsilon\ \{1,\ldots,N-1\}$ can be expressed as (5.5) using (5.4),

$$\begin{aligned}
\sum_{n=1}^{N-1}x(n)&=\frac{1}{\sqrt{N}}\sum_{k=1}^{N-1}X(k).\sum_{n=1}^{N-1}\mathrm{cas}(\frac{2\pi nk}{N}),\\
&=\frac{1}{\sqrt{N}}\sum_{k=1}^{N-1}X(k).\sqrt{2}\sum_{n=1}^{N-1}\sin(\frac{2\pi nk}{N}+\frac{\pi}{4}).
\end{aligned} \tag{5.5}$$

The law of sum of sines [163] where, $\sum_{n=0}^{N-1}sin(A+Bn)=0$ can be applied to $\sum_{n=1}^{N-1}sin(\frac{2\pi nk}{N}+\frac{\pi}{4})$ to obtain its value ($\forall\ n,k\ \varepsilon\ \{1,\ldots,N-1\}$). Therefore, availing $x(0)$ expression from (5.4) and applying law of sum of sines to (5.5), $x(0)$ can be derived in terms of $x(n)$ as

$$\begin{aligned} \because\ \sqrt{2}\sum_{n=1}^{N-1}\sin\left(\frac{2\pi nk}{N}+\frac{\pi}{4}\right) &= -1, \\ \therefore\ \sum_{n=1}^{N-1} x(n) &= -\frac{1}{\sqrt{N}}\sum_{k=1}^{N-1} X(k), \\ \implies x(0) &= -\sum_{n=1}^{N-1} x(n). \end{aligned} \tag{5.6}$$

Thus, at the receiver side $x(0)$ can be estimated using the derived expression in (5.6). Interestingly, QAM have bipolar and complex output data, whereas PAM has bipolar ($\mathrm{PAM_{Bp}}$) and real constellation symbols in RF communication. VLC can utilize these modulation techniques after converting complex symbols to real and bipolar symbols to unipolar. Therefore, to further reduce the PAPR (described in section 5.3.2), the constellation symbols of PAM has been designed between 0 and 1. PAM having real and unipolar symbols is termed as ($\mathrm{PAM_{Up}}$) in this work. The PAM symbols are adjusted at equal Euclidean distances between 0 and 1 to fulfill the criteria of real and unipolar symbols in VLC.

CSK modulation is specific to VLC, so it has real-positive constellation symbols only as discussed in Section 2.3.3 of chapter 2. In Fig. 5.4, P_r, P_g and P_b are the RGB optical powers with respect to the CSK constellation symbols and Fr, Fg and Fb are the respective filters for red, green and blue wavelengths. The total length of data for three LEDs $[P_r, P_g, P_b]$ becomes a multiple of three, so for N-point IFHT, zero prefix $z_p = N - 3\lfloor Q[N,3]\rfloor$ is padded to the input data. The $Q[N,3]$ denotes the quotient of N divided by three and the operator $\lfloor x \rfloor$ denotes the greatest integer equal to x.

5.2.1.2 LiFi AP to IoT Devices

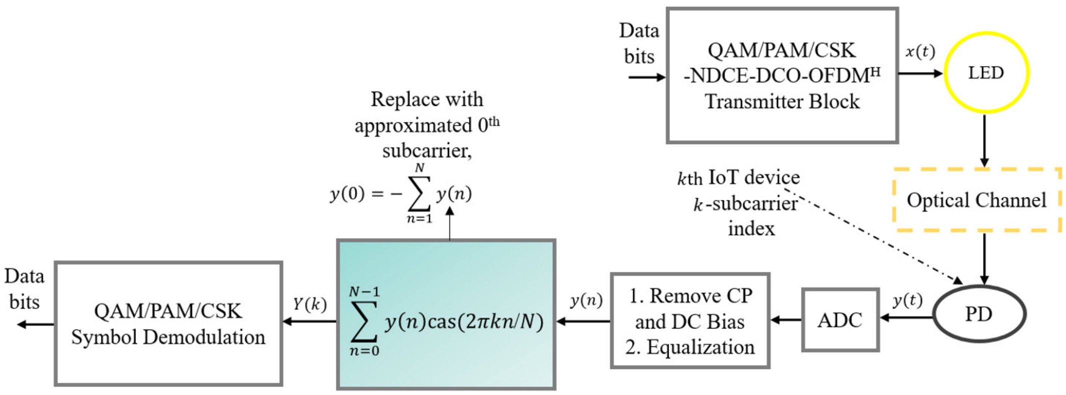

Figure 5.5: Downlink PHY design for IoT device as a receiver for receiving data from LiFi AP.

The LiFi AP can operate on the legacy architecture of WiFi 802.11 [161] to enable fast integration of the physical layer (PHY) to transmit and receive O-OFDM modulated light signals. The AP preserves its legacy architecture (i.e., transmitter block) as seen in Figs. 5.2-5.4. The key idea for a greener LiFi-IoT coexistence is that the AP uses a single subcarrier, say subcarrier k for data transmission to kth IoT device. Specifically, the AP does not require hardware alteration to serve $\mathbb{D}_I$. The PHY design for narrowband IoT device receiver for receiving data from an O-OFDM-based AP_L (as shown in Fig. 5.5 for NDCE-DCO-OFDM$^{\mathrm{H}}$) can be extended to K IoT devices. It is assumed that AP informs the users and devices about their respective indexed subcarrier through control frame [68]. The technique of decoding a single subcarrier data from NDCE-DCO-OFDM$^{\mathrm{H}}$ modulated transmitted data without FHT operation at the receiver has been shown in Fig. 5.5. The kth indexed IoT device receives data for whole time duration t $(0 < t < T)$, and can obtain its $Y(k)$ data corresponding to kth subcarrier using (5.2). Therefore, D_I does not require computation-intensive DHT/IDHT operations in their signal processing (requires only N multiplication for extracting data from kth subcarrier signal), thereby minimizing its computational complexity and power consumption.

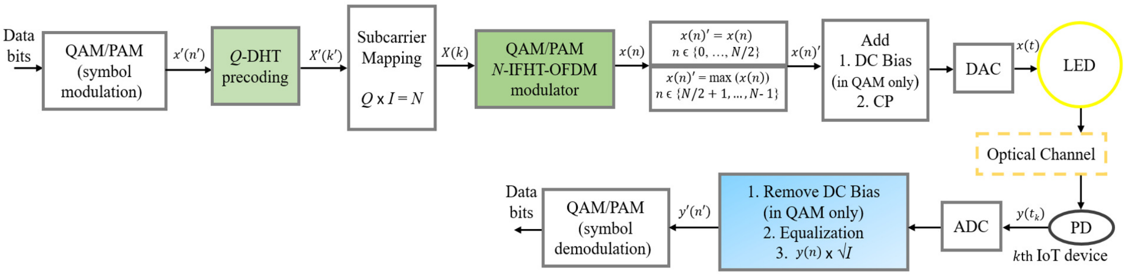

Figure 5.6: Downlink PHY design for data transmission from LiFi AP to IoT device with precoding, interleaving and modified $x(n)$.

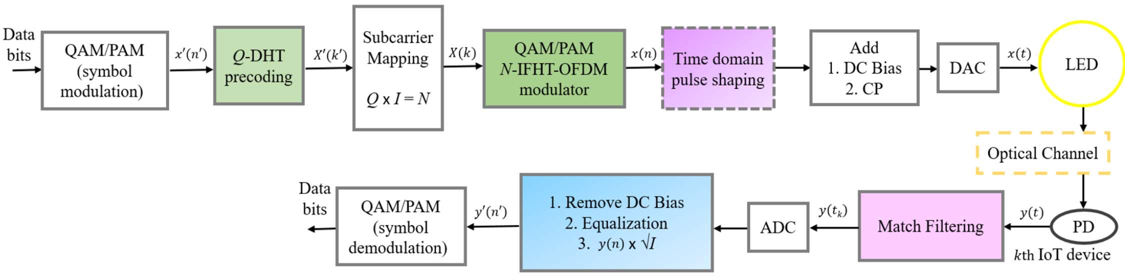

Figure 5.7: Downlink PHY design for data transmission from LiFi AP to IoT device with precoding, interleaving and TD pulse shaping.

To achieve a greener communication solution for the coexistence system, the authors have further simplified the receiver architecture by adopting DHT precoding of the input data sequence and its subcarrier mapping at the transmitter [69]. The final TD transmitted data $x(n)$

becomes equal to the ratio of input data sequence $x'(n')$ and subcarrier mapping factor I, as shown in Fig. 5.6. Moreover, for a legacy AP, each O-OFDM symbol has 64 samples/elements (e.g., number of data subcarriers, $N = 64$ in 802.11ac) in the data part and 16 samples in the CP part, totalling up to 80 samples [161]. Hence, the symbol rate at the IoT device is 250 ksps (20 Msps (AP's sampling rate) divided by 80). With this, the $\mathbb{D}_I$ operate on its required lower sampling rate (250 ksps) for signal reception. The subcarrier mapping factor I can be directly utilized to detect data, reducing the computational complexity and, therefore, energy consumption at the receiver side. The periodicity property of DHT [162, 163] sequence can be applied to (5.1) to derive the relation between $x'(n')$ and $x(n)$ after Q-point precoding and subcarrier mapping in (5.7).

$$
\begin{aligned}
x(n) &= \frac{1}{\sqrt{N}} \sum_{k=0}^{N-1} X(\frac{k}{I}).\text{cas}(\frac{2\pi nk}{N}), \\
&= \frac{1}{\sqrt{N}} \sum_{k'=0}^{\lfloor \frac{N-1}{I} \rfloor} X'(k').\text{cas}(\frac{2\pi nIk'}{N}), \\
\text{s.t. } k' &= \frac{k}{I}, \text{ where, } n,k \in \{0,1,\ldots,N-1\} \\
&= \frac{1}{\sqrt{QI}} \sum_{k'=0}^{Q-1} X'(k').\text{cas}(\frac{2\pi nIk'}{QI}), \\
\text{as } N = QI&, \text{ where, } k' \in \{0,1,\ldots,Q-1\} \\
&= \frac{1}{\sqrt{I}} \left[\frac{1}{\sqrt{Q}} \sum_{k'=0}^{Q-1} X'(k').\text{cas}(\frac{2\pi nk'}{Q}) \right], \\
x(n) &= \frac{x'\left[(n)_Q\right]}{\sqrt{I}}.
\end{aligned}
\tag{5.7}
$$

Where, $X(\frac{k}{I})$ is the subcarrier mapped version of $X'(k')$. The time sequence data $x'(n')$ has a length of Q samples defined for all $n' \in \{0,1,\ldots,Q-1\}$. For $n > n'$, $x(n)$ can be interpreted by the periodic extension with the help of modulus operator as $x(n) = x'\left[(n)_Q\right]$. The two types of subcarrier mapping [69], i.e., interleaved and localized, produce repeated and interleaved versions of size N after N-IFHT operation at the transmitter from input data sequence of size Q, respectively. The PAPR can be reduced by interchanging the repeated or interleaved data sequence with the maximum value of the $x(n)$ element in an OFDM$^{\text{H}}$ symbol. The modified data sequence (MDS) helps in higher average illumination, and energy harvesting from the indoor solar cell [164] as higher light power excites the solar cell to produce higher voltage and hence, more energy. The proposed scheme in Fig. 5.6 can be termed as PAM$_{\text{Up}}$-precoded (P)-MDS-O-OFDM$^{\text{H}}$ (PAM$_{\text{Up}}$-P-MDS-O-OFDM$^{\text{H}}$). With precoded FHT and then IFHT at the transmitter, the PAM$_{\text{Up}}$-P-MDS-O-OFDM$^{\text{H}}$ data sequence $x(n)$ and $x(n)'$ has all positive values (interpreted from (5.7)), hence do not require DC bias as such. Therefore, to keep a common scheme DCO-OFDM$^{\mathrm{H}}$ intact for a better flow and understanding of this work, the PAM$_{\mathrm{Up}}$-P-MDS-O-OFDM$^{\mathrm{H}}$ has been renamed as *PAM$_{\mathrm{Up}}$-P-MDS-DCO-OFDM$^{\mathrm{H}}$, where * signifies that there is zero DC biasing. With Q precoding, the SE decreases by $\frac{N}{Q}$ factor because the repeated values from the interleaved data sequence [69] do not contribute to information bits.

Additionally, precoded DCO-OFDM$^{\mathrm{H}}$ (P-DCO-OFDM$^{\mathrm{H}}$) have been investigated with Gaussian based FD pulse shaping (FDPS) [69] and TD pulse shaping (TDPS) [165]. Fig. 5.7 illustrates system architecture with TDPS, which allows N subcarriers to send information data with reduced PAPR but with a surge in computational complexity. TDPS makes the OFDM$^{\mathrm{H}}$ data sequence non-positive, so DC biasing is required even in PAM. As DC biasing increases, the average power of P-DCO-OFDM$^{\mathrm{H}}$ signal increases which reduce the PAPR [96]. Therefore, in various schemes of P-DCO-OFDM$^{\mathrm{H}}$, where ever DC biasing is required, the schemes have been investigated for DC biasing equivalent to the maximum value of $x(n)$ ($^{+}$). It should be noted that there is no clipping distortion in variants of PAM$_{\mathrm{Up}}$-DCO-OFDM$^{\mathrm{H}}$ as the value of $x(t)$ does not go beyond one even after DC biasing. Further, FDPS [69] has also been analyzed in which the FDPS block comes before the N-IFHT-OFDM modulator as $X(k)$ is in FD. The performance of the several proposed coexistence schemes have been analyzed and compared to conventional coexistence schemes (such as QAM/PAM/CSK-DCO-OFDM$^{\mathrm{H}}$) with respect to various performance metrics in the results section (Section 5.5).

Since many clients ($\mathbb{U}_L$ and $\mathbb{D}_I$) of AP will try to transmit and receive data at the same time, so they need to be coordinated. To achieve this coordination, the AP sends trigger frames to the clients to inform them which subcarriers they can use to send and receive data. The receiver ($\mathbb{U}_L$ and $\mathbb{D}_I$) receives data of its interest as it knows apriori during the handshake which subcarrier is meant for them and at what time it will receive data [68, 166–168]. Therefore, IoT devices could go to sleep for most of the time and only wake up at its data time instant to receive data [169]. The synchronization among users, devices, and AP is out of the scope of this work. Nevertheless, efficient synchronization can be adopted from these works [166–168]. The upper-layer control mechanism can readily support it [68].

5.2.2 Uplink Transmission

The visible light as a communication medium is less preferred for uplink, as light would be continuously emitting in an upward direction, which is aesthetically not pleasing from a user's perspective. Therefore, either a WiFi or an IR LED can be used for uplink transmission. The signals from both the WiFi and IR LED transmitters are invisible to human eyes and thus do not distract users. Further, for a bidirectional LC, the use of the infrared spectrum is deemed most appropriate in the literature as it completely obliterates the use of RF waves [12, 13]. Since, the work in this chapter aims to coexist heterogeneous users with bidirectional LC, for uplink, IR LED has been considered. Therefore, the UL transmission has been accomplished through IR LED and its respective PD. The LC channel utilizing IR LED [12, 102] is similar to VLC channel in (2.9), modeled using a generalized Lambertian radiant intensity for LOS channel [104]. The thermal noise component at the receiver is higher for IR LEDs based communication than the phosphorous coated LEDs and the RGB LEDs based VLC as infrared light induces more thermal energy [170]. Consequently, the communication with IR LED requires more transmitted optical power than VLC to maintain the same error rate. However, the performance trend (e.g., "poor", "average", "good") of the results shown in this work will remain the same as that of DL coexistence schemes.

5.2.2.1 LiFi Users to LiFi AP

The data required in UL is usually lower than DL in $\mathbb{U}_L$, whereas, in $\mathbb{D}_I$, UL requires significant data depending on applications. The $\mathbb{U}_L$ and $\mathbb{D}_I$ are the transmitters in the case of UL, and the ultimate aim is to have lesser complexity at $\mathbb{D}_I$ and $\mathbb{U}_L$ as transceivers. The choice of MA affects the choice of coexistence scheme for UL. The MA techniques have two most important parameters, i.e., delay and throughput; hence delay-throughput analysis is an essential aspect of communication. The simplest MA technique possible is TDMA. It has been stated that in the case of TDMA for heterogeneous users, the QoS of $\mathbb{U}_L$ degrades due to less airtime. Further, since this work explores O-OFDM; hence OFDMA can be deployed effortlessly [171]. Therefore, the analysis of access techniques (TDMA and OFDMA) is necessary to decide a suitable one as per the VLC coexistence requirements. The delay-throughput analysis of TDMA and OFDMA in VLC has been presented in section 5.4.2).

5.2.2.2 IoT Devices to LiFi AP

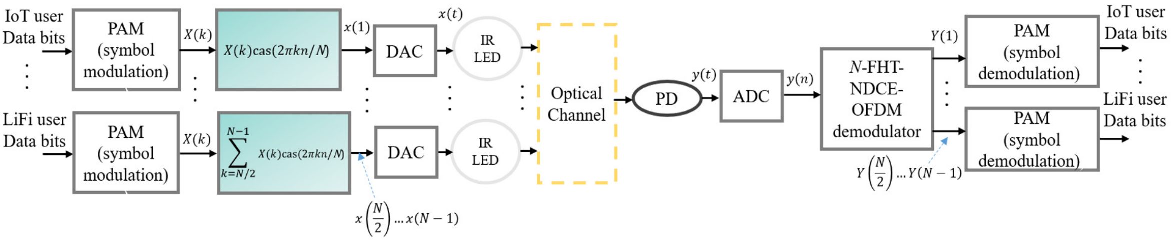

Figure 5.8: Uplink PHY design for data transmission from LiFi user and IoT devices to LiFi AP.

In single-user OFDM, significant overhead is caused by medium contention at each frame transmission. Whereas in OFDMA, medium contention overhead is less since transmitting opportunities are shared by several frames bundled together. Therefore, efficient use of the channel leads to overall increased efficiency [171]. Additionally, while proposing a coexistence scheme for the IoT device in the UL, it should be noted that IoT device is severely energy limited (especially, if it harvests energy as well), so the optical transmitter at the IoT device has a limited optical power at the UL, in contrast to the DL, where in theory there is no energy limitation at the AP (i.e., AP is connected to the power line). Further, as compared to the IoT devices, even the LiFi users have ample energy. The UL PHY design can be seen in Fig. 5.8 with an OFDMA scheme, based on the concept of Fig. 5.5 with reversed transmitter and receiver. Further, the results obtained for various coexistence schemes for DL can be interpreted for UL as well, just by interchanging the understanding of transmitter and receiver.

Timing synchronization is crucial in uplink OFDMA communication among IoT devices to ensure signals are transmitted and received accurately. It can be challenging to achieve as devices need to be precisely coordinate in both time and frequency. The complexity of timing synchronization depends on the number of devices, subcarrier bandwidth, and timing measurement accuracy. Maintaining synchronization is vital, as any drift or delay can cause significant signal interference. Achieving synchronization is necessary to ensure the IoT devices operate at their required lower sampling rates, enabling efficient signal reception. The issue of timing synchronization among IoT devices is not within the scope of this work. As a result, it has been presumed that perfect synchronization exists. Nonetheless, other studies can offer valuable knowledge regarding effective timing synchronization techniques that can be utilized [172–174].

5.3 Performance Metrics

In an attempt to have a fair comparison, the resource units (RUs), i.e., the number of subcarriers (N) for all the considered and proposed coexistence schemes, are kept the same while calculating all the performance metrics. In the following subsections, the different performance metrics have been discussed as per their preference to achieve a greener communication solution for LiFi-IoT coexistence.

5.3.1 System Complexity

The complexity of a system is quantified in terms of the total number of arithmetic operations (such as multiplications) required at the transceiver. The transceivers that require N-point FHT/IFHT (or FFT/IFFT) operations with complex constellation symbols achieve a computational complexity of $4N\log_2 N$. Compared to FHT/FFT with complex input constellation, the complexity of FHT with real input constellation is halved [96] (explained in section 5.2.1.1). The system complexity of the proposed schemes consisting of various modulation techniques is analyzed separately for D_I, U_L and AP_L. The equalization process can be realized in $O(N)$ operations. It should be noted that an IoT user has power and computation constraints. Therefore, a transceiver with low complexity is highly preferred for an IoT device. In contrast, the main requirement of $\mathbb{U}_L$ is high data rate, so it can tolerate some relaxation in complexity and power consumption. Thus, a transceiver with low to moderate complexity supporting a high data rate is desirable for $\mathbb{U}_L$. The AP_L in the coexistence system can handle further higher complexity. Therefore, system complexity of various coexistence schemes have been calculated separately for U_L, D_I and AP_L, which becomes a crucial performance metric for choosing schemes in the coexistence environment. The PHY design of different DCO-OFDM$^{\mathrm{H}}$ utilize numerous different techniques which can be seen in Figs. 5.2-5.7 in the form of various system blocks. Therefore, the system complexity varies for various coexistence schemes considered in this work.

5.3.2 Peak-to-Average Power Ratio

The ratio between the peak power and the average power of the transmitted signal is known as PAPR. PAPR of a transmitted O-OFDM signal $x(t)$ can be defined as

$$\mathrm{PAPR}_{x(t)} = \frac{\max\left(x(t)^2\right)}{\mathbb{E}[x(t)^2]}, \tag{5.8}$$

where $\mathbb{E}[.]$ denotes the expectation operator. High PAPR has always been an issue in O-OFDM. Firstly, a high PAPR can cause clipping distortion if the LED dynamic range is not sufficiently large. Secondly, high PAPR reduces illumination to communication conversion efficiency and a lifetime of the LED [69, 96, 175]. Therefore, it has been given second priority in terms of performance metrics for the coexistence system. For CSK, the concept of calculating PAPR has been borrowed from multi-input multi-output system [176]. PAPR is calculated individually for red, green and blue LEDs and then averaged out to get an average PAPR for CSK. The probability of PAPR greater than a threshold value (ζ) is defined by the complementary cumulative distribution function (CCDF). CCDF of PAPR is commonly used to measure the performance of PAPR reduction techniques [69]. The CCDF of PAPR can be obtained as:

$$\begin{aligned} CCDF_{PAPR} &= \mathrm{Prob}(\mathrm{PAPR}_{x(t)} > \zeta), \\ &= 1 - \mathrm{Prob}(\mathrm{PAPR}_{x(t)} < \zeta), \\ &= 1 - \mathrm{Prob}(\frac{\max x(t)^2}{\mathbb{E}[x(t)^2]} < \zeta). \end{aligned} \tag{5.9}$$

The different DCO-OFDM$^{\mathrm{H}}$ schemes vary the transmitted signal due to various subcarrier modulation techniques, precoding, subcarrier mapping, modified data sequence, and the PAPR changes with peak power and average power of the O-OFDM (in this work DCO-OFDM$^{\mathrm{H}}$) signal $x(t)$. Therefore, the CCDF of PAPR differs for various coexistence schemes considered in this work.

5.3.3 Effective Spectral Efficiency

SE is the data rate that can be transmitted over a given bandwidth. However, the VLC channel also impacts the reliable achievable data rate. Hence, the consideration of error rate at a given SNR in the calculation of SE gives a better realization of efficiency termed as ESE (SE_e) [157], defined as:

$$SE_e = \frac{(1-e)N_s}{Tf_s}, \tag{5.10}$$

where e is the SER of one O-OFDM symbol at a particular SNR, which consists of a data sequence corresponding to N subcarriers. N_s is the number of subcarriers meant for data per O-OFDM symbol. T is the time duration per O-OFDM symbol, and f_s is the subcarrier bandwidth. The term (Tf_s) is normalized to unity for simplicity [157]. In this work the normalized ESE $\tilde{SE}_e$ has been considered for better understanding, so normalization has been done by a factor of 2, i.e., maximum ESE value. With different DCO-OFDM$^{\mathrm{H}}$ schemes, the $\tilde{SE}_e$ changes as e and subcarriers meant for actual data per O-OFDM symbol varies. ESE has the third priority concerning all other performance metrics as it drives the maximum number of D_I a coexistence scheme can support.

5.3.4 Maximum number of IoT devices

The maximum number of D_I a coexistence scheme can support is an essential aspect of this work. When considering just SE, the coexistence scheme can support communication of N IoT devices at a low sampling rate of $\frac{SE}{N}$. Since SE does not consider the varying error performance of various schemes, therefore SE_e has been utilized to obtain K_m in (5.11). Further, the impact on SNR as N_s increases can be seen in Fig. 5.9. This impact is valid for all the schemes considered in this work because the SNR gain degrades as N_s increases due to the reduced gaps between data subcarriers. In VLC term, it increases the nearness of light intensity levels for adjacent subcarriers. One wants to support large number of D_I at lower SNR, however from Fig. 5.9, it is clear that there is a trade-off between desirable SNR and N_s. To support large number of D_I at lower SNR, the intermediate number ($K_s = \frac{N_s}{2}$, also considered in RF [68]) has been considered in (5.11) for all the schemes except P-DCO-OFDM$^{\mathrm{H}}$. The P-DCO-OFDM$^{\mathrm{H}}$ automatically sends data to subcarriers within K_s due to the specific subcarrier mapping used.

K_m for various DCO-OFDM$^{\mathrm{H}}$ schemes vary due to SE_e and N_s.

$$K_m = SE_e K_s. \tag{5.11}$$

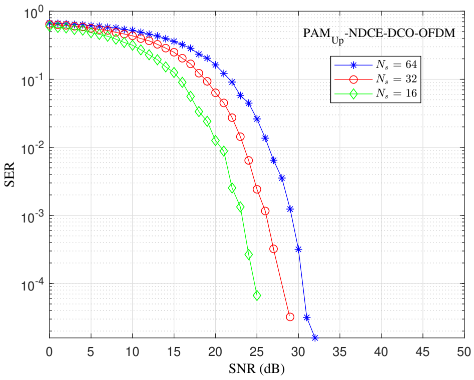

Figure 5.9: SNR versus SER of PAM$_{\mathrm{Up}}$-NDCE-DCO-OFDM$^{\mathrm{H}}$ for varying data subcarriers.

5.3.5 Power Saving

The power saving (P_{sav}) tells us how much power can be saved at the transmitter with regard to the PAPR. It is imperative for AP in DL and $\mathbb{U}_L$ in UL as it operates on DCO-OFDM$^{\mathrm{H}}$ schemes. $\mathbb{D}_I$ in UL operates on single subcarrier modulation techniques, hence PAPR is not an issue and thus power saving with respect to PAPR. The generic formula for power at a given PAPR (P_p) [69] is

$$P_p = \xi P_{\mathrm{avg}}, \tag{5.12}$$

where ξ is the inverse function of the CCDF for a given probability, i.e., Prob (PAPR $> \zeta$) and P_{avg} is the average power per O-OFDM symbol. The value of ξ is calculated for probability Prob (PAPR $> \zeta$) set to 10^{-1} from the CCDF plots in Sec. 5.5. The power savings of the different DCO-OFDM$^{\mathrm{H}}$ schemes are evaluated with respect to one of classical state-of-the-art schemes, i.e., QAM-DCO-OFDM$^{\mathrm{H}}$. Since, P_p varies for different coexistence schemes, hence P_{sav} also differs. The power saving achieved by the different DCO-OFDM$^{\mathrm{H}}$ schemes over the QAM-DCO-OFDM$^{\mathrm{H}}$, is given by

$$P_{\mathrm{sav}} = 10\log_{10}\left(\frac{P_p^{\mathrm{DCO\text{-}OFDM^H\ scheme}}}{P_p^{\mathrm{QAM\text{-}DCO\text{-}OFDM^H}}}\right). \tag{5.13}$$

5.3.6 Energy Harvesting

An energy-autonomous IoT device would facilitate additional energy efficiency in the coexistence system. An indoor solar cell of size 4 cm^2 [164] can be attached to $\mathbb{D}_I$ to support its energy demand. The energy harvesting (EH) from an O-OFDM symbol for unit second in an indoor VLC channel (2.9) is expressed as

$$EH = \frac{(m+1)P_{\text{avg}}\eta A_{\text{cell}}t}{2\pi d_r^2}, \tag{5.14}$$

where η represents the power conversion efficiency of the indoor solar cell, A_{cell} is the physical area of the indoor solar cell, t is the duration of energy harvesting and P_{avg} is the average transmitted optical power of an O-OFDM symbol. $P_{\text{avg}} = \mathbb{E}[x(t)\rho]$ and ρ is the electrical to optical conversion efficiency of an LED. All other parameters except P_{avg} in (5.14) are fixed to same value for all the schemes to have a fair comparison. Moreover, as these are physical parameters, they would not change based on modulation or MA techniques. However, P_{avg} changes with different subcarrier modulation techniques such as QAM, PAM, CSK as P_{avg} depends on the symbol data. Further, the impact of precoding, subcarrier mapping, modified sequence data also impacts the optical output data and hence the P_{avg} of the transmitted signal. Therefore, EH performance will vary with varying P_{avg} due to the different coexistence schemes.

5.3.7 SNR versus SER

In VLC, the transmitter LEDs are used for both illumination and communication. The illumination condition intrinsically increases the power at the transmitter and thus received SNR. Hence, for achieving the FEC limit SER, the requirement of higher SNRs can be met through the condition of illumination in DL. Also, solar cells' utilization for generating power can resolve the power requirement for achieving higher SNR in UL. Hence, it has the least priority in the coexistence system. Nevertheless, the effect of SNR has been included while calculating other performance metrics such as ESE and K_m. Further, SNR gain can be improved using state-of-the-art error-correcting codes [177]. Different modulation techniques, data subcarriers, and modifications in the communication technique of DCO-OFDM$^{\text{H}}$ causes variations in SNR gain performance.

5.4 Analytical Performance Expressions

The analytical evaluation of PAPR and SER validate the simulation results. The theoretical expressions of PAPR [69, 96, 125] and closed-form BER expression [178] of the standard schemes such as PAM have been utilized to derive the proposed scheme's PAPR and SER expressions. Moreover, for delay-throughput analysis, the probability density function (PDF) of the received SNR for random way-point user movement in a square area has been derived for VLC.

5.4.1 PAPR and SER Performance

5.4.1.1 PAPR

In literature, PAPR of DCO-OFDM has been obtained theoretically [96, 125]. In [96], the author derives analytical expression of PAPR for hermitian symmetry free precoded O-OFDM. However, for our proposed coexistence scheme *PAM$_{Up}$-MDS-P-DCO-OFDM$^{\mathrm{H}}$, we require to evaluate the PAPR theoretically. A novel approach has been introduced to evaluate the PAPR: the PDF ($f_u(\zeta_i)$) of input symbols $x'(n')$ (as shown in Fig. 5.6) is almost uniform as a large set of random numbers reproduce uniform distribution (as stated in Section 3.2.1.1). For modulation order (M= 4), the $x'(n')$ belongs to symbol set $\mathbb{A} = \{s_1, s_2, s_3, s_4\}$ and the probability of occurance of each symbol is $\frac{1}{M}$. Consequently, for a precoded O-OFDM scheme the distribution of $x(t)$ can be directly obtained from $x'(n')$ as $x(t) \propto x'(n')$. The PDF $f(\zeta_i)$ of $x(t)$ can be obtained based on the modified data sequence $x(n)'$ in Fig. 5.6. Therefore, the probability of occurance of $\max(\mathbb{A}) = \max(x(t))$ becomes $(2.\frac{1}{M} + \frac{1}{2M})$. The probability of rest data symbol becomes $\frac{1}{2M}$. The required modified PDF $f(\zeta_i)$ can be obtained from the Hadamard product ($\odot$) of $f_u(\zeta_i)$ and modifying vector ($\mathbf{V}_i$) as represented in (5.15). Based on the modified data sequence, $\mathbf{V}_i$ becomes $[\frac{1}{2}, \frac{1}{2}, \frac{1}{2}, (2+\frac{1}{2})]$. The CCDF of PAPR can be derived from the PDF of the O-OFDM symbols [69]. The evaluation of PAPR expressions for the remaining approaches are skipped for brevity, which can be derived from the above stated modified PDF concept for P-O-OFDM. For DCO-OFDM$^{\mathrm{H}}$ these works [69, 96, 125] can be referred.

$$\begin{aligned} CCDF &= 1 - \text{Prob(PAPR} < \zeta) = 1 - \sum_{\zeta_i \leq \zeta} f(\zeta_i), \\ f(\zeta_i) &= f_u(\zeta_i) \odot \mathbf{V}_i, \ \forall\, i \in \{1, \ldots, M\}. \end{aligned} \tag{5.15}$$

5.4.1.2 SER

The approximate average BER analytical expression of M-ary QAM and PAM$_{\mathrm{Bp}}$ in AWGN [178] can be exploited to evaluate the SER behaviour of DCO-OFDM$^{\mathrm{H}}$. The closed-form expression of BER for M-PAM$_{\mathrm{Bp}}$ under AWGN channel [178] is given as:

$$\begin{aligned} P_e &= \frac{1}{\log_2 M}\sum_{b=1}^{\log_2 M} P_e(b), \\ P_e(b) &= \frac{1}{M}\sum_{q=0}^{(1-2^{-b})M-1}\Bigg[(-1)^{c1}(2^{b-1}-c2) \\ &\quad .\mathrm{erfc}\Big((2q+1)\sqrt{\frac{(3\log_2 M)\gamma_b}{M^2-1}}\Big)\Bigg], \end{aligned} \tag{5.16}$$

where, $c1 = \lfloor \frac{q.2^{b-1}}{M} \rfloor$ and $c2 = \lfloor \frac{q.2^{b-1}}{M} + 0.5 \rfloor$. The probability that the bth bit is in error is denoted by $P_e(b)$ and P_e is the average BER. The SNR per bit (γ_b) needs to be evaluated for specific O-OFDM schemes [96]. The estimated γ_b for PAM$_{\mathrm{Up}}$-MDS-P-DCO-OFDM$^{\mathrm{H}}$ can be obtained from the derived relation shown below:

$$\gamma_b = \frac{(10^{\frac{\gamma_s}{10}})}{2\log_2 M}\mathbb{E}[s(t)^2_{\mathrm{PAM_{Up}}}], \tag{5.17}$$

where, γ_s is the SNR per sample in dB, $\mathbb{E}[s(t)^2_{\mathrm{PAM_{Up}}}]$ is the normalized average power of the constellation symbols ($s(t)$) corresponding to VLC based PAM. It should be noted that the real input signal reduces the ratio of symbol time to sample time, to half when SNR per sample is considered. Furthermore, the factor $2\log_2 M$ in the denominator is included in order to convert γ_s to γ_b, which closely approximates the conversions and is widely accepted in literature [140]. For a given γ_s, the γ_b for a P-O-OFDM system (interleaved/localized) depends directly on the normalized P-O-OFDM signal power $x(t)$, which is proportional to the input data sequence (PAM$_{\mathrm{Up}}$) belonging to the set $\mathbb{A}$ due to subcarrier mapping. Therefore, the theoretical SER plot of *PAM$_{\mathrm{Up}}$-MDS-P-DCO-OFDM$^{\mathrm{H}}$ has been obtained by utilizing (5.16), (5.17) and $\log_2 M$.

5.4.2 Delay-Throughput Performance

The choice of MA technique impacts the overall performance of the system. Further, MA techniques affect the choice of modulation techniques in the coexistence schemes especially in UL (as discussed in section 5.2.2.1). The MA techniques have two most important parameters i.e., delay and throughput, hence delay-throughput analysis is an important aspect of communication. The simplest MA technique possible is TDMA. However, this work explores O-OFDM, hence OFDMA can be deployed effortlessly [171]. Therefore, analytical delay-throughput framework for TDMA and OFDMA have been derived in this work. The AP_L based on O-OFDM technique may operate as O-OFDM-TDMA or optical OFDMA (O-OFDMA). The O-OFDM-TDMA allocates time slots to users while O-OFDMA allocates subcarriers to users. The VLC channel conditions vary with the mobility of users. However, within a frame, the VLC channel can be assumed quasi-static [80]. This section demonstrates the comparison between dynamic O-OFDM-TDMA and dynamic O-OFDMA. The dynamic nature in O-OFDM-TDMA is because each time frame is allocated to a mobile user with the best channel gain, whereas the dynamism in O-OFDMA allows multiple mobile users to share subcarriers in an O-OFDM symbol. A more general queueing model, i.e., the M/G/1 model [179], is adopted for analysis of the queuing delay. The average delay $\overline{D}$ in the M/G/1 model [179] is given by

$$\overline{D} = \frac{\Lambda \mathbb{E}[T_{ps}^2]}{2(1-\Lambda \mathbb{E}[T_{ps}])}, \tag{5.18}$$

where T_{ps} is the packet service time and Λ is the Poisson packet arrival rate, same for both O-OFDM-TDMA and O-OFDMA. Further, $\overline{D}$ can be quantified mathematically by Little's Theorem [179].

$$\overline{D} = \frac{\overline{N_p}}{\Lambda}, \tag{5.19}$$

where, $\overline{N}_p$ is the average number of packets in the queue. This work assumes a queue of an infinite size which makes throughput proportional to Λ value. The delay-throughput plot of O-OFDM-TDMA and O-OFDMA has been obtained using these two equations (5.18) and (5.19). The delay can be measured in the unit of the number of subcarriers as a packet is served by subcarrier allocation in the O-OFDM transmission systems. The time unit in an O-OFDM scheme can be denoted by the number of subcarriers. Therefore, the packet service time can also be defined as the number of subcarriers N_{ps} satisfying

$$T_{ps} = \{N_{ps} : U \triangleq \sum_{n=1}^{N_{ps}} \mu_n = \alpha\}, \tag{5.20}$$

where U is the number of bits loaded in N_{ps} subcarriers, μ_n is the number of bits loaded to subcarrier n, which is identically distributed over all n, and α is the fixed packet size in the unit of bits.

$$\begin{aligned} \mathbb{E}[T_{ps}|U=\alpha] &= \frac{\alpha}{\mathbb{E}(\mu_n|U=\alpha)} = \frac{\alpha}{\sum_{i=0}^{1} \pi_i b_i} \ , \\ \mathbb{E}[T_{ps}^2|U=\alpha] &\geq \frac{\alpha^2}{\mathbb{E}(\mu_n^2|U=\alpha)} \geq \frac{\alpha^2}{\sum_{i=0}^{1} \pi_i b_i^2} \ , \end{aligned} \tag{5.21}$$

where, the first two moments of T_{ps} has been expressed in terms of first two moments of μ_n which can be obtained by steady-state probabilities π_i's and modulation bit order b_i [180]. The

b_i equals to 1 and $\log_2 M$, for i =0 and 1, respectively. The channel state in the link layer is often modeled by a finite-state Markov (FSM) chain model. This work considers two states VLC channel model in which one state (s_0) corresponds below 15 dB SNR threshold and another (s_1) equal to and above 15 dB (The value of SNR threshold is chosen to be 15 dB as beyond this value most of the schemes achieve FEC limit SER as shown in Figs. 5.16 and 5.17). The π_i's (in (5.22)) are calculated according to the FSM model. They can be obtained by integrating received SNR (γ) PDF of O-OFDM-TDMA and O-OFDMA over each state regions illustrated in Fig. 5.10.

$$\pi_i = \int_{\gamma_i}^{\gamma_{i+1}} f_\gamma(\gamma)_{VLC}\, d\gamma. \tag{5.22}$$

For a VLC channel the closed form expression of received SNR statistics (i.e., PDF) for a given random waypoint (RWP) mobility model [181] can be obtained by estimating the spatial user distributions for the RWP mobility models in terms of distance $r_i = \sqrt{d_r^2 - z^2}$ where, r_i ranges from 0 to R. For a room area of 5x5 m^2, R becomes 3.5 m. The PDF of r_i can be fit to a Gaussian expressions as in (5.23) and shown in Fig.5.11.

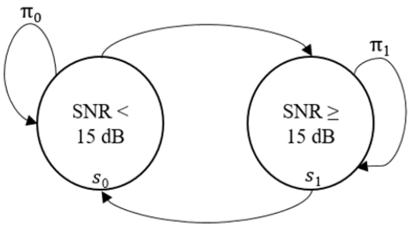

Figure 5.10: A finite-state Markov chain model for the VLC channel.

$$f_r(r_i) = \sum_{j=1}^{J} a_j.\exp\left\{-\left(\frac{r_i - b_j}{c_j}\right)^2\right\}, \tag{5.23}$$

where, the parameter J and its related coefficients a_j, b_j and c_j are approximated at 0.001281 root mean square error (RMSE) goodness of fit. The coefficients are approximated with 95% confidence bounds as $[a_1 = -1.492e+06, a_2 = 0.01387, a_3 = 0.009461, a_4 = 0.02809, b_1 = 213.5, b_2 = 2.489, b_3 = 2.382, b_4 = 2.049, c_1 = 48.58, c_2 = 0.04622, c_3 = 0.4451, c_4 = 1.723]$. The $\mathbb{U}_L$ and $\mathbb{D}_I$ are assumed to move on a horizontal surface with zero orientation of the PD. The zero tilting assumption and the angle around the z-axis (altitude between AP_L and the users' plane) uniformly distributed between 0 to 2π leads to a system that is only dependent on the user motion [182]. The movement pattern of independent users have been modelled using the RWP mobility model where the direction, velocity and the destination point of the users are selected randomly and uniformly under LOS VLC channel. The pause time is set to zero, so a

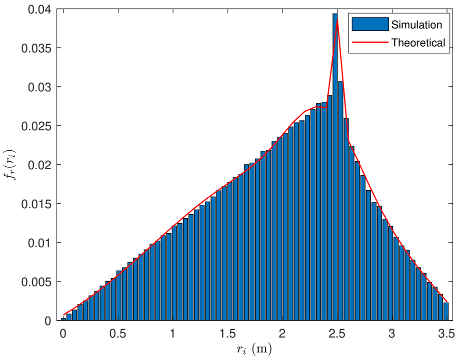

Figure 5.11: PDF of r_i in a square area with RWP mobility model.

user continuously moves along a zigzag line from one waypoint to the next with a constant velocity chosen at the start of each path from the uniformly distributed range [0.1, 1] m/s in the square room cell. Consequently, the PDF of the instantaneous received SNR (γ) in O-OFDM can be derived by utilizing the relation between $H(0)_{\mathrm{LOS}}$ (in (2.9)) and average received SNR $\overline{\gamma}$ in (5.24) [182].

$$\begin{aligned} \overline{\gamma} &= \frac{(\rho P_t H(0)_{\mathrm{LOS}})^2}{N_o B_{\mathrm{w}}}, \\ H(0)_{\mathrm{LOS}} &\propto \frac{1}{d_r^2} \propto \frac{1}{(r_i^2 + z^2)}, \end{aligned} \tag{5.24}$$

where, ρ, P_t, N_o and B_{w} MHz values for simulation are considered from Table 5.1. Applying a change of variable to (5.23) using (5.24), the received SNR PDF expression ($f_{\gamma}(\gamma)$) can be derived as:

$$f_{\gamma}(\gamma) = \sum_{j=1}^{4} a_j . \exp\left\{ - \left(\frac{\sqrt{C . \sqrt{\frac{\overline{\gamma}}{\gamma}} - z^2} - b_j}{c_j} \right)^2 \right\}, \tag{5.25}$$

where, the $C = \frac{(m+1)A\rho}{2\pi} \cos^m(\phi_r)\cos(\psi)$. The values obtained from the $f_{\gamma}(\gamma)$ expression fits well with the simulated received SNR as shown in Fig. 5.12. It is observed that for higher SNR values (beyond 35 dB) the analytical expression does not fit well because the impact of $\phi_r = atan(\frac{r_i}{z})$ with changing r_i has not been considered in the derived theoretical PDF expression of received SNR. It was ignored for simplicity to obtain a closed fitting expression. The expression obtained in (5.25) applies to O-OFDM. However, in an O-OFDMA scheme a subcarrier is assigned to the user with the highest SNR, the subcarrier SNR is equal to the maximum of K independent and identically distributed (i.i.d.) exponential random variables, where K is number of users. Hence, the received SNR PDF ($f_{\gamma}^{*}(\gamma)$) of O-OFDMA can be

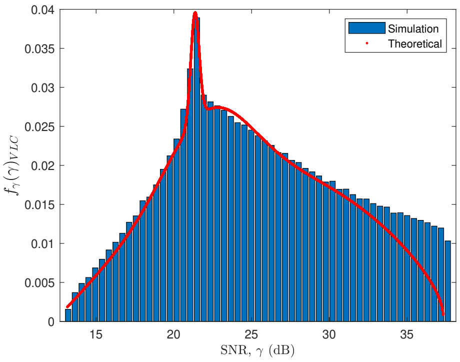

Figure 5.12: PDF of γ in a square area with RWP mobility model for VLC.

derived as:

$$f^*_\gamma(\gamma) = K.f_\gamma(\gamma)(1-f_\gamma(\gamma))^{(K-1)}. \tag{5.26}$$

The results in Fig. 5.13 shows that for a given fixed delay, O-OFDMA has larger throughput

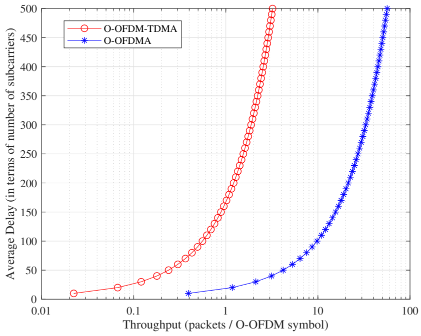

Figure 5.13: Comparison of packet throughput and delay for O-OFDM-TDMA and O-OFDMA.

(measured in packets/O-OFDM symbol) than the O-OFDM-TDMA scheme. The α is chosen to be 80 bits as used in speech applications [180], $K = 24$ and a frame size of one O-OFDM symbol is considered for evaluation. Finally, by plugging (5.25) and (5.26) in (5.22) and then (5.21) in (5.18) the theoretical throughput-delay lower bound curves can be obtained as shown in Fig. 5.13.

5.5 Results and Discussion

This section presents and analyzes the performance of various proposed and conventional coexistence schemes. The simulation parameters are stated in Table 5.1. The performance has been graded based on the number of stars from five to one, which has been color coded for lucid understanding in Table 5.2. Further, Table 5.3 summarizes different variants of DCO-OFDM$^{\mathrm{H}}$ based schemes (proposed and conventional) and their corresponding acronym

Table 5.2: The color scheme and star rating for different performance metrics.

Rating	**Performance Metrics Range for five different levels**								
	System Complexity for $N = 64$								
Five different levels with color marking and respective stars	**LiFi AP** (AP_L)	**LiFi user** (U_L)	**IoT device** (D_I)	**PAPR (dB) at CCDF probability = 0.1**	**Normalized ESE) at 15 dB (b/s** /hz)	**Max. no. of IoT device support** (K_m)	**Power Saving (dB) P$_{\text{sav}}$**	**EH (joule/ watt. sec)**	**SNR** (γ_o) **(dB) at FEC limit SER** (10^{-3})
***** Very Good	1-800	1-200	1-25	0-2	$\geq$ 0.85	$\geq$ 20	$\geq$ 15	$\geq$ E-07	9-15
**** Good	800-1600	200-500	25-100	2-4	$\geq$ 0.65	19-15	15-10	$\geq$ 5E-08	15-20
*** Average	1600-3000	500-1200	100-250	4-6	$\geq$ 0.4	14-12	10-5	$\geq$ E-08	20-25
** Below Average	3000-4000	1200-2000	250-500	6-8	$\geq$ 0.2	11-8	5-0	$\geq$ E-09	25-30
* Poor	> 4000	> 2000	> 500	8-10	0.2 <	7-4	0 <	$\geq$ E-10	30-35

Note: The authors have introduced the rating scale to improve the understandability of the results by intuitively determining the performance rating ranges. The maximum rating ("Very Good", five stars) belongs to the best value and the minimum rating ("Poor", one star) for the worst value corresponding to a particular performance metric, among all the different schemes considered. Further, the ranges for intermediate performance ratings are divided as equally as possible between the best and worst values for most of the performance metrics. However, owing to the larger variations in performance metric values of different schemes, the intermediate performance rating ranges have been defined intuitively.

for quick reference and better understanding. Table 5.4 and 5.5, tabulates the values of all the performance metrics for various DCO-OFDM$^{\mathrm{H}}$ coexistence schemes with respective color code. The simulation results of the performance metrics PAPR, ESE and SNR for all the coexistence schemes considered in this work have been shown in Figs. 5.14-5.19.

In **Fig. 5.14**, the CCDF of PAPR of various DCO-OFDM$^{\mathrm{H}}$ schemes are shown. It has been observed that the PAPR reduces significantly for PAM$_{\mathrm{Up}}$ and CSK with NDCE-DCO-OFDM$^{\mathrm{H}}$ from their standard DCO-OFDM$^{\mathrm{H}}$ schemes. It is due to the larger impact of DC element on PAPR for unipolar PAM and CSK constellation symbols. It should be noted that the $x(0)$ expression derived in (5.6) is beneficial when all input data sequences are unipolar (i.e., positive) in an O-OFDM scheme as all unipolar input data sequence $X(k)$ lead to highest $x(0)$ value among all $x(n)$ elements. Therefore, on removing the DC element from the transmitted signal, PAPR reduces drastically. On the other hand, when the input data sequence is bipolar, as in the case of QAM and PAM$_{\mathrm{Bp}}$, then although $x(0)$ still holds the property as expressed in (5.6) the value of $x(0)$ becomes equivalent to the rest of the $x(n)$ elements. Therefore, there is no significant impact of DC element on PAPR, hence no advantage of NDCE for bipolar input data. The TDPS and FDPS reduce PAPR a little more than PAM$_{\mathrm{Up}}$ and QAM with NDCE-DCO-OFDM$^{\mathrm{H}}$. However, it causes substantial complexity overhead (system complexity of coexistence schemes, number 10, 11, 12 and 13 in Table 5.4).

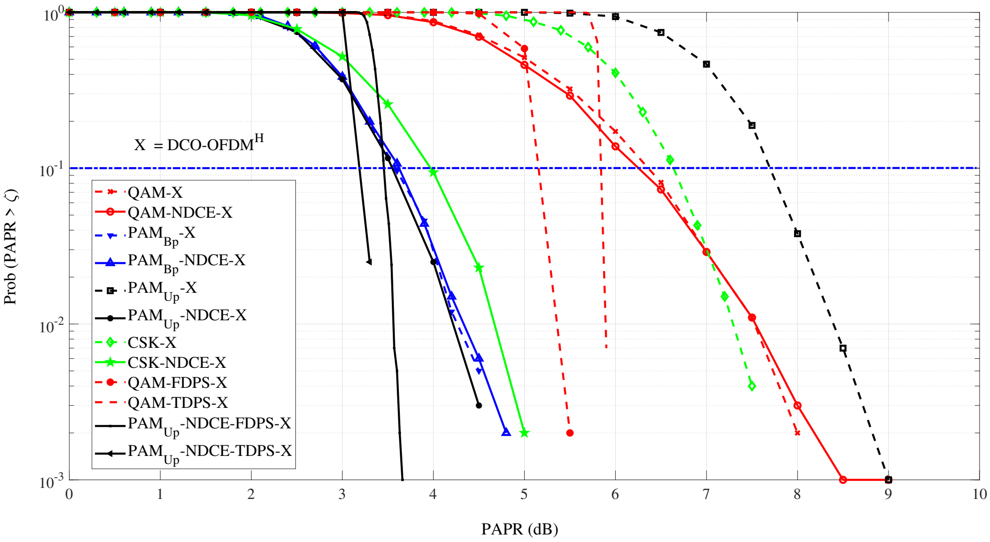

Figure 5.14: CCDF distribution of PAPR for various DCO-OFDM$^{\mathrm{H}}$ coexistence schemes.

In **Fig. 5.15**, the CCDF of PAPR of various P-DCO-OFDM$^{\mathrm{H}}$ schemes are shown. It can be observed that PAPR reduces drastically with precoding because it results in a quasi single-carrier like behavior without imposing a significant complexity overhead as demonstrated in Table 5.5. The proposed *PAM$_{\mathrm{Up}}$-MDS-DCO-OFDM$^{\mathrm{H}}$ coexistence scheme achieves lowest PAPR of 1.35 dB at Prob (PAPR $>\zeta$) = 0.1. Analytical PAPR (dashed purple plot in Fig. 5.15)

Table 5.3: Definition of acronyms used for different variants of the proposed and conventional DCO-OFDM$^{\mathrm{H}}$ coexistence schemes.

No.	**Schemes Acronym**	**Definition**
1.	**QAM-DCO-OFDM$^{\mathrm{H}}$**	Quadrature amplitude modulation (QAM) of subcarriers in DC bias optical-OFDM based on DHT
DCO-OFDM$^{\mathrm{H}}$ = X		
2.	**QAM-NDCE-X**	QAM of subcarriers with null DC element (NDCE) of the transmitted O-OFDM signal in X
3.	**PAM$_{\mathrm{Bp}}$-X**	Bipolar constellation symbols used for pulse amplitude modulation (PAM) of subcarriers in X
4.	**PAM$_{\mathrm{Bp}}$-NDCE-X**	Bipolar constellation symbols used for PAM of subcarriers with null DC element in X
5.	**PAM$_{\mathrm{Up}}$-X**	Unipolar constellation symbols used for PAM of subcarriers in X
6.	**PAM$_{\mathrm{Up}}$-NDCE-X**	Unipolar constellation symbols used for PAM (PAM$_{\mathrm{Up}}$) of subcarriers with null DC element in X
7.	**CSK-Fig. 1 [157]-X**	Color shift keying (CSK) modulation of subcarriers in X with three separate FHT blocks corresponding to red, green and blue LEDs data
8.	**CSK-Fig.5.4-X**	Color shift keying modulation of subcarriers in X with one FHT block corresponding to red, green and blue LEDs data
9.	**CSK-Fig.5.4-NDCE-X**	CSK modulation of subcarriers in X with one FHT block corresponding to red, green and blue LEDs data with null DC element of the transmitted O-OFDM signal
10.	**QAM-FDPS-X**	QAM of subcarriers with frequency domain pulse shaping (FDPS) of the transmitted O-OFDM signal in X
11.	**QAM-TDPS-X**	QAM of subcarriers with time domain pulse shaping (TDPS) of the transmitted O-OFDM signal in X
12.	**PAM$_{\mathrm{Up}}$-NDCE-FDPS-X**	PAM$_{\mathrm{Up}}$ of subcarriers with frequency domain pulse shaping (FDPS) of the transmitted O-OFDM signal in X
13.	**PAM$_{\mathrm{Up}}$-NDCE-TDPS-X**	PAM$_{\mathrm{Up}}$ of subcarriers with time domain pulse shaping (TDPS) of the transmitted O-OFDM signal in X
14.	**QAM-P-DCO-OFDM$^{\mathrm{H}}$**	QAM with DHT precoded DC bias optical-OFDM based on DHT
P-DCO-OFDM$^{\mathrm{H}}$ = X$^{\mathrm{P}}$, $^{+}$ = maximum DC bias, * = no DC bias		
15.	**$^{+}$QAM-X$^{\mathrm{P}}$**	QAM with DHT precoded maximum DC bias optical-OFDM based on DHT
16.	***PAM$_{\mathrm{Up}}$-X$^{\mathrm{P}}$**	Unipolar constellation symbols used for PAM with no DC bias in optical-OFDM signals in X$^{\mathrm{P}}$
17.	***PAM$_{\mathrm{Up}}$-MDS-X$^{\mathrm{P}}$**	Unipolar constellation symbols used for PAM with modified data sequence and no DC bias in optical-OFDM signals in X$^{\mathrm{P}}$
18.	**$^{+}$QAM-FDPS-X$^{\mathrm{P}}$**	QAM with DHT precoded and frequency domain pulse shaping data with maximum DC bias in X$^{\mathrm{P}}$
19.	***PAM$_{\mathrm{Up}}$-FDPS-X$^{\mathrm{P}}$**	PAM$_{\mathrm{Up}}$ with DHT precoded and frequency domain pulse shaping (FDPS) data with no DC bias in X$^{\mathrm{P}}$
20.	**QAM-TDPS-X$^{\mathrm{P}}$**	QAM with DHT precoded and time domain pulse shaping (TDPS) data in X$^{\mathrm{P}}$
21.	**$^{+}$QAM-TDPS-X$^{\mathrm{P}}$**	QAM with DHT precoded and time domain pulse shaping (TDPS) data with maximum DC bias in X$^{\mathrm{P}}$
22.	**PAM$_{\mathrm{Up}}$-TDPS-X$^{\mathrm{P}}$**	PAM$_{\mathrm{Up}}$ with DHT precoded and TDPS of input data in X$^{\mathrm{P}}$
23.	**$^{+}$PAM$_{\mathrm{Up}}$-TDPS-X$^{\mathrm{P}}$**	PAM$_{\mathrm{Up}}$ with DHT precoded and time domain pulse shaping (TDPS) data with maximum DC bias in X$^{\mathrm{P}}$

Note: The proposed coexistence schemes have been highlighted with cyan color.

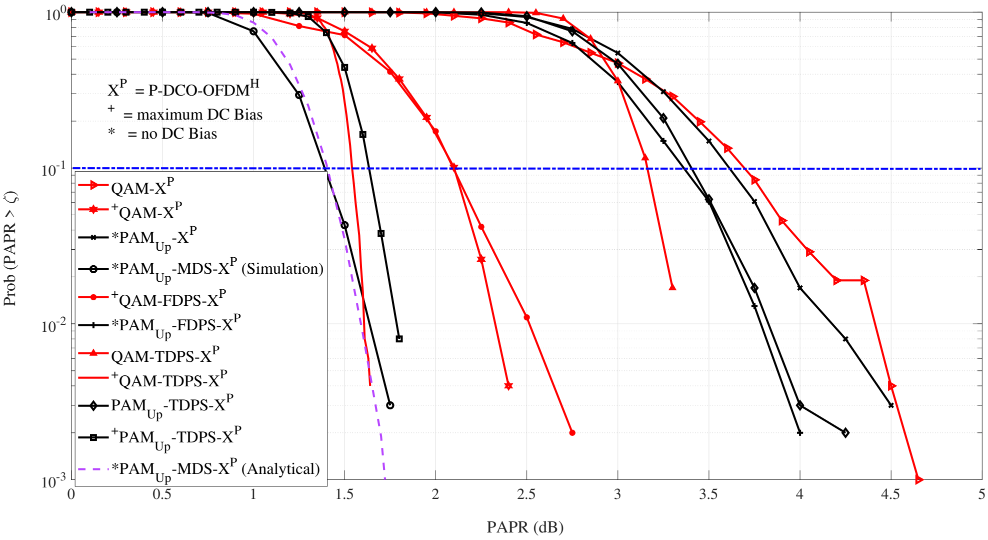

Figure 5.15: CCDF distribution of PAPR for various precoded DCO-OFDM^H coexistence schemes.

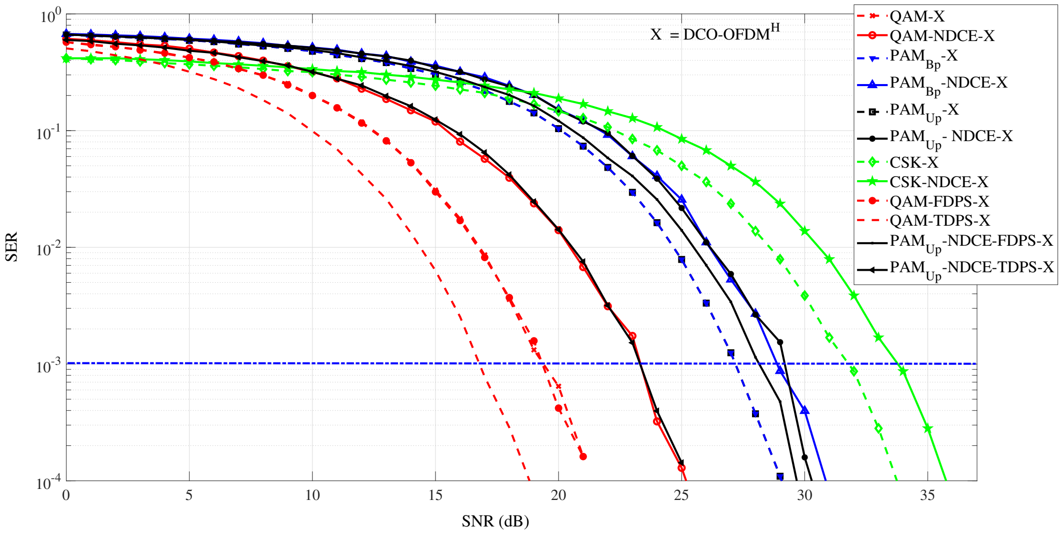

Figure 5.16: SNR versus SER performance of various DCO-OFDM^H coexistence schemes.

is presented to corroborate the simulated plot. Further, CSK modulation technique have not been analyzed for precoding variants due to higher PAPR and system complexity (coexistence schemes, number 7 and 8 in Table 5.4).

In **Fig. 5.16**, the SNR versus SER plot of various DCO-OFDM$^{\mathrm{H}}$ schemes are shown. The SNR required at 10^{-3} SER increases approximately by 2 dB and 3 dB, in PAM$_{\mathrm{Up}}$/PAM$_{\mathrm{Bp}}$/CSK-NDCE-DCO-OFDM$^{\mathrm{H}}$ and QAM-NDCE-DCO-OFDM$^{\mathrm{H}}$ scheme, respectively from their respective standard DCO-OFDM$^{\mathrm{H}}$ schemes. It is due to the approximation of DC elements at the receiver from the noise affected received signal. The performance of QAM-NDCE-DCO-OFDM$^{\mathrm{H}}$ degrades more (approximately 1 dB) as compared to PAM$_{\mathrm{Up}}$/PAM$_{\mathrm{Bp}}$-NDCE-DCO-OFDM$^{\mathrm{H}}$ from their respective standard DCO-OFDM$^{\mathrm{H}}$ schemes due to the complex data sequence. TDPS version of schemes reduces the error rate at particular SNR by shaping the DCO-OFDM$^{\mathrm{H}}$ symbols for less inter subcarrier interference (ISI). N RUs constrain the length of FDPS data, hence it performs close to the conventional PAM/QAM DCO-OFDM$^{\mathrm{H}}$ schemes.

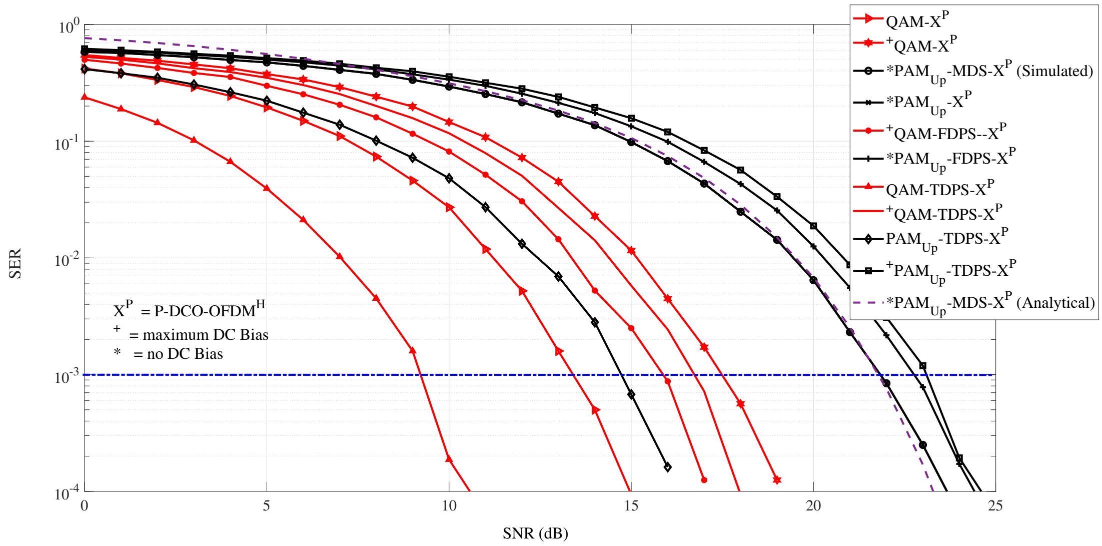

Figure 5.17: SNR versus SER performance of various precoding DCO-OFDM$^{\mathrm{H}}$ coexistence schemes.

In **Fig. 5.17**, the SNR versus SER plot of various P-DCO-OFDM$^{\mathrm{H}}$ schemes are shown. It is observed that the PAM$_{\mathrm{Up}}$/PAM$_{\mathrm{Bp}}$/QAM with P-DCO-OFDM$^{\mathrm{H}}$ schemes require less SNR to maintain FEC limit SER (i.e., 10^{-3}) from their respective standard DCO-OFDM$^{\mathrm{H}}$ schemes shown in Fig. 5.16. The reduction in error rate is because of the FHT precoding and subsequent subcarrier mapping, which increases the Euclidean distance between P-DCO-OFDM$^{\mathrm{H}}$ elements compared to conventional DCO-OFDM$^{\mathrm{H}}$, where the data sequence is spread to all the available subcarriers. The maximum DC bias variants ($^{+}$) of P-DCO-OFDM$^{\mathrm{H}}$ increases the error rate due to increased variance of noise (signal dependent/shot noise [53, 69, 156]) which decreases the gap between the elements of O-OFDM symbol, thus requires larger SNR at 10^{-3} SER. In contrast, QAM-TDPS-P-DCO-OFDM$^{\mathrm{H}}$ requires least SNR at 10^{-3} SER, howbeit with highest complexity. Hence, when TDPS and maximum DC bias are used together in $^{+}$QAM-TDPS-P-DCO-OFDM$^{\mathrm{H}}$, it requires 1 dB less SNR than $^{+}$QAM-P-DCO-OFDM$^{\mathrm{H}}$. Whereas, $^{+}$PAM$_{\mathrm{Up}}$-TDPS-P-DCO-OFDM$^{\mathrm{H}}$ requires 1dB more SNR than *PAM$_{\mathrm{Up}}$-P-DCO-OFDM$^{\mathrm{H}}$ to achieve 10^{-3} SER. The overall effect of maximum DC bias with TDPS in $^{+}$PAM$_{\mathrm{Up}}$-TDPS-P-DCO-OFDM$^{\mathrm{H}}$ reduces the gap between O-OFDM elements of PAM$_{\mathrm{Up}}$-P-DCO-OFDM$^{\mathrm{H}}$ as compared to *PAM$_{\mathrm{Up}}$-P-DCO-OFDM$^{\mathrm{H}}$. The FDPS QAM/PAM variants provide lesser SNR gain with respect to their QAM/PAM variants with P-DCO-OFDM$^{\mathrm{H}}$ schemes. Analytical SER of *PAM$_{\mathrm{Up}}$-MDS-P-DCO-OFDM$^{\mathrm{H}}$ obtained from (5.16), (5.17) has been plotted (dashed purple plot in Fig. 5.17) to corroborate the simulated results.

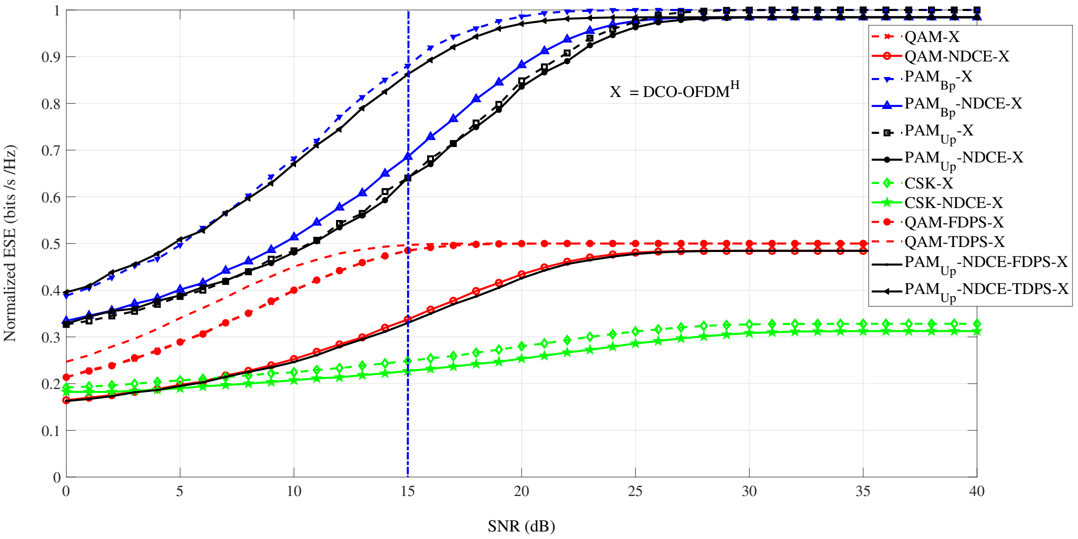

Figure 5.18: SNR versus ESE performance of various DCO-OFDM$^{\mathrm{H}}$ coexistence schemes.

In **Figs. 5.18 and 5.19**, the PAM based schemes achieve the highest normalized ESE of 1 bps/Hz at higher SNRs with FDPS and TDPS in P-DCO-OFDM$^{\mathrm{H}}$. In these cases, the data subcarriers are equal to N as the interleaved subcarriers can also be utilized for data transmission without increasing the PAPR and SNR. Whereas, *PAM$_{\mathrm{Up}}$-P-DCO-OFDM$^{\mathrm{H}}$ and *PAM$_{\mathrm{Up}}$-P-MDS-DCO-OFDM$^{\mathrm{H}}$ saturate at 0.5 bps/Hz normalized ESE (as shown in Fig. 5.19) because only $N/2$ RUs gets utilized for information symbols. All variants of QAM in Figs. 5.18 and 5.19 can achieve maximum of 0.5 bps/Hz only due to the constraint of complex to real conversion. However, due to its lower error rate, the normalized ESE reaches its maximum around 15 dB at a fast pace except for QAM-NDCE-DCO-OFDM$^{\mathrm{H}}$ and *QAM-FDPS-P-DCO-OFDM$^{\mathrm{H}}$ because of higher SNR requirement (as shown in Figs. 5.16 and 5.17). The poor normalized ESE of CSK (in Fig. 5.16) can be attributed to its highest error rate and system

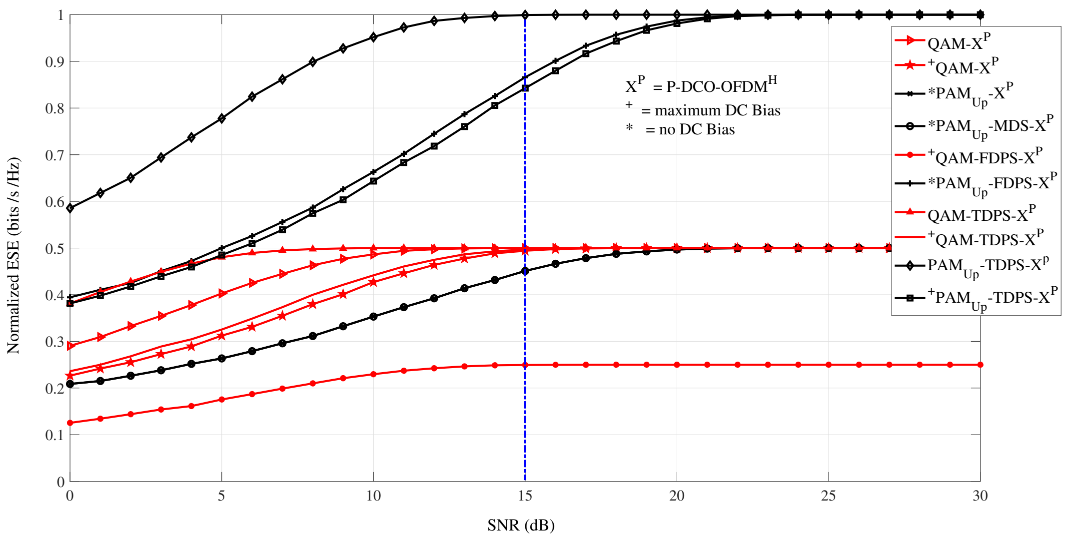

Figure 5.19: SNR versus ESE performance of various precoded DCO-OFDM$^{\text{H}}$ coexistence schemes.

architecture, where three RGB LEDs data at a time corresponds to a single symbol only, which reduces effective data to $1/3$ of data subcarriers. With pulse shaping, the data can be sent to a maximum number of subcarriers with less error rate, as seen in Figs. 5.16 and 5.17 and provide comparatively less PAPR in $^{+}$PAM$_{\text{Up}}$-TDPS-P-DCO-OFDM$^{\text{H}}$. However, the main drawback of the FDPS/TDPS technique is its huge system complexity that does not reduce much even with low complex pulse shaping techniques [165].

Table 5.4 and Table 5.5 present a comprehensive overview of the various DCO-OFDM$^{\text{H}}$ schemes. For the DL coexistence scheme, the first priority is to have the least complexity at the U_L and D_I, especially D_I. ***PAM$_{\text{Up}}$-MDS-P-DCO-OFDM$^{\text{H}}$** coexistence scheme has the least computational complexity of $O(1)$ and $O(Q)$, for U_L and D_I, respectively, as compared to rest of the considered coexistence schemes and is because of utilizing the sub-carrier mapping technique (interleaved or localized). The TD signal of *PAM$_{\text{Up}}$-MDS-P-DCO-OFDM$^{\text{H}}$ behaves as time-division kind of scheme within an O-OFDM symbol, which can be detected at the receiver directly by using subcarrier mapping factor I. Further, *PAM$_{\text{Up}}$-MDS-P-DCO-OFDM$^{\text{H}}$ (in Table 5.5) has five green columns ("Very Good" ***** performance rating) of performance metrics as compared to rest of the schemes. The three green columns correspond to PAPR, the system complexity of LiFi user and IoT device, which are the most preferred metrics for choosing a LiFi-IoT DL coexistence scheme. In *PAM$_{\text{Up}}$-MDS-P-DCO-OFDM$^{\text{H}}$, PAPR reduces due to the MDS technique (discussed in section 5.2.1.2). The scheme can support 22 IoT devices with an ESE of 0.92 bps/Hz. Additionally, the power saving, energy harvesting and SNR values at FEC limit SER are 5.83 dB, 1.84E-07 J/Ws and 21.9 dB, respectively, which falls under the average performance category. Further, none of its rest performance metrics lies in the poor category. Hence, comprehending the results in Table

Table 5.4: The comprehensive overview of the performance of different variants of proposed and conventional DCO-OFDM$^{\mathrm{H}}$ coexistence schemes for different metrics.

Coexistence Schemes	**Performance Metrics**								
X = DCO-OFDM$^{\mathrm{H}}$	**System Complexity**								
	AP_L	U_L	D_I	**PAPR**	$S\tilde{E}_e$	K_m	$\mathbf{P_{sav}}$	**EH**	γ_o
1. QAM-X	$4N\log_2 N$	$4N\log_2 N + N$	$2N$	6.4	0.49	11	0	2.21E-08	19.5
2. QAM-NDCE-X	$4N\log_2 N$	$4N\log_2 N + (N-1)$	$N+(N-1)$	6.3	0.335	8	0.1	2.21E-08	23.3
3. PAM$_{\mathbf{Bp}}$-X	$2N\log_2 N$	$2N\log_2 N + N$	$2N$	3.6	0.89	21	-1.17	5.51E-08	27.1
4. PAM$_{\mathbf{Bp}}$-NDCE-X	$2N\log_2 N$	$2N\log_2 N + (N-1)$	$N+(N-1)$	3.6	0.69	16	-1.13	5.46E-08	29
5. PAM$_{\mathbf{Up}}$-X	$2N\log_2 N$	$2N\log_2 N + N$	$2N$	7.75	0.65	15	8.72	2.17E-09	27.1
6. PAM$_{\mathbf{Up}}$-NDCE-X	$2N\log_2 N$	$2N\log_2 N + (N-1)$	$N+(N-1)$	3.51	0.65	15	14.48	1.53E-09	29.1
7. CSK*-X	$6N\log_2 N$	$6N\log_2 N + 3N$	$6N$	6.62	0.75	18	2.78	1.11E-08	32
8. CSK-Fig.5.4-X	$2N\log_2 N$	$2N\log_2 N + N$	$2N$	6.62	0.25	6	9.94	2.13E-09	32
9. CSK-Fig.5.4-NDCE-X	$2N\log_2 N$	$2N\log_2 N + (N-1)$	$N+(N-1)$	4	0.225	5	14.17	1.47E-09	34
10. QAM-FDPS-X	$8N\log_2 N + N$	$4N\log_2 N + 2N$	$3N$	5.15	0.49	11	1.26	2.20E-08	19.5
11. QAM-TDPS-X	$4N\log_2 N + N^2$	$4N\log_2 N + N + N^2$	$3N$	5.85	0.5	12	11.73	1.68E-09	16.9
12. PAM$_{\mathbf{Up}}$-NDCE-FDPS-X	$4N\log_2 N + N$	$4N\log_2 N + 2(N-1)$	$N+2(N-1)$	3.45	0.34	8	15.55	1.21E-09	28
13. PAM$_{\mathbf{Up}}$-NDCE-TDPS-X	$2N\log_2 N + N^2$	$2N\log_2 N + (N-1)^2$	$N+2(N-1)$	3.18	0.88	21	20.71	3.94E-10	23.3

Note: CSK* has been considered same as Fig. 1 of [157].
The color marking represents: Very Good *****, Good ****, Average ***, Below Average ** and Poor * performance.
For more details regarding color scheme and star rating for different performance metrics, refer to Table 5.2.

5.4 and Table 5.5, *PAM$_{\mathrm{Up}}$-MDS-P-DCO-OFDM$^{\mathrm{H}}$ is the most suitable choice for greener communication in the DL scenario.

The MA techniques (OFDMA or TDMA) governs the overall system performance. OFDMA is better than TDMA as it provides a considerable advantage in terms of delay and throughput as the number of devices increases (as shown in Fig. 5.13). Therefore, the DL coexistence scheme considering WDM with RGB LED utilizes the O-OFDM technique for each red, green, and blue LED data and thus can use O-OFDMA to support more LiFi users and IoT devices.

Table 5.5: The comprehensive overview of the performance of different variants of proposed precoded DCO-OFDM$^{\mathrm{H}}$ coexistence schemes for different metrics.

Coexistence Schemes	**Performance Metrics**								
	System Complexity								
X$^{\mathrm{P}}$= P-DCO-OFDM$^{\mathrm{H}}$ $^{+}$ **= maximum DC bias** *** = no DC bias**	AP_L	U_L	D_I	**PAPR**	$\tilde{SE}_e$	K_m	**P$_{\mathrm{sav}}$**	**EH**	γ_o
14. QAM-X$^{\mathrm{P}}$	$4Q\log_2 Q$ $+4N\log_2 N$	N	2	3.67	0.5	24	-1.06	5.28E-08	13.3
15. $^{+}$QAM-X$^{\mathrm{P}}$	$4Q\log_2 Q$ $+4N\log_2 N$	N	2	2.1	0.5	24	2.52	3.32E-08	17.4
16. *PAM$_{\mathrm{Up}}$-X$^{\mathrm{P}}$	$2Q\log_2 Q$ $+2N\log_2 N$	Q	1	3.57	0.46	22	6.15	1.32E-07	21.9
17. *PAM$_{\mathrm{Up}}$-MDS-X$^{\mathrm{P}}$	$2Q\log_2 Q$ $+2N\log_2 N$	Q	1	1.35	0.46	22	5.83	1.84E-07	21.9
18. $^{+}$QAM-FDPS-X$^{\mathrm{P}}$	$4Q\log_2 N+$ $8N\log_2 N+N$	$8N\log_2 N$ $+$ $2N$	$4N$	2.1	0.25	12	2.71	3.18E-08	16
19. *PAM$_{\mathrm{Up}}$-FDPS-X$^{\mathrm{P}}$	$2Q\log_2 N+$ $4N\log_2 N+N$	$4N\log_2 N$ $+$ $Q+N$	$4N$	3.35	0.86	20	7.49	7.93E-09	22.8
20. QAM-TDPS-X$^{\mathrm{P}}$	$4Q\log_2 Q+$ $4N\log_2 N+N^2$	$N+N^2$	N^2	3.15	0.5	24	2.98	2.35E-08	9.1
21.$^{+}$**QAM-TDPS-X$^{\mathrm{P}}$**	$4Q\log_2 Q+$ $4N\log_2 N+N^2$	$N+N^2$	N^2	1.54	0.5	24	3.91	2.75E-08	16.7
22. PAM$_{\mathrm{Up}}$-TDPS-X$^{\mathrm{P}}$	$2Q\log_2 Q+$ $2N\log_2 N+N^2$	$N+N^2$	N^2	3.37	1	24	13.43	2.01E-09	14.7
23.$^{+}$**PAM$_{\mathrm{Up}}$-TDPS-X$^{\mathrm{P}}$**	$2Q\log_2 Q+$ $2N\log_2 N+N^2$	$N+N^2$	N^2	1.63	0.85	20	6.69	1.42E-08	23

The color marking represents: Very Good *****, Good ****, Average ***, Below Average ** and Poor * performance.
For more details regarding color scheme and star rating for different performance metrics, refer to Table 5.2.

For UL coexistence scheme, time synchronizing all the users and devices within an O-OFDM symbol for *PAM$_{\mathrm{Up}}$-MDS-P-DCO-OFDM$^{\mathrm{H}}$ scheme requires communication among the users and devices. It increases the complexity of the $\mathbb{U}_L$ and $\mathbb{D}_I$ transmitters. As stated above, OFDMA has an advantage over TDMA. Further, the modulation technique for IoT devices should have low complexity, low PAPR and should be able to support O-OFDMA with

LiFi users. $\mathrm{PAM_{Up}}$ is a suitable option as it does not exacerbate the nonlinear distortions from the LED due to inherent low PAPR. Since IoT device as a transmitter operates on a single subcarrier, the PAPR is low for $\mathrm{PAM_{Up}}$. The computational complexity for LiFi users and IoT devices for UL (as per Fig. 5.8), becomes $N\log_2 N/2$ and N, removing the equalization complexity which is not required at the transmitter. The receiver AP decodes all the signals from all the users utilizing FHT-NDCE-OFDM block. Therefore, $\mathrm{PAM_{Up}}$-NDCE-DCO-OFDM$^\mathrm{H}$ scheme becomes the most suitable green communication solution for $\mathbb{U}_L$ and $\mathbb{D}_I$ as a transmitter due to its low system complexity, low PAPR (which reduces with the number of RUs < N), high power-saving and suitability to O-OFDMA. Further with this UL scheme, K_m=15 can be supported for an ESE of 0.92 bps/Hz. EH has not been considered in UL in this work. However, IR LED's operated specific photovoltaic cells can be utilized for EH at the AP_L. Further, apart from the proposed green communication coexistence schemes, Table 5.4 and 5.5, provide a comprehensive overview and analysis of the twenty-three coexistence schemes. It can be referred to choose a suitable coexistence scheme as per the demand and requirement of the LiFi-IoT coexistence application.

5.6 Summary

For the first time, this work explores the coexistence of LiFi users and LC enabled IoT devices under a common LiFi AP for green DL and UL communication. The proposed coexistence schemes one for DL and another for UL communication utilize the amalgamation of WDM, OFDMA, DCO-OFDM$^\mathrm{H}$, NDCE, DHT precoding, interleaved subcarrier mapping and MDS to enable concurrent interference-free, low complex and reliable communication. The proposed and conventional DCO-OFDM$^\mathrm{H}$ based coexistence schemes have been extensively analyzed with respect to seven performance metrics as iterated in order of preference, viz. system complexity, PAPR, ESE, the maximum number of IoT devices (K_m), power saving with respect to QAM-DCO-OFDM$^\mathrm{H}$, EH, and SNR. The results imply that *$\mathrm{PAM_{Up}}$-MDS-P-DCO-OFDM$^\mathrm{H}$ offers the least computational complexity (against other schemes examined in this work) of $O(1)$ and $O(Q)$ at the LC enabled IoT and LiFi user's terminal, respectively. Therefore *$\mathrm{PAM_{Up}}$-MDS-P-DCO-OFDM$^\mathrm{H}$ is most appropriate for DL scenarios with massive IoT devices and few LiFi users. The derived analytical results and the simulated results agree fairly well. The theoretical CCDF of PAPR at Prob (PAPR $> \zeta$)= 0.1 validates the improvements (i.e. 1.35 dB PAPR) attained by the $\mathrm{PAM_{Up}}$-MDS-P-DCO-OFDM$^\mathrm{H}$ scheme. In terms of throughput for a fixed delay, the O-OFDMA system clearly outperforms O-OFDM-TDMA. Therefore, $\mathrm{PAM_{Up}}$-NDCE-DCO-OFDM$^\mathrm{H}$ is a superior option among the twenty-three coexistence schemes examined for the uplink case using O-OFDMA. It is noteworthy that as per different demands and requirements, the choice of LiFi-IoT coexistence scheme can be reviewed from the comprehensive analysis of the twenty-three different schemes (as shown in Table 5.4 and 5.5).

Chapter 6

3-D Deployment of VLC-UAV Networks with Energy and User Mobility Awareness

The recent proliferation of LEDs in unmanned aerial vehicles (UAVs) for inspection, first response, environmental protection monitoring, surveillance and urban safety especially at night time, have paved the way for VLC enabled UAVs. Consequently, the use of visible light for communication and illumination in UAVs for day and night scenario has been investigated in this chapter due to numerous research gaps in earlier related research works (refer Section 1.4.3 and 1.5). This chapter is also motivated by the goal of supporting green communication in resource-constrained UAVs. The rest of the chapter is organized as follows:

Section 6.1 outlines the contributions of this work in detail. Section 6.2 presents the VLC enabled UAV network model and QoS metrics. Section 6.3 formulates the 3-D deployment problem and describes the solution. Section 6.4 analyzes and discusses the results obtained. Finally, Section 6.5 summarizes the work.

6.1 Contributions

The 3-D deployment of $\mathrm{UB_v}$ in an outdoor scenario provides flexibility to vary altitude (L) of $\mathrm{UB_v}$ for enhancing the coverage radius (r). Therefore, the proposed work thoroughly investigates the relationship between L and r which has not been extensively studied in literature for a $\mathrm{UB_v}$ network. This work [98] is first of its kind to derive and provide the theoretical expressions of enhanced coverage radius as a function of L for the two QoS metrics to ultimately obtain optimal altitude and its respective maximum coverage radius analytically. Initially, the impact of illuminance and SNR threshold is discussed on the the maximum coverage radius of $\mathrm{UB_v}$ and based on that, optimal altitude is determined. For both day and night scenarios, the coverage radius has been increased with the inclusion of holographic light shaping diffuser

(LSD) [100, 101, 183] as LED front end. Holographic LSD has been utilized with the motive of adopting an energy-aware and greener aspect of communication. The optimum angle of the LSD has been obtained based on the LED optical transmit power to achieve maximum coverage radius and its optimum altitude for the desired QoS metrics. Further, a novel RGB LED solution based on light sensitivity to human eye have been proposed specific to night scenario which increases the coverage radius by increasing the illuminance, thereby supporting green communication. Additionally, the analytical solution has been provided to obtain the maximum coverage radius and its optimal altitude with the proposed enhancement techniques. Subsequently, we would like to emphasize on the novel optimization problem being solved in this work [98]: a joint optimization of the UB_v 2-D positioning and the update interval has been proposed to maximize the number of covered users with VLC specific QoS constraints (i.e., illumination and reliable communication) at an update instant by ensuring user fairness and flight time constraint. This work presents two energy-aware algorithms (i.e., farthest user based strategy (FU) and shifting UAV based strategy (SU)) to achieve performance close to the exhaustive one whilst reducing the complexity.

The key contributions of the proposed work can be summarized as follows:

1. In this work, the altitude deployment of UB_v have been optimized for maximum coverage of ground mobile users while fulfilling illumination and reliable communication requirements.

2. The maximum coverage radius has been enhanced with energy-aware techniques: novel RGB LED based solution and holographic LSD. The analytical solution for optimum coverage radius with the proposed techniques has been derived.

3. A joint optimization of the UB_v 2-D positioning and the update interval has been proposed to maximize the number of covered users with VLC specific QoS constraints at an update instant by ensuring the user fairness as well as UB_v flight time constraint.

4. This work proposes two energy-aware solutions based on farthest user and shifting strategy for the above mentioned joint optimization problem. The proposed methods have been compared with the standard exhaustive search based strategy.

6.2 VLC enabled UAV network model

In literature, mainly two types of UAVs have been considered, i.e., multirotor (or rotary UAVs) and fixed-wing UAVs. Rotary UAVs have greater manoeuvrability, compact design, and are easy to control and fly in any direction, whereas fixed-wing UAVs are less manoeuvrable, cannot hover, but can provide increased range and payload capacity [184, 185]. Therefore, rotary UAVs become more suitable for communication and illumination purposes because of their greater manoeuvrability and ability to hover in a stationary position. Further, the reduced range of rotary UAVs is not an issue as $\mathrm{UB_v}$ are capable of providing service only within a small area (in hundreds of meters). However, it is crucial to reduce the energy consumption in rotary UAVs due to their limited energy. Therefore, energy-efficient schemes are required for the 3-D deployment of rotary UAVs.

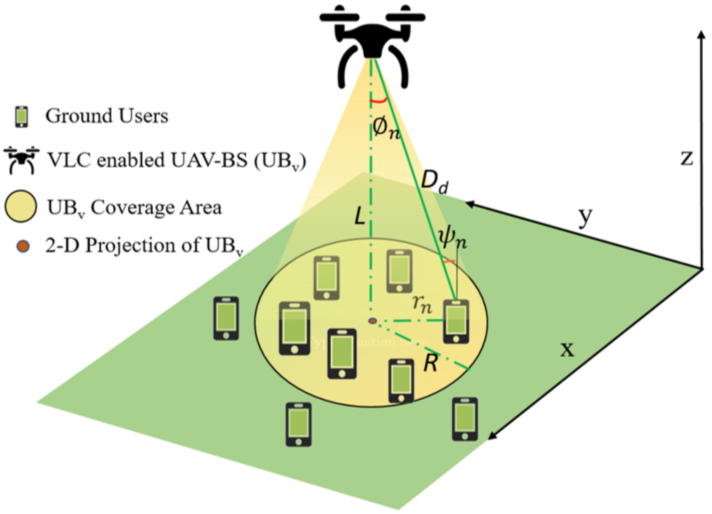

Figure 6.1: VLC enabled UAV Network Model.

We consider a $\mathrm{UB_v}$ network model which serves N mobile ground users as shown in Fig. 6.1. The operating time of $\mathrm{UB_v}$ is considered as 'T' seconds to serve N ground users. The users are moving around following a random walk mobility model. The communication network decides $\mathrm{UB_v}$ altitude (L) and its maximum coverage radius (R) as shown in Fig. 6.1 based on two QoS metrics: desired illuminance and reliable communication. The reliable communication metric is decided based on the SNR at the edge of the coverage area. Therefore, reliable communication and SNR has been used interchangeably in this work [98]. We have considered illuminance (in Lux) and SNR (in dB) at FEC limit BER. Further, $\mathrm{UB_v}$ does not require to serve as an illuminaire for day scenarios assuming daylight is enough for visibility, so only SNR QoS metric has been considered in the day scenario. However, for night scenarios, $\mathrm{UB_v}$ can simultaneously communicate with users and illuminate the users' plane. Hence, both illuminance and SNR have been considered as QoS metrics in determining R and its corresponding optimum altitude $L_o = L$ in Fig. 6.1. Once L_o has been obtained, then we focus on the x-y axes (i.e., 2-D) placement of $\mathrm{UB_v}$ in the horizontal plane. In the following subsections, we introduce the two QoS metrics.

6.2.1 SNR in VLC channel

The received SNR [102, 104] at the ground users' plane can be defined as

$$\mathrm{SNR} = \frac{[\rho H(0)P_t]^2}{N_o B}, \tag{6.1}$$

where, P_t is the transmitted optical power of LED, B is the VLC channel bandwidth, N_o is the noise power spectral density (PSD) of AWGN with zero mean generated at PD. It has been assumed that the impact of ambient light noise can be removed with a high pass filter [10, 30]. $H(0)$ [102, 104] is the channel gain of the dominant LOS component of the VLC channel as shown in (2.9). The $\mathrm{UB_v}$ can serve users indoor and outdoor both. However, we have considered outdoor scenarios without atmospheric turbulence in this work for simplicity. $\mathrm{UB_v}$ serve users at an open area, so there will be less possibility of strong reflections from outdoor buildings and infrastructures, hence only the dominant component i.e., LOS link of the optical channel [30, 31] has been considered.

The Euclidean distance (D_d) between the $\mathrm{UB_v}$ (VLC transmitter) and the ground user (VLC receiver) is equal to $\sqrt{L^2 + r^2}$ as inferred from Fig. 6.1. With zero elevation and orientation of the users, the angle of incidence becomes equal to the angle of irradiance [106]. Hence, the term $\cos(\phi)$ and $\cos(\psi)$ become equal to $\frac{L}{D_d}$. We compute the SNR required to fulfill the QoS metric by utilizing (2.5), (2.9) and (6.1) to plot BER versus the SNR curve. The SNR threshold (SNR_{th}) is the minimum average received SNR required at the LOS user end for reliable communication at FEC limit BER with OOK modulation scheme comes out to be around 13 dB in the VLC channel. Therefore, $SNR_{th} = 13$ dB has been considered for the final maximum coverage radius and optimal altitude (L_o) calculation.

6.2.2 Illuminance

Illuminance is the amount of light falling over a given surface area which correlates with how humans perceive the brightness of an illuminated area [24, 186]. The unit of illuminance is "lux," where one lux is defined as the illuminance at which one-lumen luminous flux is uniformly radiated to 1 m^2 area. The amount of light landing on the users' plane (horizontal surface) is determined by

$$E = \frac{I(0)\cos^m(\phi)}{D_d^2}, \quad -\pi/2 \leq \phi \leq \pi/2 \tag{6.2}$$

where $I(0)$ is the central luminous intensity of an LED. The commercial LED follows the Lambertian radiation pattern. Thus, the radiant intensity $R_I(\phi)$ and luminous intensity $I(\phi)$ both depend on the angle of irradiance [24, 104, 186]. The relation between $I(\phi)$ and $R_I(\phi)$

has to be taken into account to obtain $I(0)$ in terms of $R_I(0)$ (central radiant intensity) and then finally in terms of P_t as expressed in (6.3). The SNR and illuminance of the ground users are obtained for a particular P_t which is then compared to their respective threshold value in order to check if it fulfills the desired QoS.

$$\begin{aligned} R_I(\phi) &= \frac{(m+1)P_t}{2\pi}\cos^m(\phi), \\ R_I(0) &= \frac{(m+1)P_t}{2\pi}. \end{aligned} \tag{6.3}$$

The requirement of $\mathrm{UB_v}$ to serve as a luminaire is important for night scenarios for safety and visibility purposes, since during daytime sunlight is enough for outdoor scenarios. Hence, $I(0)$ has been calculated as per humans' sensitivity to low light conditions.

$$\begin{aligned} I(0) &= (1700)R_I(0)V_\lambda, \\ I(0) &= \frac{(1700)(m+1)P_tV_\lambda}{2\pi}, \end{aligned} \tag{6.4}$$

where, the value 1700 in lumens/watt is based upon the sensitivity of the eye at 507 nm, the peak efficiency of the night (scotopic) vision curve and V_λ is the luminous efficacy of the eye. It is noted that the luminous intensity is the part of the optical intensity which is perceived as light by the human eye. Further, the response of the eye as a function of frequency is known as the luminous efficacy of the eye. The V_λ and its converted value in lumens/watt has been tabulated for both the day scenario (photopic) case and the night scenario (scotopic) case in [187]. Therefore, for the dark-adapted (scotopic) case, V_λ is one at 507 nm. Similarly for photopic case, V_λ is one at 555 nm which is 683 lumens/watt [187]. Therefore, $I(0)$ varies for day and night scenarios and depends on the dominant light frequency. This in turn varies E, and thus E should be calculated specifically for day and night scenarios.

As stated earlier, illumination from $\mathrm{UB_v}$ is usually meant for night safety along with sustainable street lighting. In [188], the recommended levels of illumination required have been tabulated for different road characteristics to maintain visibility for safety purposes as per the World Bank report for Indian streets. Therefore, in our work, we have considered the scenario nearby secondary roads [188], hence E_{th} is fixed to 4 Lux as QoS metric to obtain R and L_o. Nevertheless, the illuminance threshold can not only be specific to Indian road scenarios; it can be decided as per the applications (such as environmental protection monitoring) and its requirements.

6.3 Problem Formulation and Solution

The problem is to optimize the 3-D $\mathrm{UB_v}$ placement and update interval while maintaining the desired threshold of illuminance and SNR. Specifically, we determine the coverage radius of $\mathrm{UB_v}$ and its optimal altitude based on the predefined QoS metrics. Assuming that the minimum illuminance and SNR requirement does not change during $\mathrm{UB_v}$ operational time (T), the optimal altitude can be fixed during T. However, there is a possibility that $\mathrm{UB_v}$ may not cover all the ground users at a particular time instant due to their random mobility and fixed R. Consequently, $\mathrm{UB_v}$ 2-D placement needs to be updated after certain time intervals. It may be noted that the altitude optimization can be decoupled from the 2-D $\mathrm{UB_v}$ placement updates which occur more frequently. Therefore, the optimization of 3-D placements of $\mathrm{UB_v}$ is divided into two problems- where the placement in the z-axis (altitude) is done first and then x-y axes placement is updated from time to time based on the user mobility. Nevertheless, even in the case of non-flat areas, the altitude placement can be updated as per users' elevation with respect to the lowest elevation as a reference. However, the update time for altitude placement would be larger than x-y placement due to users' less frequent displacement in the z-axis. In this work [98], we have assumed that if there is elevation at the user's plane, then after T, the altitude can be updated once. In the following sections, we discuss $\mathrm{UB_v}$ optimal altitude first and then joint optimization of 2-D $\mathrm{UB_v}$ placement and update interval.

6.3.1 Optimal Altitude

The altitude (L) placement of $\mathrm{UB_v}$ should provide the maximum possible coverage radius (R) at the users' plane. The coverage radius (r) can be expressed in terms of L and other parameters known to us from SNR and illuminance equation (as shown in (6.1) and (6.2)). The expressions of coverage radius in terms of L, E_{th} and SNR_{th} are as follows:

$$\begin{aligned} r_{SNR} &= \sqrt{(\Upsilon^{\frac{1}{m+3}} - L^2)}, \\ \Upsilon &= \frac{\left[\rho P_t (m+1) A \cos^m(\phi) T_s(\psi) g(\psi) \cos(\psi) L^{m+1}\right]^2}{4\pi^2 SNR_{th} N_o B}, \end{aligned} \tag{6.5}$$

$$r_E = \sqrt{\left[\left(\frac{(1700) V_\lambda \rho P_t L^m}{\pi E_{th}}\right)^{\frac{2}{m+2}} - L^2\right]}. \tag{6.6}$$

The second-order derivative of r_{SNR} and r_E are obtained to get the optimum values of L, respectively. Thus, the optimized altitude (L_o^{SNR}) obtained from r_{SNR} is used to calculate R for SNR QoS, whereas L_o^E obtained from r_E is used to calculate R for illuminance QoS. The minimum of [$r_{SNR}(L_o^{SNR})$, $r_E(L_o^E)$] (can be rewritten as min [max(r_{SNR}), max(r_E)]) obtained from (6.5) and (6.6), respectively, provides final R which satisfies both illuminance and communication. The R and coverage area thus obtained gets limited due to the QoS constraints. The most common way to increase R is by increasing the altitude of $\mathrm{UB_v}$. However, with increasing height, the VLC channel gain (refer (2.9)) reduces, as it is inversely proportional to the square of the distance between transmitter and receiver (in this case, the distance is the altitude of $\mathrm{UB_v}$ from the ground users). Hence, for reliable communication at the ground users, the transmitted optical power can be increased [88], thereby increasing the received power. However, increasing power is not an energy-aware choice, especially when the focus is on the energy-aware deployment of resource-constrained devices such as UAVs. Further, many recent papers have increased the reliable communication distance between VLC transmitter and receiver to a hundred meters in an outdoor scenario [189–191]. Nevertheless, these techniques will alleviate the issue of reliable communication at high altitudes of $\mathrm{UB_v}$, but with additional energy and hardware cost. In this work, the coverage area of $\mathrm{UB_v}$ has been enhanced with energy-aware techniques complying with the greener aspect of communication.

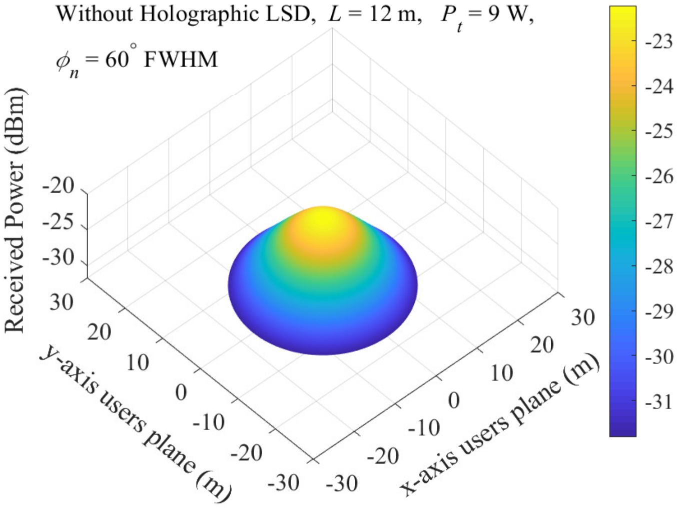

Figure 6.2: Received power distribution in the coverage area without holographic LSD.

6.3.1.1 holographic LSD

Holographic LSDs of different angles are employed to increase the coverage area of an LED with uniform power distribution [101, 183]. In order to ensure larger coverage and optimum link performance, holographic shaping lenses can be used at the transmitter. Using holographic LSD, the effective divergence angle of the transmitter LED can be extended to

$$\phi_e = \sqrt{\phi_n + \phi_d}, \tag{6.7}$$

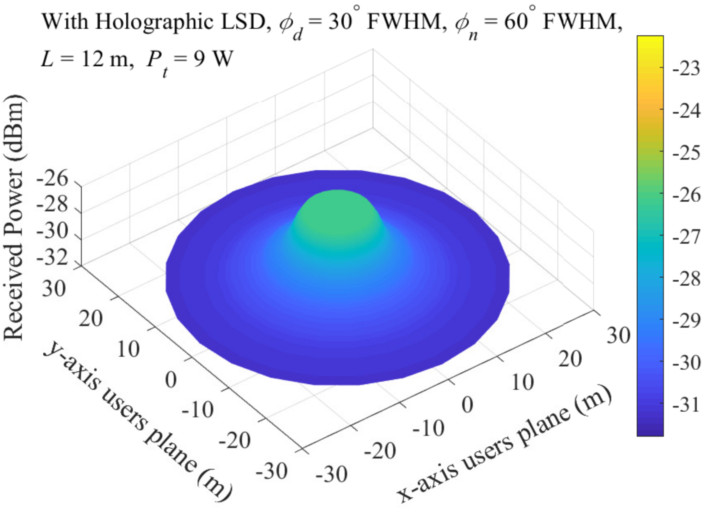

Figure 6.3: Received power distribution in the coverage area with holographic LSD.

where ϕ_e is the effective output angle of the light, ϕ_n is the irradiance angle of the LED in full width half maximum (FWHM), and ϕ_d is the viewing angle of LSD. The calculation of beam intensity through holographic LSD has been simplified in Fig. 4 of [183], where LSD is divided into an array of pixels, and the beam profile for every pixel follows the VLC channel. The light intensity can be considered uniform for a very tiny beam profile after passing through a single pixel. Finally, the effective coverage radius by a transmitter LED at an altitude of L utilizing LSD at its front head can be obtained as follows:

$$r_{LSD} = L\tan(\phi_e). \tag{6.8}$$

The coverage area now depends on the increased coverage radius, r_{LSD}. Further, with the utilization of LSD, the received power distribution at the coverage area becomes more uniformly distributed, which can be observed from Figs. 6.2 and 6.3. The received optical power becomes the average of the sum of individual footprints per pixel.

6.3.1.2 RGB LED

The central luminous intensity of an LED depends on V_λ. At 507 nm, $V_\lambda = 1$ and 1700 lumens/watt is sensed by the human eye [187], which is highest for scotopic case. It is difficult to design the peak wavelength of a yellow phosphorus-based LED at 507 nm or close to 507 nm to get higher illuminance with radiated light as white light. However, RGB LEDs can be designed for certain dominant wavelengths while maintaining white light as discussed in chapter 2. The combined effect of red, green and blue light wavelengths can be utilized to obtain the value of V_λ as close as possible to one, which in turn will increase the illuminance. The central wavelength of RGB LEDs and its coordinates from the CIE 1931 color space

[49] are shown in Table 6.1. The luminous efficacy of red (V_λ^r), green (V_λ^r) and blue (V_λ^r) wavelengths are 0.001497, 0.811 and 0.676, respectively [187]. The optical power of different wavelengths can be adjusted such that it increases the overall luminous efficacy. The overall luminous efficacy of RGB LED can be expressed as:

Table 6.1: The corresponding coordinates of central wavelengths of RGB LEDs in CIE 1931 color space.

LED light color	**Wavelength**	**Coordinates**	
		x	y
Red	640 nm	0.7190	0.2809
Green	530 nm	0.1547	0.8059
Blue	465 nm	0.1355	0.0399

$$\begin{aligned} V_\lambda^{rgb} = (1700)V_\lambda^r P_r + (1700)V_\lambda^g P_g + (1700)V_\lambda^b P_b, \\ P_r + P_g + P_b = 1, \end{aligned} \tag{6.9}$$

where, P_r, P_g and P_b are the normalized optical power of red, green and blue LEDs, respectively. Further, while increasing V_λ^{rgb}, the value of P_r, P_g and P_b should also maintain white tone light. The final x, y chromaticity coordinates of an RGB LED must fall inside the white region of CIE 1931 chromaticity diagram (as shown in Fig. 4.2 and 4.3) so as to emit white colour light. The relation between P_r, P_g, P_b and x, y chromaticity coordinates is shown below:

$$\begin{aligned} x = x_r \cdot P_r + x_g \cdot P_g + x_b \cdot P_b, \\ y = y_r \cdot P_r + y_g \cdot P_g + y_b \cdot P_b, \end{aligned} \tag{6.10}$$

where the coordinates of central wavelength of red LED light is (x_r, y_r), green LED light is (x_g, y_g) and blue LED light is (x_b, y_b) in the CIE chromaticity color space. (6.10) can be re-written using coordinate values from Table 6.1 as:

$$\begin{aligned} x = 0.7190 \cdot P_r + 0.1547 \cdot P_g + 0.1355 \cdot P_b, \\ y = 0.2809 \cdot P_r + 0.8059 \cdot P_g + 0.0399 \cdot P_b. \end{aligned} \tag{6.11}$$

Using (6.9) and (6.11), the possible values of P_r, P_g and P_b are obtained which increases V_λ^{rgb} while satisfying the white tone light constraint. $P_r = 0.15$, $P_g = 0.3$ and $P_b = 0.55$ have been considered in this work. Therefore, while calculating r_E for scotopic case utilizing RGB LED based solution, the V_λ in (6.6) is replaced with V_λ^{rgb} as shown in (6.9).

6.3.2 Analytical Solution for Optimum Coverage Radius

The analytical solution for optimum coverage radius with the proposed RGB LED and holographic LSD utilizes (6.12) and (6.13), which have been derived using (6.5) and (6.6), as fundamental equations for illuminance and SNR QoS metrics, respectively. Therefore, the r_E and r_{SNR} (as shown in (6.6) and (6.5)) must incorporate the effect of holographic LSD and RGB LED concept to analytically obtain the maximum coverage radius which satisfies both illuminance and communication. The modified expressions of coverage radius incorporating the effect of holographic LSD and RGB LED concept are as follows:

$$
\begin{aligned}
r'_{SNR} &= \sqrt{\left(\Upsilon'^{\frac{1}{m'+3}} - L^2\right)}, \\
\Upsilon' &= \frac{\left[\rho P_t \xi_{SNR}(m'+1) A \cos^{m'}(\phi_e) \chi L^{m'+1}\right]^2}{4\pi^2 SNR_{th} N_o B},
\end{aligned}
\tag{6.12}
$$

$$
\chi = T_s(\psi) g(\psi) \cos(\psi),
$$

$$
r'_E = \sqrt{\left[\left(\frac{(1700) V_\lambda^{rgb} \rho P_t \xi_E L^{m'}}{\pi E_{th}}\right)^{\frac{2}{m'+2}} - L^2\right]}, \tag{6.13}
$$

While using holographic LSD, the effective divergence angle of the transmitter LED (ϕ_e) should be considered for calculating Lambertian order. Therefore, instead of conventional Lambertian order (m) in (6.5) and (6.6), modified Lambertian order ($m' = \frac{-\ln(2)}{\ln(\cos(\phi_e))}$) has been used in (6.12) and (6.13). LEDs, with no shaping lenses, behave as a Lambertian source. However, the holographic LSD changes the intensity pattern, which in turn changes the received SNR distribution (as seen in Fig. 6.3). Since we have derived the expressions ((6.12) and (6.13)) based on conventional intensity pattern in (6.5) and (6.6). Therefore, the transmitted power is adjusted with a factor of ξ_{SNR} and ξ_E, in (6.13) and (6.12), respectively, to incorporate the changes in intensity pattern due to holographic LSD. The factor $\xi_{SNR} = \frac{P_r^{LSD}}{P_r}$, where, P_r^{LSD} and P_r are the optical power received at the circumference of coverage area for particular L with and without holographic LSD, respectively. Similarly, the factor $\xi_E = \frac{E_r^{LSD}}{E_r}$, where, E_r^{LSD} and E_r are the illuminance received at the circumference of coverage area for particular L with and without holographic LSD, respectively. Further, the V_λ of LED changes as per the RGB LED concept. Thus, the overall luminous efficacy of RGB LED (V_λ^{rgb}) as obtained from (6.9) is considered in (6.12).

The second-order differentiation of (6.12) and (6.13) is derived to obtain the maximum value of altitude L_o^E and L_o^{SNR}, respectively. The respective altitude values are used in (6.12) and (6.13) to obtain the respective coverage radius. The holographic LSD and RGB LED concept alters the illuminance and SNR. Therefore, the r_{SNR} and r_E (as shown in (6.5) and (6.6)) are modified to include the impact of holographic LSD and RGB LED concept in the calculation of coverage radius in (6.5) and (6.6). However, with the use of holographic LSD, the direct impact is the increased coverage radius (as seen in Figs. 6.2 and 6.3), so when the QoS metrics are satisfied till a certain $\mathrm{UB_v}$ altitude, the r_{LSD} limits the R. Therefore, r_{LSD} calculated from (6.8) for L_o^E and L_o^{SNR}) has been considered in (6.14).

$$\begin{aligned} R = \min \ \Big[\ & r'_E(L_o^E), \ r'_{SNR}(L_o^{SNR}), \\ & r_{LSD}(L_o^E), \ r_{LSD}(L_o^{SNR}) \ \Big], \end{aligned} \tag{6.14}$$

The maximum coverage radius, as seen in (6.14), can be obtained by finding the minimum of different optimized r as per the required QoS metrics. Therefore, a network engineer can directly deduce the maximum coverage radius and its optimum altitude utilizing the proposed novel analytical expressions ((6.12) and (6.13)) at a given QoS metric for the proposed RGB LED and holographic LSD technique.

6.3.3 Joint Optimization of 2-D Placement and Update Interval

Fig. 6.4 illustrates the $\mathrm{UB_v}$ placement update timeline for operational time, T seconds. The time at which $\mathrm{UB_v}$ 2-D positioning is updated, is termed as an update instant. The time difference between two consecutive update instants (k and $k+1$) is denoted as the update interval $t_{up}(k)$. After optimizing the altitude of $\mathrm{UB_v}$ in terms of maximum coverage radius, the proposed work in this chapter optimizes the x-y placement of $\mathrm{UB_v}$ in order to maximize the number of users covered subject to the fairness of coverage. The coordinates of the projection of $\mathrm{UB_v}$ in the 2-D user plane at the k^{th} update instant is denoted as $[U_{\mathrm{x}}(k), U_{\mathrm{y}}(k)]$. We require an indicator variable $G_n(k)$ to represent users coverage, when user n is covered at the update instant k, $G_n(k) = 1$ otherwise $G_n(k) = 0$. It should be noted that during $t_{up}(k)$ update interval the user's coverage indicator varies due to user's mobility between k^{th} and $(k+1)^{th}$ update instants. Hence, the coverage probability of user n at k^{th} update instant for $t_{up}(k)$ (denoted by

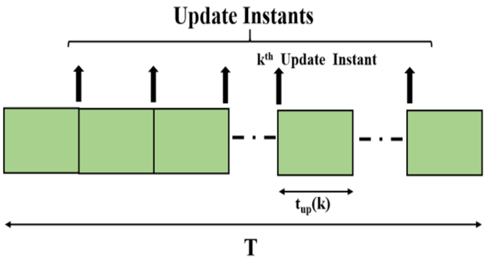

Figure 6.4: $\mathrm{UB_v}$ placement timeline.

$P_{n,t_{up}(k)}$) should be considered to obtain the effective number of users covered in an update interval. Therefore, the average number of effective users covered in l^{th} UB_v operation period is determined by $G_{n,k}$ and $P_{n,t_{up}(k)}$ as follows:

$$\begin{aligned}\bar{U_e} = \underset{l}{\mathbb{E}}\left[\frac{1}{K_l}\sum_{k=1}^{K_l}\sum_{n=1}^{N} G_{n,k}(k)P_{n,t_{up}(k)}\right], \\ = \underset{l}{\mathbb{E}}\left[E_{cov}(l)\right],\end{aligned} \tag{6.15}$$

where $\mathbb{E}[.]$ is the expectation operator and N is the total number of mobile users considered. K_l denotes the number of update instants in l^{th} UB_v operation period. The number of effective users covered in l^{th} UB_v operation period is termed as $E_{cov}(l)$ in (6.15).

Further, maintaining the coverage fairness of mobile users become important, since there may be possibility of same set of users being covered more often than the other users [88]. According to Jain's fairness index [192], the fairness for the overall network at update instant k is defined as follows:

$$fair(k) = \frac{\left(\sum_{n=1}^{N}\sum_{i=0}^{i=k} G_n(i)\right)^2}{N\left(\sum_{n=1}^{N}\left(\sum_{i=0}^{i=k} G_n(i)\right)^2\right)}, \tag{6.16}$$

where i variable denotes the range of update instants.

The fly-hover communication protocol for UAV operation [193] suggest that UAVs serve users for communication only when it is in the hovering mode. Therefore, considering the fly-hover protocol in this work, at every update instants we require the time taken ($F(k)$) by the UB_v to fly to its new 2-D location with velocity v_U, as expressed in (6.17)). The UB_v hovering time is equivalent to its service time. The service time ($\mathscr{S}$) of UB_v out of operation time T can be estimated from $F(k)$ in (6.18).

$$F(k) = \frac{1}{v_U}\sqrt{(U_\text{x}(k)-U_\text{x}(k-1))^2+(U_\text{y}(k)-U_\text{y}(k-1))^2}, \tag{6.17}$$

$$\mathscr{S} = T - \underset{l}{\mathbb{E}}\left[\sum_{k=1}^{K_l} F(k)\right]. \tag{6.18}$$

The optimal UB_v placement problem at k^{th} update instant can be formulated as follows:

$$\begin{aligned} \text{P1:} \quad & \max \sum_{n=1}^{N} G_n(k) \\ \text{s.t.} \quad & \text{C1: } fair(k) > fair_{thres}, \\ & \text{C2: } F(k) < t_{up}(k). \end{aligned} \tag{6.19}$$

Here, the P1 objective function maximizes the total number of users covered at update instant k subject to constraints C1 and C2. C1 puts a lower bound on fairness with a threshold of $fair_{thres} \in [0,1]$ in the network. In contrast, C2 puts an upper bound on $F(k)$ to ensure non-zero service time during the upcoming $t_{up}(k)$ seconds, hence $F(k)$ must be less than $t_{up}(k)$. The optimization problem, in this case, falls under the fair maximum coverage (FMC) type of problem [194]. Let's assume the considered hovering area (just above the user's plane at a certain altitude) as a complete graph and the possible hovering points as vertices. The paths to the hovering points are edges. The optimization problem reduces to Traveling Purchaser Problem (TPP). Further, with relaxed constraints, the optimization problem imitates the classical Traveling Salesman Problem (TSP) [195]. TSP and thus TPP are NP-hard, making the optimization problem (6.19) NP-hard as well [88]. Therefore, the FMC optimization problem of this work becomes difficult to be solved directly using traditional optimization techniques. The first approach to solve FMC problems is to go for an exhaustive search-based strategy (ES) to obtain the best possible performance results, which is considered a benchmark for other optimization methods. One of the state-of-the-art optimization algorithms for FMC is the greedy approximation algorithm [84, 194], where one picks the hovering point of UB$_\mathrm{v}$ that covers the maximum number of users. ES method integrates the greedy approximation method in its algorithm. For a given $t_{up}(k)$, P1 has been solved with the exhaustive search-based strategy [83] as shown in Algorithm 4. ES method depends on the number of hovering points considered. A larger number of hovering points provide higher accuracy but with increased time complexity. Therefore, in order to achieve energy-aware deployment of UB$_\mathrm{v}$, two energy-aware solutions are proposed to solve P1.

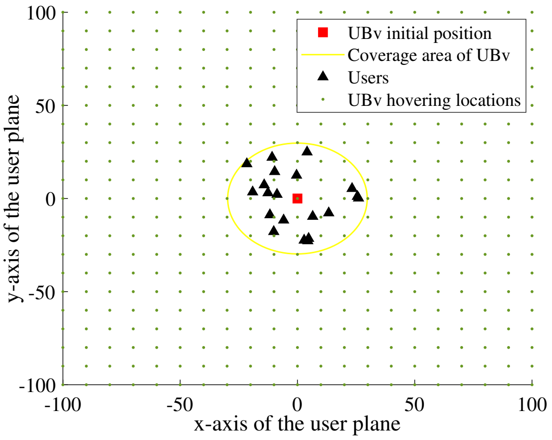

Figure 6.5: ES method illustrating exhaustive-search strategy to determine optimal hovering point.

In Algorithm 4, $U_\mathrm{x}^*(k-1)$ and $U_\mathrm{y}^*(k-1)$ are the optimal coordinates at the $(k-1)^{th}$ update instant. At $k=1$, $t_{up}(1)$ is initialized as t_{min}. For $k>1$, $t_{up}(k)$ is initialized as $t_{up}^*(k-1)$ where,

$t^*_{up}(k-1)$ is the optimal update interval at the $(k-1)^{th}$ update instant. Moreover, we consider that the 2-D hovering space of UB_v is discretized with a resolution of 10 m along the horizontal axis, as shown in Fig. 6.5. In Algorithm 4, Cov_{prev} is a list of $(k-1)$ vectors of length N, where an element in a vector will be '1' if user is covered otherwise '0'. For each of the hovering locations in Hov_{loc} (as represented by dots in Fig. 6.5), function Cov() determines which of the N users may get covered. In case of ES method, Algorithm 4 considers Hov_{loc}. Cov() assigns '1' if a user is covered else '0'. The output of Cov() is stored in Cov_{mat}. Then, the flight time of the UB_v is computed using function Fly(). Further, the fairness value corresponding to each hovering location is computed using Fair() and stored in *Fairness*. Finally, inspired from the greedy approximate approach [84], function Find() outputs $U_\text{x}(k)$, $U_\text{y}(k)$ that maximize the number of users covered while satisfying the constraints C1 and C2. Also, we obtain the values of $G_n(k)\,\forall\, n$.

Algorithm 4 Exhaustive / Farthest user based solution to P1 at k^{th} update instant.

```
Input: $t_{up}(k)$, $U^*_\text{x}(k-1)$, $U^*_\text{y}(k-1)$, $fair_{thres}$
$\mathscr{X}$ - List of x coordinates of $N$ users at $k^{th}$ update instant
$\mathscr{Y}$ - List of y coordinates of $N$ users at $k^{th}$ update instant
$Hov_{loc}$ - List of 2-D $\text{UB}_\text{v}$ Hovering locations
$Hov'_{loc}(k)$ - List of 2-D $\text{UB}_\text{v}$ Hovering locations till the farthest user at $k^{th}$ update instant
$Cov_{prev}$ - List of vectors containing coverage information of all users till $(k-1)^{th}$ update instant
Output: $\mathscr{G}$ - List of $G_n(k)\,\forall\, n$, $U_\text{x}(k)$, $U_\text{y}(k)$
Initialize: $Cov_{mat} = \emptyset$, $Fly_{time} = \emptyset$, $Fairness = \emptyset$
  for $s = 1:1:|Hov_{loc}|/|Hov'_{loc}(k)|$ do
    $Cov_{mat}(:,s)$ = Cov($\mathscr{X}$, $\mathscr{Y}$, $Hov_{loc}/|Hov'_{loc}(k)|$)
    $Fly_{time}(s)$ = Fly (($U^*_\text{x}(k-1)$, $U^*_\text{y}(k-1)$, $Hov_{loc}/|Hov'_{loc}(k)|$)
    $Fairness(s)$ = Fair($Cov_{mat}$,$Cov_{prev}$),
  end for
  [$U_\text{x}(k)$, $U_\text{y}(k)$, $Index1$]=Find($Cov_{mat}$,$Fairness$,$Fly_{time}$,$fair_{thres}$,$t_{up}(k)$),
  $Cov_{prev}(:,k) = Cov_{mat}(:,Index1)$,
  $\mathscr{G} = Cov_{mat}(:,Index1)$
```

The optimization problem can be approached as a combinatorial problem since all the possible hovering points (vertices in a graph) are potential candidates for optimum hovering point. The ES method to solve P1 is a time-consuming and computationally extensive process because it searches all the hovering locations of the user's plane to maximize the total number of users covered. For energy-constrained rotary UAVs, this work [98] aims to propose energy-aware solutions to position UB_v. Space reduction method (SRM) [196] is a state-of-the-art approach where the search space is reduced without losing optimal solution. SRM is particularly applicable to searching graphs with vertices and edges. Therefore, instead of searching all hovering points, the hovering points until the farthest user are searched at an update instant. For farthest user-based (FU) method, all the hovering points under the purple circle as shown in Fig. 6.6 is considered in the search space of k^{th} update instant to obtain optimal UB_v hovering point. It undoubtedly reduces the search space. However, it is interesting to explore how the performance metrics such as $\bar{U}_e$ and $\mathscr{S}$ behave in the UB$_\text{v}$ network with the FU method.

The algorithm to solve P1 by FU method follows the same steps of Algorithm 4 with same notations except Hov_{loc}. The difference between ES and FU method lies in considering the 2-D hovering space of UB$_\text{v}$. In Algorithm 4, Hov_{loc} is replaced by $Hov'_{loc}(k)$ for FU method. At k^{th} update instant, the mean location ($[\bar{\text{x}}(k), \bar{\text{y}}(k)]$) of all the users is calculated. The distance of the farthest user from the mean location is obtained, which forms the radius of the circle with $[\bar{\text{x}}(k), \bar{\text{y}}(k)]$ as the centre x-y points for calculating $Hov'_{loc}(k)$. For example, let's assume that the user's location at k^{th} update instant is as per Fig. 6.6, so all the hovering points from the list of Hov_{loc} falling inside the purple circle represents $Hov'_{loc}(k)$. Finally, P1 is solved for all the K_l update instants in l^{th} UB$_\text{v}$ operation period.

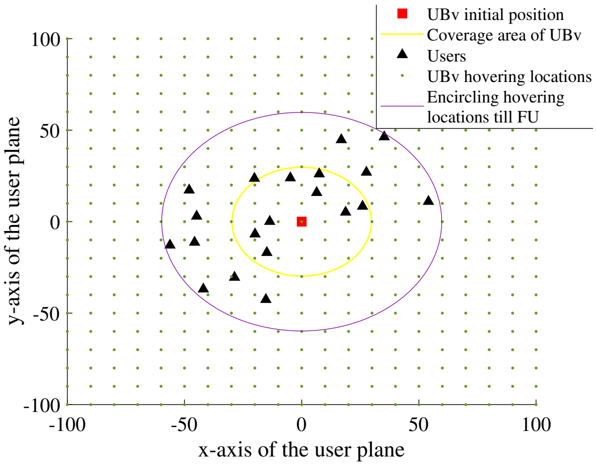

Figure 6.6: FU method illustrating farthest user strategy to determine optimal hovering point.

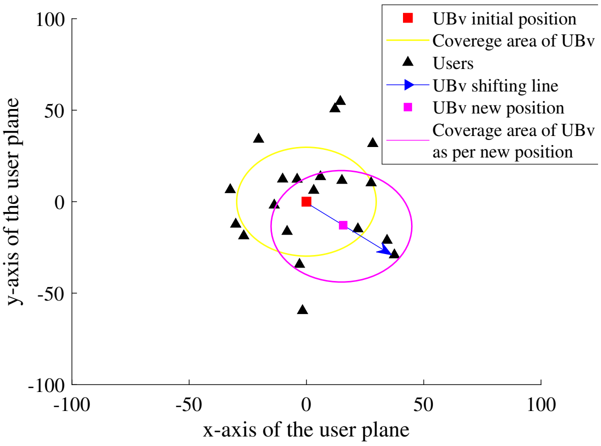

Figure 6.7: SU method illustrating shifting UAV strategy to determine optimal hovering point.

With FU method, it is observed from Algorithm 4 that the range of s reduces ($Hov'_{loc}(k) < Hov_{loc}$). However, the FU method still depends on the list of hovering locations. Therefore, in shifting UAV (SU) strategy, as illustrated in Fig. 6.7, we try to eliminate the dependency on the list of hovering locations by considering the user's location to decide the optimal UB_v placement. SU method is influenced by the random shifting technique [197, 198]. However, in our case we deterministically use the shifting method so as to get the optimum hovering point of UB_v within flight time. At k^{th} update instant, some users are covered by the UB_v for communication, whereas others are not, so let's call them uncovered users (U_{uncov}). As network fairness or covered users decreases beyond a threshold at k^{th} update instant, the UB_v shifts its position as per the previous coverage probability and closeness of U_{uncov} from UB_v's $(k-1)^{th}$ location to cover a maximum number of users while maintaining the constraints C1 and C2.

Algorithm 5 Shifting UAV based solution to P1 at k^{th} update instant.

```
**Input**: $t_{up}(k), U^*_\text{x}(k-1), U^*_\text{y}(k-1), fair_{thres}$
$\mathscr{X}$ - List of x coordinates of $N$ users at $k^{th}$ update instant
$\mathscr{Y}$ - List of y coordinates of $N$ users at $k^{th}$ update instant
$Cov_{prev}$ - List of vectors containing coverage information of all users till $(k-1)^{th}$ update instant
$U_{cov}$ - Number of covered users at $k^{th}$ update instant
**Output**: $\mathscr{G}$ - List of $G_n(k)\,\forall n, U_\text{x}(k), U_\text{y}(k)$

if $Fairness > fair_{thres}$ && $U_{cov} > 0.75N$ then
    $[U_\text{x}(k), U_\text{y}(k)] = [U^*_\text{x}(k-1), U^*_\text{y}(k-1)]$
    $Cov_{prev}(:,k) = Cov_{mat}(:,k)$,
    $\mathscr{G} = Cov_{mat}(:,k)$
else
    $\mathscr{X}'$ - List of x coordinates of uncovered users at $k^{th}$ update instant
    $\mathscr{Y}'$ - List of y coordinates of uncovered users at $k^{th}$ update instant
    $U_{uncov}$ - Number of uncovered users at $k^{th}$ update instant
    Initialize: $Cov_{mat} = \emptyset, Fly_{time} = \emptyset, Fairness = \emptyset$
    for $s = 1 : 1 : |U_{uncov}|$ do
        $S_x(s), S_y(s) = \text{Shift}(\mathscr{X}', \mathscr{Y}', Cov_{prev})$
        $[U'_x(s), U'_y(s)] = [U^*_\text{x}(k-1) + S_x(s), U^*_\text{y}(k-1) + S_y(s)]$
        $Cov_{mat}(:,s) = \text{Cov}(\mathscr{X}, \mathscr{Y}, U_\text{x}(s), U_\text{y}(s))$
        $Fly_{time}(s) = \text{Fly}\ (U^*_\text{x}(k-1), U^*_\text{y}(k-1), U_\text{x}(s), U_\text{y}(s))$
        $Fairness(s) = \text{Fair}(Cov_{mat}, Cov_{prev})$,
    end for
    $[Index1] = \text{Find}(Cov_{mat}, Fairness, Fly_{time}, fair_{thres}, t_{up}(k))$,
    $[U_\text{x}(k), U_\text{y}(k)] = [U'_x(Index1), U'_y(Index1)]$
    $Cov_{prev}(:,k) = Cov_{mat}(:,Index1)$,
    $\mathscr{G} = Cov_{mat}(:,Index1)$
end if
```

In Algorithm 5, U_{cov} and U_{uncov}, denotes the number of covered and uncovered users, at k^{th} update instant, respectively. At k^{th} update instant; if $Fairness$ and U_{cov} are greater than its respective threshold, then the UB_v placement is kept the same as the $(k-1)^{th}$ update instant. However, the UB_v position is shifted whenever the above criteria do not hold for a given update instant. The function Shift() utilizes the list of $\mathscr{X}'$ and $\mathscr{Y}'$ coordinates and Cov_{prev} to calculate new possible positions of $\mathrm{UB_v}$ as per each uncovered users. The possible shifted positions are stored in $U_x'(s)$ and $U_y'(s)$ for all U_{cov} at the $(k-1)^{th}$ update instant. The function Find() outputs the index out of range s, maximizing the number of users covered while satisfying C1 and C2. Finally, the index obtained from Find() is utilized to get optimal $\mathrm{UB_v}$ placement.

After solving P1 with three different algorithms to get $\mathscr{G}$, the next problem is to find the optimal value of $t_{up}(k)$. The choice of $t_{up}(k)$ depends on two factors: 1) temporal user coverage probability and 2) total UAV flight time. For visual clarity, Figs. 6.8 and 6.9 have been shown to depict the behaviour of above mentioned two factors with $t_{up}(k)$. The random distances covered by each mobile user in each transition follows a random walk mobility model and is presumed to be Rayleigh distributed random variable with parameter σ. Interestingly, a network engineer would require higher temporal user coverage probability and lower total UAV flight time, hence there is a trade-off between these two factors. Additionally, as expressed in (6.18), an increase in the $\mathrm{UB_v}$ flight time decreases its service time. Hence, minimization of total $\mathrm{UB_v}$ flight time during T seconds must be considered when optimizing $t_{up}(k)$.

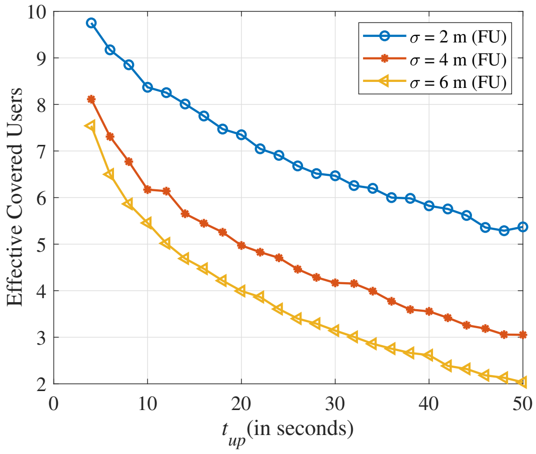

Figure 6.8: Coverage probability of users for varying random walk parameter obtained on solving P1 with FU strategy versus update interval.

6.3.3.1 Temporal Coverage Probability

The coverage probability of a user must capture the change in user locations even over an update interval. Therefore, at the k^{th} update instant, the temporal coverage probability of covered user n is the probability of it being within $\mathrm{UB_v}$ coverage area for the upcoming $t_{up}(k)$ seconds. A user may have multiple transitions during these $t_{up}(k)$ seconds. The number of transitions depends on the random walk parameter, σ and the velocity of the users, v_u. In other words, temporal coverage probability can be defined as the probability, that the displacement

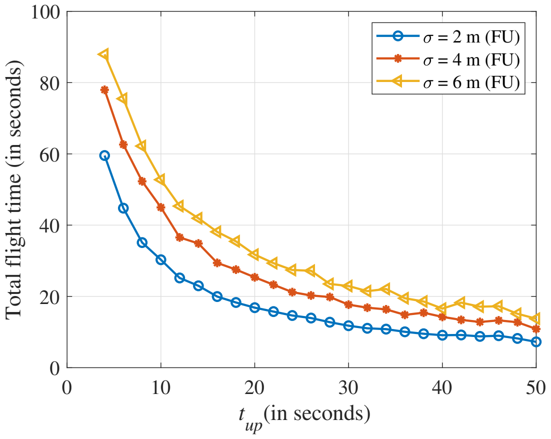

Figure 6.9: Total $\mathrm{UB_v}$ flight time for varying σ obtained on solving P1 with FU strategy versus update interval.

of the user from $\mathrm{UB_v}$ must be less than R for all the transitions within $t_{up}(k)$. The temporal coverage probability metric proposed in [83] helps in establishing a relationship between user mobility and $t_{up}(k)$.

In Fig. 6.8, as $t_{up}(k)$ increases, the effective number of users covered decreases because higher update interval corresponds to few $\mathrm{UB_v}$ placement updates and hence during that interval most of the mobile users come out of the coverage area. Since, the effective number of users covered is directly proportional to coverage probability as seen in (6.15). Therefore, $t_{up}(k)$ must be selected in such a manner that it maximizes the coverage probability. Further, while optimizing $t_{up}(k)$, the coverage probability of all the users covered at k^{th} instant must be considered.

6.3.3.2 Total Flight Time

The average $\mathrm{UB_v}$ flight time during t_{up} will be $\mathbb{E}\left[F_{t_{up}}\right]$ and can be formulated as follows:

$$\mathbb{E}\left[F_{t_{up}}\right] = \frac{\mathbb{E}\left[\sum_{i=1}^{\frac{T}{t_{up}}-1} F(i)\right]}{\left(\frac{T}{t_{up}}\right) - 1}, \tag{6.20}$$

where $\mathbb{E}\left[\sum_{i=1}^{\frac{T}{t_{up}}-1} F(i)\right]$ is the average total $\mathrm{UB_v}$ flight time when updates are done after every t_{up} seconds. First, the term $\sum_{i=1}^{\frac{T}{t_{up}}-1} F(i)$ can be determined in an offline manner by solving P1 for $\left(\frac{T}{t_{up}} - 1\right)$ update instants. Consequently, $\mathbb{E}\left[\sum_{i=1}^{\frac{T}{t_{up}}-1} F(i)\right]$ is the average of the above summation. A typical plot of average total $\mathrm{UB_v}$ flight time has been shown in Fig. 6.9. It can be observed that as t_{up} increases the total $\mathrm{UB_v}$ flight time decreases. This is because lower update interval corresponds to frequent $\mathrm{UB_v}$ placement updates or vice versa. Consequently, the $\mathrm{UB_v}$ flies more frequently resulting in higher total $\mathrm{UB_v}$ flight time.

Since there are two factors impacting the choice of $t_{up}(k)$, the first factor corresponds to the total flight time which is actually a fraction of T during which $\mathrm{UB_v}$ is in flight mode and cannot serve. Let $F_{t_{up}(k)}$ be the $\mathrm{UB_v}$ flight time during $t_{up}(k)$ with an average of $\mathbb{E}\left[F_{t_{up}(k)}\right]$ and $Q = \left\lceil \frac{T-\sum_{j=0}^{k-1} t_{up}(j)}{t_{up}(k)} \right\rceil$ denotes the number of updates that may occur when update interval is fixed as $t_{up}(k)$ until completion of operation time T. Therefore, the first term in the objective function becomes $\frac{\left(\sum_{j=1}^{k-1} F(j)+Q\mathbb{E}\left[F_{t_{up}(k)}\right]\right)}{T}$. The term $\sum_{j=1}^{k-1} F(j)$ remains same for all $t_{up}(k)$, hence the first terms is reduced to $\frac{Q\mathbb{E}\left[F_{t_{up}(k)}\right]}{T}$. The second factor is the sum of the effective covered users. A weight of α and $(1-\alpha)$ has been assigned to the two terms, respectively to propose the minimization of a weighted single objective function. Hence, the optimization problem to obtain optimal $t_{up}(k)$ can be formulated as follows:

$$
\begin{aligned}
\text{P2:} \quad & \min \left(\frac{\alpha Q \mathbb{E}\left[F_{t_{up}(k)}\right]}{T} + \frac{(1-\alpha)}{\sum_{n=1}^{N} G_{n,k} P_{n,t_{up}(k)}} \right) \\
\text{s.t.} \quad & t_{min} \leq t_{up}(k) \leq t_{max},
\end{aligned}
\tag{6.21}
$$

where t_{min} and t_{max} is the lower and upper bound for $t_{up}(k)$. The weight parameter α can be tuned according to the network operator's requirement. For instance, if maximizing the coverage probability is the only requirement, the operator may set α as 0. However, if minimizing $\mathrm{UB_v}$ flight time is the only requirement, α may be set to 1.

Algorithm 6 Solution to P2 at k^{th} update instant.

```
Input: $\mathscr{G}$ - List of $G_n(k)\,\forall n$
$t_{list}$ - List of update interval values,
Output: $t_{up}(k)$
Initialize: $r = 1$

for $t = t_{min} : 2 : t_{max}$ do
    $Factor(r) = \frac{\alpha Q \mathbb{E}[F_t]}{T} + \frac{(1-\alpha)}{\sum_{n=1}^{N} A_{n,k} P_{n,t}}$
    r=r+1
end for
$Index2 = \mathsf{Min}(Factor)$
$t_{out}(k) = t_{list}(Index2)$
```

In Algorithm 6, the update interval range has been discretized with a resolution of two seconds. The objective function in (6.21) is computed for each discretized update interval, and the values obtained are stored in *Factor*. Min() finds the index of the minimum value in *Factor*. Finally, $t_{out}(k)$ is obtained.

The $G_n(k)$ values obtained from P1 are provided to P2. P2 is then solved using Algorithm 6 to obtain the update interval. The output of P2 is then fed back to P1. It goes on iteratively till the update interval value converges. In general, for the convergence of update interval, the condition $|t_{up}(k) - t_{out}(k)| < \varepsilon$ must be met, where $t_{up}(k)$ and $t_{out}(k)$ are the input and output of P1 Algorithm and P2 Algorithm, respectively. ε is the error tolerance value. In this work, $\varepsilon = 0$ has been considered. Further, the update interval converges to $t^*_{up}(k)$ within few iterations. The number of iterations depends on the choice of ε as well as the resolution of the update interval. With an increase in ε, number of iterations required for convergence will decrease. However, with an increase in resolution, the number of iterations required for convergence increases.

6.3.4 Time Complexity Analysis

The UAVs are energy-constrained devices, hence energy-efficient algorithms are preferred for the deployment of UB_v. To demonstrate the energy efficiency of the proposed algorithms (i.e., FU and SU) over the ES algorithm, the energy complexity model of the algorithms [199, 200] should be obtained. In [199], the author proposes an energy complexity measure at circuitry level including energy $\tilde{E}$ and time t in the form of the expression $\tilde{E} \times t^2$ to be used as the measure of the efficiency of a computation. Therefore, on adopting $\tilde{E} \times t^2$ and considering the energy required for any UB_v operation and processing as constant, the $\tilde{E} \times t^2$ term becomes a function of time only. Further, assuming the algorithms to be truly sequential, the most energy-efficient algorithms are also the most time-efficient since, in both cases, the aim is to minimize the number of steps. Thus, the relationship between energy efficiency and time efficiency becomes proportional. Therefore, the time complexity of the algorithm has been obtained in this work in order to indicate its energy efficiency.

The time complexity of a set of steps is considered as $O(1)$ if it does not contain a loop, recursion and call to any other non-constant time function [201]. ES method complexity mainly depends on the number of hovering locations, the number of mobile users, and the number of update intervals. Firstly, the complexity of solving P1 is determined by computing the complexity of Algorithm 4. In Algorithm 4, the complexity mainly depends on the number of times the '**for** loop' is executed, which depends on $|Hov_{loc}|$. Further, for overall complexity, one should consider the complexity of different functions inside the '**for** loop' from steps 8-12. $Cov()$ function in step 9 determines which of the N users is covered for all hovering locations, so the complexity order for step 9 is $O(N \times M_{ES})$, symbolizing $|Hov_{loc}|$ as time-dependent variable M_{ES}. The complexity order of step 10 is $O(M_{ES})$ which evaluate the flight time of UB_v using function $Fly()$. Step 11 evaluates the fairness value of the users corresponding to each hovering location with the complexity order of $O(N \times M_{ES})$. On considering the maximum value of complexity amongst steps 9, 10 and 11, i.e., $O(N \times M_{ES})$ and after execution of '**for** loop', the complexity becomes $O(M_{ES}^2 N)$. Step 13 computes the 2-D position of UB_v

which maximizes the number of covered users using function $Find()$ with complexity order as $O(N \times M_{ES})$. Further, $O(1)$ is the complexity order for steps 14 and 15, so overall complexity for Algorithm 4 is $\max[O(M_{ES}^2 N), O(N \times M_{ES}), O(1), O(1)]$, which in turn results to $O(M_{ES}^2 N)$.

$$K = \frac{(t_{max} - t_{min})}{2} + 1, \tag{6.22}$$

Algorithm 6 is related to problem P2 solution, which depends on the output of P1 to obtain the optimum update interval. Complexity order for this case mainly depends upon the '**for** loop' which is executed for the total number of update intervals. Here t_{min} and t_{max} are the first and the last update instants. If we assume K as variable which represents the total number of update intervals (as shown in (6.22)), then the complexity order for P2 after execution of the '**for** loop' is $O(K)$. Therefore, the overall time complexity of ES method is $O(M_{ES}^2 N)$ + $O(K)$.

In case of FU method, the number of search space for UB$_\text{v}$ is reduced. This is reflected by the term $|Hov_{loc}^{'}|$ in the '**for** loop' in Algorithm 4. Assuming $|Hov_{loc}^{'}|$ as time-dependent variable M_{FU}, the complexity order of Algorithm 4 is $O(M_{FU}^2 N)$. From above discussion, it can be interpreted that $|Hov_{loc}^{'}| < |Hov_{loc}|$. In our case, for the given specific simulation setup parameters (as stated in Table 6.3) the total number of hovering locations (M_{FU}) is reduced by approximately two times i.e $M_{FU} < \frac{M_{ES}}{2}$ and thus the overall complexity order becomes $O(\frac{M_{ES}^2 N}{4})$ + $O(K)$.

The number of times the '**for** loop' is executed in Algorithm 5 depends only on the number of uncovered users. Assuming $|U_{uncov}|$ as a time-dependent variable N_{SU}, which is always a fraction of N. Therefore, in the SU method, as per specific simulation setup parameters, the $|U_{uncov}|$ value is approximated to $0.75 * N$. Further, other steps in Algorithm 5 is of order $O(1)$ or less than and equal to $O(N)$ inside or outside the '**for** loop'. Thus, the overall complexity order becomes $O(N_{SU}N)$ + $O(K)$.

6.4 Results and Discussions

This section presents and analyzes the relation between coverage radius and altitude of UB$_\text{v}$ under different QoS metrics. The impact on the relation between r and L on utilizing RGB LEDs designed for scotopic case with and without holographic LSD have been presented. Further, the results pertaining to the iterative solution for jointly optimizing P1 and P2 have been discussed in detail.

Fig. 6.10 presents UB$_\text{v}$ coverage radius with respect to its altitude at $P_t = 1$ W for different SNR threshold. It is observed that with increasing UB$_\text{v}$ altitude, the coverage radius first increases and then decreases after reaching its peak value. Undoubtedly, with increasing altitude, the coverage of light increases as per (2.9). However, in this case, the aim is to cover

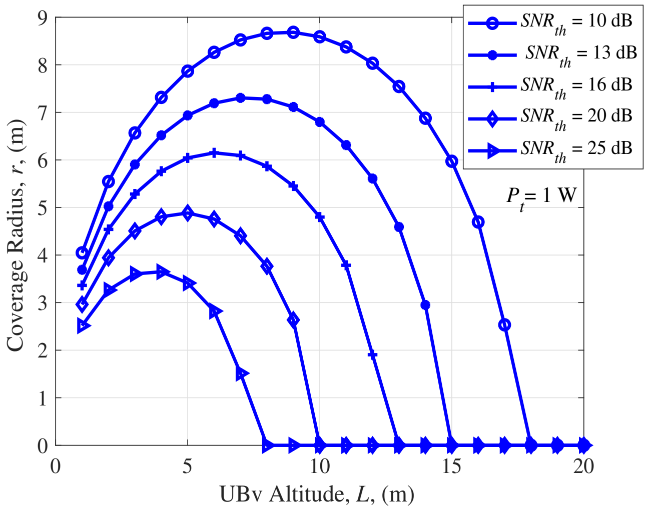

Figure 6.10: Coverage radius versus altitude of $\mathrm{UB_v}$ for varying SNR thresholds at 1 W transmitted optical power.

users with a particular SNR threshold. Therefore, until a certain altitude, the coverage radius increases as it still fulfills the SNR threshold. However, the SNR threshold is responsible for decreasing the desired coverage radius after that.

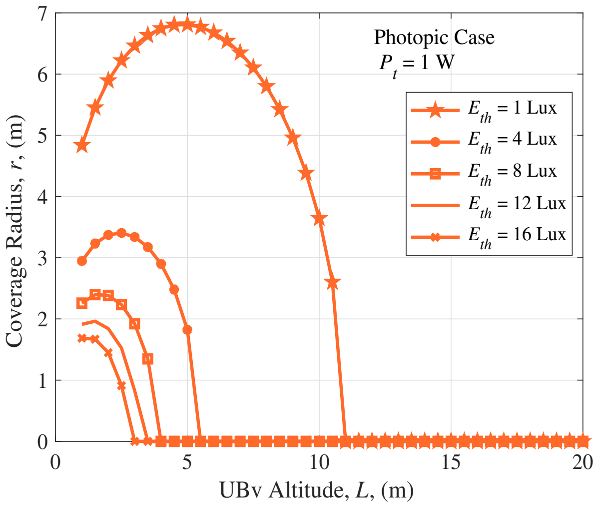

Figure 6.11: Coverage radius versus altitude of $\mathrm{UB_v}$ of photopic designed RGB LED for varying illuminance threshold at 1 W transmitted optical power.

In Fig. 6.11, the relation of $\mathrm{UB_v}$ coverage radius with its altitude have been shown for different illuminance threshold in day scenario (considering $V_\lambda = 1$ and maximum lumens/watt, i.e., 683 for photopic case) at transmitted optical power equal to one watt. It is observed that the illuminance threshold impacts the coverage radius and altitude range (defined as the highest altitude where coverage radius becomes zero) substantially as compared to the SNR threshold (in Fig. 6.10). The reason is due to the factor of light perceived by the human eye being considered in the illuminance expression (see (6.2) and (6.4)).

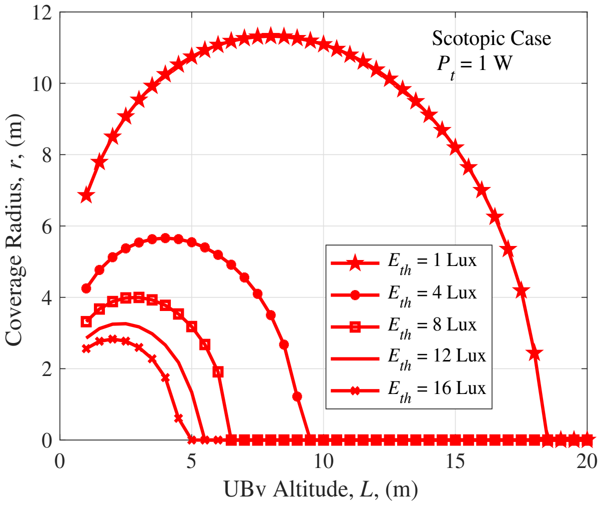

Figure 6.12: Coverage radius versus altitude of UB_V of scotopic designed RGB LED for varying illuminance threshold at 1 W transmitted optical power.

Fig. 6.12 displays the coverage radius versus altitude for night scenario considering scotopic case designed RGB LED (as discussed in section 6.3.1.2) at 1 W transmitted optical power for different illuminance threshold. The trend of first increasing and then decreasing r with respect to L remains the same. However, r has increased from the photopic case, which indicates that with RGB LED based energy-aware technique, the coverage radius can be increased without increasing the transmitted optical power. The reason behind increased r is the higher lumens/watt perceived by the human eye at night. The practical design of RGB LED makes it feasible to support the maximum possible lumens/watt while maintaining white tone light which ultimately increases the luminous efficacy and thus illuminance.

Fig. 6.13 presents the effect of transmitted optical power on UB_V altitude and its r at 13 dB SNR threshold. It is evident from (6.1) that SNR is directly proportional to transmitted optical power. Therefore, on increasing P_t, the coverage radius increases. However, this work [98] aims to increase r with sustainable and energy-aware techniques. Therefore, the utilization of holographic LSD and RGB LED based solutions have been proposed to support green communication through UB_V. Moreover, from Figs. 6.10 and 6.13, we can interpret that r increases more for lower SNR thresholds. The values of maximum coverage radius have been obtained analytically using (6.5) for different P_t.

In Fig. 6.14, UB_V altitude and its coverage radius has been plotted considering both QoS metrics i.e. SNR and illuminance at different P_t. The results have been obtained for scotopic case. Since, during day scenario only SNR QoS metrics is considered (as shown in Fig. 6.13

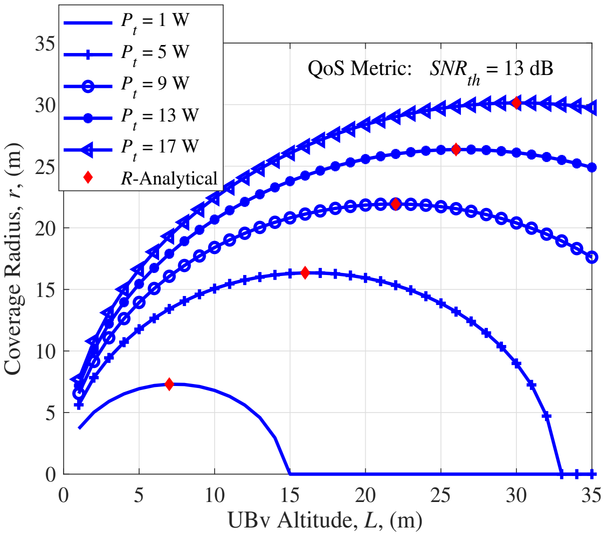

Figure 6.13: Coverage radius versus altitude of UB_v for different transmitted optical power at 13 dB SNR threshold.

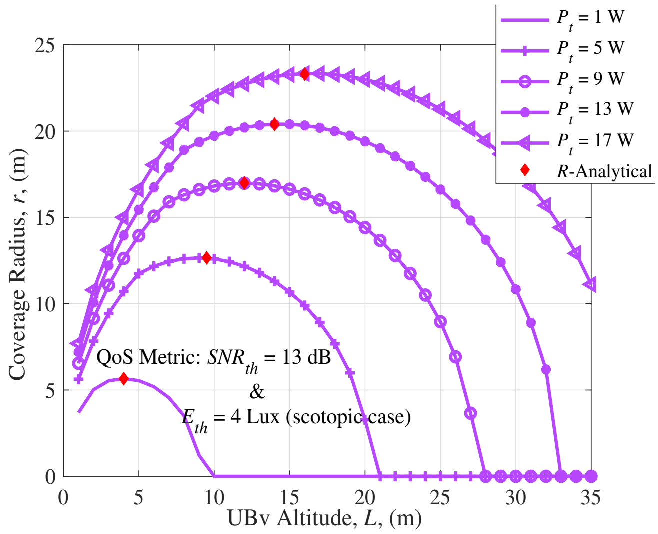

Figure 6.14: Coverage radius versus altitude of UB_v considering SNR and illuminance threshold at different transmitted optical power.

and already discussed in section 6.2.2). The peak of $\mathrm{UB_v}$ coverage radius and altitude range decreases further from results in Fig. 6.13 owing to illuminance threshold. The minimum of $[r_{SNR}, r_E]$ obtained from (6.5) and (6.6), respectively, provides R analytically. However, for scotopic case utilizing RGB LED based solution, the V_λ in (6.6) is replaced with V_λ^{rgb} as shown in (6.9).

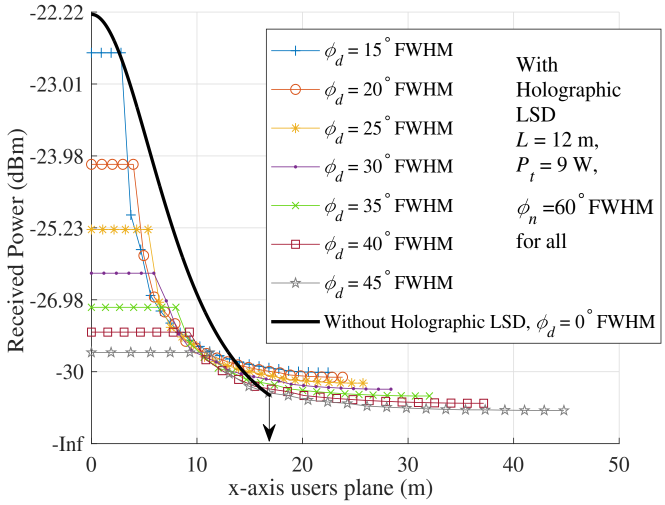

Figure 6.15: Relation of Coverage radius with varying holographic LSD angle of FOV at 9W transmitted optical power.

Fig. 6.15 shows the plot of received power distribution in 2-D versus coverage radius in the x-axis of the user's plane with varying ϕ_d of the holographic LSD at 9 W transmitted optical power. The black-lined plot displays the received power distribution without holographic LSD. The tail of all the plots ends at a certain x-axis of the user's plane, which connotes that there is no further coverage after that. This has been visually shown for the black-lined plot with a downward arrow. It is observed that as ϕ_d increases, the received power distribution becomes more uniform till a higher coverage radius. Nevertheless, this comes with a penalty of decreased received power at the user's plane. As ϕ_d increases, the effective output angle in (6.7) also increases which finally increases the coverage. Moreover, with larger ϕ_e the light diffuses more, so the average of the sum of individual footprints per pixel provides decreased received power.

Fig. 6.16 presents $\mathrm{UB_v}$ coverage radius with respect to its altitude considering SNR threshold and holographic LSD at different transmitted optical power. It is observed that as compared to Fig. 6.13, the coverage radius and altitude range has significantly increased with the adoption of holographic LSD at LED front end. The minimum of [$r'_{SNR}(L_o^{SNR})$,$r_{LSD}(L_o^{SNR})$], obtained from (6.13) and (6.8), respectively, provides R analytically. The second-order differentiation of (6.13) is derived to obtain the maximum value of altitude L_o^{SNR}. The altitude L_o^{SNR} is used

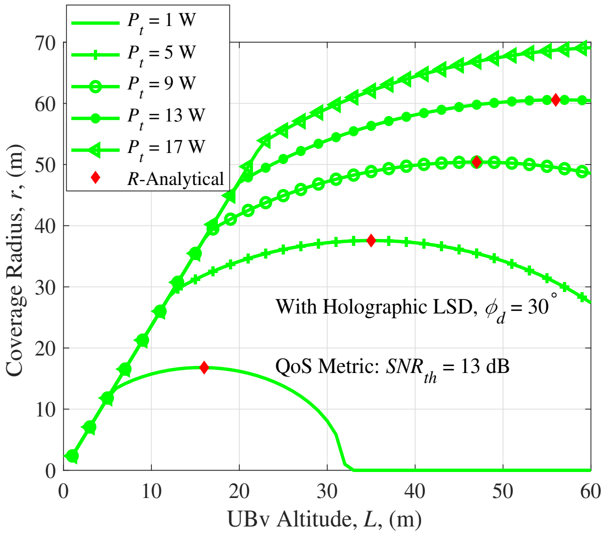

Figure 6.16: Coverage radius versus altitude of UB_v considering SNR threshold and holographic LSD at different transmitted optical power.

in (6.13) and (6.8) to obtain respective coverage radius and finally the minimum among them becomes the R. The analytical results match well with the peak value of the simulation results.

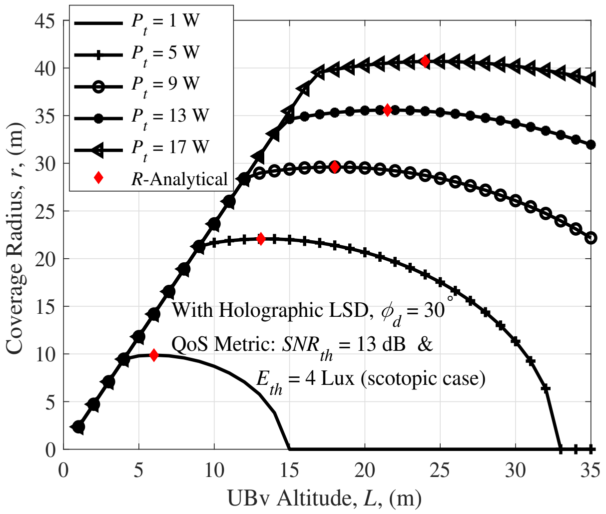

Figure 6.17: Coverage radius versus altitude of UB_v considering SNR and illuminance threshold with holographic LSD at different transmitted optical power.

Lastly, in Fig. 6.17, UB_v coverage radius and its altitude has been plotted considering SNR and illuminance threshold with holographic LSD for different P_t. It is observed that as compared to Fig. 6.14, the coverage radius and altitude range has significantly increased due to the holographic LSD. However, as compared to the results in Fig. 6.16, the coverage radius and altitude range reduce, which can be attributed to the illuminance threshold. The minimum of the four different optimized r as seen in (6.14) provides the maximum coverage radius with enhanced coverage area satisfying both E_{th} and SNR_{th}. Consequently, R is obtained

Table 6.2: Results of analytical solution for R at $P_t = 9$ W considering varying SNR and illuminance threshold with holographic LSD for night scenario.

Parameter:	E_{th} **= 1 Lux**		E_{th} **= 4 Lux**		E_{th} **= 16 Lux**	
SNR_{th} (dB)	L_o (m)	R (m)	L_o (m)	R (m)	L_o (m)	R (m)
10	43.5	58.5	17.9	29.7	9	14.8
13	46.9	50.4	17.9	29.7	9	14.8
16	39.5	42.4	17.9	29.7	9	14.8
20	31.4	33.7	17.9	29.7	9	14.8
25	23.5	25.3	23.5	25.3	9	14.8

Parameter:	SNR_{th} **= 10 dB**		SNR_{th} **= 13 dB**		SNR_{th} **= 25 dB**	
E_{th} (Lux)	L_o (m)	R (m)	L_o (m)	R (m)	L_o (m)	R (m)
1	43.5	58.5	40.9	50.4	23.5	25.3
4	17.9	29.7	17.9	29.7	23.5	25.3
8	12.7	20.9	12.7	20.9	12.7	20.9
12	10.4	17.1	10.4	17.1	10.4	17.1
16	9	14.8	9	14.8	9	14.8

analytically. The analytical results show good agreement with the peak value of the simulation results validating the derived analytical expressions.

We have analytically obtained and shown L_o and R at varying P_t in Fig. 6.17. However, the L_o and R can be obtained by varying different parameters as well such as SNR_{th} and E_{th}. Table 6.2 presents the value of L_o and its respective R for the proposed work considering varying SNR and illuminance threshold at night scenario with $P_t = 9$ W. It is observed that as E_{th} increases for varying values of SNR_{th}, L_o and R decreases and depends more on E_{th} than SNR_{th}, which is due to the increased limit imposed by E_{th}. Similarly, as SNR_{th} increases for varying values of E_{th}, L_o and R decreases which is obvious due to the increased SNR threshold value. However, from $E_{th} = 8$ Lux onwards, the L_o and R does not change even for varying SNR_{th}, which again shows the higher limit imposed by E_{th} than SNR_{th} on L_o and R. This has already been observed and discussed above while comparing Fig. 6.16 and Fig. 6.17. However, with the rigorous analytical results of Table 6.2, it has become more clear that L_o and R are more limited by E_{th} than SNR_{th}. Further, at $P_t = 9$ W, E_{th} = 4 Lux and SNR_{th} = 13 dB, the L_o and R values are 17.9 m and 29.7 m, respectively which perfectly matches with the black circle marker plot (i.e. at $P_t = 9$ W) of Fig. 6.17.

From the aforementioned analysis and discussion, a network engineer can finalize the optimum altitude for maximum coverage radius based on the network's application and requirement while supporting green communication and network. For instance, if it is decided

Table 6.3: Simulation Parameters.

Parameter	Value	Parameter	Value
v_u	1.5 m/s	N	20
v_{uav}	25 m/s	$fair_{thres}$	0.7
σ	4 m	t_{min}	4 s
L_o	17.9 m	t_{max}	50 s
T	600 s	Simulated Area	200 × 200 sq. m

to achieve the maximum coverage radius of 30 m in the night scenario with an optical power constraint of 9 W, then without LSD and RGB LED, the engineer would have no choice but to increase the P_t beyond 17 W. However, with the proposed enhancement techniques, i.e., LSD and RGB LED, the engineer can achieve $R = 30$ m with lower P_t (see Fig. 6.17), which support the energy-aware aspect of green communication and network. To achieve this aim, at first optimal altitude is obtained from the relation between UB_v altitude and its coverage radius considering both QoS metrics at $P_t = 9$ W as shown in Fig. 6.14. After that, $\phi_d = 30^\circ$ FWHM is chosen based on the plot of received power distribution and the x-axis of the user's plane as presented in Fig. 6.15. Further, the relation between UB_v coverage radius and its altitude is obtained considering both SNR and illuminance threshold with holographic LSD for night scenario and only SNR threshold with holographic LSD for day scenario at designated P_t. For night scenario, R approaches close to 30 m in Fig. 6.17 and for day scenario, the maximum coverage radius approaches close to 50 m as seen in Fig. 6.16. Further, with the proposed analytical solution, a network engineer has freedom to fix and vary parameters of his interest to directly deduce L_o and R for a given QoS metric.

Finally, the maximum coverage radius obtained is 29.7 m for the night scenario. Going ahead with $R = 29.7$ m, we present the results of the iterative solution to problems P1 and P2. In our study, all the users are initially considered inside the UB_v's coverage area. The initial placement of UB_v is at the optimum altitude just above the center of the users' plane as shown in Fig. 6.5. Further, we assume that the first UB_v placement update occurs after t_{min} seconds. The first update interval $t_{up}(1)$ and optimal UB_v placement is obtained after solving P1 and P2 iteratively. After this, the UB_v placement is updated at $(t_{min} + t_{up}(1))$ seconds. This process goes on till the total UB_v operation time, i.e., T seconds. The results are averaged over 50 UB_v operation periods. The simulation parameters are mentioned in Table 6.3.

Fig. 6.18 presents the average effective number of users covered per update interval in the UB_v network for $T = 600$ s. As α increases for all three methods, the number of users covered decreases. It is because less frequent UB_v placement updates result in lower coverage probability. Figs. 6.19 and 6.20 show the average number of update instants and average update interval, at $\sigma = 4$ m for all the three methods, respectively. With an increase in α, the number of update instants reduce, and update intervals increase. It is because an increase in α ensues more weightage to minimize the total UB_v flight time in (6.21). It causes less frequent UB_v

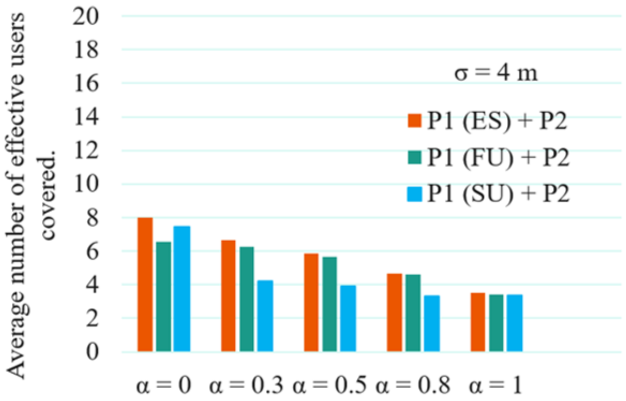

Figure 6.18: Average number of users covered at $T = 600$ seconds at $N = 20$.

placement updates and thus increases the update interval, thereby reducing energy consumption and making the deployment more energy efficient.

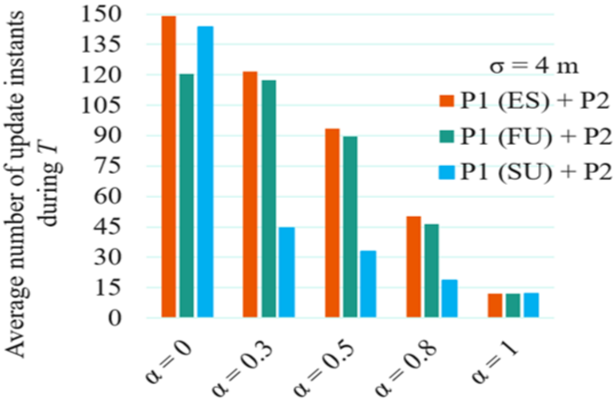

Figure 6.19: Average number of update instants during $T = 600$ seconds.

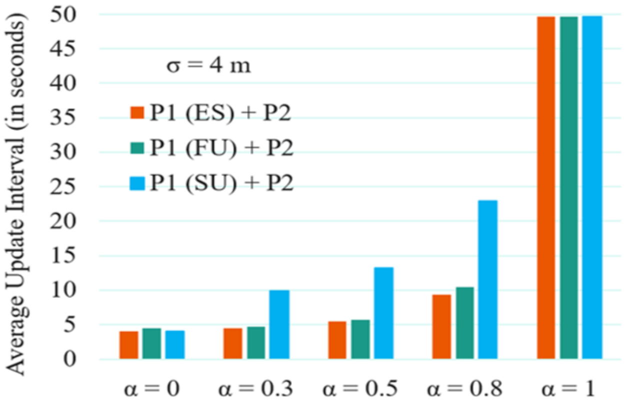

Figure 6.20: Average update interval at $T = 600$ seconds.

In Figs. 6.18-6.20, the results of FU and SU method equals ES method at $\alpha = 1$. The reason is the proposed optimization problem (6.21), where at $\alpha = 1$, the minimization problem does not have a coverage probability factor. Therefore, P2 when left with the minimization of total $\mathrm{UB_v}$ flight time only, the number of update instants reduces significantly (see Fig. 6.19) and update interval increases drastically (refer Fig. 6.20). With this, the iterative solution of P1 and P2 approaches similar values despite different solving methods. Therefore, in Fig. 6.18, the average number of effective users covered in the FU and SU method approaches the ES method. Besides, it is observed in Figs. 6.18-6.20 that for $\alpha = 0.3, 0.5, 0.8$, the results of FU method approaches close to ES method. Since the FU method is the truncated version of ES by farthest user, as the weightage of α incorporates minimization of fly time along with coverage probability, it approaches close to the ES method. However, in Fig. 6.18 for $\alpha = 0.3, 0.5, 0.8$, SU method provides less $\bar{U_e}$ as compared to ES method and this is due to Algorithm 5 where $\mathrm{UB_v}$ is shifted as per uncovered users which limits the possibility of covering users under constraint C2. Similarly, in Fig. 6.19, the number of update instants in the SU method is significantly lower than the other two methods. Hence, $\mathrm{UB_v}$ changes its position less frequently with the SU method, thereby reducing energy consumption and making the deployment more energy efficient. The lower number of update instant and higher update intervals of SU method in Fig. 6.20 leads to lower $\bar{U_e}$. The probability of the user moving outside the $\mathrm{UB_v}$ coverage area increases at a higher update interval. Consequently, for each user, coverage probability decreases with an increase in t_{up}. Moreover, in Figs. 6.18-6.20 at $\alpha = 0$, there is no minimization of fly time; hence the ES method updates frequently to cover the maximum possible number of users. However, the FU method can update hover points till the area defined by the farthest user at k^{th} update instant, which reduces the update frequency. Further, for $\alpha = 0$ SU method approaches ES method, as $\mathrm{UB_v}$ can shift anywhere within C1 and C2 constraints with the sole aim to maximize coverage probability.

Fig. 6.21 presents the average service time (i.e., average hovering time) for varying α. It can be observed that with an increase in α, average service time increases. Since in the FU method, $\bar{U_e}$ is slightly lower than the ES method due to a slightly reduced number of update instants. Therefore, in Fig. 6.21, we can observe slight higher $\mathscr{S}$ than ES method for all α value except zero. The reason behind almost exact value at $\alpha = 0$ for all the three methods has already been discussed above. Further, in the SU method, $\mathscr{S}$ is higher for most of the α due to the fewer number of update instants (as shown in Fig. 6.19) as compared to the ES method.

It should be noted that for the SU method, constraint C1 is relaxed with a delta value (δ) in $fair_{thres}$ so as to avoid the non-feasible solution set and proceed further with the iterative solution of P1 and P2 based on uncovered users only. The fairness threshold now becomes $fair_{thres} - \delta$. Table 6.4 shows the error margins, i.e., the average percentage of times (error %) $fair_k$ does not follow strict C1 as per (6.19) and the average delta value considered at $fair_k$ for

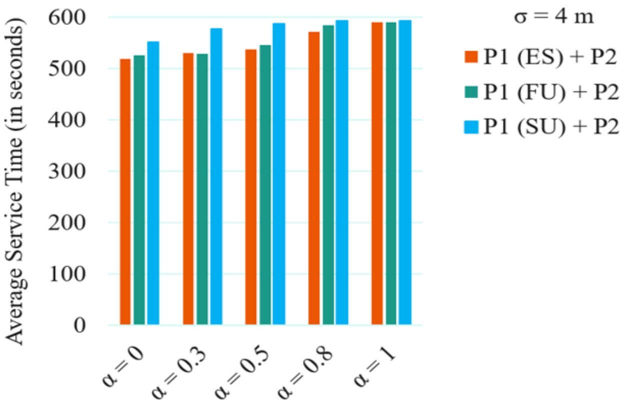

Figure 6.21: Average service time at $T = 600$ seconds.

Table 6.4: SU Method Error Margin.

α	error %	δ
0	1.06 %	0.0075
0.3	2.41 %	0.0082
0.5	0.69 %	0.0077
0.8	0.46 %	0.0052
1	0.1 %	0.0140

Table 6.5: Average effective number of users covered and average total service time for ES, FU and SU Method.

α	$\bar{U}_e$	$\mathscr{S}$
ES Method:		
0	8.01	519.10 s
0.5	5.83	537.65 s
1	3.50	590.70 s
FU Method:		
0	6.54	526.07 s
0.5	5.64	546.30 s
1	3.41	590.16 s
SU Method:		
0	7.47	552.65 s
0.5	4.00	587.64 s
1	3.36	59.68 s

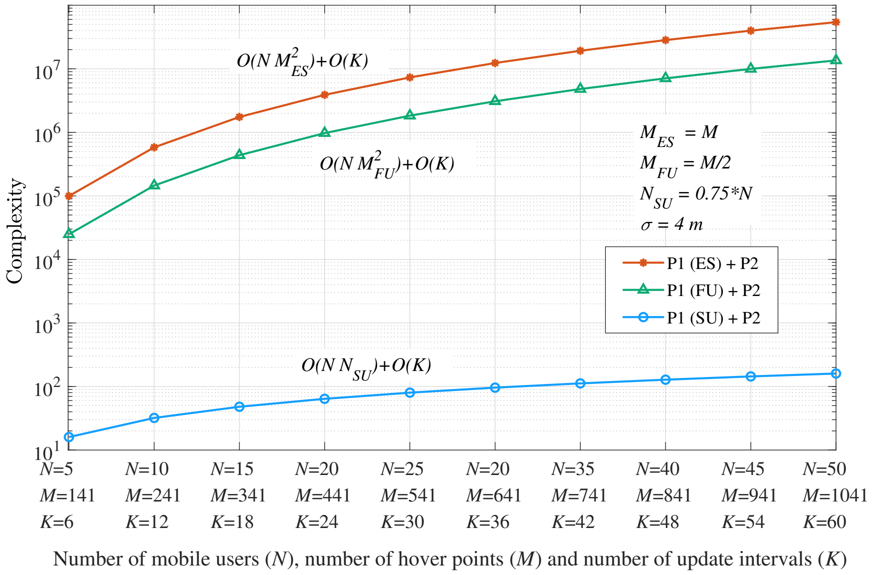

Figure 6.22: Computational complexity of solving P2 and P1 with different algorithms.

T seconds. It is observed that the error margins are very less. Further, the results of Figs. 6.18 and 6.21 for all the three methods has been compiled in Table 6.5 for clear comparison. Fig. 6.22 depicts the complexity of ES, FU and SU methods which has been explained in detail in section 6.3.4.

The aim of this work [98] is that eventually, a network engineer can take insight from the above-discussed results and tune α based on the requirement to cover more users or provide a larger service time with user mobility and energy awareness. Further, SU method can be chosen for optimal $\mathrm{UB_v}$ placement when time complexity thus energy required at $\mathrm{UB_v}$ is a big issue and the network engineer is ready to compromise in $\bar{U_e}$ with slight error margin as inferred from Tables 6.4-6.5 and Fig. 6.22. The decimal values of $\bar{U_e}$ in Table 6.5 implies that at $t_{up}(k)$ update interval few users are covered for time duration less than $t_{up}(k)$. Moreover, SU can be preferred to provide higher service time with energy efficiency over ES and FU methods. However, the FU method can be considered when the network engineer can not compromise on the number of covered users as it provides coverage close to the ES method with less energy and time complexity.

6.5 Summary

This work optimizes the 3-D placement of $\mathrm{UB_v}$ and update interval while maintaining illuminance and SNR threshold. The best altitude is initially chosen based on the $\mathrm{UB_v}$ maximum coverage radius while taking into account QoS metrics specific to day and night scenarios. Holographic LSD has increased the coverage area with the goal of implementing a more energy-aware and greener VLC. Additionally, a cutting-edge RGB LED-based solution has been put out for the nighttime situation, taking into account the human eye's light sensitivity to boost the illuminance and therefore the coverage radius. Thus, for the scotopic situation with no improvements and with the suggested energy-aware enhancements, the greatest coverage radius obtained is 16.98 m and 29.7 m, respectively. The proposed enhancements increase the coverage area of $\mathrm{UB_v}$ by 207%. Additionally, the analytical solution has been provided to obtain the maximum coverage radius and its optimal altitude with the proposed enhancements techniques. In order to maximise the number of covered users and reduce $\mathrm{UB_v}$ flight time at an update instant while accounting for user fairness, the joint optimization of 2-D $\mathrm{UB_v}$ placement and update interval has been presented. The proposed FU and SU methods to solve the objective function achieve performance close to the exhaustive-search method with reduced complexity. The effective number of users covered by the SU method at $\alpha = 0.5$ is 4, the least among all the three methods. However, selecting the SU method is an energy-aware decision to achieve a greener network since it provides the maximum service time and drastically reduced time complexity compared to the FU and ES methods.

Chapter 7

Conclusion and Future Work

Due to unprecedented growth in wireless devices and internet traffic over the past few decades, there is a pressing need to develop new communication technologies that utilize the untapped regions of the electromagnetic spectrum. To this end, extensive research is being undertaken in the area of optical wireless communication, particularly VLC, which utilizes the illumination infrastructure of LEDs for data communication. VLC enables green and sustainable energy solutions by fusing data transfer with illumination. In recent years, VLC has gained tremendous attention and has emerged as a complementary technology to mm-wave communication in short-range communication scenarios for beyond 5G networks. VLC supports green and heterogeneous communication networks, offers higher data rates and inherent security, making it a potential 6G enabler. Out of many expectations, the 6G communication is expected to support green communication, massive heterogeneous device connection density of 10^7 connections/km^2, seamless coverage, latency reduction, security improvement, higher user QoE level, autonomous, intelligent, and energy-efficient systems. These requirements are quite ambitious, and thus, the VLC technology should be evolved on various aspects, as addressed in this thesis by tackling the associated issues that obstruct the prudent application of VLC technology for impending 6G communication.

In this dissertation, VLC has been enhanced and improved in order to support green communication for both LiFi users and resource-constrained devices such as IoT and UAVs. It is anticipated that 6G would offer completely new service quality and improve user experience in existing IoT systems. VLC as 6G enabler technology can be integrated to IoTs for furture 6G-IoT applications such as industrial IoT (IIoT), internet of health things (IoHT), vehicular IoT (VIoT) and UAVs. Firstly, a generalized improvement in performance of different CSK schemes is investigated by employing PS technique. The proposed PS-CSK schemes (PS-CSK-3PD, PS-CSK-1PD and PS-CSK-1APD) provide different SNR gains for different source distributions (viz. uniform, exponential, Maxwell-Boltzmann and Pareto) at a given SER.

A comprehensive performance evaluation of various PS-CSK schemes in terms of SER and computational complexity is provided. Secondly, the constellation points of non-uniform source distributions in PS-CSK-1PD are designed and optimized with and without white tone constraint to achieve higher power efficiency than their uniform source distribution counterpart. The aforementioned works concentrate on the energy-efficiency of the VLC system, which can be used for IoT communication with low cost and computation, enabling high connection density, secure and energy-efficient 6G-IoT sensor networks. A further objective is to facilitate enormous heterogeneous device communication while maintaining sustainability in line with 6G aspirations, various coexistence schemes for heterogeneous users have been discussed to support concurrent communication with LiFi and LC-enabled IoT users. A comprehensive performance evaluation of different variants of proposed and conventional DCO-OFDM$^{\mathrm{H}}$ coexistence schemes is illustrated in terms of system complexity, PAPR, ESE, the maximum number of IoT devices (K_m), power saving with respect to QAM-DCO-OFDM$^{\mathrm{H}}$, EH, and SNR. Additionally, for intelligent seamless coverage of ground users with green communication and autonomous system (such as UAVs) in 6G networks, the following work optimizes the 3-D placement of VLC enabled UAVs and its update interval while maintaining illuminance and SNR threshold. The performance of energy-aware methods to jointly optimize 2-D UB$_{\mathrm{v}}$ placement and update interval in order to maximize the number of covered users and minimize UB$_{\mathrm{v}}$ flight time have been compared against the exhaustive search method based on average update interval, the average number of effective users, the average number of update instants, average service time and complexity. The rest of the chapter is organized as follows: Section 7.1 provides a summary of the main contributions, followed by Section 7.2, which highlights the possible future research direction.

7.1 Summary of Contribution

The main contributions of this dissertation can be summarized as follows:

- **Design and Analysis of Probabilistic Shaping in CSK:** Probabilistic shaping of input symbols (uniform, exponential, Maxwell-Boltzmann and Pareto) have been integrated in the various CSK modulation schemes (CSK-3PD, CSK-1PD, CSK-1APD). The source distributions have been designed to realize unity AIR for a fair comparison. It has been observed that the M symbols in CSK could be shaped by assigning any probability order out of ${}^{n=M}P_{r=M}$ probability orders. However, all the probability orders do not necessarily give the same performance. Algorithms have been developed to obtain the OPO, i.e., the probability order at which the maximum SNR gain is achieved. The maximum SNR gain is achieved at FEC limit SER of 10^{-3} in case of Pareto PS-CSK-1APD. The derived analytical SER expressions validate the gain improvements of the simulated results. The proposed work illustrates the suitability and compatibility of the PS technique in various CSK VLC schemes. The proposed work shows the importance of OPO for attaining best possible performance gain in the PS-CSK system for better power-efficiency. The PS using non-uniform source distributions, especially Pareto, improves the performance of the CSK schemes. The PS-CSK-1PD and PS-CSK-1APD have the potential to enable power-efficient, less computationally complex and low-cost architecture for VLC in IoT such as sensor networks in indoor scenarios (e.g., homes and industries) [70].

- **Constellation Design of CSK-1PD with White Color Balance:** The constellation points of CSK-1PD with and without average white tone for uniform and non-uniform (exponential, Maxwell-Boltzmann, and Pareto) source distributions have been designed and optimized rigorously to reduce the received SER. The constellation points of non-uniformly distributed input symbols in CSK-1PD are optimized by geometrically shaping the symbols based on their preceding probabilistic shaping. A relaxed white tone constraint has been formulated by considering the whole white light region in CIE 1931 chromaticity diagram to maintain a white color balance with reduced SER. A novel technique to maintain any desired average white tonality light without degrading the SNR gain by inserting an extra RGB LED at the transmitter (one LED for modulation and another LED for maintaining white tone) have been proposed. The specific OCPs without white tone constraint gives improved SNR performance gain in all the source distributions with respect to the uniform OCPs utilized in chapter 3. The OCPs with strict white tone constraint maintains the white tone on an average, however with reduced SNR gain. The optimization process for OCPs with relaxed white tone constraint considers the whole white region in white tone constraint to boost the SNR gain. It has been observed from that the RGB optical powers of extra RGB LED can be designed for any desired chromaticity coordinates inside the white light region retaining maximum SNR gain with specific OCPs for uniform and non-uniform source distributions [71].

- **Energy-Efficient Coexistence of LiFi Users and Light Enabled IoT Devices:** Green coexistence VLC schemes have been proposed for heterogeneous LiFi users and LC enabled IoT devices under a common LiFi AP. The proposed coexistence schemes, one for DL and another for UL communication, utilize the amalgamation of WDM, OFDMA, DCO-OFDM$^{\mathrm{H}}$, NDCE, DHT precoding, interleaved subcarrier mapping and MDS to achieve concurrent interference-free, low complex and reliable communication. A comprehensive analysis of the various proposed and existing variants of DCO-OFDM$^{\mathrm{H}}$ in the coexistence schemes in terms of several performance metrics viz. system complexity, PAPR, ESE, K_m, power saving, EH and SNR at FEC limit SER have been illustrated in order to suggest best-suited coexistence schemes. The theoretical closed-form SER and PAPR expressions for the proposed coexistence schemes have been derived and validated. *PAM$_{\mathrm{Up}}$-MDS-P-DCO-OFDM$^{\mathrm{H}}$ provides the least computational complexity of $O(1)$ and $O(Q)$ at the LC enabled IoT and LiFi user's terminal, therefore is most suitable for DL scenarios with massive IoT devices and few LiFi users. The O-OFDMA scheme provides a clear advantage over O-OFDM-TDMA in terms of throughput for a fixed delay. For the uplink case utilizing O-OFDMA, PAM$_{\mathrm{Up}}$-NDCE-DCO-OFDM$^{\mathrm{H}}$ is a better option among all twenty-three coexistence schemes analyzed [97].

- **3-D Deployment of VLC-UAV Networks with Energy and User Mobility Awareness:** The altitude deployment of UB$_{\mathrm{v}}$ have been optimized for maximum coverage of ground mobile users while fulfilling illumination and reliable communication requirements. The coverage radius has been enhanced with holographic LSD with the motive of adopting an energy-aware and greener aspect of communication. Further, a novel RGB LED-based solution has been proposed for the night scenario considering the human eye's light sensitivity to increase the illuminance and thus coverage radius. The proposed enhancements increase the coverage area of UB$_{\mathrm{v}}$ by 207%. Additionally, the analytical solution has been provided to obtain the maximum coverage radius and its optimal altitude with the proposed enhancements techniques. Subsequently, the joint optimization of the UB$_{\mathrm{v}}$ 2-D positioning and the update interval has been proposed to maximize the number of covered users with VLC specific QoS constraints at an update instant by ensuring the user fairness as well as UB$_{\mathrm{v}}$ flight time constraint. The proposed energy-aware solutions based on farthest user and shifting strategy for the joint optimization problem achieve performance close to the exhaustive-search method with reduced complexity. The SU method is an energy-aware decision to achieve a greener network since it provides the maximum service time and drastically reduced time complexity with slightly lower effective number of users covered compared to the FU and ES methods [98].

This dissertation can be utilized to enhance and improve VLC in order to support moderate communication speed for both resource constrained devices and LiFi users with more green, energy-aware, low cost and complexity. It can also be utilized for greener coexistence of high-speed LiFi users and low speed LC enabled IoT devices under a common LiFi AP. Moreover, this dissertation can be referred for 3-D deployment of VLC enabled UAVs.

7.2 Future Work

There are many possible directions in which the work articulated in this dissertation can be extended. Some of the future research directions are as follows:

- Fundamental to the operation of a LC enabled IoT node is the amount of energy harvested by indoor solar cell, so clearly, a LC enabled IoT node can be considered as energy limited. In [202], the authors have developed a full-duplex energy autonomous light communication enabled IoT (LIoT) node using printed electronics technology. An interesting future work of this dissertation can be energy-efficient allocation of resources such as O-OFDM subcarriers in the coexistence environment (LiFi users and LC enabled IoT devices under a common LiFi AP) such that indoor solar cell-based IoT receiver terminals can utilize energy harvesting to become completely energy-autonomous. The operation of an LIoT node and its energy autonomy depends on the amount of energy harvested, which in turn depends on the type, size and orientation of the photovoltaic cell in the LIoT node, as well as the level of illumination and exposure time. Therefore, the future work can be to investigate the indoor solar cell [202, 203] for various IoT applications (IoT service requirement) to support energy-autonomous LIoT receivers in the coexistence environment.
- This dissertation has considered typical random way point mobility model to model the movement of users in indoor and outdoor setup of VLC scenario. The typical RWP model does not consider the effect of time, space (room setup and furnishing layouts), receiver orientation, interaction with other users and fails to capture realistic spatio-temporal channel characteristics. Further, orientation based RWP has been proposed in [204] which considers the effect of receiver orientation, however the effect of mobility pattern with blockages which depends upon indoor or outdoor layout and other user movement has been neglected in RWP and OWRP model. Additionally, in [215] the effect of shadowing and blocking of the signal path due to obstacles present in the room has been considered to empirically model the VLC dynamic channel, however the ORWP mobility of people is not considered. Hence, a more realistic user mobility model should be adopted to investigate the performance of indoor/outdoor UAV based VLC systems in our future work.
- Since many clients (LiFi users and LIoT devices) of AP may try to transmit and receive data at the same time, so they need to be coordinated in the coexistence environment. To achieve this coordination, the AP sends trigger frames to the clients to inform them which subcarriers they can use to send and receive data. The receiver (LiFi user and LIoT device) receives data of its interest as it knows apriori during the handshake

which subcarrier is meant for them and at what time it will receive data [68, 166–168]. The current coexistence scheme in chapter 5 focuses on the selection of best suitable coexistence scheme, hence the synchronization among users, devices, and AP have been assumed to be perfect. Nevertheless, in future work of this dissertation, efficient synchronization can be adopted and modified from these works [166–168] in order to make it more suitable for the coexistence environment.

- In this dissertation, a simple outdoor scenario without the environmental effects have been considered. However, it is would be interesting to consider the impact of fog and rain in the 3-D deployment of VLC enabled UAVs and evaluate the impact of external environmental conditions on the quality of service and coverage area. Additionally, in case of centralized AP or UAV, a centralized controller is responsible for all the decision making and it is assumed that the central controller has all the information available instantaneously. However, this is not practical. Therefore, another subject of future work can be to optimize the decision making at central controller with less possible information and less performance degradation.

- The proposed analysis of VLC enabled UAV system in this dissertation can be extended to multi-VLC enabled UAVs communication network and the fair maximum coverage problem can be solved using some learning techniques such as reinforcement learning. The current work is limited to downlink UAV-VLC system. In future, this can be extended to bi-directional communication. Moreover, based on the user service requirement, the 3-D deployment of network can be further optimized. These topics will be studied in our future research.

- In future, the optimization of the UAV network coverage can take into practical consideration of limited energy at the UAV. Another work can be to harvest data from distributed IoT devices at ground level with multiple autonomous UAVs. In some scenarios there could be energy limitation on both the AP (attached to a UAV) and energy autonomous IoT nodes on the ground and thus the problem can be to optimize the path planning of UAVs for maximum coverage of IoT nodes.

Chapter 8

Publications

8.1 Transactions / Journals (Published)

[J1] **Dil Nashin Anwar** and Anand Srivastava, “Design and Analysis of Probabilistic Shaping in Color Shift Keying Modulation Schemes,” ***IEEE System Journal***, vol. 15, no. 1, pp. 1433-1444, March 2021, doi: 10.1109/JSYST.2020.3007391.

[J2] **Dil Nashin Anwar** and Anand Srivastava, “Constellation Design for Single Photodetector based CSK with Probabilistic Shaping and White Color Balance,” ***IEEE Access***, vol. 8, pp. 159609-159621, August 2020, doi: 10.1109/ACCESS.2020.3020403.

[J3] **Dil Nashin Anwar**, Rizwana Ahmad and Anand Srivastava, "Energy-Efficient Coexistence of LiFi Users and Light Enabled IoT Devices," ***IEEE Transactions on Green Communications and Networking***, vol. 6, no. 2, pp. 930-950, June 2022, doi: 10.1109/TGCN.2021.3116267.

[J4] **Dil Nashin Anwar**, Mansi Peer, Kanak Lata, Anand Srivastava and Vivek Ashok Bohara, “3-D Deployment of VLC Enabled UAV Networks with Energy and User Mobility Awareness”, ***IEEE Transaction on Green Communications and Networking***, doi: 10.1109/TGCN.2022.3171920.

[J5] Saumya Chaturvedi, **Dil Nashin Anwar**, Vivek Ashok Bohara, Anand Srivastava and Zilong Liu, “Low-Complexity Codebook Design for SCMA-Based Visible Light Communication”, ***IEEE Open Journal of the Communications Society***, vol. 3, pp. 106-118, 2022, doi: 10.1109/OJCOMS.2022.3141800.

8.2 Conferences (Published)

[C1] **Dil Nashin Anwar** and Anand Srivastava, “VLC-based safe, low-cost, and accurate healthcare system for video EEG using colour constellation scheme,” in *Proc. SPIE Photon. Europe*, Strasbourg, France, Apr. 2018, p. 1068549.

[C2] **Dil Nashin Anwar** and Anand Srivastava, “Energy saver VLC using off-the-shelf devices: an experimental study,” in *Proc. IEEE International Conference on Advanced Networks and Telecommunications Systems (ANTS)*, Indore, India, Dec. 2018, pp. 1-6.

[C3] **Dil Nashin Anwar**, Anand Srivastava and Vivek Ashok Bohara, “Adaptive Channel Estimation in VLC for Dynamic Indoor Environment,” in *Proc. 21st International Conference on Transparent Optical Networks (ICTON)*, Angers, France, 2019, pp. 1-5.

[C4] Anand Singh, **Dil Nashin Anwar**, Anand Srivastava, Vivek Ashok Bohra, and G. S. VRK Rao, “Power and SER analysis of VLC- and RF-based links in indoor environment,” in *Proc. SPIE 10945, Broadband Access Communication Technologies XIII, 109450R*, San Francisco, U.S., Feb. 2019, p.109450R.

Chapter 9

Auxiliary VLC Related Research Works

The last chapter of this thesis discusses briefly the additional research works published during the tenure of PhD to further support VLC adoption in wireless communication, its challenges and viable solutions. In Section 9.1, CSK modulation scheme has been explored for Healthcare applications. Followed by Section 9.2 which provides an experimental study of VLC with off-the-shelf LEDs. Section 9.3 discusses the VLC work with dynamic indoor environment. The comparison of RF and VLC modulation schemes as standalone technology has been done with the objective of power saving and is presented in Section 9.4.

9.1 VLC for Healthcare Applications

One of the potential applications of VLC is in the indoor healthcare system such as monitoring. A long-term video-EEG monitoring requires continuous monitoring by video along-with EEG signals. So, overall a significant amount of data needs to be streamed fast for real-time monitoring. In this work [128], a low-cost RF radiation-free system is proposed using VLC technology which can be integrated into a wearable EEG device to transmit video and multi-channel EEG signal. Data streams are modulated using CSK, since output optical power remains constant in CSK thereby preventing light flashes. To further support green communication, the cost and complexity of the conventional CSK in IEEE 802.15.7 has been reduced by utilizing single-photodetector at the receiver. As seen in Fig. 2.3, standard CSK needs a complicated and expensive set of filters (each for red, green and blue color light) for three PDs. However, in single PD as a receiver, the CSK-based color coding format as outlined in IEEE 802.15.7 is replaced by a direct mapping from data bits to RGB power intensities. Fig. 9.1 shows the block diagram of CSK-1PD modulated VLC system [92]. In this case, the wearable device is mounted to the patient's head, and a VLC-enabled RGB LED is present on the wearable device. For simplicity, it is assumed that the RGB LED in the wearable device is

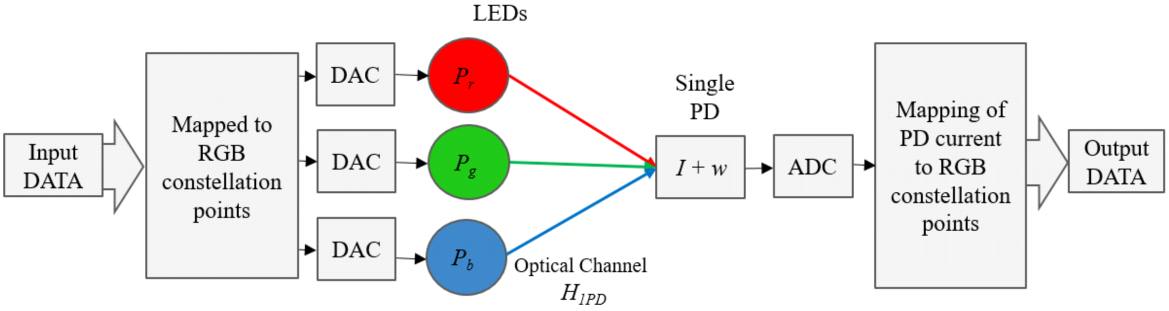

Figure 9.1: Block diagram of CSK-1PD (color shift keying with one photodetector) system.

in LOS with the receiver PD mounted on the roof. Since the patient is wearing the wearable gadget and the RGB LED is pointed at the ceiling of the room, the patient seldom experiences uncomfortable lighting problems. It is also noted that the ambient light effects because of illumination infrastructure can be significantly removed with the use of a high pass filter at the VLC receiver [10, 30]. Additionally, PD is facing the RGB LED of the wearable device rather than the illumination infrastructure. Therefore, the proposed communication system can be replicated close to a downlink VLC system.

9.1.1 CSK-1PD (Single photodetector CSK)

In CSK-3PD, symbol mapping process includes two necessary steps, color coding and mapping from x-y color coordinates to RGB intensity vector. CSK-1PD reduces complexity by mapping symbols directly to three different RGB intensities obtained from optimized constellation points [92]. Moreover, the technique to detect symbols with just one PD in CSK-1PD eliminates the need for three filters, two PDs and two ADCs, thereby reducing the hardware cost. The property of PD to generate specific electrical current to an incident optical power of a given wavelength is known as the responsivity of the PD for that wavelength. CSK-1PD utilizes this concept to detect the received symbols. The conversion of the optical power into the electrical current I_c is a linear combination of the LED power and the PD responsivity at each RGB wavelength of the RGB LED, equated as:

$$I_c = \langle \boldsymbol{\rho} \cdot \mathbf{p} \rangle. \tag{9.1}$$

The arithmetic operator $\langle \cdot \rangle$ in (9.1) defines the inner product between the transmitted RGB optical power vector, $\mathbf{p} = [P_r, P_g, P_b]^T$ such that $P_r + P_g + P_b = 1$ and PD responsivity vector, $\boldsymbol{\rho} = [\rho(red), \rho(green), \rho(blue)]$. The central wavelength of the red, green, and blue, monochromatic color LEDs are 640, 530, and 465 nm, respectively. The vector $\boldsymbol{\rho} = [0.42, 0.32, 0.22]$ has been obtained from the response curve of a practical PD (PDA36A2) from Thorlabs [205] for the central wavelength of red, green, and blue light, respectively. PDA36A2 detects light signals ranging from 350 to 1100 nm and comes with an inbuilt gain amplifier. Thus, the transmitted symbols in the form of electric currents are obtained by incorporating the respective red, green, and blue light responsivities of a PD in (9.1). The structure for CSK demodulation using a single-PD topology is introduced in Fig. 9.2. The received power at the PD is the power received after LOS channel gain. Finally, the received electrical signal at the output of the single PD is written as

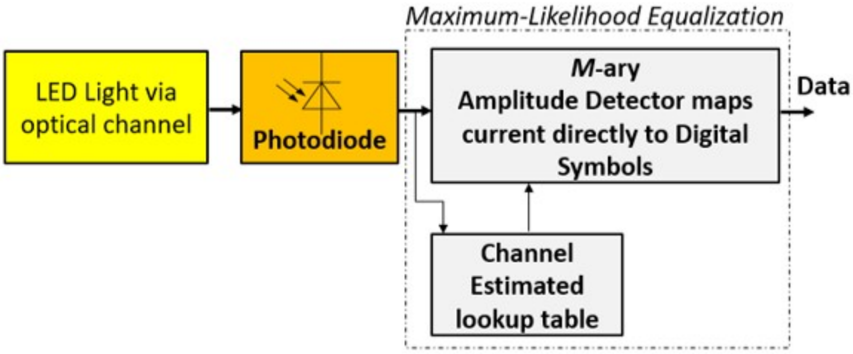

Figure 9.2: Single PD 4-CSK receiver

$$I_k = i_{LOS,k} + w_k \ , \tag{9.2}$$

where I_k defines the k_{th} received symbol. The M-ary amplitude detection is performed by computing the minimum Euclidean distances between received signal and four unique $i_{LOS,k=1,2,3,4}$ levels as follows:

$$d_{min} = \min_{i_{LOS,k} \in \mathbb{C}} |I_k - i_{LOS,k}| \ , \tag{9.3}$$

where the set $\mathbb{C}$ is updated by considering optical channel in the projections of the M different RGB vectors onto the sensitivity response of the single PD as given in Table. 9.1. This symbol decision process finds the constellation symbol that is closest to the received signal I_k which is equivalent to applying the maximum likelihood (ML) detector. The optical receiver converts the optical signal to electrical signal, and then these electrical signals are mapped to standard bits using channel estimation and a lookup table. The constellation mapping rule is generated for unity total power of RGB LED. The respective symbols, RGB optical powers and currents are shown in Table. 9.1.

Table 9.1: Look-up table for 4-CSK single PD system.

Symbols	Red LED power	Green LED power	Blue LED power	Current (ℂ)
10	1	0	0	0.42
01	0	0	1	0.22
00	0	0.6326	0.3674	0.28
11	0.3236	0.5872	0.0892	0.34

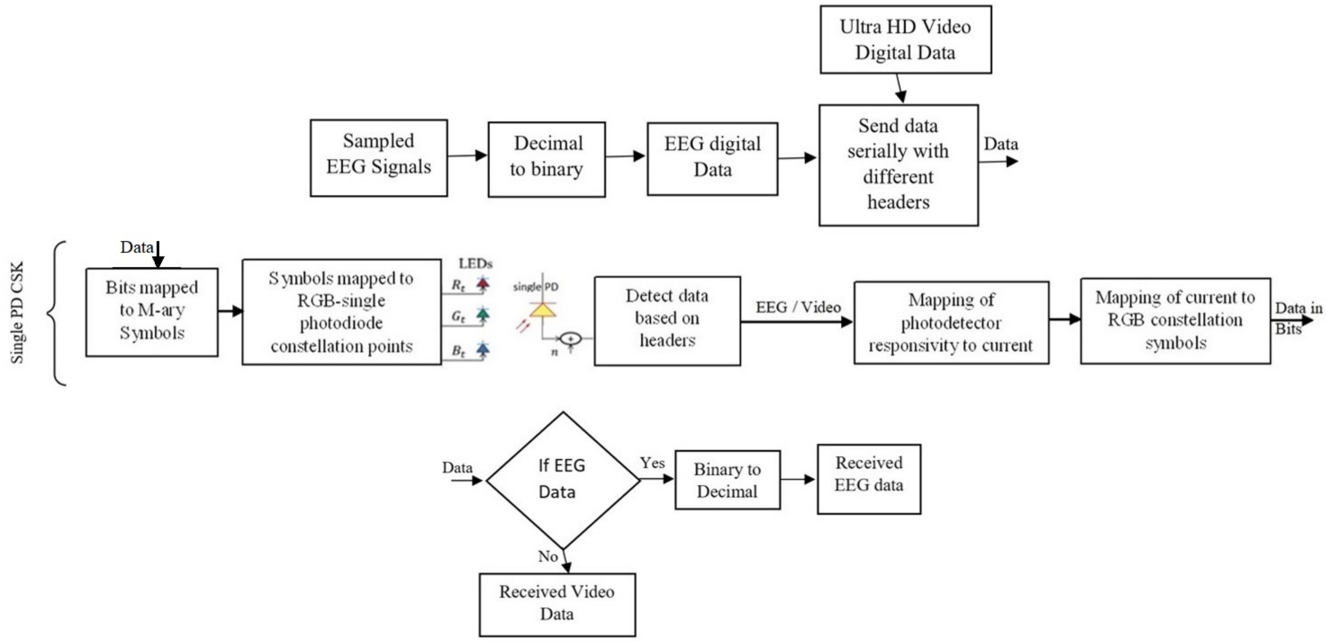

Figure 9.3: Block diagram of system architecture transmitting EEG data with CSK-1PD

9.1.2 Proposed System

The complete system architecture to transfer video and EEG data based on single PD CSK scheme is illustrated in Fig. 9.3. This system consists of three parts namely transmitter, optical channel and receiver. First, EEG data is converted to all positive values and then to digital bits to drive the LED source according to 1s and 0s. The video data is too converted to bits. Since the rate of EEG data is lower than the video data, so the packet size of EEG and video is decided according to their sampling data rate. In this work, both EEG and video data are sent serially instead of time-hopping since, in the case of time-hopping, the difference in data rate results in time intervals with no data, thereby wasting resources [206]. It is imperative to obtain accurate estimates of the optical channel gain between receiver and light source. Results in Fig. 9.4 show the importance of channel estimation. Pilot symbols from the transmitter can be sent in a sequence of lookup table periodically within the coherence time, and hence channel gain can be estimated at the receiver. In our case coherence bandwidth [207] comes out to be approximately 276 MHz as the distance between transmitter and receiver is 100 cm. The total bit rate in our system does not exceed 13 Mbps including frame bits apart from data bits. The coherence bandwidth is much greater than the required data transmission bandwidth (B) of the system (since, $B = \frac{\text{bit rate}}{\log_2(1+SNR)}$, based on Shannon limit). Hence it can be assumed that the channel is flat. Also, inside a room, a patient on which recording is being done has speed smaller than the standard walking speed, i.e. 1.4 m/s. The coherence time [208] is 3.322 sec if the transmitter moves at a walking speed inside a room. Hence, considering the worst scenario in our case pilot signals are sent at an interval of 3.3 s. The data from optical channel fall on a PD which gets converted to current. The current signal is mapped and demodulated.

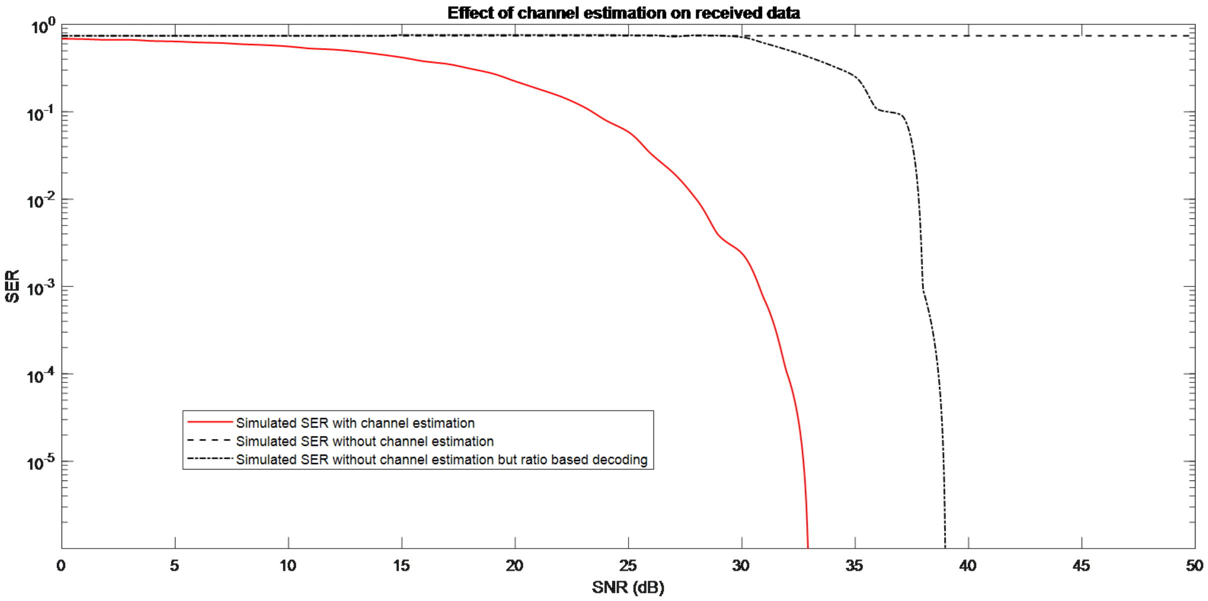

Figure 9.4: Effect of CSK-1PD receiver with different decoding schemes

9.1.3 Results and Discussion

The performance of the proposed safe, low-cost and accurate video EEG VLC system is evaluated on the basis of SER. The SER is plotted at various SNR under the assumption of LOS optical channel and AWGN noise. The effect of channel estimation is evaluated on the received data. There is severe degradation in the received data in case of no channel estimation as can be seen in Fig. 9.4. Further, the decoding without channel estimation is improved by using the

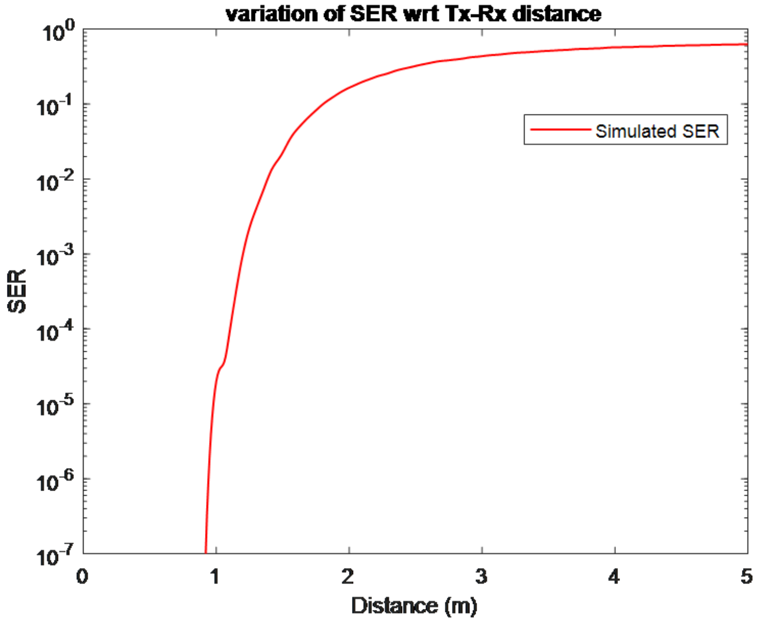

Figure 9.5: SER as a function of the distance between the transmitter and the receiver

ratio of the four different PD currents with the minimum current value for 4-CSK intensity levels. The video EEG data is transmitted using the proposed scheme to get SER performance at various levels of SNR. The decoding with channel estimation gives improvement of around 8 dB at SER 1×10^{-5}, thereby giving the best performance among the three cases.

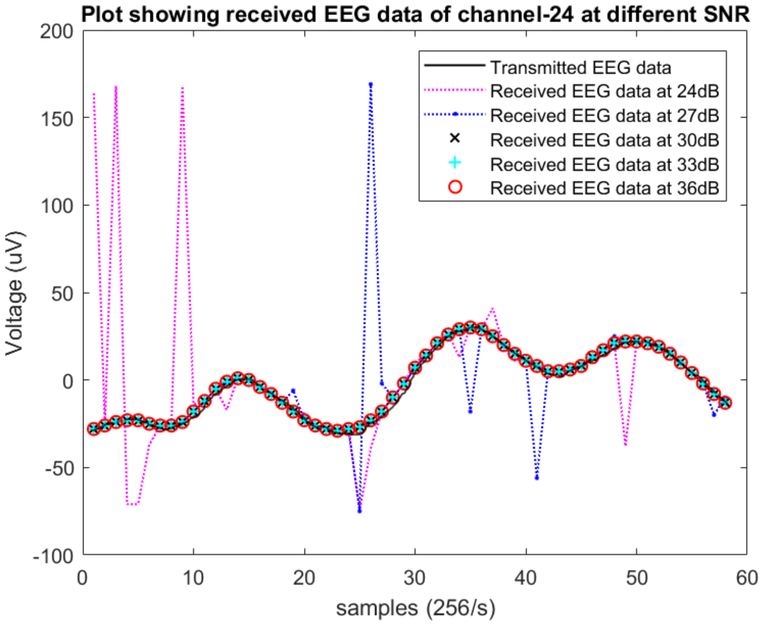

Figure 9.6: Comparison of received EEG data at varying SNR using proposed system

In Fig. 9.5, the SER rises rapidly and the system's accuracy declines as the distance between the transmitter and receiver is increased past 100 cm. It should be noted that an SNR value of 33 dB results in a SER of 1×10^{-5}. Due to the single PD decoding approach, a high SNR value is necessary for reliable communication. As a result, it is noted that there is a trade-off between the system's reliability and complexity. Since the indoor LED luminaire will also be utilized for illumination, which by default demands high optical intensity, therefore the need for high SNR is not a major barrier to reliable communication. A comparison of the sent and received EEG data at various SNRs is shown in Fig. Fig. 9.6. The system receives data more precisely and consistently as the SNR gets closer to 30 dB. EEG data can therefore be reliably sent above 30 dB. Furthermore, as can be seen in Tab. 9.2, the received video data is correlated with transmitted video data. It demonstrates the amount of SNR needed for accurate video data transmission. It gives high correlation at SNR greater than or equal to 33 dB. The video data limits the lower value of reliable SNR as slight decorrelation in video data causes substantial visible blur.

Table 9.2: Correlation of transmitted and received video data at different SNR.

SNR (in dB)	Correlation between Tx and Rx video data
24	0.8440
27	0.9519
30	0.9944
33	1
36	1

9.1.4 Summary

In this study, the RF radiation-free indoor healthcare VLC system is designed to transmit EEG and video data. To design a low complexity and low-cost system, single-PD receiver is used. While reducing complexity, the projection property of transmitted RGB signals over the sensitivity response of a single-PD has a negative impact on error performance. The simulation results demonstrate that the suggested system is capable of detecting EEG and video data inside a room at a variable distance ranging from 10 cm to 100 cm with a SER of 1×10^{-5}. The proposed system uses the ratio-based lookup table which improves the BER versus SNR performance at the receiver, even without channel estimation. Therefore, when using a ratio-based lookup table, the changing indoor environment has less of an impact on the demodulation of data. Further, when channel estimation is used the SNR decreases by 8 dB as compared to ratio-based decoding without channel estimation. The suggested system is demonstrated to be reliable at 33 dB SNR and can be further enhanced with lenses, high-speed LEDs, and high responsivity PD. Besides, source and channel coding may further reduce the SNR at a particular SER. The proposed system has the potential to enable VLC based healthcare system on a larger scale.

Dil Nashin Anwar and Anand Srivastava, “VLC-based safe, low-cost, and accurate healthcare system for video EEG using colour constellation scheme,” in *Proc. SPIE Photon*, Europe, Strasbourg, France, Apr. 2018, p. 1068549.

9.2 An experimental study of VLC

This work [209] illustrates that VLC utilizing on-the-shelf devices such as laptops and mobile phones can provide various attractive solutions to future communication challenges. Firstly, VLC has been experimentally demonstrated by developing a GUI for laptop-based system, where texts, files and images have been successfully transferred (*demonstration link*: https://drive.google.com/drive/folders/1ajuM9t0jKiQv6eU-gy47GaoJFhn6cUrj?usp=share_link). Secondly, for point-to-point reliable VLC to send text messages between two android based smart phones is developed and operated via an app. This study investigates how well a smartphone’s ambient light sensor functions as a VLC receiver.

9.2.1 System Architecture

The application layer is the graphical user interface (GUI), and the physical layer is the transmission of data using light. For simplicity, medium access control (MAC) layer has not been considered as the proof of concept is done for point-to-point communication. Conversion of data is required in the physical layer to transmit and receive data, to and from the upper layers. Physical layer does the modulation and demodulation of information. The transmitter and receiver of the proposed VLC systems are described below.

Transmitter: In case of the laptop, it consists of an Arduino Uno board [210] and a transmitter circuit. Laptops are connected to an external microcontroller ‘Arduino’. Users can create interactive electronic objects with this open-source electronic prototyping platform. LEDs in the transmitter circuit can be turned on and off to transmit data. For communication, two laptops having USB connection are used, one of which serves as a transmitter and the other as a receiver. The transmitter in the smartphone is an LED intended for flashlights.

Receiver: It too consists of an Arduino Uno board and a receiver circuit in a laptop-based VLC system. The receiver circuit has photoresistor (low cost off-the-shelf light sensor) which receives light pulses from the LED. The laptop gets data from the receiver circuit via the Arduino board. In smartphone system, receiver is the ambient light sensor.

(a) (b)

Figure 9.7: (a) Architecture diagram for laptop VLC system and (b) Demonstration setup for smartphone VLC.

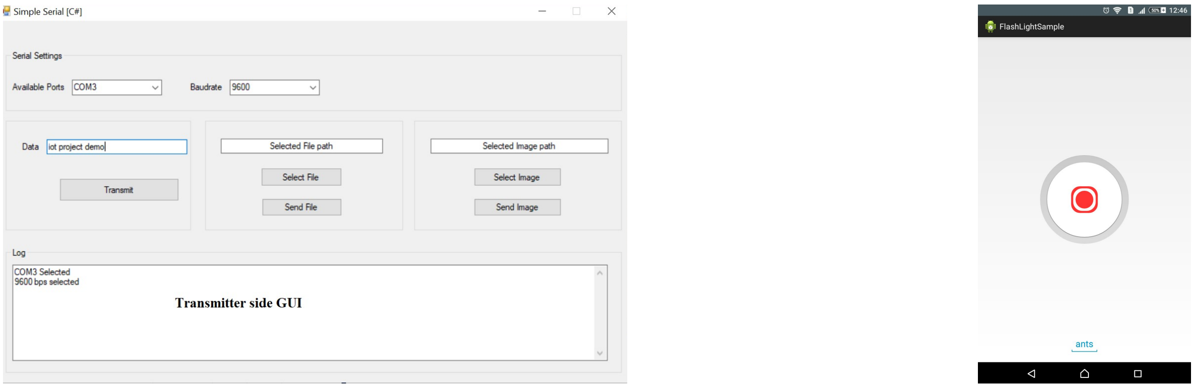
Simple Serial [C#]

Serial Settings

Available Ports: COM3

Baudrate: 9600

Data: iot project demo

Log

```
COM3 Selected
9600 bps selected
```

(a) (b)

Figure 9.8: (a) GUI for laptop VLC Transmitter and (b) App for Smartphone VLC Transmitter.

9.2.2 System Components

The system consists of three major components: sensing, processing, user interface (UI). These components can be hardware, software or both.

Sensing component: In the context of the photoresistor, a kind of light sensor: visible light coming out of the LED can be assumed to be the sensing component in this system. The presence of ambient light such as light from lamps inside a room or sunlight coming

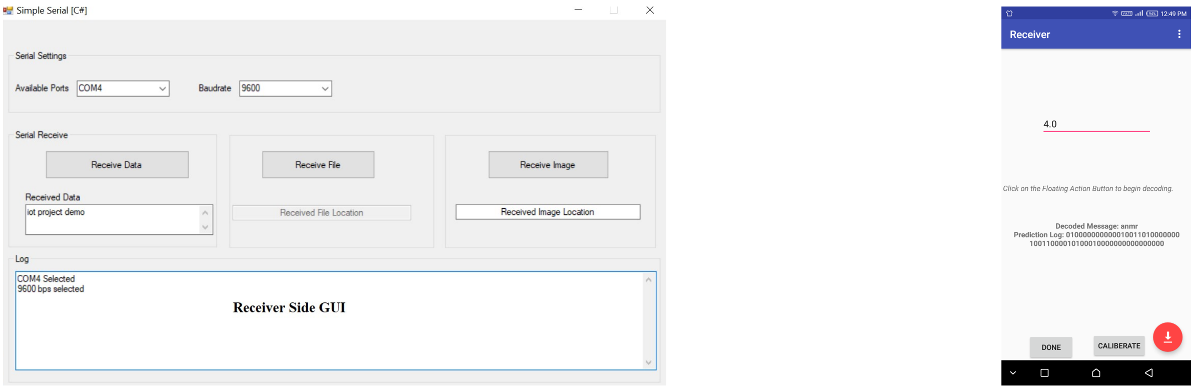

Available Ports: COM4

Baudrate: 9600

Received Data: iot project demo

```
COM4 Selected
9600 bps selected
```

4.0

Click on the Floating Action Button to begin decoding.

Decoded Message: anmr
Prediction Log: 0100000000000010011010000000 10011000010100010000000000000000

(a)

(b)

Figure 9.9: (a) GUI for laptop VLC Receiver and (b) App for Smartphone VLC Receiver.

from a window may hinder the sensing of the designated visible light coming from the LED. Typically, a high pass filter can be used to remove ambient light. However the aim is to utilize off-the-shelf devices and its processing power, therefore, the voltage value at the photoresistor is recorded when LED is turned on and off, to calibrate the “ON" threshold of LED. Taking the difference between the two values and applying it as "ON" "threshold renders ambient light ineffective. While the aforementioned process is carried out on a laptop-based system, it is made easier on smartphones by the ambient light sensor. The ambient light sensor eases out work of setting the appropriate threshold. Since the dominant part of the sensing component is LOS, the transmitter and receiver are in close proximity (LOS) for improved accuracy [211].

Processing component: The transmission is accomplished by representing the data as a sequence of bits. Processing the multimedia data from text or image to bitstream, then from bitstream to standard text or image format needs specific software and logic. Two Arduino Uno boards are used, one for processing data from transmitter laptop and another to process data at the receiver side. Data processing is carried out at both software and hardware level using C# and Arduino Uno board respectively in laptop VLC system. Here, processing happens at two places, one at the laptop and second at the Arduino. The data in a laptop is processed from text or image to bits using C# code and then modulated and sent to Arduino board.

This data is further handled and transformed into voltage levels to drive LED light by codes uploaded to the Arduino Uno board via Arduino IDE [212]. At the receiver, the current in photoresistor generates voltage, the analogue voltage value is converted to digital and then mapped to 0 or 1 bits at the Arduino board. The data received from Arduino board is processed again at the receiver laptop while demodulating and decoding it to text or image. All data is stored in the respective laptops having enough memory space.

The microprocessor inside smartphone powers the computing required for processing and memory chips provide data storage. Java supported software platforms [213] does all the processing of data. The basic steps of processing are the same as laptop-based VLC system.

UI component: For both the systems, GUI applications have been developed and demonstrated to interact user's with the VLC system. To send data such as text or image, GUI for transmitter and receiver application in Visual studio is designed for laptop-based VLC system. The transmitter and receiver GUI for smartphone is in the form of Java-based apps.

9.2.3 Demonstration: its challenges and solutions

In Fig. 9.7(a), the architecture of a laptop-based VLC system is displayed. The Arduino board is serially connected to the laptops. Bits of modulated data are sent from the transmitter laptop to the serial port, where the Arduino board receives them and drives the LED to blink in response. LED placed in the breadboard circuit goes on and off according to data bits. A photoresistor at the receiver detects the data, which Arduino then reads and converts from analogue to digital before writing to the serial port. The GUI displays the received file on the recipient laptop after reading the data from the serial port. The Fig. 9.8(a), 9.9(a) depict the transmitter and receiver GUI for laptop VLC system. For an accurate reading, the sensitivity of the photoresistor is adjusted using a resistor. Calibration is always performed before beginning communication since the threshold of photoresistor sensitivity changes with changing ambient light. All alphabets are represented by seven bits each for reliable transmission. The threshold value is again adjusted by heuristic method on getting the correlation between transmitted (all letters) and received data (all letters). Along with threshold, delay is also adjusted between bits to ensure that no overlap occurs between consecutive bits from the same alphabet incurring error due to the rapid transition of LED.

The system transmits data end-to-end reliably at a fixed baud rate only above a particular synchronised delay between LED blink and photoresistor detection. The prototype developed in this work [209] uses elementary synchronization by inserting header and footer. A user sends input data via the GUI, the GUI has different tabs for sending group of alphabets, text file or image file. Single alphabet or a group of alphabets are sent immediately to the serial port. However, for a text or an image file, conversion to suitable bits format is required which is done at the back end of the GUI and then is sent for modulation via serial port. Now, when Arduino is busy blinking LED according to a particular alphabet, the serial port is not in reading mode and losses data sent during that period. So, a delay according to the LED blinking time of an alphabet as well as the letter is inserted in C# code. The serial port write data after that delay only. This is how the synchronization is achieved between the user interface and a processing component.

In the case of smartphones, the inbuilt hardware system is used to communicate through the visible light as shown in Fig. 9.7(b). Sony xperiaT2 ultra smartphone is used for sending data whereas Infinix hotS3 is used for receiving data. The transmitter and receiver apps built for a mobile system are shown in Fig. 9.8(b) and Fig. 9.9(b), respectively. The ambient light sensor on a smartphone works well with practically any type of light source, including incandescent, fluorescent, and natural sunlight. Therefore, smartphones no longer need sensitivity settings. The front face of the smartphone serving as the receiver and the back surface serving as the transmitter are held in LOS. The delay between consecutive transitions of LED should be in such a way so that light sensor can detect it or else loss of data will occur. Similar to the laptop-based VLC system, the smartphone VLC system includes delays and synchronization on both the transmitter and receiver sides.

9.2.4 Results and Analysis

The performance of experimental results with respect to three parameters viz. synchronization delay, the distance between receiver and transmitter and varying indoor illuminance have been evaluated for laptop-based VLC system. The number of letters in error out of 26 letters for laptop-based VLC system can be seen in Fig. 9.10 for varying synchronization delay. As the synchronization delay increases, the error reduces to zero and reliable communication happens. The system works reliably till a limited distance between transmitter (Tx) and receiver (Rx) as shown in Fig. 9.11 and performs drastically poor after 5cm. This can be attributed to the lowest cost LED and photoresistor used in the prototype which is easily available in the labs of electronic engineering institutes and market. The value of varying indoor illuminance has been obtained from the smartphone receiver app which senses the ambient light. Since the amount of light received is measured in terms of voltage in smartphones, the intensity of indoor light has been displayed in digital values of voltage ranging from 0 to 5V. Even after calibrating the threshold voltage value, increasing ambient light intensity causes error (refer Fig. 9.12) because it saturates the photoresistor after a certain amount.

In smartphone to smartphone communication, the plot of delay versus error (Fig. 9.13) follows the same pattern like laptop-based VLC system, the only difference is that it requires high synchronization since a single computing element performs all the function in smartphone. Fig. 9.14 shows the letter error rate with respect to the distance in an indoor environment with light intensity of 4 (digital value of voltage). The distance performance is better than that of laptop VLC system as the flashlight LED and ambient light sensor of smartphone have longer range. The errors can be reduced by increasing synchronization delay up to a level only. Thereafter, no amount of delay can work as the intensity of flashlight will not be detected by the light sensor when distance increases.

The performance fluctuates in accordance with the indoor lighting conditions, as depicted in Fig. 9.15. The separation is maintained at 20 cm. When threshold voltage is 2 i.e. a dark environment, there is error as the sensor reads two ones instead of single one. This error is

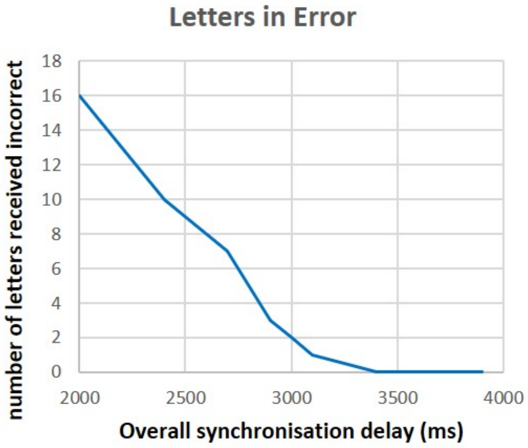

Figure 9.10: Laptop system: Letter error rate with respect to synchronization delay

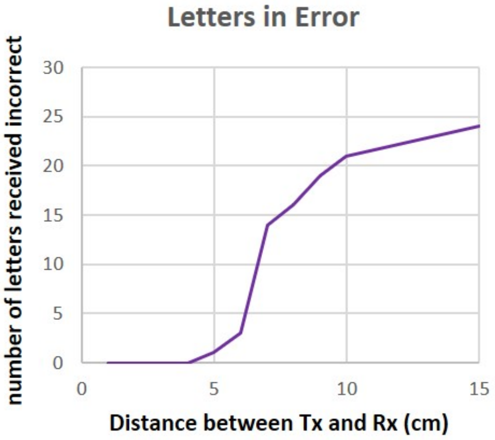

Figure 9.11: Laptop system: Letter error rate with respect to distance between Transmitter and Receiver

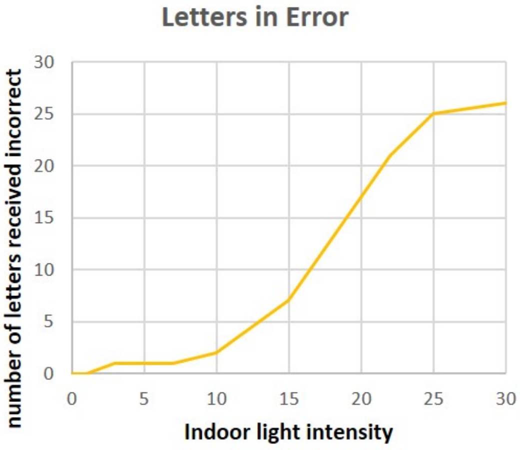

Figure 9.12: Laptop system: Letter error rate with respect to light intensity

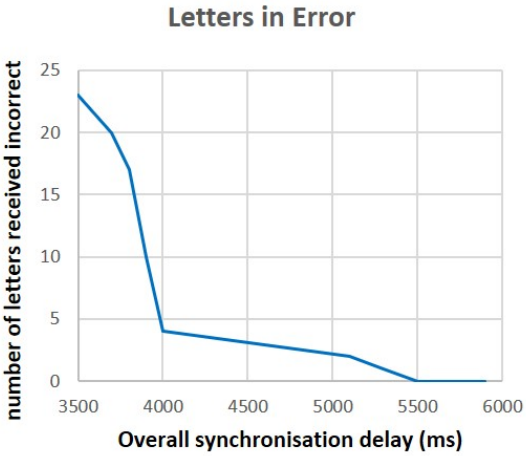

Figure 9.13: Smartphone: Letter error rate with respect to synchronization delay

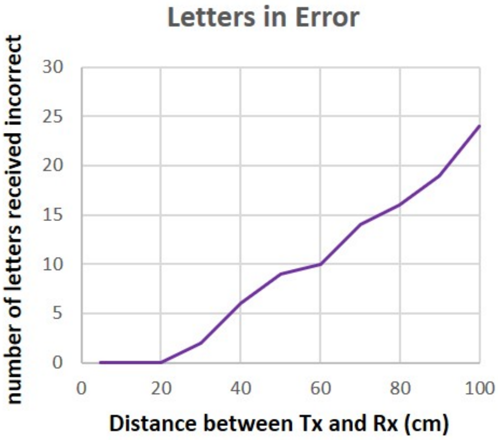

Figure 9.14: Smartphone: Letter error rate with respect to distance between sending and receiving mobiles

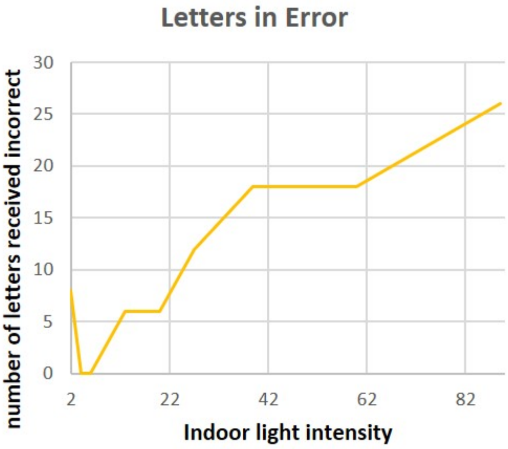

Figure 9.15: Smartphone: Letter error rate with respect to indoor illuminance

due to the instant increase in voltage at the light sensor, which takes some time to fall to the flashlight's off level and, as a result, also reads "one" in the second bit duration. Otherwise, it follows the intuitive pattern of increased errors with increased indoor ambient light intensity.

9.2.5 Limitations

The limitations and open issues of this work are as follows:

• *LED and a PD as hardware bottlenecks*: Regarding intensity of output light, off-the-shelf LED has limitations. The laptop system makes use of the least expensive, lowest-intensity LEDs available. The photoresistor struggles to detect the fast transition of bits from 0 to 1 or 1 to 0, as the resistance value takes time to increase or decrease. Hence, the performance is more constrained by the photoresistor's sensitivity than by the LED's transition speed. Performance can be enhanced by high-quality PD that is sensitive to various channel circumstances, such as in a dark room, a lighted room, and in the presence of sunlight.

• *No effect of increasing serial baud rate*: In a single Arduino board VLC system with one laptop serving as both the transmitter and the receiver, increasing the serial baud rate in the laptop system typically reduces the delay. Increasing serial baud rate, however, has no effect on transmission delay when the system uses two separate laptops, one as the transmitter and the other as the receiver, and there is no other form of communication between the two except for visible light. This is because of the constant synchronization delay between the GUI and processing component (GUI and Arduino in laptop system) to ensure reliable communication. Similar to laptop based system, the smartphone based VLC system is also constrained by the synchronization delay. As a result, the transmission latency is constrained by the synchronization delay.

9.2.6 Conclusion

Photoresistor sensitivity and synchronization between user input and processing component bottlenecks the speed of transmission. This work aimed for reliable VLC with off-the-shelf electronic devices which was achieved at the cost of compromised speed. In this work, the two-way communication between a laptop and a mobile device is experimentally shown. The communication speed of smartphone system is slower than that of the laptop system as delay in smartphone VLC system is greater than the laptop, because unlike laptop work is not divided into many processing components. Due to the use of inexpensive hardwares, the laptop system performs poorly when compared to smartphones in terms of distance and light intensity. In mobile system, ambient lights sensor adjusts itself to the surrounding light, so here by default, we do not need to adjust the threshold. The ambient threshold voltage value is utilized every-time to detect on or off of flashlight whereas in laptop system one needs to spare time and resources for calibration. A smartphone's built-in hardware is convenient, whereas a laptop-based system requires other hardware and is a little more complicated in terms of wires and external circuits. This work demonstrates adaptability of VLC for communication between IoT devices by achieving reliable communication of the order of a few Kbps between laptops and smartphones. The results of the experimental demonstration show that basic smartphones and laptops has enormous potential for on-the-fly VLC links.

Dil Nashin Anwar and Anand Srivastava, "Energy saver VLC using off-the-shelf devices: an experimental study," in *Proc. IEEE International Conference on Advanced Networks and Telecommunications Systems (ANTS)*, Indore, India, Dec. 2018, pp. 1-6.

9.3 VLC in Dynamic Indoor Environment

The channel of indoor VLC system is usually considered static for ease in most of the cases however in a real-world scenario, the changing effect due to people density, shadowing, dimming, background lights and interiors create dynamism in the VLC channel albeit with slow variation. Thus, the channel time-varying effect cannot be ignored entirely in modeling the VLC system. The impact of the dynamic channel can not be mitigated just by increasing LED transmission power. Fortunately, a possible alternative way is to estimate the channel state information (CSI) in dynamic VLC environment. This work [214] considers a dynamic VLC environment where a decrease in the normalized received power follows Rayleigh distribution. In this work, we propose the estimation of the channel coefficients using variants of least mean square (LMS) algorithm such as normalized (NLMS), zero attracting (ZA-LMS), block (BLMS) and fast block (FBLMS). This work tests the suitability of adaptive algorithms in terms of mean square error (MSE) and tap-weights convergence, computational complexity and the number of pilot symbols required in VLC dynamic channel.

9.3.1 Dynamic VLC Channel

The mobility of people within a room certainly affect the channel characteristics expressed in (2.9) and (2.11). The movement of the users inside a room can be modeled using effective people density (people/m^2). The authors in [215] take VLC LOS and NLOS channel [216] to simulate the effect of shadowing and blocking of the signal path due to obstacles present in the room. In the VLC channel with user movement, a decrease in the normalized received power can be empirically modelled to follow Rayleigh distribution given by the following equation:

$$p(x) = \frac{x}{\sigma^2}\exp\left(\frac{-x^2}{2\sigma^2}\right), \tag{9.4}$$

where, x is the normalized received power and (σ) represents the scale parameter. The scale parameter varies with the effective people density inside the room. For example, in furnished room with effective people density of 1.11 people/m^2, σ is 1.77 and in the case of non-furnished room with effective people density of 0.17 people/m^2 and 0.37 people/m^2, σ is 0.98 and 1.33, respectively. The Rayleigh channel defines the SNR pattern inside a room with user presence and movement.

The operation of any communication system is highly dependent on the channel behavior. Multi-path fading is typically absent from VLC channels. VLC channel may act as a frequency selective channel only when the LED modulation bandwidth exceeds B_c (channel coherence bandwidth), due to dispersion [217]. This uncertainty if not estimated correctly leads to an inaccurate analysis of the VLC channel. In VLC, varied settings of offices, corridors, rooms; changing Tx-Rx distances, different people density with mobility and various furniture setup may lead to a noticeable ISI at higher data transmission rates [215]. These channel characteristics will distort the signal received at the receiver so it is important to accurately estimate the slow time-varying channel and compensate at the receiver for reliable communication. As a result, channel estimation is necessary to provide detector with channel information within coherence time [218]. Additionally, the maximum data transmission rate should be within the coherence bandwidth of the VLC dynamic channel. The coherence time plays an important role in deciding the number of pilot symbols to estimate a channel. The coherence time of the channel can be calculated using the 50% coherence time formula $\tau_c = \frac{0.423c}{vf}$, where c is the speed of light and f is the transmitted signal frequency [208]. For a typical interior office setting, 5 km/hr is considered the maximum user mobility, or v. The coherence bandwidth B_c of the VLC dynamic channel changes with people density due to change in the root mean square (RMS)Root Mean Square delay spread [215]. For a flat channel, B_c sets an upper bound on f and the data rate R_b. The coherence time of the VLC channel can be computed using $f = B_c$. For, an office room B_c changes from 25 MHz to 19 MHz for an empty room to highest people density (1.11 people/m^2) considered in [215]. Hence, as the people density increase the coherence bandwidth B_c decreases, and the coherence time increases from 3.65 sec to 4.8 sec. Therefore, the number of samples (M) required to estimate the channel should satisfy, M<< $(R_b \times \tau_c)$. Consequently, the suitability of the different types of LMS estimation algorithms for estimating the VLC dynamic channel for an indoor setting has been analyzed. The block diagram of the proposed work is shown in Fig.9.16.

9.3.2 LMS ADAPTIVE ALGORITHM

The several adaptive filters based on least mean square methods are described in this part in order to estimate the channel coefficients. The output of the adaptive filter is $y = w^H x$, where, w

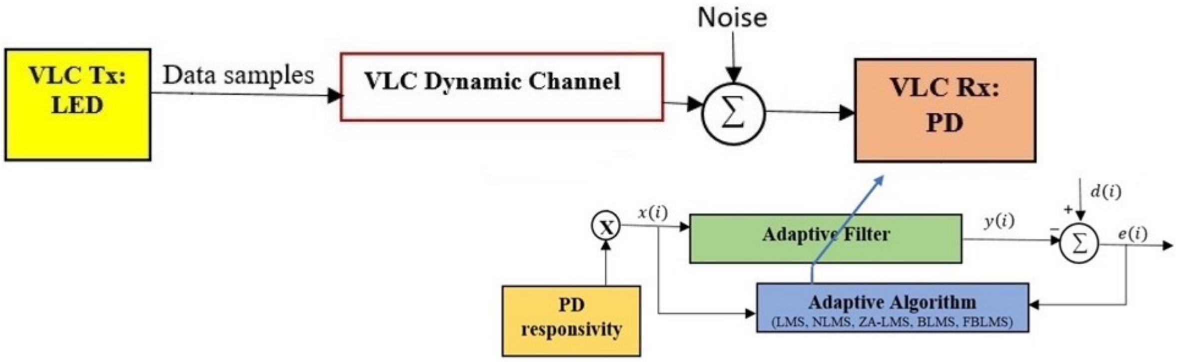

Figure 9.16: Block diagram of the proposed VLC system with adaptive channel estimation.

is the weight coefficient and x is the input signal. The error signal of a filter is $e(i) = d(i) - y(i)$, $d(i)$ is the desired response signal. The tap weights are time varying as they are functions of the time index i. The $(i+1)$th iteration i.e. $w(i+1)$ depends on (i)th iteration tap-weight, w is increased and estimated in such a way that it minimizes the error to ideal zero. The step-size parameter of the respective algorithms is μ [219]. The basic LMS algorithm remain stable when $0 < \mu < 2/tr[R]$, where $tr[R]$ is the trace of the auto correlation matrix $R = Ex(i)x^H(i)$ [220]. In the case of LMS, upper bound on μ comes out to be 2. Additionally, the upper limit on μ for any other LMS variant used in this work [214] is higher than the upper bound for the standard LMS μ. The choice of step-size μ influences the MSE convergence of adaptive algorithms. For each iteration, larger μ causes more change in the tap-weights, reducing error more quickly, but the reduced error does not approach the ideal solution, whereas smaller μ changes the tap-weights very slowly to approach resulting error to an ideal solution but is computationally intensive and MSE converges to a higher M value [220]. For fair comparison, the value of M is taken at 1×10^{-3} MSE. In order to ensure MSE convergence at 1×10^{-3} and tap-weights stability at the least number of pilot symbols, μ is selected differently for different algorithms within the practical bounds.

1. Least mean square (LMS): It is the most fundamental and widely applied algorithm. Tap-weights are adjusted continuously with $\mu = 1$. The LMS algorithm adjusts w, so that e is minimized in the mean-square logic.

$$w(i+1) = w(i) + \mu e(i)x(i). \tag{9.5}$$

2. Normalized LMS (NLMS): It considers the signal level variation at the filter input by selecting a normalized step-size parameter which results in stability and fast convergence. Here, μ is chosen to be 0.1. δ is a small positive constant i.e., 0.1 and

$$||x(i)||$$

is the Euclidean norm.

$$w(i+1) = w(i) + (10\mu)/(\delta + \|x(i)\|^2)e(i)x(i). \tag{9.6}$$

3. Zero attracting LMS (ZA-LMS): It is a special case of the regularized LMS family [221] where it favours sparsity in the input signal. For signum function, $sgn(x) = 0$, if $x = 0$ and $sgn(x) = x/|x|$ if $x \neq 0$. $\psi = \mu\varepsilon$ is the weight assigned to the penalty term, where $\mu = 1.5$ and ε (positive constant) = 0.002.

$$w(i+1) = w(i) + \mu e(i)x(i) - \psi sgn(w(i)). \tag{9.7}$$

4. Block LMS (BLMS): In this case, the tap-weights updates on blocks. The kth block and the sample time i relates as, $i = kL + i, i = 0, 1, ..., L-1$ &, $k = 1, ..., L$, where $L = 10$ is the block length assumed in the algorithm. $\mu = 0.5$ is considered [220].

$$w(i+1) = w(i) + \mu \sum_{j=0}^{L-1)} x(iL+j)e(iL+j). \tag{9.8}$$

5. Fast block LMS (FBLMS): It is a computationally efficient BLMS algorithm where tap-weights are adapted in the frequency domain. For $W(i)$ = FFT($[w^T(i), [0]^T_{m\times 1}]^T$), N-point FFT is used such that $N = 2m$. $\phi(i)$ consists of the first m elements of IFFT($X(i) \odot W(i)$), where $\odot$ is the Schur product operator. $X(i)$ is the FFT of x(t), where $t = im - m, ..., im + (m-1)$ [220]. The block length is 120 and the step-size is 0.04. The time domain tap-weights w as shown in (9.10) are finally plotted with respect to the number of samples.

$$W(i+1) = W(i) + \mu \text{FFT}([\phi(i)0]^T), \tag{9.9}$$

$$w = \text{IFFT}(W). \tag{9.10}$$

9.3.3 Results and Discussion

This study presents simulation results of the proposed work inside a standard office room of size of 6m×7m×3m. LED is kept “ON” to send pilot samples as long array of “1s” after that data is modulated in OOK. The responsivity of the PD is considered 1 ideally. The increasing people density inside an office room increases the number of pilot symbols required to estimate the channel as seen in Figs. 9.17. The tap-weight convergence value of the filter also increases with increase in people density as observed in Figs. 9.18.

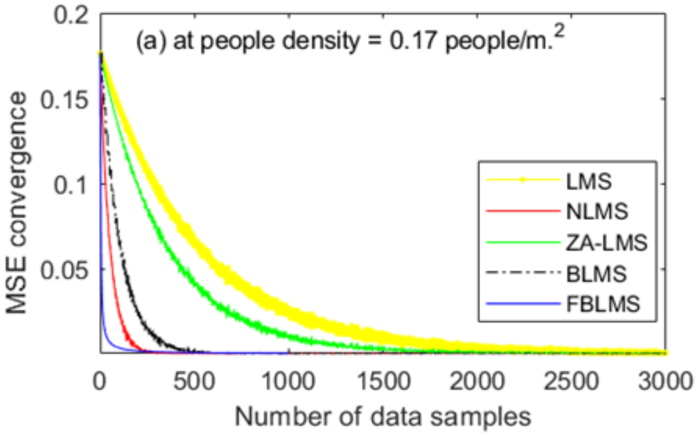

(a)

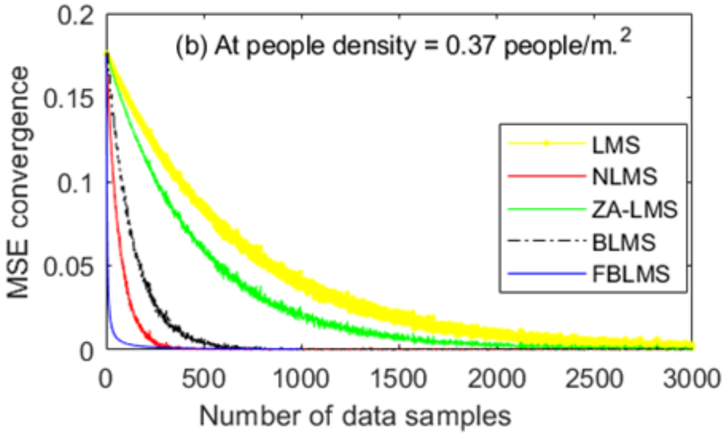

(b)

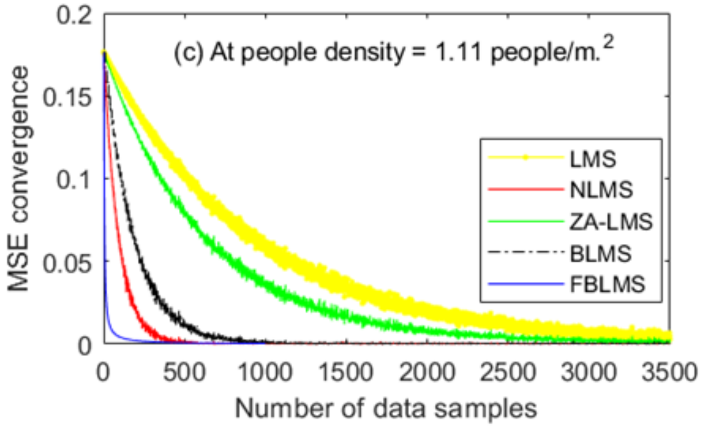

(c)

Figure 9.17: MSE convergence of the different channel estimations in VLC dynamic channel having people density (a) 0.17 people/m^2, (b) 0.37 people/m^2, (c) 1.11 people/m^2

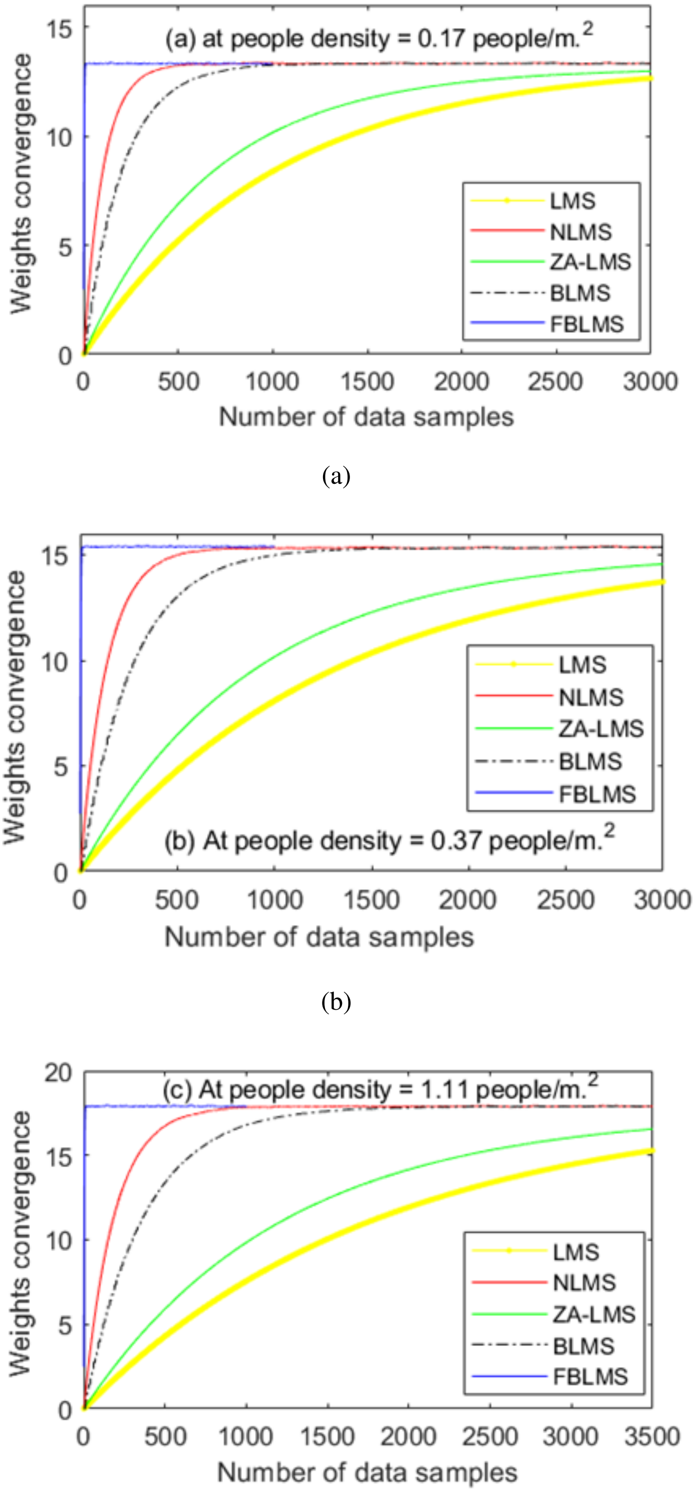

(a)

(b)

(c)

Figure 9.18: Filter weights convergence for different channel estimators in VLC dynamic channel having people density (a) 0.17 people/m^2, (b) 0.37 people/m^2, (c) 1.11 people/m^2

Table 9.3 shows M, the number of data samples or iterations at which MSE is of order 1x10^{-3}. The basic LMS method has the drawback of being sensitive to the input signal amplitude level $x(i)$, which results in greater values of M. ZA-LMS works better for sparse input signals which is not the case here. NLMS solves the problem of varying input by normalising with the power of the input, hence it gives better performance in this work. If the step-size is increased to 1, BLMS can perform similarly to NLMS in terms of M, and if the block size is increased to higher values, it can do better than NLMS, but the fall in convergence is sharp and the error floor is larger. Also, for tap-weights the convergence is very fast in FBLMS than any other algorithm due to estimation in blocks of samples in frequency domain. NLMS, BLMS, ZALMS and LMS tap-weights converges a little beyond their respective MSE convergence iteration number (referred as M in this work) as they all are adapted in time domain. The computational complexity of the algorithms are quoted in the table and its ratio with respect to standard LMS algorithm is calculated for a filter of 120-tap weights and sample block length, $L = 120$. As L increases beyond 39, the frequency domain LMS becomes superior to conventional LMS [222]. It is observed from Table 1 that finally FBLMS is the best choice as MSE converges very fast, the change in M is not much with the change in people density and the computational complexity is the least [223]. Therefore, in a VLC dynamic channel where the people density will change significantly, taking M = 300 will estimate the varying channel accurately.

Table 9.3: The number of MSE convergence iterations in estimating VLC channel with varying people density and the computational complexity of the respective estimation algorithms.

Adaptive Algorithms	**People density (0.16 people /m^2)**	**People density (0.37 people /m^2)**	**People density (1.11 people /m^2)**	**Computational complexity for a block of L samples in one iteration***	**Complexity ratio w.r.t. standard LMS**
	M	M	M	Multiplication	for $Q = L$=120
LMS	2700	3000	3500	(2Q+1) x L	1
NLMS	300	400	570	(3Q+1) x L	1.5
ZA-LMS	1700	2450	3450	(2Q+3) x L	1.008
BLMS	480	750	1000	(2Q x L+1)	0.995
FBLMS	200	240	300	10L x log2(L)+26L	0.394

*In order to have fair comparison between all algorithms, the computational complexity per sample per iteration is converted to per block (L samples per block) per iteration for calculating complexity ratio [222]. Q is the number of taps in a filter.

9.3.4 Summary

VLC in an indoor office environment with dynamic channel characteristic requires a suitable adaptive filter to estimate the channel. The number of samples required to estimate the dynamic channel depends highly on people density. With regard to the number of samples, FBLMS and NLMS have better error and tap-weights convergence. The difference in the number of samples for convergence at lower people density in FBLMS and NLMS is less. However, at increased people density FBLMS converges much faster to ideal zero MSE than NLMS. The results clearly show that, for the dynamic VLC channel under consideration, FBLMS is the most computationally efficient algorithm among LMS, NLMS, ZA-LMS, and BLMS. If someone wishes to estimate a channel in time domain with a little bit more complexity, NLMS would be a better choice.

Dil Nashin Anwar, Anand Srivastava and Vivek Ashok Bohara, “Adaptive Channel Estimation in VLC for Dynamic Indoor Environment,” in *Proc. 21st International Conference on Transparent Optical Networks (ICTON)*, Angers, France, 2019, pp. 1-5.

9.4 VLC versus RF communication in indoor environment

With the aim of saving power, this work [79] compares RF and VLC modulation techniques as standalone technologies in static and dynamic VLC environments. This work analyzes and compares the performance between RF and VLC modulation schemes of the same constellation order for a single user in an indoor setup. For instance, VLC OOK can be compared with RF binary phase shift keying (BPSK) and VLC M-CSK can be compared with RF quadrature-amplitude-modulation (M-QAM) schemes. Additionally, it has been computed how much power is saved by the VLC link in comparison to the RF link. The proposed system model as shown in Fig. 9.19 compares RF communication link coming from the BTS, and VLC from rooftop LED for an indoor environment. For the VLC connection, the channel gain indicated in (2.9) has been taken into account. The channel for RF is modeled as a frequency non-selective Rayleigh faded channel [224]. This work analyzes VLC link for two different channel models; i.e. static and dynamic with respect to WINNER-II path loss [224] modeled RF link.

This work compares the SER performance of the same size constellation-based modulation schemes of the RF and VLC link in an indoor room. As one looks for better performance, i.e., beyond SER 10^{-3}, the performance of VLC in various channel types (either static or dynamic) is significantly better than RF. Furthermore, as the constellation size grows, the SER gap between the VLC and RF narrows. This study demonstrates that there is a sizable power savings when using VLC link within a room as opposed to RF link, and at higher SNR the power savings approaches a very high percentage of 99.81. As SNR increases, both the

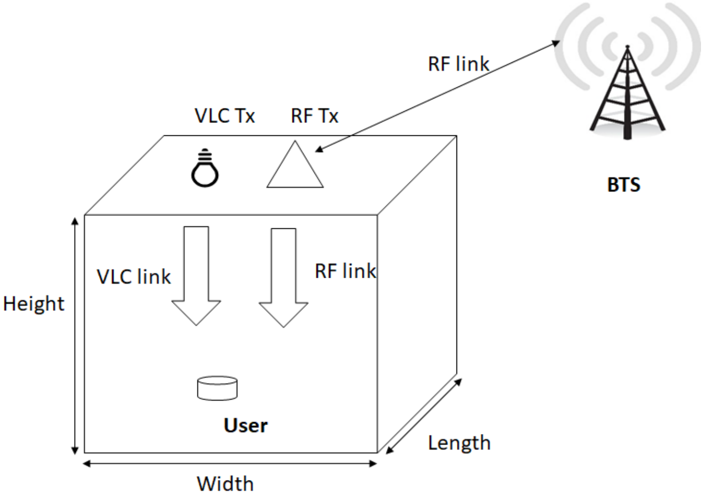

Figure 9.19: System model comparing RF communication link coming from the BTS, and VLC from rooftop LED for an indoor environment

VLC and RF systems experience a rise in signal power, however the VLC system experiences significantly less noise than the RF connection, resulting in a substantially smaller increase in VLC signal power than RF. Therefore, as SER decreases, the disparity between the average signal strengths of the RF and VLC likewise grows. Therefore, the huge difference in the value of noises in RF and VLC system allow for a significant power savings in VLC links. In general, VLC performs significantly better than RF in terms of power conservation. Additionally, the necessity for lighting is met by the high SNR requirement needed for greater performance.

Anand Singh, **Dil Nashin Anwar**, Anand Srivastava, Vivek Ashok Bohra, and G. S. VRK Rao, “Power and SER analysis of VLC- and RF-based links in indoor environment,” in *Proc. SPIE 10945, Broadband Access Communication Technologies XIII, 109450R*, San Francisco, U.S., Feb. 2019, p.109450R.

References

[1] V. Cisco, “Cisco annual internet report (2018–2023),” White Paper, 2019. [Online]. Available: https://www.cisco.com/c/en/us/solutions/collateral/executive-perspectives/annual-internet-report/white-paper-c11-741490.html

[2] ARM, “The route to a trillion devices:The outlook for IoT investment to 2035,” White Paper, 2017. [Online]. Available: https://community.arm.com/arm-community-blogs/b/internet-of-things-blog/posts/white-paper-the-route-to-a-trillion-devices

[3] T. Cogalan and H. Haas, “Why would 5G need optical wireless communications?,” in *IEEE 28th Annual International Symposium on Personal, Indoor, and Mobile Radio Communications (PIMRC)*, 2017, pp. 1–6.

[4] S. Arai, M. Kinoshita, and T. Yamazato, “Optical wireless communication: A candidate 6G technology? ,” *IEICE Transactions on Fundamentals of Electronics, Communications and Computer Sciences*, vol. 1, no. 104, pp. 227-234, 2021.

[5] W. Jiang, B. Han, M. A. Habibi, and H. D. Schotten, “The road towards 6G: A comprehensive survey,” *IEEE Open Journal of the Communications Society*, vol. 2, pp. 334–366, 2021.

[6] Z. Qadir, K. N. Le, N. Saeed, and H. S. Munawar, “Towards 6g internet of things: Recent advances, use cases, and open challenges,” *ICT Express*, 2022.

[7] “Light Communication Alliance,” [Online]. Available: http://lightcommunications.org/

[8] M. Z. Chowdhury, M. K. Hasan, M. Shahjalal, M. T. Hossan, and Y. M. Jang, “Optical wireless hybrid networks: Trends, opportunities, challenges, and research directions,” *IEEE Communications Surveys Tutorials*, 2020.

[9] L. U. Khan, “Visible light communication: Applications, architecture, standardization and research challenges,” Digital Communications and Networks, vol. 3, no. 2, pp. 78–88, 2017.

[10] N. Chi, H. Haas, M. Kavehrad, T. D. C. Little and X. Huang, “Visible light communications: demand factors, benefits and opportunities,” *IEEE Wireless Commun.*, vol. 22, no. 2, pp. 5–7, Apr. 2015.

[11] D. Karunatilaka, F. Zafar, V. Kalavally and R. Parthiban, “LED Based Indoor Visible Light Communications: State of the Art,” *IEEE Commun. Surveys Tut.*, vol. 17, no. 3, pp. 1649-1678, Mar. 2015.

[12] M. Alresheedi, A. T. Hussein, and J. Elmirghani, “Uplink design in VLC systems with IR sources and beam steering,” *IET Commun.*, vol. 11, no. 3, pp. 311-317, Feb. 2017.

[13] *ITU-T Rec. G.9991 - High-speed indoor visible light communication transceiver – System architecture, physical layer and data link layer specification*, Mar. 2019.

[14] I. Demirkol, D. Camps-Mur, J. Paradells, M. Combalia, W. Popoola and H. Haas, “Powering the Internet of Things through Light Communication,” *IEEE Commun. Mag.*, vol. 57, no. 6, pp. 107-113, Jun. 2019.

[15] H. Haas, L. Yin, Y. Wang and C. Chen, “What is LiFi?,” *J. Lightw. Technol.*, vol. 34, no. 6, pp. 1533-1544, Mar. 2016.

[16] D. C. Nguyen et al., “6G Internet of Things: A Comprehensive Survey,” *IEEE Internet of Things Journal*, vol. 9, no. 1, pp. 359-383, Jan. 2022, doi: 10.1109/JIOT.2021.3103320.

[17] M. Mozaffari, X. Lin and S. Hayes, “Toward 6G with Connected Sky: UAVs and Beyond,” *IEEE Communications Magazine*, vol. 59, no. 12, pp. 74-80, Dec. 2021, doi: 10.1109/MCOM.005.2100142.

[18] Xu Jiang, Min Sheng, Nan Zhao, Chengwen Xing, Weidang Lu, Xianbin Wang, “Green UAV communications for 6G: A survey,” *Chinese Journal of Aeronautics*, vol. 35, pp. 19-34, 2022.

[19] G. J. Holzmann and B. Pehrson, *The Early History of Data Networks (Perspectives)*, Wiley, 1994.

[20] A. A. Huurdeman, *The Worldwide History of Telecommunications*, Wiley Interscience, 2003.

[21] N. Haq, “Infrared wireless communication" (1996). Thesis. Rochester Institute of Technology.[Online]. Available: https://scholarworks.rit.edu/cgi/viewcontent.cgi?article=1055&context=theses

[22] A. G. Bell, W. Adams, W. Preece et al., “Discussion on the photophone and the conversion of radiant energy into sound,” *Journal of the Society of Telegraph Engineers*, vol. 9, no. 34, pp. 375–383, 1880.

[23] H. Haas, J. Elmirghani and I. White, “Optical wireless communication ,” *Phil. Trans. R. Soc. A.*, pp. 378: 2020005120200051, 2020. doi.org/10.1098/rsta.2020.0051

[24] T. Komine and M. Nakagawa, “Fundamental analysis for visible-light communication system using LED lights,” *IEEE transactions on Consumer Electronics*, vol. 50, no. 1, pp. 100–107, 2004.

[25] U. S. D. of Energy, “Energy savings forecast of solid-state lighting in general illumination applications,” *Global Market Insights*, 2020. [Online]. Available: http://apps1.eere.energy.gov/buildings/publications/pdfs/ssl/energysavingsforecast14.pdf

[26] P. S. Preeti Wadhwani, “LiFi market size forecast worth 8 billion usd by 2030,” Global Market Insights, 2020. [Online]. Available: https://www.gminsights.com/pressrelease/LiFi-market

[27] IEEE 802.15 WPAN task group 13 (TG13) multi-Gigabit/s optical wireless communications. [Online]. Available: https://www.ieee802.org/15/pub/TG13.html

[28] IEEE 802.11 Light Communication TG. [Online]. Available: https://www.ieee802.org/11/Reports/tgbb_update.htm

[29] ITU-T G.9991 (G.VLC). [Online]. Available: https://www.itu.int/ITU-T/workprog/wp_item.aspx?isn=13397

[30] Y. Yang, M. Chen, C. Guo, C. Feng, and W. Saad, “Power efficient visible light communication with unmanned aerial vehicles,” *IEEE Commun. Lett.*, vol. 23, no. 7, pp. 1272–1275, 2019.

[31] Z. Zhu, Y. Yang, C. Guo, M. Chen, S. Cui and H. V. Poor, "Power efficient deployment of VLC-enabled UAVs," in *IEEE 31st Annual Int. Symp. Pers. Indoor Mobile Radio Commun. (PIMRC)*, London, UK, Sept. 2020, pp. 1-6.

[32] H. Kaushal and G. Kaddoum, “Underwater optical wireless communication,” *IEEE access*, vol. 4, pp. 1518–1547, 2016.

[33] R. Bian, I. Tavakkolnia, and H. Haas, “15.73 Gb/s visible light communication with off-the-shelf LEDs,” *Journal of Lightwave Technology*, vol. 37, no. 10, pp. 2418–2424, 2019.

[34] H. Kazemi, M. Safari and H. Haas, “A wireless backhaul solution using visible light communication for indoor Li-Fi attocell networks,” in *proc. IEEE International Conference on Communications (ICC)*, May 2017, pp. 1-7.

[35] Y.-K. Cheong, X.-W. Ng, and W.-Y. Chung, “Hazardless biomedical sensing data transmission using VLC,” *IEEE sensors journal*, vol. 13, no. 9, pp. 3347-3348, 2013.

[36] S. Muhammad, S. H. A. Qasid, S. Rehman, and A. B. S. Rai, “Visible light communication applications in healthcare,” *Technology and Health Care*, vol. 24, no. 1, pp. 135-138, 2016.

[37] A. Memedi and F. Dressler, “Vehicular visible light communications: A survey,” *IEEE Communications Surveys Tutorials*, 2020.

[38] Air France, “In a world first, Air France tests Li-Fi technology during a flight, in partnership with Latécoère and Ubisoft,” [Online]. Available: https://corporate.airfrance.com/en/news/world-first-air-france-tests-li-fi-technology-during-flight-partnership-latecoere-and-ubisoft

[39] Y. Zhuang, L. Hua, L. Qi, J. Yang, P. Cao, Y. Cao, Y. Wu, J. Thompson, and H. Haas, “A survey of positioning systems using visible LED lights,” *IEEE Communications Surveys & Tutorials*, vol. 20, no. 3, pp. 1963–1988, 2018.

[40] G. Pang, T. Kwan, C.-H. Chan, and H. Liu, “LED traffic light as a communications device,” in *Proc. IEEE/IEEJ/JSAI International Conference on Intelligent Transportation Systems (Cat. No. 99TH8383)*. IEEE, 1999, pp. 788–793.

[41] K. Kulhavy, “Home: ronja,” RONJA, 2012.

[42] Y. Tanaka, S. Haruyama, and M. Nakagawa, “Wireless optical transmissions with white colored LED for wireless home links,” in *Proc. IEEE International Symposium on Personal Indoor and Mobile Radio Communications (PIMRC)*, vol. 2. IEEE, 2000, pp. 1325–1329.

[43] J. Vucic, C. Kottke, S. Nerreter, K. Habel, A. Buttner, K.-D. Langer, and J. Walewski, “125 Mbit/s over 5 m wireless distance by use of OOK-modulated phosphorescent white LEDs,” in *Proc. IEEE European Conference on Optical Communication*, 2009, pp. 1–2.

[44] J. Vucic, C. Kottke, S. Nerreter, K.-D. Langer, and J. W. Walewski, "513 Mbit/s visible light communications link based on DMT-modulation of a white LED," *Journal of lightwave technology*, vol. 28, no. 24, pp. 3512–3518, 2010.

[45] J. Vucic, C. Kottke, K. Habel, and K.-D. Langer, "803 Mbit/s visible light WDM link based on DMT modulation of a single RGB LED luminary," in *Proc. OSA Optical Fiber Communication Conference*, 2011, p. OWB6.

[46] C. Kottke, K. Habel, L. Grobe, J. Hilt, L. F. del Rosal, A. Paraskevopoulos, and K.-D. Langer, "Single channel wireless transmission at 806 Mbit/s using a white-light LED and a PIN-based receiver," in *Proc. IEEE 14th International Conference on Transparent Optical Networks (ICTON)*, 2012, pp. 1–4.

[47] L. E. M. Matheus, A. B. Vieira, L. F. M. Vieira, M. A. M. Vieira and O. Gnawali, "Visible light communication: concepts, applications and challenges," *IEEE Commun. Surveys Tut.*, vol. 21, no. 4, pp. 3204-3237, Apr. 2019.

[48] R. Ahmad, M. D. Soltani, M. Safari, A. Srivastava, and A. Das, "Reinforcement learning based load balancing for hybrid LiFi WiFi networks," *IEEE Access*, vol. 8, pp. 132273–132284, Jul. 2020.

[49] *IEEE Standard for Local and metropolitan area networks–Part 15.7: Short-Range Optical Wireless Communications*, IEEE Std 802.15.7-2018 (Revision of IEEE Std 802.15.7-2011), pp.1-407, Apr. 2019.

[50] P. H. Pathak, X. Feng, P. Hu, and P. Mohapatra, "Visible light communication, networking, and sensing: A survey, potential and challenges," IEEE communications surveys tutorials, vol. 17, no. 4, pp. 2047–2077, 2015.

[51] D. O'Brien, S. Rajbhandari, and H. Chun, "Transmitter and receiver technologies for optical wireless," Philosophical Transactions of the Royal Society A, vol. 378, no. 2169, p. 20190182, 2020.

[52] A. Wilkins, J. Veitch and B. Lehman, "LED lighting flicker and potential health concerns: IEEE standard PAR1789 update," in *Proc. IEEE Energy Convers. Congr. Expo. (ECCE)*, Atlanta, GA, USA, Nov. 2010, pp. 171–178.

[53] E. Monteiro and S. Hranilovic, "Design and Implementation of Color-Shift Keying for Visible Light Communications," *J. Lightw. Technol.*, vol. 32, no. 10, pp. 2053-2060, May 15, 2014.

[54] R. Singh, T. O'Farrell and J. P. R. David, "An Enhanced Color Shift Keying Modulation Scheme for High-Speed Wireless Visible Light Communication," *J. Lightw. Technol.*, vol. 32, no. 14, pp. 2582-2592, July 15, 2014.

[55] J. M. Luna-Rivera, R. Perez-Jimenez, V. Guerra-Yañez, C. Suarez-Rodriguez and F. A. Delgado-Rajo, "Combined CSK and pulse position modulation scheme for indoor visible light communications," *Electron. Lett.*, vol. 50, no. 10, pp. 762-764, May 8, 2014.

[56] N. Murata, Y. Kozawa and Y. Umeda, "Digital Color Shift Keying With Multicolor LED Array," *IEEE Photonics J.*, vol. 8, no. 4, pp. 1-13, Aug. 2016.

[57] S. Igata, Y. Kozawa, Y. Umeda and H. Habuchi, "BER performance of digital color shift keying with target color control," in *Proc. 10th Int. Conf. Sig. Processing Commun. Sys. (ICSPCS)*, Gold Coast, QLD, Dec. 2016, pp. 1-6.

[58] D. Pilori, L. Bertignono, A. Nespola, F. Forghieri and G. Bosco, "Comparison of Probabilistically Shaped 64QAM With Lower Cardinality Uniform Constellations in Long-Haul Optical Systems," *J. Lightw. Technol.*, vol. 36, no. 2, pp. 501-509, Jan. 15, 2018.

[59] T. A. Eriksson, M. Chagnon, F. Buchali, K. Schuh, S. ten Brink and L. Schmalen, "56 Gbaud Probabilistically Shaped PAM8 for Data Center Interconnects," in *Proc. European Conf. Opt. Commun. (ECOC)*, Gothenburg, Sep. 2017, pp. 1-3.

[60] X. Han and I. B. Djordjevic, "Probabilistically Shaped 8-PAM Suitable for Data Centers Communication," in *Proc. 20th Int. Conf. Transparent Opt. Netw. (ICTON)*, Bucharest, July 2018, pp. 1-4.

[61] D. U. Campos-Delgado, J. M. Luna-Rivera, R. Perez-Jimenez, C. A. Gutiérrez, V. Guerra, and J. Rabadán, "Constellation design for color space-based modulation in visible light communications," *Phy. Commun.*, vol. 31, pp. 154-159, Apr. 2018.

[62] R.J. Drost, and B.M. Sadler, "Constellation design for color-shift keying using billiards algortihms," in *Proc. IEEE Globecom Workshops*, Miami, FL, Dec. 2010, pp. 980-984.

[63] R. J. Drost and B. M. Sadler, "Constellation design for channel precompensation in multi-wavelength visible light communications," *IEEE T. Commun.*, vol. 62, no. 6, pp. 1995-2005, Jun. 2014.

[64] E. Monteiro and S. Hranilovic, "Constellation design for color-shift keying using interior point methods," in *Proc. IEEE Globecom Workshops*, Anaheim, CA, Dec. 2012, pp. 1224-1228.

[65] Q. Gao, Rui Wang, Z. Xu and Y. Hua, “Power-efficient high-dimensional constellation design for visible light communications," in *Proc. Opto-Electron. Commun. Conf. (OECC)*, Shanghai, June/July 2015, pp. 1-3.

[66] Q. M. Qadir, T. A. Rashid, N. K. Al-Salihi, B. Ismael, A. A. Kist and Z. Zhang, “Low Power Wide Area Networks: A Survey of Enabling Technologies, Applications and Interoperability Needs,” *IEEE Access*, vol. 6, pp. 77454-77473, Nov. 2018.

[67] Qualcomm Technologies, “Narrowband IoT (NB-IoT),” RP-151621, 3GPP TSG RAN Meeting 69, Sep. 2015. [Online]. Available: http://www.3gpp.org/ftp/tsg_ran/TSG_RAN/TSGR_69/Docs/RP-151621.zip

[68] H. Pirayesh, P. K. Sangdeh and H. Zeng, “Coexistence of WiFi and IoT Communications in WLANs,” *IEEE Internet Things J.*, vol. 7, no. 8, pp. 7495-7505, Aug. 2020.

[69] R. Ahmad and A. Srivastava, “PAPR reduction of OFDM signal through DFT precoding and GMSK pulse shaping in indoor VLC,” *IEEE Access*, vol. 8, pp. 122092-122103, Jul. 2020.

[70] D. N. Anwar and A. Srivastava, “Design and Analysis of Probabilistic Shaping in Color Shift Keying Modulation Schemes,” *IEEE System Journal*, vol. 15, no. 1, pp. 1433-1444, Mar. 2021, doi: 10.1109/JSYST.2020.3007391.

[71] D. N. Anwar and A. Srivastava, “Constellation Design for Single Photodetector based CSK with Probabilistic Shaping and White Color Balance,” *IEEE Access*, vol. 8, pp. 159609-159621, Aug. 2020, doi: 10.1109/ACCESS.2020.3020403.

[72] D. A. Basnayaka and H. Haas, “A New Degree of Freedom For Energy Efficiency of Digital Communication Systems,” *IEEE Trans. Commun.*, vol. 65, no. 7, pp. 3023-3036, Jul. 2017.

[73] R. Raj, G. Pandey and A. Dixit, “Tunable Receiver Design for Spatially Distributed Wireless Optical Sensors in IoT Networks,” in *Proc. IEEE Int. Conf. Commun. (ICC)*, Dublin, Ireland, 7-11 Jun. 2020, pp. 1-6.

[74] A. Fotouhi, H. Qiang, M. Ding, M. Hassan, L. G. Giordano, A. Garcia-Rodriguez, and J. Yuan, “Survey on uav cellular communications: Practical aspects, standardization advancements, regulation, and security challenges,” *IEEE Commun. Surv. Tut.*, vol. 21, no. 4, pp. 3417–3442, Fourthquarter 2019.

[75] Y. Zeng, Q. Wu, and R. Zhang, “Accessing from the sky: A tutorial on uav communications for 5g and beyond,” *Proceedings of the IEEE*, vol. 107, no. 12, pp. 2327–2375, Dec. 2019.

[76] Y. Tanaka, S. Haruyama, and M. Nakagawa, “Wireless optical transmissions with white colored LED for wireless home links,” in *Proc. IEEE 11th Symp. Pers. Indoor Mobile Radio Commun. (PIMRC)*, London, UK, Sept. 2000, pp. 1325–1329.

[77] H. Deng, J. Li, A. Sayegh, S. Birolini, and S. Andreani, “Twinkle: A flying lighting companion for urban safety,” in *Proc. of the ACM 12th Int. Conf. Tangible, Embedded, Embodied Interaction*, Stockholm, Sweden, Mar. 2018, pp. 567–573.

[78] Draganfly, [Online]. Available: https://draganfly.com/

[79] A. Singh, D. N. Anwar, A. Srivastava, V. A. Bohara, and G. S. VRK Rao "Power and SER analysis of VLC- and RF-based links in indoor environment", in *SPIE 10945, Broadband Access Commun. Technol. XIII*, Feb. 2019, p. 109450R.

[80] M. Obeed, A. M. Salhab, M. -S. Alouini and S. A. Zummo, “On Optimizing VLC Networks for Downlink Multi-User Transmission: A Survey,” *IEEE Commun. Surveys Tut.*, vol. 21, no. 3, pp. 2947-2976, 3rd Quart., 2019.

[81] F. Lagum, I. Bor-Yaliniz, and H. Yanikomeroglu, “Strategic densification with uav-bss in cellular networks,” *IEEE Wirel. Commun. Lett.*, vol. 7, no. 3, pp. 384–387, Jun. 2018.

[82] C. Zhan, Y. Zeng, and R. Zhang, “Trajectory design for distributed estimation in uav-enabled wireless sensor network,” *IEEE Trans. Veh. Technol.*, vol. 67, no. 10, pp. 10 155–10 159, Oct. 2018.

[83] M. Peer, V. A. Bohara, A. Srivastava, and G. Ghatak, “User mobility aware time stamp for uav-bs placement,” in *IEEE Wirel. Commun. Netw. Conf. Workshops (WCNCW)*, Mar. 2021, pp. 1–6.

[84] Lecture notes, “COMPSCI 530: Design and analysis of algorithms,” chapter 16 slides, Fall 2013, Computer Science and Engineering Department, Duke University, North Carolina, [Online]. Available: https://courses.cs.duke.edu//fall13/compsci530/notes/lec16.pdf.

[85] L. Liu, S. Zhang, and R. Zhang, “CoMP in the sky: UAV placement and movement optimization for multi-user communications,” *IEEE Trans. Commun.*, vol. 67, no. 8, pp. 5645–5658, Aug. 2019.

[86] R. Ghanavi, E. Kalantari, M. Sabbaghian, H. Yanikomeroglu, and A. Yongacoglu, “Efficient 3D aerial base station placement considering users mobility by reinforcement learning,” in *IEEE Wirel. Commun. Netw. Conf. (WCNC)*, Barcelona, Spain, Apr. 2018, pp. 1–6.

[87] X. Liu, Y. Liu, Y. Chen, and L. Hanzo, “Trajectory design and power control for multi-uav assisted wireless networks: A machine learning approach,” *IEEE Transactions on Vehicular Technology*, vol. 68, no. 8, pp. 7957–7969, 2019.

[88] H. V. Abeywickrama, Y. He, E. Dutkiewicz, B. A. Jayawickrama, and M. Mueck, “A reinforcement learning approach for fair user coverage using uav mounted base stations under energy constraints,” *IEEE Open J. Veh. Technol.*, vol. 1, pp. 67–81, Feb. 2020.

[89] J. Wang, C. Jiang, Z. Han, Y. Ren, R. G. Maunder and L. Hanzo, “Taking drones to the next level: cooperative distributed unmanned-aerial-vehicular networks for small and mini drones,” *IEEE Veh. Technol. Mag.*, vol. 12, no. 3, pp. 73-82, Sept. 2017.

[90] Y. Wang, M. Chen, Z. Yang, T. Luo, and W. Saad, “Deep learning for optimal deployment of UAVs with visible light communications,” *IEEE Trans. Wirel. Commun.*, vol. 19, no. 11, pp. 7049– 7063, Nov. 2020.

[91] Q.-V. Pham, T. Huynh-The, M. Alazab, J. Zhao, and W.-J. Hwang, “Sum-rate maximization for uav-assisted visible light communications using noma: Swarm intelligence meets machine learning,” *IEEE Internet Things J.*, vol. 7, no. 10, pp. 10 375–10 387, Oct. 2020.

[92] J. M. Luna-Rivera, C. Suarez-Rodriguez, V. Guerra, R. Perez-Jimenez, J. Rabadan-Borges and J. Rufo-Torres, “Low-complexity colour-shift keying-based visible light communications system,” *IET Optoelectron.*, vol. 9, no. 5, pp. 191-198, Oct. 2015.

[93] A. A. Khan, M. H. Rehmani, and A. Rachedi, “When cognitive radio meets the Internet of Things?” in *Proc. Int. Wireless Commun. Mobile Comput. Conf. (IWCMC)*, Paphos, Cyprus, Sep. 2016, pp. 469–474.

[94] D. Yang, Y. Xu, and M. Gidlund, “Wireless coexistence between IEEE802.11-and IEEE 802.15.4-based networks: A survey,” *Int. J. of Distrib. Sens. Netw.*, vol. 7, no. 1, pp. 912152, Jul. 2011.

[95] A. Shahini, A. Kiani and N. Ansari, "Energy Efficient Resource Allocation in EH-Enabled CR Networks for IoT," *IEEE Internet Things J.*, vol. 6, no. 2, pp. 3186-3193, Apr. 2019.

[96] A. W. Azim, “Signal processing techniques for optical wireless communication systems,” Ph.D. dissertation, Université Grenoble Alpes, France, Jan. 2019. [Online]. Available: https://tel.archives-ouvertes.fr/tel-01973203

[97] D. N. Anwar, R. Ahmad and A. Srivastava, "Energy-Efficient Coexistence of LiFi Users and Light Enabled IoT Devices," *IEEE Transactions on Green Communications and Networking*, vol. 6, no. 2, pp. 930-950, Jun. 2022, doi: 10.1109/TGCN.2021.3116267.

[98] D. N. Anwar, M. Peer, K. Lata, A. Srivastava and V. A. Bohara, “3-D Deployment of VLC Enabled UAV Networks with Energy and User Mobility Awareness”, *IEEE Transaction on Green Communications and Networking*, vol. 6, no. 4, pp. 1972-1989, Dec. 2022, doi: 10.1109/TGCN.2022.3171920.

[99] S. D. Dissanayake and J. Armstrong, "Comparison of ACO-OFDM, DCO-OFDM and ADO-OFDM in IM/DD Systems," *J. Lightw. Technol.*, vol. 31, no. 7, pp. 1063-1072, Apr. 2013.

[100] Luminit, “Technical data sheet on light shaping diffusers,” USA, 2012. [Online]. Available: https://www.luminitco.com/sites/default/files/LSD_Tech_Datasht_5_21_12_lo_0.pdf

[101] D. Wu, Z. Ghassemlooy, H. Le-Minh, S. Rajbhandari, and L. Chao “Channel characteristics analysis of diffuse indoor cellular optical wireless communication systems", in *proc. SPIE 8309, Opt. Transmission Syst., Subsystems, Technol. IX*, Shanghai, China, Dec. 2011, p. 83090P.

[102] J. M. Kahn and J. R. Barry, “Wireless infrared communications,” *Proceedings of the IEEE*, vol. 85, no. 2, pp. 265–298, 1997.

[103] J. R. Barry, J. M. Kahn, W. J. Krause, E. A. Lee, and D. G. Messerschmitt, “Simulation of multipath impulse response for indoor wireless optical channels,” *IEEE journal on selected areas in communications*, vol. 11, no. 3, pp. 367–379, 1993.

[104] Y. Qiu, H.-H. Chen, and W.-X. Meng, “Channel modeling for visible light communications: a survey,” *Wireless Commun. Mob. Comput.*, vol. 16, no. 14, pp. 2016–2034, Oct. 2016.

[105] A. Burton, H. Le Minh, Z. Ghassemlooy, S. Rajbhandari and P. A. Haigh, “Performance analysis for $180 PhDComprehensiveExamination$ receiver in visible light communications,” in *Proc. 4th Int. Conf. Commun. Electron. (ICCE)*, Hue, Aug. 2012, pp. 48-53.

[106] M. A. Arfaoui, M. D. Soltani et al., “Measurements-Based Channel Models for Indoor LiFi Systems,” *IEEE Trans. Wireless Commun.*, vol. 20, no. 2, pp. 827-842, Feb. 2021.

[107] H. Schulze, “Frequency-domain simulation of the indoor wireless optical communication channel,” *IEEE Transactions on Communications*, vol. 64, no. 6, pp. 2551–2562, June 2016.

[108] V. Jungnickel, V. Pohl, S. Nonnig, and C. von Helmolt, “A physical model of the wireless infrared communication channel,” *IEEE Journal on Selected Areas in Communications*, vol. 20, no. 3, pp. 631–640, 2002.

[109] S. M. Moser, “Capacity results of an optical intensity channel with input-dependent gaussian noise,” *IEEE Trans. Inform. Theory*, vol. 58, no. 1, pp. 207-223, Jan. 2012.

[110] Q. Gao, S. Hu, and Z. Xu, “Modulation designs for visible light communications with signal-dependent noise," *J. Lightwave Technol.*, vol. 34, no. 23, pp. 5516-5525, Dec. 2016.

[111] J. Wang, H. Ge, J. Zhu, J. Wang, J. Dai, and M. Lin, “Adaptive spatial modulation for visible light communications with an arbitrary number of transmitters,” *IEEE Access*, vol. 6, pp. 37 108–37 123, 2018.

[112] J. Grubor, S. Randel, K.-D. D. Langer, and J. Walewski, “Broadband information broadcasting using LED-based interior lighting,” *J. Lightw. Technol.*, vol. 26, no. 24, pp. 3883–3892, Dec. 2008.

[113] J. M. Senior, and M. Y. Jamro, *Optical Fiber Communications: Principles and Practice*. 3rd ed. Prentice Hall, 2008.

[114] K.-I. Ahn and J. K. Kwon, “Capacity analysis of M-PAM inverse source coding in visible light communications,” *J. Lightw. Technol.*, vol. 30, no. 10, pp. 1399–1404, Jan. 2012.

[115] J.-B. Wang, Q.-S. Hu, J. Wang, M. Chen, and J.-Y. Wang, “Tight bounds on channel capacity for dimmable visible light communications,” *J. Lightw. Technol.*, vol. 31, no. 23, pp. 3771–3779, Dec. 2013.

[116] A. Chaaban, Z. Rezki, and M.-S. Alouini, “Fundamental limits of parallel optical wireless channels: capacity results and outage formulation,” *IEEE Trans. Commun.*, vol. 65, no. 1, pp. 296–311, Jan. 2017.

[117] D. Tsonev, S. Videv, and H. Haas, “Light fidelity (li-fi): towards all-optical networking,” in *proc. Broadband Access Communication Technologies VIII*, vol. 9007. International Society for Optics and Photonics, 2014, p. 900702.

[118] D. N. Anwar and A. Srivastava, “Energy saver VLC using off-the-shelf devices: an experimental study,” in *proc. IEEE International Conference on Advanced Networks and Telecommunications Systems (ANTS)*, Indore, India, Dec. 2018, pp. 1-6.

[119] JH. Yoo, SY. Jung, “Modeling and analysis of variable PPM for visible light communications,” *J Wireless Com Network*, vol. 134, May 2013.

[120] K. Lee and H. Park, “Modulations for visible light communications with dimming control,” *IEEE Photonics Technology Letters*, vol. 23, no. 16, pp. 1136-1138, Aug., 2011.

[121] S. Arnon, Visible light communication. Cambridge University Press, 2015.

[122] A. Yokoi, J. Son, and T. Bae, “More description about CSK constellation,” Mar. 2011, IEEE 802.15 contribution 15-11-0247-00-0007. [Online]. Available: http://mentor.ieee.org/802.15/dcn/11/15-11-0247-00-0007-csk-constellation-in-all-color-bandcombinations.pdf.

[123] J. Armstrong and B. J. Schmidt, “Comparison of asymmetrically clipped optical OFDM and DC-biased optical OFDM in AWGN,” IEEE Communications Letters, vol. 12, no. 5, 2008.

[124] Z.-p. Wang and S.-z. Zhang, “Grouped DCT precoding for PAPR reduction in optical direct detection OFDM systems,” Optoelectronics Letters, vol. 9, no. 3, pp. 213–216, 2013.

[125] J. Wangetal, “PAPR analysis for OFDM visible light communication”, *Opt. Express*, vol. 24, no. 24, pp. 27457–27474, Nov. 2016.

[126] N. Fernando, Y. Hong, and E. Viterbo, “Flip-OFDM for optical wireless communications,” in Information Theory Workshop (ITW). IEEE, 2011, pp. 5–9.

[127] R. Singh, T. O’Farrell and J. P. R. David, “Performance evaluation of IEEE 802.15.7 CSK physical layer,” in *Proc. IEEE Globecom Workshops*, Atlanta, GA, Dec. 2013, pp. 1064-1069.

[128] D. N. Anwar and A. Srivastava, “VLC-based safe, low-cost, and accurate healthcare system for video EEG using colour constellation scheme,” in *Proc. SPIE Photon*, Europe, Strasbourg, France, Apr. 2018, p. 1068549.

[129] Thorlabs, *Avalanche Photodetector APD120A Operational Manual.* (2020). Accessed: Jun. 18, 2020. [Online]. Available: https://www.thorlabs.com/drawings/4f5dccb6170aa80-C472A90B-9433-7458-BF40EEB470A3E8AF/APD120A-Manual.pdf

[130] S. Baur and G. Boecherer, "Arithmetic Distribution Matching," in *Proc. 10th Int. ITG Conf. Syst., Commun. Coding*, Hamburg, Germany, Feb. 2015, pp. 1-6.

[131] T. M. Cover, J. A. Thomas, *Elements of information theory*. Wiley-Interscience, 2006.

[132] G.Bocherer, "Capacity-achieving probabilistic shaping for noisy and noiseless channels," Ph.D. dissertation, RWTH Aachen University, Germany, 2012. [Online]. Available: http://www.georg-boecherer.de/capacityAchievingShaping.pdf

[133] Z. Qu and I. B. Djordjevic, "On the Probabilistic Shaping and Geometric Shaping in Optical Communication Systems," *IEEE Access*, vol. 7, pp. 21454-21464, Feb. 2019.

[134] Aditya K. Jagannatham, *Principles of modern wireless communication systems*. New Delhi, India: McGraw-Hill Education India Pvt.Ltd, 2015.

[135] S. Arora, and B. Barak, *Computational Complexity: A Modern Approach*. Cambridge, U.K.: Cambridge Univ. Press, 2009.

[136] J. Rissanen and G. G. Langdon, "Arithmetic Coding," *IBM J. Res. Dev.*, vol. 23, no. 2, pp. 149-162, Mar. 1979.

[137] A. F. Finger, A. B. Loreto and V. S. Furlan, "The Computational Complexity of Random Variables with Uniform, Exponential and Pareto Distributions in Real and Interval Forms," in *Proc. 2nd Workshop-School Theor. Comput. Sci. (WEIT)*, Rio Grande, Oct. 2013, pp. 79-83.

[138] T. Yoshida, M. Karlsson and E. Agrell, "Low-Complexity Variable-Length Output Distribution Matching with Periodical Distribution Uniformalization," in *Proc. Opt. Fiber Commun. Conf. Expo. (OFC)*, San Diego, California, Mar. 2018, pp. 1-3.

[139] J. G. Proakis and D. G. Manolakis, *Digital Signal Processing: Principles, Algorithms and Applications*. 3rd ed. New Delhi, India: Prentice-Hall, 2005.

[140] K. Vasudevan, *Digital Communications and Signal Processing*. 2nd ed. Chennai, India: Universities Press (India) Private Limited, 2010.

[141] L. Jia, J. Wang, W. Zhang, M. Chen and J. Wang, “Symbol error rate analysis for colour-shift keying modulation in visible light communication system with RGB light-emitting diodes,” *IET Optoelectron.*, vol. 9, no. 5, pp. 199-206, Oct. 2015.

[142] J. Tang, L. Zhang and Z. Wu, “Exact Bit Error Rate Analysis for Color Shift Keying Modulation,” *IEEE Commun. Lett.*, vol. 22, no. 2, pp. 284-287, Feb. 2018.

[143] R. Chen, “Solution of minimax problems using equivalent differentiable functions," *Comput. Math. Appl.*, vol. 11, pp. 12, pp. 1165–1169, 1985.

[144] Qu, Zhen, Ivan B. Djordjevic, and Jon Anderson, “Two-dimensional constellation shaping in fiber-optic communications,” *Appl. Sci.*, vol. 9, no. 9, p. 1889, May 2019.

[145] J. Nocedal and S. J. Wright, *Numerical Optimization*, New York: Springer-Verlag, 1999.

[146] P. Charbonnea, “An Introduction to Genetic Algorithms for Numerical Optimization," National Center for Atmospheric Research, Colorado, U.S., Tech. Note NCAR/TN-450+IA, Mar. 2002. [Online]. Available: http://cobweb.cs.uga.edu/~potter/CompIntell/no_tutorial.pdf

[147] B. Moore, G. Takahara, and F. Alajaji, “Pairwise optimization of modulation constellations for non-uniform sources,” *Can. J. Elect. Comput. Eng.*, vol. 34, no. 4, pp. 167-177, fall 2009.

[148] E. F. Schubert, *Light Emitting Diodes*, 2nd ed., NY: Cambridge University Press, 2006.

[149] W. Y. Kim, Y. H. Kim, C. G. Jhun, R. Wood, P. Mascher and C. B. Moon, “Spectroscopic study of white organic light-emitting devices with various thicknesses of emissive layer,” *J. Appl. Phys.*, vol. 111, no. 1, p. 014507, Jan. 2012.

[150] K. L. Kosanke and B. J. Kosanke, “Selected pyrotechnic publications of KL and BJ Kosanke, Part 1: 1981 through 1989,” in *Pyrotechnic Literature Series*, illustrated ed., Journal of Pyrotechnics, Inc., 1995.

[151] V. Singh and A. K. Mishra, “White light emission from vegetable extracts,” *Sci. Rep. 5*, p. 11118, Jun. 2015.

[152] P. Babu, K. H. Jang, E. S. Kim, L. Shi and H. J. Seo, “Optical properties and white-light emission in Dy3+-doped transparent oxyfluoride glass and glass ceramics containing CaF2 nanocrystals,” *J. Korean Phys. Soc.*, vol.54, no.4, pp.1488-1491, Apr. 2009.

[153] A. Narkhede and D. Manocha, “Fast polygon triangulation based on seidel’s algorithm,” in *Graphics Gems V*, Academic Press, Inc., Elsevier, 1995, ch. VII.5, pp. 394-397.

[154] K. Hormann, Kai and A. Agathos, “The point in polygon problem for arbitrary polygons,” *Comput. Geom.* vol. 20, no. 3, pp. 131-144, Mar. 2001.

[155] M. W. Hodapp, “Applications for high-brightness light-emitting diodes,” in *Semiconductors and Semimetals*, Academic Press, Inc., Elsevier, 1997, ch. 6, pp. 227-356.

[156] S. Chaturvedi, D. N. Anwar, V. A. Bohara, A. Srivastava and Z. Liu, “Low-Complexity Codebook Design for SCMA-Based Visible Light Communication”, *IEEE Open Journal of the Communications Society*, vol. 3, pp. 106-118, 2022, doi: 10.1109/OJCOMS.2022.3141800.

[157] J. Tang and L. Zhang, “Efficient Real-Fourier Domain-Based Color Shift Keying OFDM Implemented with Hartley Transform for Visible Light Communication System,” in *Proc. IEEE 85th Veh. Technol. Conf. (VTC-Spring)*, Sydney, Australia, Jun. 2017, pp. 1-5.

[158] A. W. Azim, Y. Le Guennec and G. Maury, “Spectrally Augmented Hartley Transform Precoded Asymmetrically Clipped Optical OFDM for VLC,” *IEEE Photon. Technol. Lett.*, vol. 30, no. 23, pp. 2029-2032, Dec. 2018.

[159] X. Liang, M. Yuan, J. Wang, Z. Ding, M. Jiang and C. Zhao, “Constellation Design Enhancement for Color-Shift Keying Modulation of Quadrichromatic LEDs in Visible Light Communications," *J. Lightw. Technol.*, vol. 35, no. 17, pp. 3650-3663, Sep. 2017.

[160] L. Cui, Y. Tang, H. Jia, J. Luo and B. Gnade, “Analysis of the Multichannel WDM-VLC Communication System," *J. Lightw. Technol.*, vol. 34, no. 24, pp. 5627-5634, Dec. 2016.

[161] *IEEE P802.11bb - Standard for Information Technology Telecommunications and Information Exchange Between Systems Local and Metropolitan Area Networks– Part 11: Wireless LAN Medium Access Control (MAC) and Physical Layer (PHY): Light Communications*, Mar. 2021.

[162] A. D. Poularikas, “The Hartley Transform” *The Handbook of Formulas and Tables for Signal Processing*. USA: CRC and IEEE Press, 1999.

[163] Michael P. Knapp, “Sines and cosines of angles in arithmetic progression,” *Math. Mag.*, vol. 82, no. 5, pp. 371-372, Dec. 2009.

[164] Y. Cui, Y. Wang and J. Bergqvist et al., “Wide-gap non-fullerene acceptor enabling high-performance organic photovoltaic cells for indoor applications,” *Nat. Energy*, vol. 4, no. 9, pp. 768-775, Sep. 2019.

[165] Fowdur, Tulsi Pawan, and Louvi Doorganah. “Performance of modified and low complexity pulse shaping filters for IEEE 802.11 OFDM transmission.” *J. Inf. Telecommun.*, vol.3, no. 3, pp. 361-380, Jul. 2019.

[166] F. B. Offiong, S. Sinanović and W. O. Popoola, “Pilot-Aided Frame Synchronization in Optical OFDM Systems,” *Appl. Sci.*, vol. 10, no. 11, pp. 4034, Jan. 2020.

[167] M. M. Freda and J. M. Murray, “Low-complexity blind timing synchronization for ACO-OFDM-based optical wireless communications,” in *Proc. IEEE Globecom Workshops*, Miami, USA, Dec. 2010, pp. 1031-1036.

[168] D. Bankov, A. Didenko, E. Khorov and A. Lyakhov, “OFDMA Uplink Scheduling in IEEE 802.11ax Networks,” in *Proc. IEEE Int. Conf. Commun. (ICC)*, Kansas City, USA, May 2018, pp. 1-6.

[169] J. S. Ramos, I. Demirkol, J. Paradells, D. Vössing, K. M. Gad and M. Kasemann, “Towards energy-autonomous wake-up receiver using Visible Light Communication,” in *Proc. IEEE Consumer Commun. Netw. Conf. (CCNC)*, Las Vegas, USA, Jan. 2016, pp. 544-549.

[170] Humamatsu Photonics, K. K. “Technical Information-SD12-Characteristics and use of Infrared Detectors." *Hamamatsu-Solid State Division*, Japan 2004.

[171] Arubha networks, “802.11ax white paper”, USA, 2018. [Online]. Available: https://www.arubanetworks.com/assets/wp/WP_802.11AX.pdf

[172] T. Beke, E. Dijk, T. Ozcelebi and R. Verhoeven, “Time Synchronization in IoT Mesh Networks," in *Proc. International Symposium on Networks, Computers and Communications (ISNCC)*, Montreal, QC, Canada, 2020, pp. 1-8, doi: 10.1109/ISNCC49221.2020.9297296.

[173] Z. Idrees et al., “IEEE 1588 for Clock Synchronization in Industrial IoT and Related Applications: A Review on Contributing Technologies, Protocols and Enhancement Methodologies," *IEEE Access*, vol. 8, pp. 155660-155678, 2020, doi: 10.1109/ACCESS.2020.3013669.

[174] X. Guo, M. Mohammad, S. Saha, M. C. Chan, S. Gilbert and D. Leong, “PSync: Visible light-based time synchronization for Internet of Things (IoT)," in *Proc. IEEE INFOCOM 2016 - The 35th Annual IEEE International Conference on Computer Communications*, San Francisco, CA, USA, 2016, pp. 1-9, doi: 10.1109/INFOCOM.2016.7524358.

[175] Z. Yu, R. J. Baxley, and G. T. Zhou, “Peak-to-average power ratio and illumination-to-communication efficiency considerations in visible light OFDM systems,” in *Proc. IEEE Int. Conf. Acoust., Speech Signal Process.*, May 2013, pp. 5397–5401.

[176] R. Zayani, H. Shaiek and D. Roviras, “PAPR-Aware Massive MIMO-OFDM Downlink,” *IEEE Access*, vol. 7, pp. 25474-25484, Feb. 2019.

[177] Shieh, William, and Ivan B. Djordjevic, “*OFDM for optical communications*”, Academic press, 2009. [Online]. Available: https://www.arubanetworks.com/assets/wp/WP_802.11AX.pdfhttps://www.sciencedirect.com/book/9780123748799/ofdm-for-optical-communications

[178] Kyongkuk Cho and Dongweon Yoon, “On the general BER expression of one- and two-dimensional amplitude modulations,” *IEEE Trans. Commun.*, vol. 50, no. 7, pp. 1074-1080, Jul. 2002.

[179] D. Bertsekas and R. Gallager, *Data Networks*, 2nd ed. NJ, USA: Prentice-Hall, 1991.

[180] Y. Chang, F. Chien and C. J. Kuo, “Performance Comparison of OFDM-TDMA and OFDMA with Cross-Layer Consideration,” in *Proc. IEEE Veh. Technol. Conf. (VTC)*, Montreal, Canada, Sep. 2006, pp. 1-5.

[181] C. Bettstetter, H. Hartenstein, and X. Pérez-Costa, “Stochastic properties of the random waypoint mobility model,” *Wireless Netw.*, vol. 10, no. 5, pp. 555-567, Sep. 2004.

[182] A. Gupta and P. Garg, “Statistics of SNR for an Indoor VLC System and its Applications in System Performance,” *IEEE Commun. Lett.*, vol. 22, no. 9, pp. 1898-1901, Sep. 2018.

[183] D. Wu, Z. Ghassemlooy, H. LeMinh, S. Rajbhandari and Y. S. Kavian, “Power distribution and Q-factor analysis of diffuse cellular indoor visible light communication systems," in *proc. 16th European Conf. Netw. Opt. Commun.*, Newcastle upon Tyne, UK, Jul. 2011, pp. 28-31.

[184] M. A. Boon, A. P. Drijfhout, and Solomon Tesfamichael, “Comparison of a fixed-wing and multi-rotor uav for environmental mapping applications: A case study,” *Int. Arch. Photogramm. Remote Sens. Spat. Inf. Sci. (ISPRS)*, vol. 42, p. 47, Aug. 2017.

[185] M. Mozaffari, W. Saad, M. Bennis, Y. H. Nam and M. Debbah, “A tutorial on UAVs for wireless networks: applications, challenges, and open problems,” *IEEE Commun. Surv. Tut.*, vol. 21, no. 3, pp. 2334-2360, thirdquarter 2019.

[186] I. Din and H. Kim, “Energy-efficient brightness control and data transmission for visible light communication,” *IEEE photon. technol. lett.*, vol. 26, no. 8, pp. 781–784, Apr. 2014.

[187] HyperPhysics: Light and Vision [Online]. Available: http://hyperphysics.phy-astr.gsu.edu/hbase/vision/efficacy.html#c1

[188] A. Sarkar, S. K. Singh, N. Jain, and V. Dwidedi, “India-energy-efficient street lighting: implementation and financing solutions,” The World Bank, Tech. Rep., 2015.

[189] Yiguang Wang, Xingxing Huang, Jianyang Shi, Yuan-quan Wang, and Nan Chi, “Long-range high-speed visible light communication system over 100-m outdoor transmission utilizing receiver diversity technology,” *SPIE: Optical Engineering*, vol. 55, no. 5, p. 056104, May 2016.

[190] P. Cherntanomwong and P. Namonta, “The repeater system for visible light communication,” in *proc. 7th Int. Conf. Inf. Technol. Elect. Eng. (ICITEE)*, Chiang Mai, Thailand, Oct. 2015, pp. 489-493.

[191] P. Namonta and P. Cherntanomwong, “The improvement of repeater system for visible light communication,” in *proc. 13th Int. Conf. Elect. Eng./Electron., Comp., Telecommun. Inf. Technol. (ECTI-CON)*, Chiang Mai, Thailand, Jun.-Jul. 2016, pp. 1-6.

[192] R. Jain, D.-M. Chiu, and W. R. Hawe, *A quantitative measure of fairness and discrimination for resource allocation in shared computer system*, Hudson, MA, USA: Eastern Research Laboratory, Digital Equipment Corporation, 1984, vol. 38.

[193] Y. Zeng, J. Xu, and R. Zhang, “Energy minimization for wireless communication with rotary-wing uav,” *IEEE Trans. Wirel. Commun.*, vol. 18, no. 4, pp. 2329–2345, Apr. 2019.

[194] A. Asudeh, T. Berger-Wolf, B. DasGupta, and A. Sidiropoulos, “Maximizing coverage while ensuring fairness: a tale of conflicting objective,” *arXiv preprint arXiv:2007.08069*, Jul. 2020.

[195] G. Laporte, “The traveling salesman problem: An overview of exact and approximate algorithms,” *Eur. J. Oper. Res.*, vol. 59, pp. 231–247, Jun. 1992.

[196] L. Siklóssy, E. Tulp, “The space reduction method: a method to reduce the size of search spaces,” *Inf. Processing Lett.*, vol. 38, pp. 187-192, May 1991.

[197] S. Arora, “Polynomial time approximation schemes for euclidean traveling salesman and other geometric problems,” *J. ACM*, vol. 45, pp. 753-782, Sep. 1998.

[198] V. Vazirani, *Approximation Algorithms*, 1st ed., Berlin: Springer, 2001.

[199] A. J. Martin, “Towards an energy complexity of computation,” *Inf. Process. Lett.* 77.2-4, pp. 181-187, Feb. 2001.

[200] R. Jain, D. Molnar, and Z Ramzan, “Towards a model of energy complexity for algorithms,” in *proc. IEEE Wirel. Commun. Netw. Conf.*, New Orleans, LA, USA, Mar. 2005, vol. 3, pp. 1884-1890.

[201] T. H. Cormen, C. E. Leiserson, R. L. Rivest and C. Stein, *Introduction to Algorithms*, 3rd ed., Cambridge, England: MIT Press, Massachusetts, London, 2009.

[202] MA. Perera, M. Katz, J. Häkkinen, R. Godaliyadda, “Light-Based IoT: developing a full-duplex energy autonomous IoT node using printed electronics technology,” *Sensors*, vol. 21, no. 23, p.8024, Dec. 2021.

[203] A. Perera, M. Katz, R. Godaliyadda, J. Hakkinen, E. Strommer, “Light-Based Internet of Things: implementation of an optically connected energy-autonomous node,” in *Proc. IEEE Wireless Commun. Networking Conf. (WCNC)*, Nanjing, China, Mar. 2021; pp. 1–7.

[204] M. D. Soltani, A. A. Purwita, Z. Zeng, H. Haas and M. Safari, “Modeling the random orientation of mobile devices: measurement, analysis and LiFi use case,” *IEEE Trans. Commun.*, vol. 67, no. 3, pp. 2157-2172, Mar. 2019.

[205] Thorlabs, *PDA36A2 Si Switchable Gain Detector User Guide.* (2020). Accessed: Jun. 18, 2020. [Online]. Available: https://www.thorlabs.com/drawings/4f5dccb6170aa80-C472A90B-9433-7458-BF40EEB470A3E8AF/PDA36A2-Manual.pdf

[206] J. An and W.-Y. Chung, “A novel indoor healthcare with time hopping-based visible light communication”, in *proc. IEEE 3rd World Forum on Internet of Things (WF-IoT)*, 2016, p. 19-23.

[207] Miramirkhani, F. and Uysal, M., “Channel modeling and characterization for visible light communications”, *IEEE Photonics Journal*, vol. 7, no. 6, pp. 1-16, Dec. 2015.

[208] Theodore S. Rappaport, “Wireless communications: principles and practice”, vol. 2, New Jersey: prentice hall PTR, 1996.

[209] D. N. Anwar and A. Srivastava, “Energy saver VLC using off-the-shelf devices: an experimental study,” in *Proc. IEEE International Conference on Advanced Networks and Telecommunications Systems (ANTS)*, Indore, India, Dec. 2018, pp. 1-6.

[210] Arduino, “Arduino - Home,” Accessed on July 03, 2018. [online] Available: https://www.arduino.cc/.

[211] K. Cui, G. Chen, Z. Xu, and R. D. Roberts, “Line-of-sight visible light communication system design and demonstration,” in *7th International Symposium on. IEEE, Communication Systems Networks and Digital Signal Processing (CSNDSP)*, 2010 , 2010, pp. 621–625.

[212] Arduino, “Arduino - Software,” Accessed on July 03, 2018. [online] Available: https://www.arduino.cc/en/Main/Software.

[213] G. Developers, “Androidstudio,” Accessed on July 04, 2018. [online] Available: https://developer.android.com/studio/.

[214] D. N. Anwar, A. Srivastava and V. A. Bohara, “Adaptive Channel Estimation in VLC for Dynamic Indoor Environment,” in *Proc. 21st International Conference on Transparent Optical Networks (ICTON)*, Angers, France, 2019, pp. 1-5.

[215] Chvojka, Petr, et al., “Channel characteristics of visible light communications within dynamic indoor environment,” *Journal of Lightwave Technology*, vol. 33, no .9, pp. 1719-1725, 2015.

[216] Burton, Andrew, et al., “Performance analysis for 180 receiver in visible light communications,” *IEEE Fourth International Conference on Communications and Electronics (ICCE)*, 2012.

[217] Al-Kinani, Ahmed, et al, “Optical wireless communication channel measurements and models." IEEE Communications Surveys & Tutorials 20.3 (2018): 1939-1962.

[218] Shawky, Eman, et al, “Optical channel estimation based on Kalman filtering for VLC systems adopting DCO-OFDM,” *IEEE 20th International Conference on Transparent Optical Networks (ICTON)*, 2018.

[219] Haykin, Simon, Adaptive Filter Theory, Prentice-Hall, Inc., 1996.

[220] Farhang-Boroujeny, B., Adaptive Filters: Theory and Applications, Chichester, England, Wiley, 1998.

[221] Chen, Yilun, Yuantao Gu, and Alfred O. Hero, “Regularized least-mean-square algorithms,” arXiv preprint arXiv:1012.5066 (2010).

[222] Block Adaptive Filters and Frequency Domain Adaptive Filters, Tampere University of Applied science, [online] Available: http://www.cs.tut.fi/~tabus/course/ASP/SGN2206LectureNew6.pdf

[223] Farhang-Boroujeny, Behrouz, and Kheong Sann Chan,“Analysis of the frequency-domain block LMS algorithm,”*IEEE Transactions on Signal Processing*, vol. 48, no. 8, 2000, pp. 2332-2342.

[224] Y. D. J. Bultitude and T. Rautiainen, IST-4-027756 WINNER II D1. 1.2 V1. 2 WINNER II channel models," EBITG, TUI, UOULU, CU/CRC, NOKIA, Tech. Rep., Tech. Rep, 2007.